# Remote sensing of rapidly draining supraglacial lakes on the Greenland Ice Sheet



**Andrew Graham Williamson**

Scott Polar Research Institute

University of Cambridge

This dissertation is submitted for the degree of

*Doctor of Philosophy*

Girton College

June 2018

For my parents, Helen and Graham,
and my sister, Rebecca,
without whose unfailing love, support and
inspiration, I could have never succeeded.

*Once a photograph of the Earth, taken from outside, is available…*
*a new idea as powerful as any in history will be let loose.*

Sir Fred Hoyle, 1948

# Declaration

This dissertation is the result of my own work and includes nothing which is the outcome of work done in collaboration except as declared in the Acknowledgements or where specifically indicated in the text. It is not substantially the same as any dissertation that has already been submitted or is being concurrently submitted for a degree, diploma or other qualification at the University of Cambridge or at any other University or similar institution except as declared in the Acknowledgements or where specifically indicated in the text. This dissertation does not exceed the length limits prescribed by the Degree Committee for the Faculty of Earth Sciences and Geography.

Andrew G. Williamson
Cambridge, UK
June 2018

# Acknowledgements

This thesis draws to a close not only the research contained within the following six chapters, but also the Cambridge chapters of my life, and what chapters they have been!

First, I wish to begin by thanking my three PhD supervisors, Neil Arnold, Ian Willis and Alison Banwell, for diligently guiding this research to completion. I could not have hoped for a better group of individuals to add their strengths to supervising my PhD and to hold a genuine interest in my success and welfare. Attempting to emulate even a fraction of their success both as researchers and as educators has kept me motivated throughout this PhD. Although the PhD topic was originally conceived by them, I am also grateful to Nick Selmes for his early discussions that helped to generate ideas for extending his initial work on a similar subject. Allen Pope, with his enviable remote-sensing expertise, has also provided a suite of helpful advice throughout, both in his capacity as a paper reviewer and more informally via e-mail. Similarly, Jerome Neufeld and Stephen Kissler are thanked for their advice on (and simple mathematical explanations of!) the statistical techniques to use with the data in Chapter 4. Additionally, Conrad Koziol provided the original version of a function to calculate the von Mises yield criterion in Chapter 4 (and shared in many discussions on the importance—or not—of supraglacial-lake drainage) and Brice Noël speedily provided the ice-sheet runoff data used in Chapters 4 and 5. I have also benefited from discussions with Gareth Rees, Pete Nienow, Poul Christoffersen, Evan Miles, Nick Toberg, Matt Hoffman, Christine Dow, Alex Messerli, Adrian Luckman, Marco Tedesco, Amber Leeson, Chris Stokes, Lauren Andrews, Victor Tsai, Helen Dahlke, Caroline Clason and Andrew Tedstone.

This research was generously funded by a Natural Environment Research Council (NERC) PhD studentship awarded through the Cambridge Earth System Science Doctoral Training Partnership (DTP). Laura Bonesi, Kathleen McDougall, Yvonne Gibbs and Eric Wolff especially are thanked for their support through this avenue during my PhD. I also greatly appreciate having received additional funding for attending conferences and courses from the Geography Department Philip Lake II Fund, the Girton College Pillman Academic Fund, the Cambridge Philosophical Society, the International Glaciological Society, and the Scott Polar Research Institute (SPRI) B. B. Roberts

Fund. A Cambridge Philosophical Society Research Studentship also helped me to fund some extra work stemming from this thesis following its initial submission.

For my PhD, I have been extremely privileged to be part of the community at SPRI, which is one of the most tightly-knit groups of which I am aware in Cambridge. SPRI has provided me with probably too many distractions, often because of the high-calibre and, above all, interesting people it attracts, many of whom I have fortunately been able to name among my friends over the years. Some people have been more distracting than others, namely: Rhiannon Cogbill, Ollie Cohen, Helena Nathan-King, Morgan Seag, Mike McCarthy, Henry Anderson-Elliott, Tom Chudley, Samuel Cook, Katie Miles, Corinne Benedek, James Kirkham, Johanna Grabow, Emily Haggard, Jim Marschalek, Becky Dell, Rob Law, Cameron Mackay, Peter Martin, Johanna Shönecker and Sophie Vineberg. A handful of these people deserve special mention: Becky laid a path for me to become mildly obsessed with rowing (much to most of my friends' dislike, but acting as a perfect outlet during write-up) and added a welcome new vitality to SPRI; Corinne, aside from translating conversations between Becky and me, has reliably been there to discuss my research ideas, always with enviable enthusiasm, at every opportunity; Samuel has engaged me in never-ending debate over hyphenating compound adjectives; Tom has kept my hand 'steady' via the bottle(s) stored in the bottom drawer of his filing cabinet (not forgetting his crucial suggestion of the iconic name for the "FAST" algorithm); Katie has tested my MATLAB skills thoroughly, and has always been there to listen even when she moved to Aberystwyth; Rhiannon, Ollie and Helena have let off steam with me in London; finally, and most significantly, James has shared in many of my most memorable highs (some extending to above 5500 m in Nepal) over the last couple of years, and has been there to offer loyal support whenever it has been needed. Being surrounded by these people means that, during my PhD, I've gained so many skills other than those required to be a successful academic.

Aside from these 'colleagues', there are far too many other significant people with whom I've shared notable times during my PhD to name, but I'll do my best, with apologies to anyone I have forgotten (but let's face it, they'll probably never read this anyway!): Tom Gray, Tom Perry and Mike Cooper (alias the original SPRI 'sports fans'), Adrien Lefauve, Juliette Monquil, Helen Brooks, Vicky Ward, Chris Hewetson, David Hoyle, Mark Jackson, Zekang Cheng, Camilla Penney, Vera Kleinken, Philip and Bridget Boyle, Michael Hahn, James Dobson, Grant Macdonald, Josh Williams, Bertie Miles, Frazer Christie, Paul Tepes, Emily Hill, Devin Harrison, Adam Hepburn, Jade Bowling, my housemates, Girton Spring Ball 2016 Committee members, Cambridge University Hillwalking Club friends, and Girton College Boat Club boaties. During my PhD, I've been lucky to have a go at passing on my understanding of glaciology to undergraduates, many of whom added fresh perspectives on my knowledge, but especially Laura Gledhill, Sam Lumley, Joe Horrocks-Taylor and Karla Boxall during my supervision of their dissertations. Owing to all of the above individuals,

I know that Cambridge, the friends I've made, and the defining period of my life spent here (extending back to my beginnings as an undergraduate in 2010) will remain very significant for me for many years to come.

Finally, and more fundamentally, I'd like to thank my family who have always been there to depend on, to care for me, and to provide me with encouragement. During the final year of my PhD, I was very saddened to lose my Grandpa, Leslie Williamson, who always showed the deepest interest in all of my endeavours, both academic and otherwise, and who would have been overjoyed to see me complete this thesis. His love of the outdoors is something that he undoubtedly passed on to me, and this was likely to have ultimately been responsible for my decision to follow an academic pathway to glaciology. He will be sorely missed.

# Abstract

Supraglacial lakes in the ablation zone of the Greenland Ice Sheet (GrIS) often drain rapidly (in hours to days) by hydraulically-driven fracture ("hydrofracture") in the summer. Hydrofracture can deliver large meltwater volumes to the ice-bed interface and open-up surface-to-bed connections, thereby routing surface meltwater to the subglacial system, altering basal water pressures and, consequently, the velocity profile of the GrIS. The study of rapidly draining lakes is thus important for developing coupled hydrology and ice-dynamics models, which can help predict the GrIS's future mass balance. Remote sensing is commonly used to identify the location, timing and magnitude of rapid lake-drainage events for different regions of the GrIS and, with the increased availability of high-quality satellite data, may be able to offer additional insights into the GrIS's surface hydrology. This study uses new remote-sensing datasets and develops novel analytical techniques to produce improved knowledge of rapidly draining lake behaviour in west Greenland over recent years.

While many studies use 250 m MODerate-resolution Imaging Spectroradiometer (MODIS) imagery to monitor intra- and inter-annual changes to lakes on the GrIS, no existing research with MODIS calculates changes to individual and total lake volume using a physically-based method. The first aim of this research is to overcome this shortfall by developing a fully-automated lake area and volume tracking method ("the FAST algorithm"). For this, various methods for automatically calculating lake areas and volumes with MODIS are tested, and the best techniques are incorporated into the FAST algorithm. The FAST algorithm is applied to the land-terminating Paakitsoq and marine-terminating Store Glacier regions of west Greenland to investigate the incidence of rapid lake drainage in summer 2014. The validation and application of the FAST algorithm show that lake areas and volumes (using a physically-based method) can be calculated accurately using MODIS, that the new algorithm can identify rapidly draining lakes reliably, and that it therefore has the potential to be used widely across the GrIS to generate novel insights into rapidly draining lakes.

The controls on rapid lake drainage remain unclear, making it difficult to incorporate lake drainage into models of GrIS hydrology. The second aspect of this study therefore investigates whether various hydrological, morphological, glaciological and surface-mass-balance controls can explain the incidence of rapid lake drainage on the GrIS. These potential controlling factors are examined within an Exploratory Data Analysis statistical technique to elicit statistical similarities and differences between the rapidly and non-rapidly draining lake types. The results show that the lake types are statistically indistinguishable for almost all factors, except lake area. It is impossible, therefore, to elicit an empirically-supported, deterministic method for predicting hydrofracture in models of GrIS hydrology.

A frequent problem in remote sensing is the need to trade-off high spatial resolution for low temporal resolution, or vice versa. The final element of this thesis overcomes this problem in the context of monitoring lakes on the GrIS by adapting the FAST algorithm (to become "the FASTER algorithm") to use with a combined Landsat 8 and Sentinel-2 satellite dataset. The FASTER algorithm is applied to a large, predominantly land-terminating region of west Greenland in summers 2016 and 2017 to track changes to lakes, identify rapidly draining lakes, and ascertain the extra quantity of information that can be generated by using the two satellites simultaneously rather than individually. The FASTER algorithm can monitor changes to lakes at both high spatial (10 to 30 m) and temporal (~3 days) resolution, overcoming the limitation of low spatial or temporal resolution associated with previous remote sensing of lakes on the GrIS. The combined dataset identifies many additional rapid lake-drainage events than would be possible with Landsat 8 or Sentinel-2 alone, due to their low temporal resolutions, or with MODIS, due to its inferior spatial resolution.

# Table of contents

**Declaration** vii

**Acknowledgments** ix

**Abstract** xiii

**Table of contents** xv

**List of figures** xix

**List of tables** xxiii

**Nomenclature** xxv

**1 Introduction** 1

1.1 Thesis motivation 1

1.2 Overall research objective and aims 6

1.3 Thesis structure 7

1.4 Publications from this thesis 8

**2 Remote sensing and hydrology of the Greenland Ice Sheet: A review** 9

2.1 Executive summary 9

2.2 Fundamentals of remote sensing 10

2.2.1 Development of the remote-sensing discipline 10

2.2.2 The electromagnetic spectrum 10

2.2.3 Quality of remotely-sensed data 11

2.3 Remote sensing of the cryosphere 12

2.4 Applying remote sensing to the Greenland Ice Sheet 12

2.4.1 MODIS 15

2.4.2 Landsat 8 16

2.4.3 Sentinel-2 17

2.5 Mass balance of the Greenland Ice Sheet 19

2.6 Hydrology of the Greenland Ice Sheet 21

2.6.1 Supraglacial hydrology 22
2.6.2 Englacial hydrology 33
2.6.3 Subglacial hydrology 34
2.7 Controls on rapid supraglacial lake drainage 43
2.8 West Greenland study regions 50
2.9 Summary 51

**3 Developing, testing and applying a fully-automated lake-tracking algorithm for MODIS 55**
3.1 Executive summary 55
3.2 Objective and aims 56
3.3 Approach, data and methods 57
3.3.1 Approach 58
3.3.2 Satellite imagery collection and pre-processing 58
3.3.3 Evaluating algorithms for deriving MODIS lake areas 60
3.3.4 Deriving and validating MODIS lake depths and volumes 66
3.3.5 Approach for fully-automated lake tracking 68
3.4 Results 72
3.4.1 Calculating lake areas 72
3.4.2 Calculating lake depths and volumes 77
3.4.3 Lake evolution within the study regions 85
3.5 Discussion 89
3.5.1 Performance of the algorithms for calculating lake area 89
3.5.2 Performance of the algorithm for calculating lake depth 92
3.5.3 Lake evolution within the study regions 93
3.6 Summary and conclusions 99

**4 Controls on rapid supraglacial lake drainage on the Greenland Ice Sheet 101**
4.1 Executive summary 101
4.2 Objective and aims 102
4.3 Data and methods 104
4.3.1 Identifying rapidly and non-rapidly draining lakes 104
4.3.2 Deriving potential controlling factors on rapid lake drainage 104
4.3.3 Exploratory Data Analysis techniques 109
4.3.4 Study sites 111
4.4 Results 112
4.4.1 Distribution of rapidly and non-rapidly draining lakes 112

4.4.2 Differences in potential controlling factors between rapidly and non-rapidly draining lakes 119
4.4.3 Associations between lake area or volume and the potential controlling factors 128
4.5 Discussion 131
4.5.1 Associations between lake area or volume and the potential controlling factors 131
4.5.2 Statistically similar rapidly and non-rapidly draining lakes 132
4.5.3 Reasons for the negative results and suggestions for future work 135
4.6 Summary and conclusions 136

**5 Fully-automated lake tracking with a dual-satellite (Sentinel-2 and Landsat 8) record 139**
5.1 Executive summary 139
5.2 Objective and aims 140
5.3 Data and methods 141
5.3.1 Study region 141
5.3.2 Satellite imagery collection and pre-processing 142
5.3.3 Lake area delineation 144
5.3.4 Lake depth and volume estimates 146
5.3.5 Lake evolution and rapid lake-drainage identification 149
5.3.6 Meltwater deliveries after moulin opening and inter-annual runoff 150
5.4 Results 151
5.4.1 Sentinel-2 lake-depth estimates 151
5.4.2 Lake evolution in summer 2016 155
5.4.3 Rapid lake drainage in summer 2016 157
5.4.4 Meltwater deliveries and moulin opening by rapid lake drainage 160
5.4.5 Inter-annual differences in lake behaviour 163
5.5 Discussion 169
5.5.1 Sentinel-2 lake-depth estimates 169
5.5.2 Lake evolution in summer 2016 171
5.5.3 Rapid lake drainage in summer 2016 171
5.5.4 Inter-annual differences in lake behaviour 173
5.6 Summary and conclusions 174

**6 Conclusions 177**
6.1 Outcomes of research aims 177

6.1.1 Aim 1 – Develop, test and apply a fully-automated method for tracking lake area and volume changes with MODIS (Chapter 3) 177
6.1.2 Aim 2 – Investigate the controls on rapid lake drainage on the Greenland Ice Sheet (Chapter 4) 179
6.1.3 Aim 3 – Develop and apply a method for fully-automated, dual-satellite (Sentinel-2 and Landsat 8) lake tracking (Chapter 5) 180
6.2 Synthesis of conclusions 182
6.3 Future directions of research 183
6.3.1 Improving the calculations of lake depth and volume 183
6.3.2 Developing the lake-tracking algorithms 183
6.3.3 Applying the lake-tracking algorithms elsewhere in Greenland 184
6.3.4 Applying the lake-tracking algorithms to other ice masses 185
6.3.5 Investigating the controls on rapid lake drainage 185
6.3.6 Improving understanding of Greenland Ice Sheet hydrology 186
6.4 Concluding remarks 186

**References** **189**

**Appendix A Supplementary data tables** **227**

# List of figures


| | | |
|---|---|---|
| 1.1 | Accelerating ice-mass loss from the Greenland Ice Sheet | 3 |
| 2.1 | Mass-balance estimates for the Greenland Ice Sheet | 21 |
| 2.2 | Idealised land-terminating Greenland Ice Sheet hydrology | 22 |
| 2.3 | Decadal-scale inland advance of lakes in north-west Greenland | 26 |
| 2.4 | Rapid *in situ* drainage of two lakes in west Greenland | 29 |
| 2.5 | Rapidly draining lakes identified with remote sensing at Russell Glacier | 30 |
| 2.6 | Distribution of different lake types across the Greenland Ice Sheet | 31 |
| 2.7 | Idealised physical relations and configurations of subglacial drainage | 36 |
| 2.8 | Effect of rapid lake drainage on short-term ice velocities | 37 |
| 2.9 | Longer-term slow-downs of land-terminating ice velocities | 39 |
| 2.10 | Persistent inter-annual acceleration of inland ice velocities | 40 |
| 2.11 | Idealised marine-terminating Greenland Ice Sheet hydrology | 41 |
| 2.12 | Ice velocities derived from a coupled hydrology and ice-dynamics model | 43 |
| 2.13 | Modelled seasonal upglacier progression of rapid lake drainage | 46 |
| 2.14 | Nearby basal water delivery as a precursor to rapid lake drainage | 48 |
| 2.15 | Thesis study sites | 51 |
| 3.1 | Chapter study sites | 57 |
| 3.2 | Techniques to validate MODIS lake areas, depths and volumes | 65 |
| 3.3 | Approach of the fully-automated lake-tracking algorithm | 71 |
| 3.4 | Comparison of MODIS and Landsat 8 lake areas for best thresholds | 74 |
| 3.5 | Lake perimeters from best method and threshold in study regions | 75 |
| 3.6 | Comparison of MODIS and Landsat 8 lake areas for best technique and threshold | 76 |
| 3.7 | Comparison of physically-based MODIS and Landsat 8 lake depths | 78 |
| 3.8 | Comparison of physically-based MODIS and Landsat 8 lake volumes | 81 |
| 3.9 | Mean difference between MODIS and Landsat 8 lake depths | 82 |

| | | |
|---|---|---|
| 3.10 | Comparison of physically-based MODIS and Landsat 8 lake depths and volumes | 83 |
| 3.11 | Total seasonal lake area, volume and cloud cover evolution | 86 |
| 3.12 | Relationship between lake number and total and mean lake volume | 87 |
| 3.13 | Number and properties of rapid lake-drainage events | 88 |
| 3.14 | Clusters of rapidly draining lakes | 95 |
| 3.15 | Relationship between lake volume and ice thickness | 96 |
| 3.16 | Paakitsoq region lake area-to-volume scaling relationship | 97 |
| 3.17 | Store Glacier region lake area-to-volume scaling relationship | 98 |
| 4.1 | Chapter study sites, ice-surface elevations and lake areas | 103 |
| 4.2 | Best-fitting an ellipse to a lake using the 'regionprops' function | 107 |
| 4.3 | Lake locations and water volumes compared with ice thickness | 113 |
| 4.4 | Lake drainage and maximum extent dates | 114 |
| 4.5 | Distribution of lakes by surface-elevation band and lake area | 117 |
| 4.6 | Distribution of lakes by ice-thickness band and lake area | 117 |
| 4.7 | Distribution of lakes by surface-elevation band and lake volume | 118 |
| 4.8 | Distribution of lakes by ice-thickness band and lake volume | 118 |
| 4.9 | Boxplots comparing potential controls for lake types | 121 |
| 4.10 | Lake locations and eccentricities compared with ice-surface slopes | 122 |
| 4.11 | Lake locations and runoff in lake catchments compared with ice-bed elevation | 123 |
| 4.12 | Principal strain rate across the study regions | 124 |
| 4.13 | von Mises yield criterion across the study regions | 124 |
| 4.14 | Principal component scores for lake types for hydro-morphological factors | 126 |
| 4.15 | Principal component scores for lake types for glaciological factors | 126 |
| 4.16 | Principal component scores for lake types for surface-mass-balance factors | 127 |
| 4.17 | Principal component scores for lake types for all 23 factors | 127 |
| 5.1 | Chapter study site | 142 |
| 5.2 | Summary of methods applied to Sentinel-2 and Landsat 8 images | 144 |
| 5.3 | Relationship between Sentinel-2 and Landsat 8 lake areas | 146 |
| 5.4 | Comparison of physically-based Landsat 8 and Sentinel-2 lake depths | 152 |
| 5.5 | Comparison of Sentinel-2 red-band reflectance and Landsat 8 lake depths | 153 |
| 5.6 | Comparison of Sentinel-2 green-band reflectance and Landsat 8 lake depths | 153 |
| 5.7 | Comparison of Sentinel-2 blue-band reflectance and Landsat 8 lake depths | 154 |
| 5.8 | 2016 time series of lake volumes for rapidly and non-rapidly draining lakes | 156 |
| 5.9 | 2016 evolution to total lake area and volume | 157 |
| 5.10 | 2016 normalised evolution to total lake area and volume | 157 |

5.11 2016 lake drainage and maximum extent dates for small and large lakes 160
5.12 2016 water volumes before drainage for small and large lakes 161
5.13 Frequency distribution of water volumes before drainage for small and large lakes 162
5.14 Cumulative runoff into moulins opened by small and large lakes 163
5.15 2017 time series of lake volumes for rapidly and non-rapidly draining lakes 164
5.16 2017 normalised evolution to total lake area and volume 165
5.17 2017 lake drainage and maximum extent dates for small and large lakes 167
5.18 2017 water volumes before drainage for small and large lakes 168
5.19 Inter-annual comparison of daily and cumulative runoff 169

# List of tables


| | | |
|---|---|---|
| 2.1 | Satellite sensors used to research Greenland Ice Sheet hydrology | 14 |
| 2.2 | Properties of MODIS satellite bands | 15 |
| 2.3 | Properties of Landsat 8 satellite bands | 17 |
| 2.4 | Properties of Sentinel-2A satellite bands | 18 |
| 2.5 | Rapidly draining lake characteristics | 49 |
| 3.1 | Performance of algorithms for calculating lake areas | 73 |
| 3.2 | Performance of physically-based lake-depth calculations | 79 |
| 3.3 | Performance of physically-based lake-volume calculations | 80 |
| 3.4 | Variation in errors of lake-depth calculations | 84 |
| 3.5 | Variation in errors of lake-volume calculations | 84 |
| 3.6 | Properties of lake-drainage events identified by the fully-automated algorithm | 88 |
| 4.1 | Potential controlling factors on hydrofracture | 106 |
| 4.2 | Distribution of lakes by area and ice-surface and ice-thickness bands | 115 |
| 4.3 | Distribution of lakes by volume and ice-surface and ice-thickness bands | 116 |
| 4.4 | Results of unpaired two-sample Student's *t*-tests for all factors | 119 |
| 4.5 | Results of unpaired two-sample Student's *t*-tests for principal components | 125 |
| 4.6 | Bivariate associations between lake area and potential controls | 129 |
| 4.7 | Bivariate associations between lake volume and potential controls | 130 |
| 5.1 | Performance of techniques for deriving Sentinel-2 lake depths | 154 |
| 5.2 | 2016 lake-drainage events identified using individual- and dual-satellite records | 159 |
| 5.3 | 2017 lake-drainage events identified using Sentinel-2 record | 166 |
| 5.4 | Differences in lake-drainage event properties between 2016 and 2017 | 166 |
| A.1 | Landsat 8 tiles used in Chapter 3 | 228 |
| A.2 | Paakitsoq testing of thresholds for calculating lake area dynamically | 229 |

A.3 Store Glacier testing of thresholds for calculating lake area dynamically 229
A.4 Paakitsoq testing of thresholds for calculating lake area with NDWI 230
A.5 Store Glacier testing of thresholds for calculating lake area with NDWI 230
A.6 Paakitsoq testing of thresholds for calculating lake area with red/blue band ratio 231
A.7 Store Glacier testing of thresholds for calculating lake area with red/blue band ratio 232
A.8 Full details of rapid lake-drainage events at Paakitsoq 233
A.9 Full details of rapid lake-drainage events at Store Glacier 234
A.10 Eigenvectors for principal component analysis 235
A.11 Sentinel-2 images used in Chapter 5 236
A.12 Landsat 8 images used in Chapter 5 239

# Nomenclature

## Abbreviations

| | |
|---|---|
| a.s.l. | above sea level |
| ASTER | Advanced Spaceborne Thermal Emission and Reflection Radiometer |
| B | Bilinear |
| BOA | Bottom of atmosphere |
| CREFL | Corrected Reflectance |
| DEM | Digital elevation model |
| df | Degrees of freedom |
| DTP | Doctoral Training Partnership |
| DoY | Numerical day of year |
| EDA | Exploratory Data Analysis |
| EPSG | European Petroleum Survey Group |
| ERTS | Earth Resources Technology Satellite |
| ESA | European Space Agency |
| ETM+ | Enhanced Thematic Mapper Plus |
| FAST | Fully-Automated Supraglacial lake Tracking |
| FASTER | Fully-Automated Supraglacial lake Tracking at Enhanced Resolution |
| FE | Fair enough |
| FP | False positive |
| GIMP | Greenland Ice Mapping Project |
| GRACE | Gravity Recovery and Climate Experiment |
| GrIS | Greenland Ice Sheet |
| HDF | Hierarchical Data Format |
| IPCC | Intergovernmental Panel on Climate Change |
| LiDAR | Light Detection and Ranging |
| LP DAAC | Land Processes Distributed Archive Center |

| | |
|---|---|
| MATLAB | MATrix LABoratory |
| MEaSUREs | Making Earth System data records for Use in Research Environments |
| MODIS | MODerate-resolution Imaging Spectroradiometer |
| MRTSwath | MODIS Reprojection Tool Swath |
| MSI | Multispectral Instrument |
| N | North |
| NASA | National Aeronautics and Space Administration |
| NDWI | Normalised Difference Water Index |
| NERC | Natural Environment Research Council |
| NIR | Near-infrared |
| NN | Nearest-neighbour |
| NRD | Non-rapidly draining |
| OLI | Operational Land Imager |
| OLS | Ordinary least-squares |
| PB | Physically based |
| PC | Principal component |
| PCA | Principal component analysis |
| RACMO | Regional Atmospheric Climate-Model Output |
| RCP | Representative Concentration Pathway |
| RD | Rapidly draining |
| RGB | Red-green-blue |
| RMSE | Root-mean-square error |
| SAR | Synthetic Aperture Radar |
| SLE | Sea-level equivalent |
| SLR | Sea-level rise |
| SMB | Surface mass balance |
| SPRI | Scott Polar Research Institute |
| SSE | Sum of squares due to error |
| SWIR | Shortwave-infrared |
| TIRS | Thermal Infrared Sensor |
| TM | Thematic Mapper |
| TOA | Top of atmosphere |
| USGS | United States Geological Survey |
| UTM | Universal Transverse Mercator |
| W | West |
| w.e. | water equivalent |

| | |
|---|---|
| w.r.t. | with respect to |
| WGS | World Geodetic System |

## Roman symbols

| | |
|---|---|
| $a$ | Absorption coefficient for pure water |
| $A$ | Creep factor ($s^{-1}$ $Pa^{-3}$) |
| $A_d$ | Lake-bottom albedo |
| $A_{SGL}$ | Lake area ($km^2$) |
| $b$ | Backscattering coefficient for molecular (Rayleigh) scattering |
| $D_u$ | Upwelling light distribution |
| $g$ | Losses in upward and downward travel through a water column ($m^{-1}$) |
| $K_d$ | Diffuse attenuation coefficient for the clearest natural freshwater |
| $n$ | Number (of data points) |
| $N$ | Creep exponent |
| $p$ | Statistical probability indicator |
| $r$ | Pearson product-moment correlation coefficient |
| $R^2$ | Coefficient of determination |
| $R_{pix}$ | Reflectance of lake pixel |
| $R_\infty$ | Reflectance of optically-deep water |
| $t$ | Student's $t$-statistic |
| $V_{SGL}$ | Lake volume ($m^3$) |
| $z$ | Lake depth (m) |

## Greek symbols

| | |
|---|---|
| $\dot{\varepsilon}_E$ | Effective strain rate ($a^{-1}$) |
| $\dot{\varepsilon}_{ij}$ | Strain-rate tensor |
| $\dot{\varepsilon}$ | Principal strain rate ($a^{-1}$) |
| $\rho$ | Spearman's rank correlation coefficient |
| $\sigma$ | Standard deviation |
| $\sigma_1$ | Maximum principal stress (Pa) |
| $\sigma_3$ | Minimum principal stress (Pa) |
| $\sigma_{ij}$ | Stress tensor |

| | |
|---|---|
| $\sigma_V$ | von Mises yield criterion (Pa) |
| $\sigma_{xx}$ | Longitudinal stress (Pa) |
| $\sigma_{yy}$ | Transverse stress (Pa) |
| $\tau_{xy}$ | Shear stress (Pa) |

# Chapter 1

# Introduction

## 1.1 Thesis motivation

Fluctuations in the Earth's climate, particularly during switches between glacial and interglacial cycles, have driven the waxing and waning of the Earth's palaeo-ice sheets over centuries to millennia, leading to past sea-level change (e.g. Hays *et al.*, 1976; Cuffey and Marshall, 2000; Huybers, 2006; Raymo *et al.*, 2006; Dutton *et al.*, 2015; Strunk *et al.*, 2017). Ice within the two contemporary Greenland and Antarctic ice sheets, and within smaller glaciers and ice caps, covers ~10% of the global land surface, with a total sea-level equivalent (SLE) of just over 66 m (Vaughan *et al.*, 2013). Although the majority (~58 m) of the total SLE is contained within the Antarctic Ice Sheet, the Greenland Ice Sheet (GrIS) holds the bulk of the remainder (~7 m), with glaciers and ice caps containing only 0.4 m (Vaughan *et al.*, 2013). The GrIS is by far the largest ice mass in the Northern Hemisphere, extending ~2500 km latitudinally, from 60°N to 83°N, and ~1000 km longitudinally (Benn and Evans, 2010; Kargel *et al.*, 2012).

A major concern today is that the GrIS and, to a lesser degree, the Antarctic Ice Sheet are undergoing accelerated ice-mass loss (Velicogna and Wahr, 2006; Shepherd and Wingham, 2007; Rignot *et al.*, 2008a, 2008b, 2011; Velicogna, 2009; Zwally *et al.*, 2011; Shepherd *et al.*, 2012; Miles *et al.*, 2013; Jin *et al.*, 2016; Gardner *et al.*, 2018). In the case of the GrIS, these changes are probably being forced by amplified Arctic air temperatures since the late twentieth century (Hall *et al.*, 2013), which cannot simply be accounted for by inter-annual temperature variations due to changes in the North Atlantic Oscillation (Hall *et al.*, 2008). These air-temperature rises, combined with a warmer ocean (Holland *et al.*, 2008; Hanna *et al.*, 2009), are thought to explain the current acceleration and thinning of many of the GrIS's outlet glaciers, even if the interior of the ice sheet remains in a state of balance (Bamber *et al.*, 2000; Rignot and Kanagaratnam, 2006; Pritchard *et al.*, 2009). The extra ice lost from the GrIS

is being delivered to the oceans, and thus contributing to continually accelerating rates of global average sea-level rise (SLR) (Nerem *et al.*, 2018): in 2005–2010, the total SLR from the GrIS was 0.63 (0.47–0.80) mm $a^{-1}$ compared with the much lower total of 0.33 (0.26–0.41) mm $a^{-1}$ in the longer 1993–2010 period (Vaughan *et al.*, 2013; Figure 1.1). This SLR contribution from the GrIS compares with that from the Antarctic Ice Sheet (including Antarctic peripheral glaciers) of 0.41 (0.20–0.61) mm $a^{-1}$ in 2005–2010 (Vaughan *et al.*, 2013) and that from glaciers and ice caps of 0.83 (0.46–1.20) mm $a^{-1}$ in 2005–2009 (Cogley, 2009; Marzeion *et al.*, 2012). This means that, at present, SLR contributions sourced from the GrIS outweigh those from the Antarctic Ice Sheet, even though the combined global contribution from glaciers and ice caps is higher (Alley *et al.*, 2005a; Shepherd *et al.*, 2012; Vaughan *et al.*, 2013). However, while glaciers and ice caps presently contribute most significantly to total global SLR, it is widely acknowledged that within the twenty-first century, the GrIS will overtake their contribution (Raper and Braithwaite, 2006; Jevrejeva *et al.*, 2012; Bamber and Aspinall, 2013; Church *et al.*, 2013). If the present acceleration to mass loss from the GrIS continues, it is estimated that the ice sheet could contribute as much as 90 mm in total to SLR by 2050 (Church and White, 2006; Khan *et al.*, 2015). Such high rates of SLR are a concern for society because they may, for example, inundate low-lying nation states and coastal cities (Dasgupta *et al.*, 2009; Nicholls and Cazenave, 2010), increase the magnitude of storm surges (Tebaldi *et al.*, 2012; Neumann *et al.*, 2015), or negatively affect coastal ecosystems (Nicholls *et al.*, 1999; Craft *et al.*, 2008; Lovelock *et al.*, 2015). There is a need, therefore, to develop a comprehensive understanding of the causes of the accelerated mass loss from the GrIS in the present day, which should then allow improved estimates of its ongoing contribution to SLR over the coming decades and centuries.

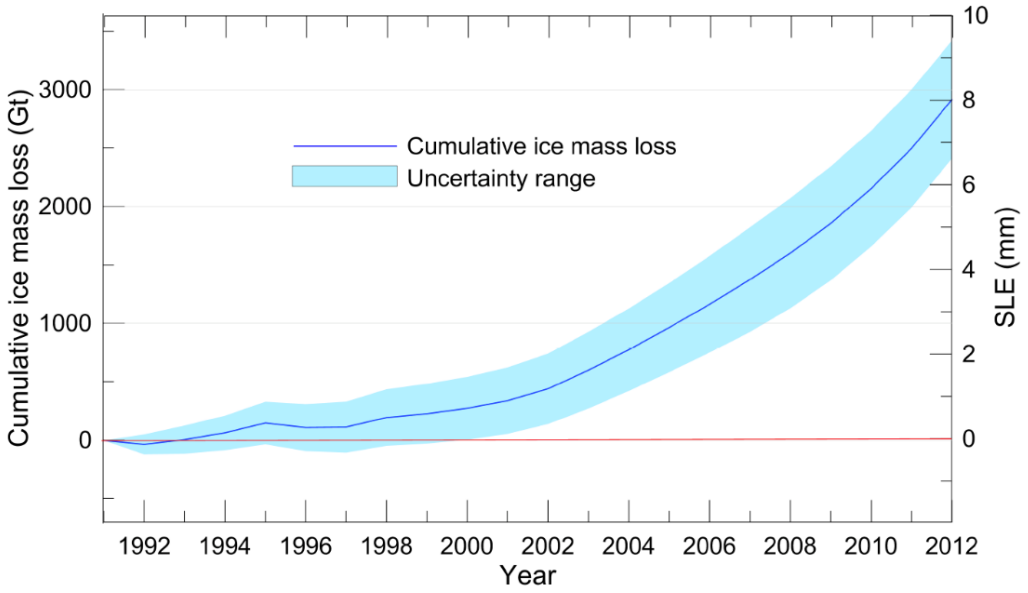



**Figure 1.1:** Cumulative ice-mass loss and SLE from the GrIS from 1991–2012, showing a notable acceleration after around 2002. Individual yearly values are averages taken from up to 18 studies. Reproduced from Vaughan *et al.* (2013).

Given this requirement for improved understanding of the GrIS, an expanding body of glaciological research has focused on developing understanding of ice-sheet processes. Research on the contemporary GrIS typically focuses on three main elements of the ice-sheet system: (i) its mass balance, which is the difference between the accumulation of snowfall and the ablation of ice, and whether this value is positive (or negative) and therefore whether the GrIS is gaining (or losing) mass; (ii) its hydrology, being the distribution and influence of water within different areas of the GrIS; and, (iii) its dynamics, referring to the velocity structure of the GrIS, including the interactions of the ocean with the ice sheet. The broad aim within this research is to understand present-day processes within these systems and the feedbacks of the systems on each other; ultimately, the goal is then to predict how the systems may respond in the future against a backdrop of projected future climate warming exceeding 1.5 °C by 2100 under all of the likely future Representative Concentration Pathway (RCP) scenarios (IPCC, 2013). Collectively, this recent research has led to an increased concern over the future stability and evolution of the GrIS. This is because the ice sheet is recognised to be thinning dynamically at its margins (Pritchard *et al.*, 2009), melt is extending over greater portions of the ice-sheet surface (Abdalati and Steffen, 2001; Box *et al.*, 2006; Hanna *et al.*, 2008; Nghiem *et al.*, 2012), and outlet glaciers that terminate in the ocean ("marine-terminating") are being affected by warmer ocean temperatures, and are consequently speeding-up (Jenkins, 2011; Christoffersen *et al.*, 2011; Ahlstrøm *et al.*, 2013; Straneo *et al.*, 2013; Rignot *et al.*, 2015; Hill *et al.*, 2017, 2018). These processes are all contributing to the increasing mass loss from the GrIS identified

above, which is separated into losses from (i) surface melting and runoff and (ii) increased ice discharge and calving for marine-terminating outlet glaciers (van den Broeke *et al.*, 2009). Until 2005, the mass loss from these two processes was approximately equally partitioned, with 58% of mass loss from ice discharge over the grounding line for marine-terminating outlets (van den Broeke *et al.*, 2009; Enderlin *et al.*, 2014). However, after 2005, ice-mass losses from surface melting and runoff increased, thereby producing a decline in the relative importance of the mass loss from ice discharge to 36% in 2005–2009 and 32% in 2009–2012 (Enderlin *et al.*, 2014).

The ice sheet's hydrological system can influence both the surface mass balance (SMB) and the dynamics of land- and marine-terminating sectors. For marine-terminating sectors of the ice sheet, hydrology can promote increasing calving by generating buoyant plumes of meltwater that can erode the calving front (e.g. Jenkins, 2011; Xu *et al.*, 2012, 2013; Hill *et al.*, 2017, 2018); alternatively, for both land- and marine-terminating regions, hydrology can cause dynamic ice speed-up because of its effect on basal water pressures and, consequently, ice-sliding rates (Schoof, 2010; Shannon *et al.*, 2013; Flowers, 2015). Thus, for both land- and marine-terminating sectors, hydrology has the potential to cause thinning of the GrIS's margins, and the subsequent draw-down of ice from the interior regions of the ice sheet to lower elevations, where melting rates increase further, initiating a potential positive feedback (Velicogna *et al.*, 2014; Hill *et al.*, 2017, 2018). This means that hydrology has become a central aspect of glaciological research on the GrIS, particularly since the early 2000s (Chu, 2014; Nienow *et al.*, 2017). Within this hydrological research, a great deal of attention has been directed towards exploring the formation and evolution of supraglacial lakes (hereafter "lakes") on the GrIS surface. These lakes, which can grow to several square kilometres in area and reach over 10 m in depth, form due to the ponding of surface meltwater in topographic depressions on the ice-sheet surface (Echelmeyer *et al.*, 1991). Over 2600 such lakes (exceeding 0.0625 $km^2$ in area) have been identified across the whole GrIS in 2005–2009, although most (~55%) have been found in the west and south-west sectors (Selmes *et al.*, 2011, 2013). In general, studies of such lakes to date have focused on: (i) identifying the locations and timings of lake formation (e.g. Box and Ski, 2007; McMillan *et al.*, 2007; Lampkin and VanderBerg, 2011; Selmes *et al.*, 2011, 2013; Fitzpatrick *et al.*, 2014); (ii) the progression of lakes towards the interior regions of the GrIS under past and future climatic warming (e.g. Leeson *et al.*, 2012, 2015; Howat *et al.*, 2013; Ignéczi *et al.*, 2016; Gledhill and Williamson, 2018); (iii) the incidence and causes of lake-drainage events in both time and space (e.g. Das *et al.*, 2008; Selmes *et al.*, 2011; Liang *et al.*, 2012; Morriss *et al.*, 2013; Tedesco *et al.*, 2013; Fitzpatrick *et al.*, 2014; Stevens *et al.*, 2015); and, finally, (iv) the influence of lakes on the development of subglacial drainage and consequently their implications for ice flow (e.g. Zwally *et al.*, 2002; Banwell *et al.*, 2013a, 2016; Joughin *et al.*, 2013; Tedstone *et al.*, 2013, 2014, 2015; Dow *et al.*, 2014; Koziol and Arnold, 2018).

Together, this research has produced a consensus on the approximate spatial extent of lakes for different years and regions of the ice sheet, as well as the frequency of lake-drainage events, and their implications for subglacial hydrology. As a result, the collective knowledge of lakes is better than other elements of the GrIS's hydrology, mainly because lakes are accessible for fieldwork (contrasting with the englacial and subglacial components of the hydrological system, for example) and because of the increasing availability of high-quality data collected remotely by satellites, meaning wide areas of the GrIS can be imaged frequently. Remote sensing has therefore been particularly helpful because it has overcome many of the logistical issues associated with fieldwork and has reduced previous concerns relating to the applicability of the findings from individual lakes to lakes found more widely on the GrIS.

A common use of remote sensing has involved investigating the location and timing of lake-drainage events, whereby some lakes are observed to disappear from the ice-sheet surface in days to weeks (e.g. McMillan *et al.*, 2007; Selmes *et al.*, 2011, 2013; Tedesco *et al.*, 2013; Fitzpatrick *et al.*, 2014; Miles, K. E. *et al.*, 2017). Within such research, a particular focus has involved identifying lakes that drain rapidly (in hours–days) *in situ* from the surface of the ice sheet into its interior. In this phenomenon, a fracture is forced through the full ice thickness by the water contained in the lake in a process referred to as hydraulically-driven fracture propagation or "hydrofracture" (van der Veen, 2007; Tsai and Rice, 2010; Chu, 2014). The rationale for exploring hydrofracture in detail is that the meltwater pulses delivered into the GrIS by these rapid lake-drainage events are thought to reach the subglacial drainage system, driving-up basal water pressures, and potentially increasing GrIS velocities. This created concern in the early 2000s of a potential hydrologically-driven collapse of the GrIS resulting from the initiation of dynamic positive feedbacks involving the draw-down of ice from the interior regions due to higher ice velocities (Zwally *et al.*, 2002). However, it has been subsequently recognised that the ice speed-ups resulting from rapid lake drainage are often only short-lived for land-terminating, ice-marginal regions (e.g. Banwell *et al.*, 2013a; Cowton *et al.*, 2013; Sole *et al.*, 2013; Tedstone *et al.*, 2015), although uncertainty still surrounds the effect of rapid lake drainage inland where the ice is much thicker (e.g. Dow *et al.*, 2014; Doyle *et al.*, 2014; Poinar *et al.*, 2015; de Fleurian *et al.*, 2016) and for marine-terminating sectors. These rapid lake-drainage events also open-up moulins (near-vertical shafts), which are the main ways for surface meltwater to reach the GrIS's basal hydrological system over the remainder of the melt season, meaning lake-drainage events can have longer-term implications after the evacuation of the initial meltwater pulse delivered during drainage (Colgan *et al.*, 2011a; Banwell *et al.*, 2016; Koziol *et al.*, 2017; Hoffman *et al.*, 2018). It is important, therefore, to understand where and when hydrofracture occurs on the ice-sheet surface in order to gain knowledge of where, when and how much water reaches the subglacial drainage system, as well as to better understand the potential controls on hydrofracture, including whether these vary between areas of the GrIS and between different years.

Collectively, this existing research has shown that rapid lake-drainage events tend to progress upglacier over the course of a melt season, and that the same lakes do not necessarily drain rapidly every year, suggesting that the controls that initiate hydrofracture might vary inter-annually. For example, research indicates that hydrofracture may not necessarily be initiated when lakes reach a specific uniform size, such as areal coverage or water volume (Selmes *et al.*, 2013; Arnold *et al.*, 2014; Fitzpatrick *et al.*, 2014), but this hypothesis has not been verified conclusively for a large sample of lakes. This is likely to be because most existing remotely-based work on GrIS lakes has been limited to examining intra-annual changes to lake areas (e.g. Selmes *et al.*, 2011, 2013; Cooley and Christoffersen, 2017) and not lake volumes.

Research that has included measurements of lake volume has, by contrast, typically been for a limited number of satellite scenes (e.g. Box and Ski, 2007; Moussavi *et al.*, 2016; Pope *et al.*, 2016) or has included only an empirical lake area-to-volume scaling relationship (e.g. Georgiou *et al.*, 2009; Liang *et al.*, 2012; Morriss *et al.*, 2013; Fitzpatrick *et al.*, 2014). This has consequently restricted knowledge of the magnitude of surface-meltwater delivery into the GrIS. Furthermore, without a clear understanding of the set of controls on rapid lake drainage, it is difficult to include the process reliably in models of the GrIS's hydrology (e.g. Banwell *et al.*, 2013a; Arnold *et al.*, 2014; Koziol *et al.*, 2017; Koziol and Arnold, 2018), with existing models including simplified empirical algorithms to predict hydrofracture rather than an algorithm with a more complex physical basis. If the controls on hydrofracture were better known, the physical basis for the algorithms within such models could be improved. Achieving this would involve investigating both the relationship between rapid lake drainage and water volumes in lakes, and the relationship within and between other potential controlling factors such as ice thickness, ice velocity, and ice-surface strain rates, among many others. Such developments could lead to the models better reproducing contemporary observations of lake-drainage events, as well as allowing the models to be more confidently forced with future climate projections to generate robust estimates of lake drainage, water runoff and the resulting possible velocity forcing of the GrIS over the coming decades and centuries. This may ultimately allow improved constraints to be placed on the GrIS's contribution to global SLR both presently and in the future.

## 1.2 Overall research objective and aims

This need to understand lake behaviour and the reasons behind it leads to the overall objective for this thesis, which is to exploit the increasing availability of high-quality remotely-sensed satellite data (from the MODerate-resolution Imaging Spectroradiometer (MODIS), Landsat 8 Operational Land Imager (OLI) and Sentinel-2 Multispectral Instrument (MSI)) to monitor the incidence of rapid lake drainage on the GrIS, and to relate this process to the water volumes contained within

lakes and to a variety of other potential controlling variables. This thesis is broadly divided into two streams of research: the first centres on the development of novel methods to analyse remote-sensing imagery to provide new datasets for monitoring changes to lakes; the second relates to using these methods alongside other data to investigate environmental controls on the behaviour of lakes. Three main aims are identified to meet this overall objective, which are to:

1. Develop, test and apply a new method for tracking changes to lake areas and volumes on the GrIS from MODIS imagery, which includes identifying the locations, timings and magnitudes (in terms of water volumes) of rapid lake-drainage events. This work is presented in Chapter 3.
2. Use the method developed and some of the resulting data from (1), alongside a suite of other remotely-sensed data, to examine whether any controls on the initiation of rapid lake drainage on the GrIS can be identified and, if they can, whether these controls vary in time and space. This investigation is presented in Chapter 4.
3. Extend the lake-tracking method presented in (1) to use a combination of Landsat 8 and newly-available Sentinel-2 imagery, the first time a dual-optical-satellite record will be developed and used for this purpose. By mosaicking data from two platforms together, this method aims to provide records of lake dynamics with both high spatial and temporal resolution, which may be able to generate new insights into lake behaviour, including for small lakes. This research is presented in Chapter 5.

## 1.3 Thesis structure

This thesis consists of six chapters. This chapter has introduced the underlying rationale for studying the GrIS, providing the global context and need for the current study. It briefly introduced existing research that has been undertaken into lakes on the GrIS to contextualise and help identify the overall objective of this research. The overall objective was then broken down into three aims forming the basis of Chapters 3–5 of this thesis, which closely resemble the order in which the PhD research was undertaken. Before these chapters, Chapter 2 reviews the literature on remote sensing and GrIS hydrology. It discusses the fundamental principles of remote sensing, the application of remote sensing to studying the cryosphere and the GrIS, and contemporary understanding of some the hydrological phenomena and processes already introduced briefly in this chapter. Chapter 3 then describes the development and validation of a fully-automated method that can track changes to lake areas and volumes on the GrIS from MODIS imagery; this is the first time that an automated, physically-based lake water volume tracking method has been developed for application to a collection of satellite imagery. Chapter 4 describes the use of the results from the application of this new method (i.e. the knowledge of the location, timing and magnitude of rapid lake-drainage

events), alongside other environmental variables and a robust exploratory statistical analysis, to examine the potential controls on rapid lake drainage on the GrIS, for two study regions in summer 2014. Chapter 5 presents the modifications to the automated method for lake tracking from Chapter 3 to allow the use of higher-resolution satellite imagery from Landsat 8 and Sentinel-2 to generate a new record of lakes on the GrIS that has both high spatial and temporal resolution. The method is applied to investigate lake behaviour in a large region of west Greenland in summers 2016 and 2017. Finally, Chapter 6 summarises the key developments from this research for each of the research aims identified above, presents a synthesis of conclusions, and outlines avenues of research that could form the basis of future studies.

## 1.4 Publications from this thesis

The material in Chapters 3 and 4 of this thesis has been published (Williamson *et al.*, 2017, 2018a), and some of the material in Chapter 5 is under interactive, public peer review (Williamson *et al.*, 2018b). The co-authors of these publications are the three supervisors of this PhD research (Neil Arnold, Ian Willis and Alison Banwell). They provided general oversight of the research, including helping to conceive the study, and discussing the approach, methods and results. All of the analysis for the publications, including the data processing and experimental design, was undertaken by the author of this thesis. Moreover, the manuscripts for publication, based on the thesis chapters, were written by the thesis author, with the co-authors providing feedback on them. Williamson *et al.* (2018a, 2018b) include author-contribution statements to explain this information.

# Chapter 2

# Remote sensing and hydrology of the Greenland Ice Sheet: A review

## 2.1 Executive summary

This chapter presents a review of recent research to contextualise the current thesis. It begins by reviewing the theoretical basis to remote sensing, which is the methodological field within which this thesis is situated, before reviewing the mass balance, hydrology and dynamics of the GrIS. Remote sensing is particularly valuable for studying the cryosphere since it can monitor processes and changes that operate over wider spatial and temporal scales than could ever be studied with individual field campaigns. The usefulness of remote sensing has included deriving information on the state of the GrIS in terms of its current mass balance, hydrology and velocity structure, particularly when remote sensing has been combined with detailed field studies of finer-scale processes. While the GrIS's surface hydrology is now relatively well understood compared with its englacial or subglacial components (Hock *et al.*, 2017), uncertainty still surrounds the effect of lake drainage on ice dynamics, and so overall mass balance, at differing timescales and for different regions of the ice sheet. This is in part because there is still ambiguity over the behaviour of lakes and how this behaviour varies for different sectors of the ice sheet and for different years, including the reasons for which rapid lake drainage occurs at specific places and times, and not at others, and whether specific water volumes or other characteristics of lakes are required to initiate rapid drainage. New remote-sensing data and novel analytical approaches offer the potential to address these questions.

## 2.2 Fundamentals of remote sensing

### 2.2.1 Development of the remote-sensing discipline

Remote sensing is the acquisition of information about an object without making physical contact with it (Campbell and Wynne, 2011); the first example of our modern conception of remote sensing involved the capture of an image with a camera in the nineteenth century (Rees, 2012; Tedesco, 2015). When cameras were used to capture photographs from the air, particularly from aeroplanes, the next major step was made towards present-day remote sensing. This continued when sensing instruments were added to spaceborne objects, notably satellites, which then permitted imaging of the vast majority of the Earth at frequent time intervals. The first such satellite was the Earth Resources Technology Satellite (ERTS), later named the Landsat 1 satellite, launched in July 1972, which marked the beginning of a prolific and ongoing number of satellite remote-sensing missions that continue to date (Rees, 2012). Each satellite mission typically has a specific objective to collect data relating to one or multiple of the Earth's systems, such as the hydrosphere, biosphere or cryosphere, with the aim being to detect and classify objects and processes operating on or near to the Earth's surface. The large volume of data generated by these missions is only possible due to the increasing availability of high-speed computers and large-volume data-storage facilities. Because remote sensing can provide near-instantaneous information for wide areas of the globe, as well as for hard or even impossible-to-access regions, it has great usefulness (Pope *et al.*, 2014). In view of this, today, Earth (and even extra-terrestrial) remote sensing is a very well-developed scientific technique, being used across the breadth of environmental-science disciplines, including oceanography, climatology, the geosciences and glaciology.

### 2.2.2 The electromagnetic spectrum

While most remote sensing exploits the visible, near-infrared (NIR) and shortwave-infrared (SWIR) parts of the electromagnetic spectrum, other areas, such as the micro-wavelengths, can be used. Remote sensing is based on the interaction between electromagnetic radiation and surface objects (such as the ocean, vegetation, glaciers). These objects result in different patterns of absorption, transmission and scattering of the electromagnetic radiation depending on their physical properties. The electromagnetic radiation signals can then be measured by remote-sensing instruments, with such instruments usually classified into active and passive types: active systems are those which involve the emittance of electromagnetic energy, and the subsequent measurement of the reflectance and/or backscatter by the target; meanwhile, passive remote-sensing systems measure the natural reflectance and/or emittance of the target, with the source of energy being either the Sun or heat. A

necessary consideration in Earth observation is whether to use a sensor that exploits the microwave or optical wavelengths of the electromagnetic spectrum; the primary advantage of using microwave sensors is their ability to image through clouds and in darkness, something that is impossible with optical and NIR sensors. Notable active systems are Light Detection and Ranging (LiDAR), involving measuring the distance to the target by illuminating it with pulses of laser light, and Synthetic Aperture Radar (SAR), involving a similar process but instead using radio waves and measuring their backscatter at the sensor. Meanwhile, passive systems are most often optical imaging systems, which measure the amount of light reflected by a surface object, with the source of the light being the Sun. The remotely-sensed satellite data used in Chapters 3, 4 and 5 of this thesis are collected by passive, optical systems, although the new algorithm presented in Chapter 3 has also been applied to data recorded by an active, SAR system (Miles, K. E. *et al.*, 2017).

### 2.2.3 Quality of remotely-sensed data

All datasets must be carefully assessed for their quality and thus usefulness for the chosen scientific applications. In the case of remote sensing, the quality of the remotely-sensed data depends on their spatial, temporal, spectral and radiometric resolutions. Spatial resolution is how much spatial detail is recorded in an image, normally indicated by the pixel size of a raster (gridded) image, assuming it is displayed at full resolution. Spatial resolution is most dependent on sensor design, notably the distance between the sensor and the target object – in the case of satellites, for example, those at higher altitudes can image larger areas but are incapable of resolving fine detail accurately within those large areas. Temporal resolution represents the frequency of data acquisition, or the number of flyovers, of a sensor, with higher temporal resolution normally being preferential since it allows data to be collected for systems that can change dynamically. The temporal resolution of a satellite dataset is a product of the satellite's orbital geometry (i.e. the shape of its orbit around the Earth), swath width (i.e. the width of a satellite's imaging strip), and whether or not data can be collected off-nadir as well as at-nadir (i.e. whether data can be collected away from as well as directly below a satellite's track). The Advanced Spaceborne Thermal Emission and Reflection Radiometer (ASTER), for example, can collect data off-nadir assuming that data have been requested, while Landsat cannot, with the result being that Landsat data typically have lower temporal resolution than ASTER data. Spectral resolution measures the number of and the bandwidth of each discrete element of the electromagnetic spectrum that the sensing instrument was designed to sample. Finally, radiometric resolution indicates the number of discrete levels that can be used to record data by the sensor; satellite sensors with 8-bit radiometric resolution ("dynamic range") have 256 levels (i.e. $2^8$) available for recording data (i.e. from 0 to 255), while those with 12-bit resolution have 4096 (i.e. $2^{12}$) levels available (i.e. from 0 to 4095), a 16-fold increase. Thus, as the satellite's radiometric

resolution is increased, the dynamic range that can be recorded increases, and so the satellite can record smaller-scale differences of the sensed object(s) more precisely; thus, a higher bit depth is preferable. Newer satellites, such as the Landsat 8 OLI (hereafter "Landsat 8") and Sentinel-2 MSI (hereafter "Sentinel-2"), record data with 12-bit resolution, while older ones, such as the Landsat Thematic Mapper (TM), on board Landsat 4 and 5, or the Landsat 7 Enhanced Thematic Mapper Plus (ETM+) (hereafter "Landsat 7") record data at 8-bit resolution (Roy *et al.*, 2014).

When using remote sensing to monitor processes on the Earth's surface, researchers must choose a remote-sensing system that fulfils as many of their requirements as possible in terms of the level of spatial, temporal, spectral and radiometric resolution. In such work, typically a trade-off must be made between one type of resolution at the expense of another: for example, by choosing imagery with a frequent temporal resolution, the high spatial resolution of imagery may be lost as a result (e.g. Townshend and Justice, 1988).

## 2.3 Remote sensing of the cryosphere

A common use of remote sensing is to study the cryosphere, which is the frozen part of the Earth's surface, and which includes permafrost, sea ice, snow cover, glaciers, ice caps and ice sheets. Research into the cryosphere is important because changes within this system have implications for other systems, such as the atmosphere and hydrosphere, with consequent implications for society (IPCC, 2013). Within the discipline of glaciology, remote sensing has become a particularly valuable approach since it allows much larger areas and longer timescales to be studied compared with field-based studies, whether this applies to valley glaciers or ice sheets. This means that patterns can be derived over many glaciers simultaneously and at higher temporal frequencies than would ever be possible without continuous field campaigns over multiple seasons. However, while remote sensing is extremely valuable to the cryospheric community, it has not replaced fieldwork; rather it has meant that greater insights can be offered by using field and remote-sensing data simultaneously (Quincey and Luckman, 2009; Pope *et al.*, 2014).

## 2.4 Applying remote sensing to the Greenland Ice Sheet

As a result of the advantages outlined above, remote sensing has now been used to study many processes operating over the wide spatial scales covered by ice sheets. Specifically, on the GrIS, satellite remote sensing has helped to document changes to its mass balance (Section 2.5), understand its hydrology (Section 2.6), and make inferences about its velocity structure over wide areas and long (multi-decadal) timescales. Many different satellite sensors are used for monitoring

different aspects of the GrIS, but with a specific focus on modern-day GrIS surface hydrology (notably lakes and streams), nine main satellite sensors are commonly used (Table 2.1). Table 2.1 shows that each sensor has different strengths and weaknesses: for example, MODIS imagery offers the ability to image the entire ice sheet at least once per day, but this must be traded-off for a lower spatial resolution of 250–500 m. By contrast, other sensors, such as the Landsat and Sentinel constellations, collect data at high spatial resolution (< 30 m), but such data are only available at low temporal resolutions. Although WorldView-1 and WorldView-2 offer imagery at very high spatial resolution (< 2 m in the multispectral bands and < 0.5 m in the panchromatic bands) with frequent revisit times, such images are not open access, meaning that they are suited to only very site-specific applications, owing to the high cost associated with using them over wider areas. This thesis involves using data from MODIS, Landsat 8, and Sentinel-2, which are therefore discussed in further detail in the next sections.

**Table 2.1:** Properties of satellite sensors used within existing research into lakes and streams on the GrIS; "pres." in the table indicates "present day". Satellite sensors used for other purposes on the GrIS (for example, for deriving ice velocities or estimating mass balance) are not included. Studies highlighted in bold text within the table footnotes involve identifying rapidly draining lakes.

| Satellite sensor | Date range | Spatial resolution (m)[1] | Temporal resolution (d)[2] | Radiometric resolution[1] | Swath width (km) | Studies |
|---|---|---|---|---|---|---|
| MODIS[*] | 1999–pres. | 250–500[3] | 1 | 12-bit | 2330 | See list[4] |
| ASTER | 1999–pres. | 15 | 16 | 8-bit | 60 | See list[5] |
| Landsat 7 ETM+ | 1999–pres. | 30 | 16 | 8-bit | 185 | See list[6] |
| Landsat 8 OLI[*] | 2013–pres. | 30 | 16 | 12-bit | 185 | See list[7] |
| Sentinel-1 SAR[8] | 2014–pres. | 25[9] | 6[9] | – | 400[9] | See list[10] |
| Sentinel-2 MSI[*] | 2015–pres. | 10 | 5 | 12-bit | 290 | – |
| RADARSAT-1[8] | 1995–2013 | 30[11] | 24[11] | – | 100[11] | See list[12] |
| WorldView-1[†,13] | 2009–pres. | 0.46[14] | 1.7[14] | 11-bit | 17.6[14] | See list[15] |
| WorldView-2[†,16] | 2009–pres. | 1.84[14] | 1.1[14] | 11-bit | 16.4[14] | See list[17] |

[*] Data from this satellite sensor are used for this thesis.

[†] Data are not open access (i.e. payment is required).

[1] Information presented for the multispectral band of the sensor, and not for any of its other bands, such as the panchromatic or thermal bands, where relevant.

[2] Data based on a repeat imaging time for the whole Earth; temporal resolution may be higher for individual sites (such as those in the polar regions), depending on the satellite's orbital geometry.

[3] Blue and green bands at 500 m resolution; red band at 250 m resolution.

[4] Lüthje *et al.*, 2006; **Box and Ski, 2007**; **Chu *et al.*, 2009**; **Bartholomew *et al.*, 2011a**, 2011b; **Messerli, 2011**; **Selmes *et al.*, 2011, 2013**; Leeson *et al.*, 2012, **2013**; **Liang *et al.*, 2012**; **Doyle *et al.*, 2013**; **Johansson and Brown, 2013**; **Johansson *et al.*, 2013**; **Morriss *et al.*, 2013**; **Bougamont *et al.*, 2014**; **Fitzpatrick *et al.*, 2014**; **Everett *et al.*, 2016**; Ignéczi *et al.*, 2016; **Cooley and Christoffersen, 2017**.

[5] **McMillan *et al.*, 2007**; Sneed and Hamilton, 2007; **Georgiou *et al.*, 2009**; **Sundal *et al.*, 2009**; Legleiter *et al.*, 2014; Yang *et al.*, 2015; **Chen *et al.*, 2017**.

[6] Lüthje *et al.*, 2006; **Hoffman *et al.*, 2011**; **Lampkin, 2011**; Lampkin and VanderBerg, 2011, 2014; **Messerli, 2011**; Howat *et al.*, 2013; **Arnold *et al.*, 2014**; Banwell *et al.*, 2014; Legleiter *et al.*, 2014; Clason *et al.*, 2015; Kingslake *et al.*, 2015; **Nathan-King, 2015**; Poinar *et al.*, 2015; Yang *et al.*, 2015; Miles *et al.*, 2016; Chen *et al.*, 2017; Gledhill and Williamson, 2018.

[7] Moussavi *et al.*, 2016; Pope *et al.*, 2016; Yang and Smith, 2016; Chen *et al.*, 2017; **Miles, K. E. *et al.*, 2017**; Gledhill and Williamson, 2018; **Macdonald *et al.*, 2018**.

[8] Active C-band radar (microwave) satellite sensor.

[9] In the extra-wide swath mode.

[10] **Miles, K. E. *et al.*, 2017**.

[11] In the standard-beam mode.

[12] Poinar *et al.*, 2015.

[13] Panchromatic bands only.

[14] At-nadir for a ground sampling distance of ≤ 1 m.

[15] McGrath *et al.*, 2011; **Joughin *et al.*, 2013**; Smith *et al.*, 2017; **Hoffman *et al.*, 2018**.

[16] Panchromatic-band measurements also collected as for WorldView-1.

[17] Yang and Smith, 2013, 2016; Smith *et al.*, 2015, 2017; Moussavi *et al.*, 2016; Koziol *et al.*, 2017; **Hoffman *et al.*, 2018**.

### 2.4.1 MODIS

MODIS is an instrument aboard the Terra and Aqua satellites, which were launched by NASA in December 1999 and May 2002, respectively. The orbits of Terra and Aqua are timed such that Terra crosses the equator from north to south in the morning, while Aqua passes it from south to north in the afternoon. Because they can image wide areas of the Earth at once (due to the wide swath width of 2330 km and the combination of the two satellites), MODIS data are exceptionally valuable for studying Earth-surface processes, even if they can sometimes be limited by their low spatial resolution. Data are collected by MODIS in 36 spectral bands at high radiometric resolution (12-bit depth) from 0.4–14.4 μm, with bands 1–7 distributed at 250 m or 500 m resolution (Table 2.2); the remaining bands (0.41–14.39 μm) have 1000 m resolution.

**Table 2.2:** Properties of the 250 m and 500 m spatial resolution MODIS bands. Asterisk denotes that data from that band are used in this thesis.

| Band | Common name | Spatial resolution (m) | Wavelengths (μm) |
|---|---|---|---|
| 1* | Red | 250 | 0.620–0.670 |
| 2 | NIR | 250 | 0.841–0.876 |
| 3* | Blue | 500 | 0.459–0.479 |
| 4* | Green | 500 | 0.545–0.565 |
| 5 | NIR | 500 | 1.230–1.250 |
| 6* | SWIR | 500 | 1.628–1.652 |
| 7 | SWIR | 500 | 2.105–2.155 |

The raw satellite data (i.e. at-satellite digital-number measurements) have various levels of processing applied to them to derive a series of data products suitable for Earth monitoring (Justice *et al.*, 2002). Level-0 data are raw satellite feeds, thus being the least processed data, distributed as 5-minute-wide swath data. These data are used to create level-1A data, which are calibrated and geolocated radiance measurements, appended with radiometric and geometric calibration coefficients and georeferencing information, which can be used for further processing. Level-1B data are the same as level-1A data except that the appended information has been applied to produce geolocated and radiometrically-calibrated data. Higher-order level-2 products are then created from these level-1 data, all of which have had atmospheric correction applied (to generate reflectance measurements as they would have been made at the surface, or "bottom-of-atmosphere (BOA) reflectance") and which are normally processed for a specific purpose. They have the same resolution and location as the level-1 source data. Level-3 data are gridded variables as composites of the level-2 data, being distributed as temporally composited or averaged grids (e.g. over 1 day,

8 days, 1 year) of level-2 data. The final, most processed data are level-4 data, which are derived from the outputs of models or other analyses using the lower-level data. MODIS data have short names associated with them, with data collected by the Terra satellite being prefixed with the abbreviation "MOD", Aqua data being prefixed with "MYD", and "MCD" data indicating composited data from both satellites.

Most previous studies involving MODIS for monitoring lakes on the GrIS used level-1B MOD02 data (e.g. Box and Ski, 2007; Sundal *et al.*, 2009; Selmes *et al.*, 2011; Liang *et al.*, 2012; Cooley and Christoffersen, 2017). However, because these data are not atmospherically corrected, a separate atmospheric correction algorithm must be first applied, with the MODIS Corrected Reflectance (CREFL) algorithm normally used to generate surface-reflectance products. A different approach involves using the level-2 MOD09 product (from the Terra satellite) following Fitzpatrick (2014) and Fitzpatrick *et al.* (2014) since atmospheric correction has already been applied. These images are distributed as daily averaged surface-reflectance values in all bands, meaning that in some cases, multiple (MOD02) scenes from the Terra satellite may have been used to composite a single image. 8-day and monthly MOD09 surface-reflectance products are also available. In this study, MODIS MOD09 data are used in Chapters 3 and 4. The MYD09 data (from the Aqua satellite) were also considered for inclusion in the analysis, but were ultimately excluded because the Aqua satellite does not pass over the GrIS with favourable illumination conditions. As these data were not used, the need to exclude images that were not collected close to solar noon, as in previous studies, was removed (Box and Ski, 2007; Selmes *et al.*, 2011; Cooley and Christoffersen, 2017). Moreover, the Aqua satellite has a degraded band-6 (SWIR) sensor, which would have complicated the cloud-masking procedure applied to the data in Section 3.3.2.

### 2.4.2 Landsat 8

The Landsat missions are the longest continuous effort to monitor the Earth with satellites, extending back to 1972 when Landsat 1 was launched, with Landsat 9 and Landsat 10 planned for launch in 2020 and the late 2020s, respectively. Landsat 8 was launched in February 2013, and these data are used in this thesis from 2014 onwards. Landsat 8 has a near-polar, Sun-synchronous orbit, which is offset by eight days from Landsat 7, meaning the two datasets could be combined if required. Landsat 8 data are collected at high spatial resolution compared with MODIS (Section 2.4.1), but with a significantly lower repeat site-imaging time. There are two instruments aboard the Landsat 8 satellite: the OLI and the Thermal Infrared Sensor (TIRS), representing an improvement on the capabilities of earlier Landsat satellites (Roy *et al.*, 2014). Data are collected by the OLI in eight multispectral bands at 30 m resolution (including an ultra-blue band) and a panchromatic band

at 15 m resolution (Table 2.3); meanwhile, the TIRS collects data for two thermal bands at 30 m distributed resolution (for wavelengths from 10.60–12.51 μm), which have been resampled from 100 m native resolution (USGS, 2013).

**Table 2.3:** Properties of the Landsat 8 multispectral bands. Asterisk denotes that data from that band are used in this thesis.

| Band | Common name | Spatial resolution (m) | Wavelengths (μm) |
|---|---|---|---|
| 1 | Ultra-blue (coastal/aerosol) | 30 | 0.435–0.451 |
| 2* | Blue | 30 | 0.452–0.512 |
| 3* | Green | 30 | 0.533–0.590 |
| 4* | Red | 30 | 0.636–0.673 |
| 5 | NIR | 30 | 0.851–0.879 |
| 6* | SWIR 1 | 30 | 1.566–1.651 |
| 7 | SWIR 2 | 30 | 2.107–2.294 |
| 8* | Panchromatic | 15 | 0.503–0.676 |
| 9 | Cirrus | 30 | 1.363–1.384 |

Similar to MODIS data, Landsat data are subjected to different levels of processing: level-0 data are raw satellite feeds, while level-1 data are at-satellite top-of-atmosphere (TOA) radiance measurements. Level-2 products have also recently become available from Landsat 8, which represent BOA or surface-reflectance measurements, accounting for the effect of the atmosphere on the radiance measurements made at the satellite. However, such processing to generate BOA from TOA reflectance is only applied to the multispectral bands and not to the panchromatic band, restricting the usefulness of these data for studying GrIS lakes in this thesis, since the panchromatic band is needed to calculate lake depth (Chapters 3 and 5). Landsat 8 data have been used widely within the cryospheric sciences, including for large-area mapping of ice flow (Fahnestock *et al.*, 2016), mapping ice-sheet velocities (Jeong and Howat, 2015; Mouginot *et al.*, 2017), estimating lake depth (Pope *et al.*, 2016), and mapping valley-glacier extents (Paul *et al.*, 2016). As a result of their high spatial resolution, Landsat 8 data can act as a valuable validation dataset for assessing the reliability of lower-resolution sensors, like MODIS, for measuring the properties of Earth-surface objects.

### 2.4.3 Sentinel-2

The Sentinel-2 instrument comprises a pair of identical satellites called Sentinel-2A (launched in June 2015) and Sentinel-2B (launched in January 2017), both of which have 290 km swath widths, producing a combined 5-day revisit time at the equator, with an even shorter revisit time at the poles,

albeit with different viewing angles. Sentinel-2 has 12-bit radiometric resolution, the same as MODIS and Landsat 8. Sentinel-2 data are collected in 13 multispectral bands, with 10 m resolution in the optical and NIR bands, varying to 20 m or 60 m resolution in the other bands (Table 2.4).

**Table 2.4:** Properties of the Sentinel-2A multispectral bands. Asterisk denotes that data from that band are used in this thesis.

| Band | Common name | Spatial resolution (m) | Wavelengths (μm) |
|---|---|---|---|
| 1 | Ultra-blue (coastal/aerosol) | 60 | 0.430–0.457 |
| 2* | Blue | 10 | 0.448–0.546 |
| 3* | Green | 10 | 0.538–0.583 |
| 4* | Red | 10 | 0.646–0.684 |
| 5 | Vegetation red edge | 20 | 0.694–0.713 |
| 6 | Vegetation red edge | 20 | 0.731–0.749 |
| 7 | Vegetation red edge | 20 | 0.769–0.797 |
| 8 | NIR | 10 | 0.763–0.908 |
| 8A | Vegetation red edge | 20 | 0.848–0.881 |
| 9 | Water vapour | 60 | 0.932–0.958 |
| 10 | SWIR (cirrus) | 60 | 1.336–1.411 |
| 11* | SWIR | 20 | 1.542–1.685 |
| 12 | SWIR | 20 | 2.081–2.323 |

As with MODIS and Landsat 8, different processing levels are applied to the raw Sentinel-2 satellite data. Level-1B data are raw, TOA radiances distributed in the sensor's geometry. Level-1C data are the next level of processed data, which are TOA reflectances in a fixed geometric projection, and which contain applied radiometric and geometric corrections, including orthorectification and spatial registration to a global grid. Level-2A are the most processed Sentinel-2 data, which are BOA reflectances with an atmospheric correction applied; these data must be generated by users of the imagery using a toolbox. Because of Sentinel-2's comparable resolution to Landsat 8, with a common registration system, the two satellites can be combined to produce an improved temporal resolution over that which is possible by using either individually. Currently, however, there is a slight misregistration of 38 m (just over one Landsat 8 pixel) between Sentinel-2 and Landsat 8, but this effect is consistent for a given site, meaning the data can still be used together (Storey *et al.*, 2016). So far, Landsat 8 and Sentinel-2 data have not been used jointly in a single study within glaciology, despite their potential for being used together (Wang *et al.*, 2017). Instead, data from Sentinel-2A only (owing to the only relatively recent (January 2017) launch of Sentinel-2B) have been used individually for mapping valley-glacier extents (Kääb *et al.*, 2016; Paul *et al.*, 2016),

monitoring changes to ice-dammed lakes (Kjeldsen *et al.*, 2017), and cross-comparing ice-albedo products (Naegeli *et al.*, 2017).

## 2.5 Mass balance of the Greenland Ice Sheet

Among the key applications of remote sensing to the cryosphere, one of the most important relates to studying the mass balance of the two ice sheets, something that was difficult to estimate reliably using data that could be obtained from just a few locations that could be accessed with fieldwork (Benn and Evans, 2010). In the same processes as tidewater glaciers and ice caps, ice sheets gain mass by accumulation and lose mass by surface ablation and calving (Benn and Evans, 2010; Cuffey and Paterson, 2010). It is now recognised that both the Greenland and Antarctic ice sheets are losing mass at accelerating rates. This is particularly true for the margins of the GrIS and the marine-terminating outlets of the West Antarctic Ice Sheet, which are often thought to be among the most unstable elements of the global cryosphere (e.g. Joughin and Alley, 2011; Favier *et al.*, 2014; Joughin *et al.*, 2014).

It was realised in the late twentieth century that the GrIS was losing mass at unprecedented rates compared with earlier in the twentieth century, and so increasing attention was given to understanding the magnitude of the losses and the processes driving them (van den Broeke *et al.*, 2016; Fettweis *et al.*, 2017). To this end, presently, three techniques are used to determine the GrIS's mass balance: gravimetry, radar/laser satellite altimetry, and the mass-budget technique (or input-output method). Gravimetry involves measuring the changing gravitational field, and so distribution of mass, over an area of the Earth's surface, which can indicate changes to an ice sheet's total mass, assuming that other processes, such as isostatic rebound and land-ocean leakage effects, are corrected for (e.g. Velicogna, 2009; Xu *et al.*, 2016). The gravimetric method involves the Gravity Recovery and Climate Experiment (GRACE) satellite mission. The GRACE measurements are indirect, involving only a proxy measurement of mass loss (through the direct measurement of the changing gravitational field), but they are thought to measure mass balance accurately (Shepherd *et al.*, 2012; Schlegel *et al.*, 2016). Gravimetric measurements indicate that in 2003–2008, the GrIS was losing 183.0 ± 19.9 Gt $a^{-1}$, which increased to a loss of 261.5 ± 6.1 Gt $a^{-1}$ in 2003–2012, with an acceleration to mass loss of 26.2 ± 1.7 Gt $a^{-2}$ (Jin and Zou, 2015). An alternative technique is radar/laser satellite altimetry, which involves measuring changes to the elevation of the GrIS surface, and then converting elevation change to mass change using a densification model, making assumptions regarding the quantity of mass represented by a given change in elevation. This technique has indicated that the GrIS has switched from gaining a net mass of 5.5 ± 32.1 Gt $a^{-1}$ in 1996–2001 to losing a net mass of 234 ± 46.9 Gt $a^{-1}$ in 2003–2008 (Hurkmans *et al.*, 2014). Finally,

the mass-budget technique measures the difference between the total inputs to and outputs from the GrIS's system; the outputs include those from surface melting and dynamic ice discharge across the grounding line (usually measured with ice-velocity and ice-thickness datasets). This technique is arguably most useful because, if the measurements of the losses/gains from the various inputs/outputs can be validated against, for example, runoff data in the present day, it is possible to test the future sensitivity of the GrIS's mass balance to the various mass-balance components under a future changing climate (IPCC, 2013). This approach suggests that the GrIS's mass loss has more than doubled in the last two decades from 91 ± 31 Gt $a^{-1}$ in 1996 to 224 ± 41 Gt $a^{-1}$ in 2005 (Shepherd *et al.*, 2012) and finally to 269 ± 51 Gt $a^{-1}$ in 2011–2014 (McMillan *et al.*, 2016). This method has also indicated that there has been a switch in the importance of losses from surface melting compared with losses due to ice discharge over the grounding line for marine-terminating outlet glaciers (van den Broeke *et al.*, 2009). Until 2005, over half (58%) of the total mass loss from the GrIS was due to dynamic ice discharge over the grounding line, but this value decreased to just 36% or 32% in the later 2005–2009 and 2009–2012 periods, respectively, due to an increase in the importance of the mass loss from higher surface melting (Enderlin *et al.*, 2014). This suggests it is vital to understand ice-surface processes as well as those at or in close proximity to the grounding line.

Thus, there are differences in the scientific basis to the three approaches outlined above, with each yielding slightly different estimates of total ice-mass loss from the ice sheet. However, the estimates from all of the approaches tend to overlap having accounted for the errors (Figure 2.1). This means that all methods agree that the GrIS's mass balance has become increasingly negative since the late twentieth century, with a pronounced acceleration in ice-mass loss from 2000. Evidence suggests that this is due to: (i) amplified air temperatures in the Arctic, which have increased more than those elsewhere, and which have consequently increased surface melting, and have been implicated in explaining the observed changes to ice velocities; and (ii) increased ocean temperatures, which have increased the undercutting of marine-terminating sectors of the GrIS, causing dynamic drawdown and thinning (e.g. van den Broeke *et al.*, 2017). The net effect is concern over the GrIS's future in the coming century. The GrIS's hydrological system has been implicated as a means of exacerbating the effects of both a warming atmosphere and ocean on the GrIS, and so many studies have focused on understanding its present and likely future configurations, the subject of the next section, and this thesis.

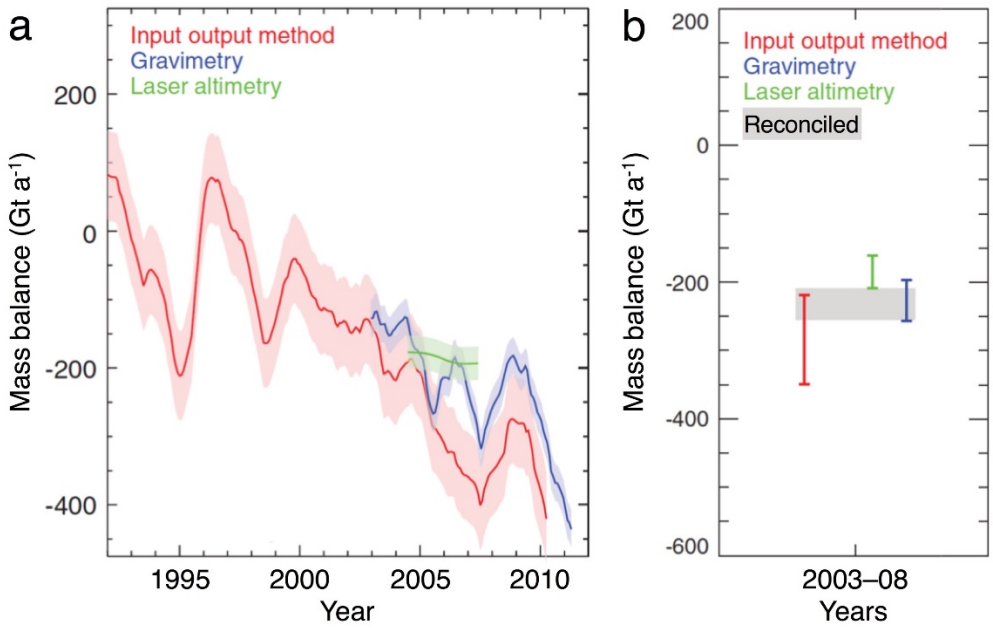



**Figure 2.1:** Increasingly negative mass-balance estimates for the GrIS for (a) 1992 to 2012 and (b) 2003 to 2008 as derived using three independent techniques: the input-output or mass-budget method (red lines), satellite gravimetry (blue lines), and laser altimetry (green lines). Uncertainty ranges are shown as light shading on (a). A reconciled estimate of GrIS mass balance using the three techniques is shown as a grey box on (b). Adapted from Shepherd *et al.* (2012).

## 2.6 Hydrology of the Greenland Ice Sheet

Broadly speaking, the hydrological system of the GrIS is divided into three individual but connected components, covering the supraglacial system (i.e. on or within the surface layers of the GrIS), the englacial system (i.e. within the main body of the ice sheet) and the subglacial system (i.e. at or just beneath the interface between the base of the ice sheet and the underlying bedrock or sediment) (Figure 2.2). All of these systems have been studied, although the inaccessibility of the englacial and subglacial components means that they are relatively under-researched compared with water on the surface, with research into these systems being dominated by theory rather than observation. The following sections review current knowledge and understanding of each of the three systems, including how water within each of them can affect the GrIS's mass balance through, for example, darkening the ice-sheet surface within the supraglacial system (Section 2.6.1), cryo-hydrologic warming within the englacial system (Section 2.6.2) and altering basal water pressures and thus basal-sliding rates within the subglacial system (Section 2.6.3).

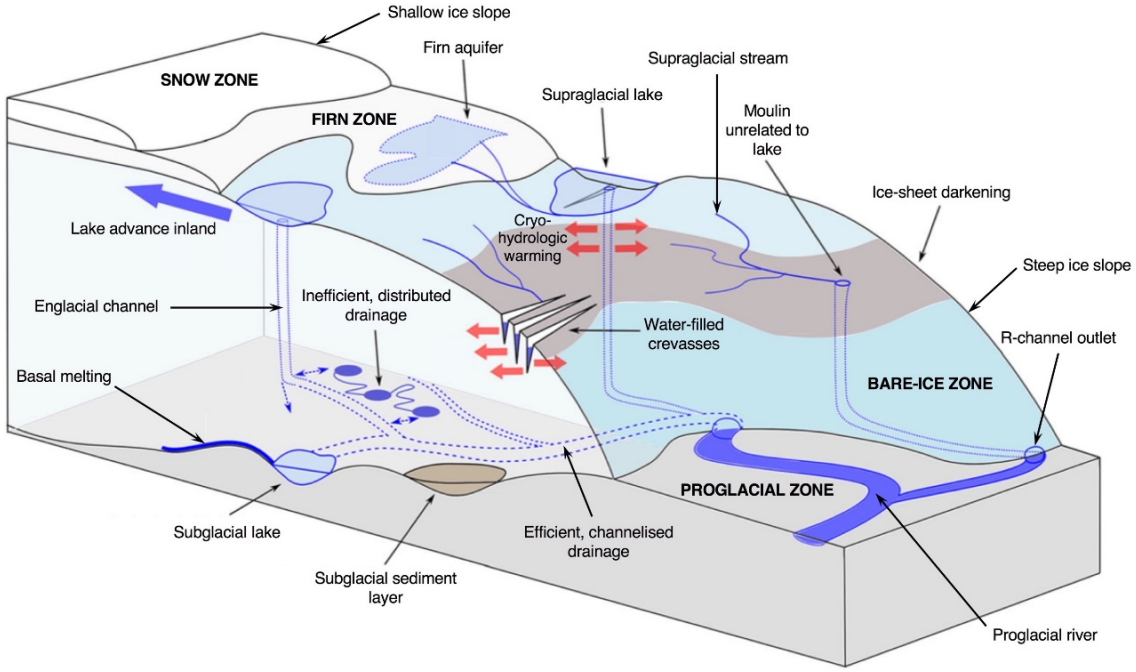



**Figure 2.2:** Schematic depicting the main components of the hydrological system for an idealised land-terminating sector of the GrIS. Adapted from Nienow *et al.* (2017).

## 2.6.1 Supraglacial hydrology

At the start of the year, most of the surface of the GrIS is covered by a thick snow layer. During the ablation season, the snow, firn and ice contained within the supraglacial system melt extensively as air temperatures and incoming shortwave radiation increase, with surface melting commonly extending to ~1400 m above sea level (a.s.l.) (Catania and Neumann, 2010; Noël *et al.*, 2016) and even higher in extreme melt years, when almost the entire surface of the ice sheet may simultaneously be melting (Nghiem *et al.*, 2012). The supraglacial-hydrological system that develops subsequent to this melting is a complex and continuously evolving system of firn aquifers, streams, rivers, lakes and water-filled crevasses (Figure 2.2).

### Processes in the firn zone

Initially, meltwater formed at the surface may become temporarily stored in the pore spaces between ice within what is commonly termed "the firn zone". The firn zone has only received limited research attention, but is now recognised to be important in delaying the runoff produced by surface melt; it may thus help to explain the reason for a discrepancy between the runoff modelled using downscaled climate-model data and direct measurements of proglacial runoff. The melt can pond to form spatially extensive firn aquifers, which may be present across much of the ice sheet, and

which allow the over-winter storage of water (Forster *et al.*, 2014). These firn aquifers are best developed within the south-eastern area of the GrIS, since this area is affected by high accumulation rates and cold winter temperatures, meaning that bare ice is often not revealed here, and the storage of water in firn is promoted (Miège *et al.*, 2013; Kuipers Munneke *et al.*, 2014). In this region, firn aquifers cover a spatial extent of 20,000–70,000 $km^2$, containing a global SLE of 0.4 mm (Forster *et al.*, 2014; Koenig *et al.*, 2014; Miège *et al.*, 2016). Initially, it was thought that firn aquifers were static features. However, more recent research has shown that the aquifers may periodically drain, perhaps through crevasses, with this water potentially able to drive fractures to the ice-sheet bed (e.g. Miège *et al.*, 2016; Poinar *et al.*, 2017a). This is potentially concerning because if the drainage of water contained within firn aquifers were more widespread, it could contribute to the enhancement of ice-deformation rates due to the dissipation of viscous heat when meltwater refreezes at depth. For example, Poinar *et al.* (2017a) modelled an average ice-temperature rise at Helheim Glacier, south-east Greenland, due to firn-aquifer drainage of close to 4 °C over ten years, leading to 50 m $a^{-1}$ increases to the ice-deformation rate, which is 25% of the current ice-flow speed in the area. However, over the longer term, the firn may densify sufficiently to produce ice, meaning that water may never reach the firn aquifer, instead being routed in an efficient supraglacial network of streams/rivers (Machguth *et al.*, 2016). Further research is therefore required to determine whether firn aquifers will become more widespread and whether they will be able to drain in the future. This will help ascertain whether water reaching the bed from firn aquifers could affect basal-sliding rates as well as ice-deformation rates, allowing these processes to be incorporated into holistic models of GrIS hydrology.

## Processes in the bare-ice zone

Over the GrIS surface in the bare-ice zone (which extends further inland over the course of the melt season when snow and firn melt to reveal ice underneath), most meltwater is routed in a network of smaller supraglacial streams or larger supraglacial rivers. These streams and rivers are thermally incised downwards into the ice, with their fluvial erosion dominating supraglacial topography at wavelengths less than the ice thickness (Knighton, 1981; Karlstrom and Yang, 2016). Most streams/rivers are likely to terminate in crevasses or moulins (which are near-vertical shafts extending from the surface into the ice-sheet body, formed by the preferential enlargement of a single crevasse by meltwater), rather than running-off the ice-sheet edge directly (Smith *et al.*, 2015). As the season progresses and more bare ice is revealed, the ice-surface albedo decreases and melting increases further, surface stream/river discharges increase and, consequently, the channel networks become increasingly complex and anastomosing (Knighton, 1972). Despite the large estimated quantities of water carried by these streams/rivers, they remain relatively under-researched; this is

probably because the channels are at most tens of metres wide, requiring satellite imagery at such a resolution, which is rarely available (Table 2.1). The most comprehensive existing study was by Smith *et al.* (2015), which involved mapping 523 supraglacial streams/rivers from 32 WorldView-2 images across a 6812 $km^2$ of south-west Greenland in July 2012, showing that they all terminated in moulins (rather than running-off the ice-sheet edge), and together, over the four-day period, they carried a total water flux of 0.135–0.150 $km^3$ $d^{-1}$. Although these values were measured during an extreme melt event (Nghiem *et al.*, 2012), they indicate a highly efficient system of meltwater evacuation from the GrIS surface through many well-organised, hydraulically-efficient stream/river networks.

## Formation of supraglacial lakes

As well as being transported by streams/rivers, supraglacial water on the GrIS can pond in lakes, and be temporarily stored, usually for days to weeks, with streams/rivers often acting to connect multiple lakes. These lakes form within depressions on the ice-sheet surface, with their positions largely fixed by the underlying bedrock topography, so that lakes are found within the same locations from year to year, instead of advecting with ice flow (Echelmeyer *et al.*, 1991; Gudmundsson, 2003; Lüthje *et al.*, 2006; Box and Ski, 2007; Lampkin, 2011; Selmes, 2011; Liang *et al.*, 2012; Sergienko, 2013; Karlstrom and Yang, 2016). Because lakes are fixed in this way, while the underlying ice is advected beneath them, they can change the colour and structure (e.g. toughness) of the ice, and so potentially alter its melt rate over longer timescales. The present understanding of lakes dates to the work of Echelmeyer *et al.* (1991) who found lakes between tens of metres and 10 $km^2$ in size and 1 to 20 metres deep in the Jakobshavn Isbræ catchment (west Greenland) from 600 m to 1450 m a.s.l., and who documented the first lake-drainage event. Since then, lakes have been identified for most sectors of the ice sheet, which has only been possible due to the increasing availability of satellite imagery with sub-daily repeat intervals, and because these lakes are spatially more extensive than their stream/river counterparts. Regional remote-sensing studies have shown that lakes tend to form closer to the ice margins earlier in the season, and progress inland with warming temperatures over the season, mirroring the inland progression of surface melting. Most of these studies have been focused in west and south-west Greenland, both for individual years and for time periods extending up to a decade (Box and Ski, 2007; McMillan *et al.*, 2007; Sneed and Hamilton, 2007; Georgiou *et al.*, 2009; Johansson and Brown, 2012, 2013; Johansson *et al.*, 2013; Leeson *et al.*, 2013; Morriss *et al.*, 2013; Banwell *et al.*, 2014; Fitzpatrick *et al.*, 2014; Moussavi *et al.*, 2016; Pope *et al.*, 2016; Miles, K. E. *et al.*, 2017; Cooley and Christoffersen, 2017). However, more recent work has begun studying other locations in more detail, including the south-east (Everett *et al.*, 2016) and the north-west (Gledhill and Williamson, 2018), as well as lakes on floating ice tongues (Macdonald *et al.*, 2018).

This additional focus is important as lakes in areas other than the west and south-west are likely to undergo the most pronounced inland advance in the coming century (Ignéczi *et al.,* 2016).

Although regional studies of lakes are numerous, there has been comparatively little attempt to study inter-annual patterns of lake evolution at the whole GrIS scale over multiple years using remote sensing. So far, the studies by Selmes *et al.* (2011, 2013) are the only ones to present an ice-sheet-wide map of lake locations, in which they documented changes to lake areas from 3704 MODIS images of the whole GrIS in 2005–2009, finding 2600 lakes in total (growing to at least 0.0625 $km^2$ or one MODIS pixel in size, once each year). Of the total number of lakes identified across the entire ice sheet, the majority (~55%) were found within the south-west (Selmes *et al.*, 2011). If such ice-sheet-wide studies became more numerous and were combined with a robust method to calculate lake volumes, it would allow improved knowledge of hydrology, and its potential interaction with ice dynamics, at the whole ice-sheet scale. Accepting this necessity, it would therefore be helpful if a method were developed to identify lake locations on an intra- or inter-annual basis for different areas of the ice sheet and to derive the water volumes contained within them automatically. This is the key focus of Chapters 3 and 5 of this thesis, using three different types of satellite imagery. Such lake filling and water-volume estimates could then be used to inform and test surface melt, routing and lake filling models for the GrIS (e.g. Banwell *et al.*, 2012b, 2013a; Arnold *et al.*, 2014; Koziol *et al.*, 2017), with the aim of generating accurate boundary conditions for coupled subglacial hydrology and ice-dynamic models (e.g. de Fleurian *et al.*, 2016; Koziol and Arnold, 2018).

## Inland advance of supraglacial lakes

Lakes are observed to advance inland not only intra-annually, but also over longer (inter-annual to decadal) timescales. Howat *et al.* (2013) were the first to show this decadal-scale advance in 12 sectors using all of the available Landsat-era imagery from 1972–2012, showing the most pronounced inland advance after 2000, where the distance of the uppermost lakes from the ice margin increased by hundreds of metres to tens of kilometres. The most significant change was observed near Jakobshavn Isbræ, where lakes extended 30 km further inland in 2012 than they did before 2000 (Howat *et al.*, 2013). However, this study examined changes to the inland progression of only the uppermost 0.1 $km^2$ of the lake areas from the images of the sites, and not the full changes across the whole of the regions, such as the total lake area or its hypsometric distribution. A more comprehensive study in a north-western sector showed changes to over 8000 manually-delimited lakes from 1985–2016, documenting higher maximum (+418 m a.s.l.) and mean (+299 m a.s.l.) surface elevations of lakes over the period (Figure 2.3), as well as a near-doubling of total regional lake areas and volumes (Gledhill and Williamson, 2018). Again, an acceleration of the inland advance of lakes post-2000 was reported, with the changes being primarily driven by increases in

lake extent at the highest (≥ 1200 m a.s.l.) surface elevations, where there was an increase in the coverage of lakes from 1.2 km$^2$ in 1985 to 34.9 km$^2$ in 2016. More studies that focus on the patterns of lake advance inland, and which compare them against the corresponding ice-velocity speed-ups or slow-downs would be useful since although the two studies mentioned above cover long time periods, they were limited to small regions of the GrIS, and did not examine the effect of lakes on ice velocities.

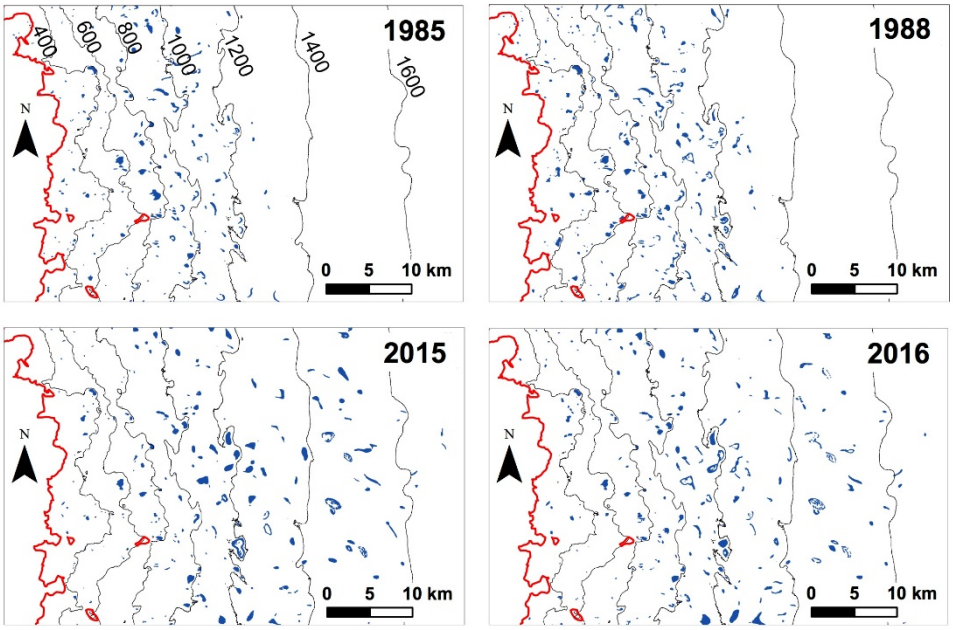



**Figure 2.3:** Inland advance of lakes in a north-western sector of the GrIS from 1985 and 1988 to 2015 and 2016, showing lakes forming at higher elevations and growing in total areal coverage over the study period. Black lines show ice-surface elevation contours from Howat *et al.* (2014) in m a.s.l. (labelled only on the 1985 panel), blue polygons show the maximum extent of lakes delineated from the available Landsat satellite imagery in that year, and red lines delineate the GrIS margin (Howat *et al.*, 2014). Adapted from Gledhill and Williamson (2018).

These two studies prompt concern over the limits to the expansion of lakes towards the ice-sheet interior since they both show no obvious upper limits to the inland advance. A separate study that focused specifically on the inland progression in the future showed that lakes are likely to advance 103 or 110 km further inland under moderate (RCP 4.5) or extreme (RCP 8.5) climate-change scenarios (Leeson *et al.*, 2015). These values were accompanied by increased total lake areas over the whole GrIS of 48% or 53%, assuming that the patterns from south-west Greenland are representative of the entire GrIS and having extrapolated them using an empirically-based technique (Leeson *et al.*, 2015). Leeson *et al.* (2015), however, only showed changes to the individual lake

elevations, rather than their spatial distributions and volumes, and it was unclear how applicable the findings from the south-west region would be for the entire ice sheet. Subsequent work (Ignéczi *et al.*, 2016) therefore took an inventory of surface depressions on the GrIS and modelled future runoff to generate estimates of lake volume to produce a future ice-sheet-wide distribution of lakes. This study raised similar concerns since it showed that, by 2070–2099, an additional 9.8 ± 3.9 $km^3$ (113% more than in 1980–2009) or 12.6 ± 5.0 $km^3$ (174% more than in 1980–2009) of water would be stored in lakes under moderate (RCP 4.5) and extreme (RCP 8.5) scenarios. The largest increases (191 or 320% more lake water storage under RCPs 4.5 or 8.5, respectively) were projected for north-east Greenland, with less severe changes for west Greenland (55 or 65% more lake water storage under RCPs 4.5 and 8.5, respectively), where lakes are presently most extensive, due to the inter-regional differences in the availability of surface depressions for the ponding of meltwater (Ignéczi *et al.*, 2016). These inland advances of lakes are worrying because the lakes are able to influence SMB directly through their effect on albedo and because lakes, if they are able to drain rapidly at these locations, may be able to route meltwater to the ice-sheet bed either directly during the drainage process or indirectly via the moulins opened during hydrofracture. These processes are discussed in further detail below.

## Influence of supraglacial lakes on surface melt rates

The presence of lakes on the GrIS can directly influence surface energy balance, and thus melt rates and SMB (i.e. the difference between ablation by melting and accumulation by snowfall; Section 2.5) because the lakes are darker than the surrounding ice, as first recognised by Echelmeyer *et al.* (1991). One-dimensional numerical modelling suggests that lakes enhance surface melt rates by 110 to 170% compared with bare ice over a 30-day period (Lüthje *et al.*, 2006). Field data collected over multiple days indicate a similar enhancement of ablation beneath lakes of 110 to 135% compared with that for bare ice (Tedesco *et al.*, 2012). However, lakes only cover a small portion of the entire GrIS surface and even when they are present, they only reach their maximum depths (and so lowest albedos, and largest effect on melt rates) either midway through or towards the end of the melt season; many lakes are also highly transient since they drain from the surface, meaning that such enhancements to ablation are likely to be only short-lived for most lakes. Indeed, even with a projected expansion to the areal coverage of lakes across the whole GrIS by 2100, the increase in the magnitude of surface melting from enhanced ablation would only be 0.7–0.8% of the entire increase to melt, indicating that the overall effect of the lakes on the ice sheet's surface albedo is probably insignificant (Leeson *et al.*, 2015). This is especially true when the effects of this process are compared with the effects of darkening of the ice itself from increased black-carbon deposition or the presence of an increasingly-active biological community near the GrIS surface (e.g. Box *et al.*,

2012; van Angelen *et al.*, 2012; Yallop *et al.*, 2012; Chandler *et al.*, 2015; Cook *et al.*, 2017; Stibal *et al.*, 2017; Tedstone *et al.*, 2017). Therefore, overall, the direct influence of lakes on the GrIS's surface-melt rates is likely to be negligible, but the influence of lakes on warming the ice sheet (altering ice-deformation rates) and affecting basal sliding (and thus ice velocity) are more concerning, discussed in the sections below.

### Supraglacial lake drainage

As reviewed above, lakes form within most sectors of the GrIS, are advancing inland over time, and have the potential to influence the GrIS's SMB directly through their effect on surface melt rates. However, lakes are also important for the GrIS because the water contained within them can be routed into the interior of the GrIS during lake-drainage events, and so affect ice-dynamic processes (Section 2.6.3). Lakes thus represent only a temporary means of water storage within the hydrological system. Lake-drainage events are usually classified based on the time period over which they occur into "slow" and "rapid" categories. Although different studies use slightly different definitions, "slow" drainage is usually acknowledged to occur over days to weeks, and involves the overflow of water at a lake's lowest edge once it has filled to the extent of the surface depression, leading to the subsequent incision of a surface stream by the meltwater flowing from the lake (Tedesco *et al.*, 2013; Chu, 2014; Kingslake *et al.*, 2015; Koziol *et al.*, 2017). Alternatively, "rapid" drainage is when a lake catastrophically drains *in situ* via a hydraulically-driven fracture propagation mechanism (termed "hydrofracture"), which usually occurs in hours to days (Figure 2.4). In this process, the water from the lake penetrates through ice that may be hundreds of metres to kilometres thick and is able to reach the ice-sheet bed in as little as two hours (Das *et al.*, 2008) but more commonly in under 24 hours (van der Veen, 2007; Doyle *et al.*, 2013; Tedesco *et al.*, 2013; Stevens *et al.*, 2015). It remains unclear whether the hydrofracture process exploits existing weaknesses in the ice, such as former moulins and crevasses that have closed up and been advected downstream into a lake's basin (Catania *et al.*, 2008), or whether entirely new fractures are formed beneath lake beds. While hydrofracture is now recognised as the process by which lakes drain rapidly, there is uncertainty over the precise factors that lead to its initiation for different areas of the ice sheet and at different times (Section 2.7). Finally, not all of the lakes on the GrIS drain slowly or rapidly: the remaining lakes usually freeze-over and so reduce in size in the autumn when surface temperatures decrease, usually after the first major snowfall event (Selmes *et al.*, 2013; Miles, K. E. *et al.*, 2017). Alternatively, some lakes can become buried and persist over winter (Koenig *et al.*, 2015; Miles, K. E. *et al.*, 2017).

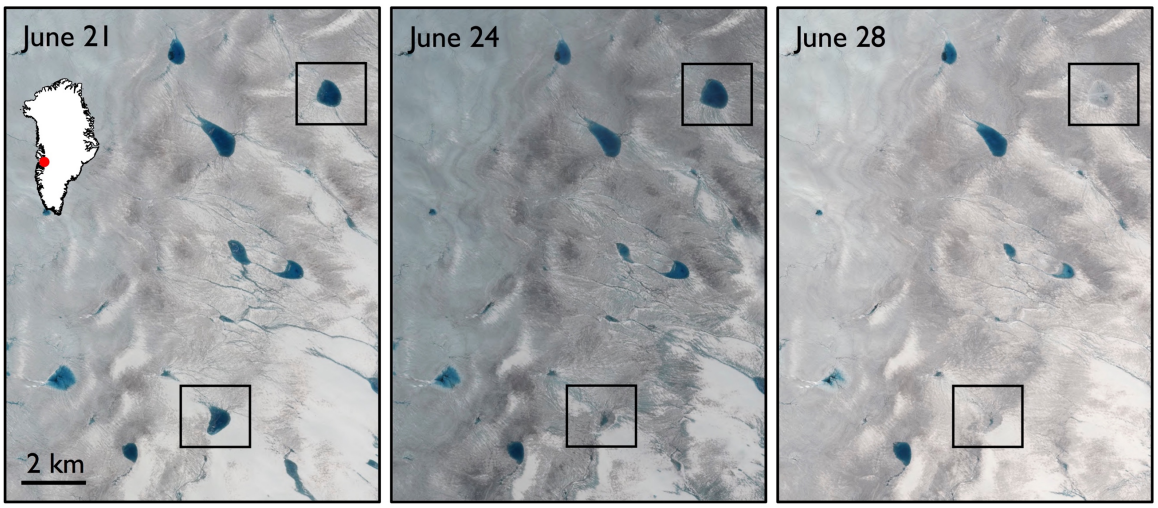



**Figure 2.4:** Rapid *in situ* drainage of two nearby lakes (black boxes) in west Greenland (inset) observed in true-colour Sentinel-2 satellite imagery from summer 2016 (see Table A.11 for image details). Scale is consistent across all images.

## Identifying supraglacial lake drainage with remote sensing

Lake drainage is particularly significant for the GrIS's mass balance because of its effect on ice dynamics (Section 2.6.3), leading a large body of research to focus on understanding the locations and timing of rapid lake-drainage events on the GrIS. Rapidly draining lakes have been studied both with fieldwork and remote sensing, with remote sensing better designed to understanding wide-scale patterns, and fieldwork better suited to understanding local-scale processes. This remote-sensing work has included identifying the numbers of lake-drainage events for different sectors of the GrIS, as well as the areas and volumes of lakes prior to rapid drainage. In this work, attempts are often made to classify lakes into slowly and rapidly draining types based on the definitions introduced above (e.g. McMillan *et al.*, 2007; Selmes *et al.*, 2011, 2013; Liang *et al.*, 2012; Doyle *et al.*, 2013; Fitzpatrick *et al.*, 2014) (Figure 2.5). Sometimes, however, rapidly draining lakes are merely identified as being distinct from those which do not drain rapidly, without separate classifications for slowly draining and freezing lakes.

Since rapidly draining lakes often disappear in under two days (Figure 2.4), remote-sensing-based research requires the collection and analysis of imagery with a sufficiently fine temporal resolution to capture these events, but a compromise is often necessary between satellite imagery with high spatial resolution versus imagery with high temporal resolution (Table 2.1). For identifying lake drainage, Landsat (e.g. Tedesco and Steiner, 2011; Morriss *et al.*, 2013; Arnold *et al.*, 2014; Banwell *et al.*, 2014; Legleiter *et al.*, 2014) and ASTER imagery (e.g. McMillan *et al.*, 2007; Sneed and

Hamilton, 2007; Georgiou *et al.*, 2009) has higher spatial resolution but lower temporal resolution, meaning that MODIS imagery is often preferred because it has up to sub-daily repeat times (Table 2.1). The result is that most studies have focused on analysing MODIS images to identify the timings of lake drainage with confidence (Figure 2.5), even if the areas and/or volumes of lakes cannot be resolved as accurately compared with higher-resolution imagery (e.g. Box and Ski, 2007; Sundal *et al.*, 2009; Selmes *et al.*, 2011, 2013; Liang *et al.*, 2012; Doyle *et al.*, 2013; Johansson *et al.*, 2013; Morriss *et al.*, 2013; Fitzpatrick *et al.*, 2014; Cooley and Christoffersen, 2017). In this work using MODIS images, it is necessary to specify time thresholds to separate lakes that drain rapidly either from those that drain slowly or those that do not appear to drain but subsequently freeze-over. Different studies have defined rapid lake drainage as having occurred if a lake disappears over timescales of two days (Selmes *et al.*, 2011, 2013), four days (Doyle *et al.*, 2013; Fitzpatrick *et al.*, 2014), five days (Liang *et al.*, 2012), or six days (Morriss *et al.*, 2013). These differing definitions were primarily chosen to account for uncertainties in the satellite record. Only one study has tested the implications of the differing definitions for identifying rapid lake drainage, showing that depending on the definition used, the number of rapidly draining lakes identified varies from 3–38% (Cooley and Christoffersen, 2017). Future studies identifying rapid lake drainage remotely may need to normalise their definition of rapid drainage, therefore, to allow comparisons between studies.

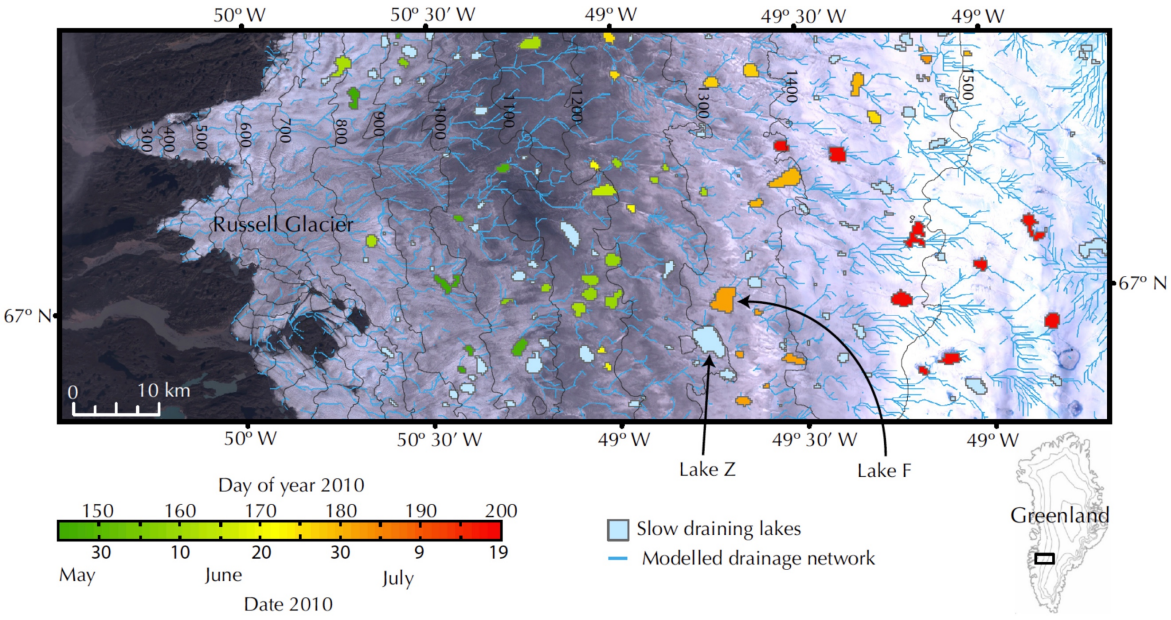



**Figure 2.5:** Sample of a regional-scale study (for the Russell Glacier land-terminating region in west Greenland, inset) involving the identification of rapidly draining lakes using MODIS imagery, separating lakes into rapidly and slowly draining types. Lakes that froze-over were not identified. Colourbar shows the date of rapid lake drainage in 2010. Reproduced from Doyle *et al.* (2013).

Collectively, this remote-sensing work has informed most of our understanding of the locations and filling rates of lakes on the GrIS and, perhaps most importantly, the number of lakes that drain by rapid or slow mechanisms. Two key studies that identified the number of rapidly draining lakes across the entire GrIS over a five-year period were those of Selmes *et al.* (2011, 2013). This work classified lakes (identified from MODIS imagery) into freezing, unknown, and slowly and rapidly draining types (Figure 2.6). They detected a mean of 263 rapid lake-drainage events across the ice sheet per year during the 2005–2009 period, with the majority of these occurring within the north-eastern and south-western sectors. Similar research has been conducted at the catchment or outlet-glacier scales with MODIS, usually in west Greenland (e.g. Sundal *et al.*, 2009; Morriss *et al.*, 2013; Fitzpatrick *et al.*, 2014). MODIS imagery is therefore very valuable for studying lake-drainage processes, with the only disadvantage being that lakes which do not grow to 0.125 km$^2$ (two MODIS pixels) at least once in the season cannot be included in the analysis because MODIS is unable to detect them with sufficient confidence (Leeson *et al.*, 2013; Fitzpatrick *et al.*, 2014). Additionally, Leeson *et al.* (2013) presented evidence that even lakes growing to above this size are often omitted from the MODIS record due to its coarse spatial resolution.

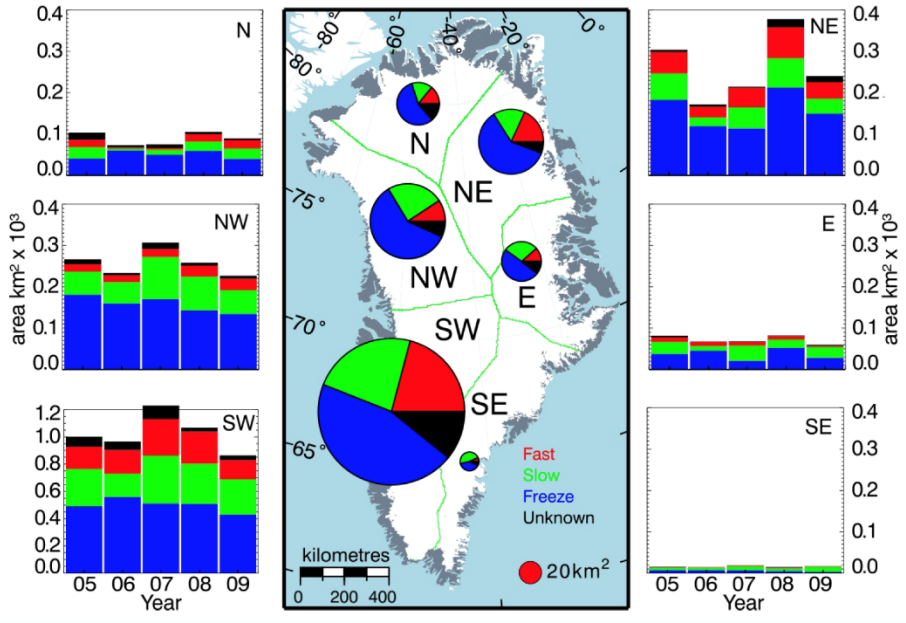



**Figure 2.6:** The distribution of different lake types (i.e. rapidly draining (red), slowly draining (green), freezing (blue), and unknown (black)) within each sector of the GrIS over the 2005–2009 period, highlighting the concentration of rapidly draining lakes in the south-west and north-east. The pie charts on the central panel indicate the mean area of each type of lake over the period, while bar graphs indicate the area of each lake type for each year in the period. Rapidly draining was defined as whenever a lake disappeared from the surface in ≤ 2 days. Reproduced from Selmes *et al.* (2013).

Higher spatial resolution imagery is an alternative to MODIS, but suffers from low temporal resolution, even though fine spatial scale changes to surface features can be resolved more accurately. As a result of the necessary trade-off between high spatial or temporal resolution, it has been suggested that greater insights into GrIS hydrology might be gained if the images from multiple satellites could be used simultaneously (Pope *et al.*, 2016). Miles, K. E. *et al.* (2017) were the first to present such a record of lake observations in west Greenland. They used imagery from the Sentinel-1 SAR (hereafter "Sentinel-1") and Landsat 8 satellites, and developed a semi-automated method allowing them to track lakes at high spatial (30 m) and temporal resolution (~3 days). Using Sentinel-1 imagery allowed them to image lakes both through clouds and in darkness (impossible with optical imagery), enabling them also to study lake freeze-over in the autumn. Their approach permitted the identification of many more lake-drainage events than would have been possible if either set of imagery had been used individually, including the drainage of numerous small ($\leq 0.125$ km$^2$) lakes that could not have been identified with MODIS imagery (Miles, K. E. *et al.*, 2017). Monitoring all lakes, including the smaller ones, many of which may also drain rapidly by hydrofracture (Krawczynski *et al.*, 2009), is important since recent work shows that a key determinant on subglacial-drainage development is the density of surface-to-bed moulins opened by hydrofracture (e.g. Banwell *et al.*, 2016; Koziol *et al.*, 2017).

Thus, Miles, K. E. *et al.*'s (2017) study represented an important step towards combining multiple satellite records, but it had three main limitations. First, their approach required the Landsat 8 imagery to guide the identification of lakes within the Sentinel-1 images, meaning lakes that were never recorded by Landsat 8 during cloud-free periods were omitted from the observations, restricting the quantity of new information that could be obtained with Sentinel-1 and partly offsetting its strength in being able to image through clouds. Second, the method needed high levels of user intervention to delineate lake areas in the Sentinel-1 imagery, meaning it could not be easily applied over multiple seasons and over wide areas of the GrIS, as would be the case with automated approaches. Finally, because the Sentinel-1 images only included radar backscatter values (and not measurements of pixel brightness), it was only possible to delineate lake areas, and not lake depths or volumes (as is possible with optical imagery), consequently limiting the amount of information that could be obtained on GrIS hydrology. Greater insights may be offered into GrIS hydrology by combining multiple satellite records to take advantage of the availability of a suite of new high-resolution satellite datasets. This is the key focus of Chapter 5 of this thesis. If such multiple-satellite records could be combined with other remotely-sensed data (e.g. ice-velocity maps or downscaled climate-model output data), it may be possible to understand why rapid lake drainage occurs in specific places and times and not others (Section 2.7), as well as the influence of lake drainage on the spatial and temporal patterns of ice velocity (Section 2.6.3).

### 2.6.2 Englacial hydrology

Englacial hydrology encompasses the distribution of water within the main body of the ice sheet prior to it reaching the bed. Although a large amount is known about the supraglacial system, less is known about the englacial environment since it is more difficult to access with fieldwork and to image using remote sensing. Because the GrIS is cold-based for most of its depth (Dahl-Jensen *et al.*, 1998; Seroussi *et al.*, 2013), and particularly at large depths close to central portions of the ice sheet (Irvine-Fynn *et al.*, 2011; Lüthi *et al.*, 2015; Poinar *et al.*, 2015, 2017b; Greenwood *et al.*, 2016), there is very limited inter-crystal water flow. Instead, crevasses and moulins are the main means by which water passes through the englacial system; in this way, the GrIS behaves similarly to temperate mountain glaciers (Fountain *et al.*, 2005). These moulins may be formed either during the rapid lake-drainage process, or during the preferential routing of meltwater into a single crevasse over a long time causing it to enlarge significantly, or during changes in far-field tensile ice stresses during a rapid lake-drainage event, which can exceed the fracture toughness of the ice, allowing moulins to open (Hoffman *et al.*, 2018). Moulins and crevasses are important because they concentrate meltwater at specific locations beneath the GrIS, thus acting as nuclei for the development of subglacial channels (Banwell *et al.*, 2016), akin to their role on valley glaciers (Gulley *et al.*, 2012). The importance of these fractures for delivering meltwater to the subglacial system appears to be increasing over time since, in the case of moulins, once they have been formed, they are likely to remain persistent in the same location from year-to-year (Catania and Neumann, 2010). Crevasses are also increasing in extent: Colgan *et al.* (2011b) identified an increase in the number of crevasses > 2 m wide by 13 ± 4% from 1985–2009 in west Greenland. As the ice sheet continues to thin dynamically at its margins, producing an increasingly steep ice-surface gradient, crevasses are also likely to become more prevalent in the future (Colgan *et al.*, 2011b).

Despite the increasing recognition of the importance of crevasses in the overall GrIS hydrological system, crevasses were largely ignored in models of the GrIS's surface hydrology (e.g. Banwell *et al.*, 2013a; Arnold *et al.*, 2014) until recently (Koziol *et al.*, 2017). This oversight of crevasses is likely to stem from the difficulty with delineating them remotely due to the relatively coarse resolution of most satellite imagery preventing their identification (Colgan *et al.*, 2016); the exception is WorldView imagery (Table 2.1). Instead, crevasse locations are often simply predicted according to an ice-toughness criterion, such as the von Mises yield criterion, which might be compared with high-resolution imagery as a first-order attempt at predicting them (Koziol *et al.*, 2017). Because of only limited understanding regarding the precise configuration of the englacial system, it is usually omitted from models of the GrIS's hydrology, with most assuming instead that water entering the ice sheet at the surface simply reaches the bed directly beneath the input location instantaneously,

without any delay (Banwell *et al.*, 2013a, 2016; Arnold *et al.*, 2014; Koziol *et al.*, 2017; Koziol and Arnold, 2018).

### Cryo-hydrologic warming

The amount of water entering the englacial system, as well as the duration of its storage there, has implications for cryo-hydrologic warming, which can affect the GrIS's mass balance indirectly. Owing to the strong temperature dependency of the rate factor in the Glen-Nye flow law (Cuffey and Paterson, 2010), changes to ice temperature have the potential to influence ice-flow rates directly. A mechanism of cryo-hydrologic warming has therefore been proposed whereby the increasing quantities of warmer (> 0 °C) surface water reaching the englacial system via moulins and crevasses have the potential to increase the ice-deformation rate over longer timescales, which may explain the increased ice-flow rates observed within certain areas of the GrIS, which are out of line with model predictions (Phillips *et al.*, 2010, 2013). If water can reach the interior of the GrIS further inland through an increased number of lake-drainage events, cryo-hydrologic warming is another mechanism by which such events may be able to affect the long-term velocity structure of the GrIS. This might result in the increased transport of ice to lower elevations, where temperatures are higher, thereby increasing overall ice-loss rates and potentially leading to a positive feedback. However, the magnitude of cryo-hydrologic warming is debated: Poinar *et al.* (2017b) modelled cryo-hydrologic warming within the Paakitsoq region, which is broadly representative of all land-terminating ice in west Greenland, finding that the refreezing of water at depths of ~300 m warms the ice by up to 10 °C, but this only causes a minimal increase to ice-flow rates of 10 m $a^{-1}$. Similarly, Poinar (2015) indicated that most (> 60%) of ice in Greenland flows too quickly through the ablation zone for cryo-hydrologic warming to be significant. However, studies of cryo-hydrologic warming are still quite few in number, meaning it is still a plausible mechanism by which water entering the GrIS interior may affect long-term dynamics and mass balance.

## 2.6.3 Subglacial hydrology

Perhaps of key importance is how the englacial drainage system affects the locations and timings of surface meltwater delivery to the GrIS's subglacial drainage system, since surface meltwater is by far the most important source of water input to the subglacial system (Fahnestock *et al.*, 2001). In this sense, lake-drainage events are particularly important because the moulins opened by lake drainage provide concentrated access routes for meltwater to reach the ice-sheet bed, and hence act as nuclei for channelisation.

## Idealised configurations of subglacial drainage

Drainage systems beneath the GrIS are often thought to operate under one of two configurations: a hydraulically-inefficient, widely-distributed system or a hydraulically-efficient set of channels that grow in size towards the ice margin (Schoof, 2010; Flowers, 2015). It is important to note that these two configurations are simply end-member states, and a given portion of the GrIS is likely to be underlain by systems that are simultaneously channelised and distributed, with a third type of weakly-connected drainage also now proposed (Hoffman *et al.*, 2016). The key difference between the two currently-accepted systems is the way in which they respond to fluctuations in water inputs, and their consequent influence on ice-flow rates. In a distributed system, which is usually thought to be comprised of cavities linked by a series of orifices, there is a direct relation between the water volume reaching the system and the water pressure within it (Figure 2.7 (a)), whereby increased discharge is driven through the system at increased water pressures, which increases the size of cavities due to higher sliding associated with increased water pressure (Kamb, 1987; Schoof, 2010) (Figure 2.7 (b)). There is therefore a lowering of effective pressure, defined as the difference between the water pressure in the subglacial system and the ice-overburden pressure (Iken, 1981; Kamb, 1987; Iken *et al.*, 1993; Schoof, 2010). However, with a continual increase to discharge, a "critical threshold for channelisation" is reached (Figure 2.7 (a)), where a switch occurs to a system of channels. In this system, there is an inverse relation between discharge and water pressure (Figure 2.7 (a)). An increased discharge reaching the system results in a lowering of water pressure (or rise in effective pressure) since channel cross-sectional areas increase proportionally more than cavities for a given water discharge, due to the effects of channel wall melting from flowing meltwater (Röthlisberger, 1972; Schoof, 2010) (Figure 2.7 (c)). This enlargement effect may be enhanced further by the large quantities of warmer (> 0 °C) surface meltwater within basal channels causing increased viscous heat dissipation (Mankoff and Tulaczyk, 2017).

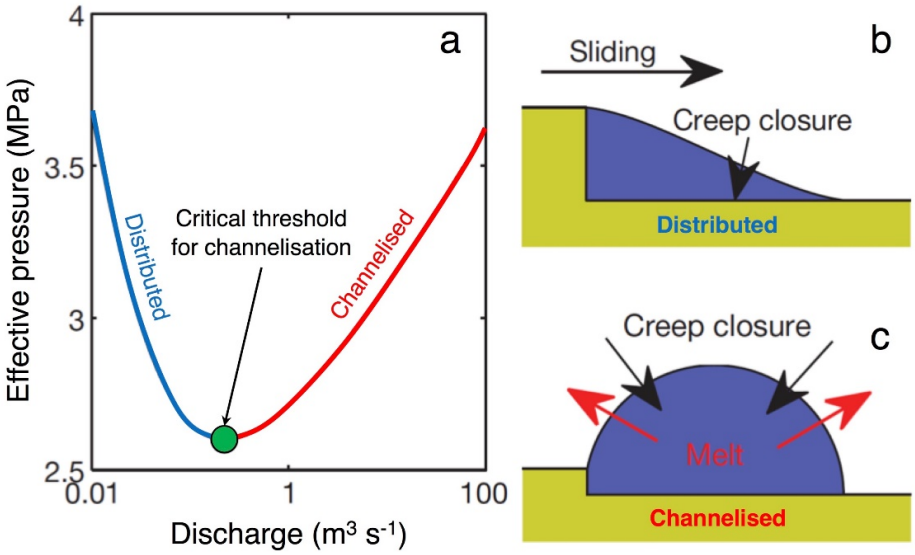



**Figure 2.7:** The physical relation between discharge and effective pressure in a conduit under steady-state conditions (a), to highlight the contrasting relationship for distributed and channelised systems due to the difference between the controls on the size of distributed cavities (b) versus channels (c). Adapted from Schoof (2010).

## Short-term impacts of rapid lake drainage on subglacial hydrology

Earlier work on Alpine valley glaciers showed a seasonal evolution of the subglacial drainage system in response to changing meltwater inputs, whereby increased water volumes reaching the subglacial drainage system in a season drove the system to change from an inefficient distributed state (Figure 2.7 (b)), where water pressures and thus ice-sliding rates are high, to a hydraulically-efficient channelised system that could evacuate water rapidly (Figure 2.7 (c)), leading to decreased ice-sliding rates (Hubbard and Nienow, 1997; Fountain and Walder, 1998; Bell, 2008). Initially, it was thought that the GrIS may be too thick to allow such evolution to occur, and it was postulated that a continued speed-up may occur when increasing quantities of water reached the subglacial system from increased surface-melt rates and lake-drainage events (Zwally *et al.*, 2002). However, for ice-marginal, land-terminating regions, there is now widespread agreement that the effects of water reaching the subglacial drainage system depend on the timescale under consideration. At timescales immediately following lake-drainage events, there are often speed-ups associated with the large meltwater volumes reaching the bed, which cannot be evacuated sufficiently quickly since the system cannot switch immediately from cavities to channels, and so is perturbed from steady-state conditions (Schoof, 2010). Thus, the key determinant at this point in time is the fact that large meltwater pulses are delivered to an inefficient, distributed or poorly-connected system (e.g. Meierbachtol *et al.*, 2016; Hoffman *et al.*, 2016). The result is ice speed-ups of typically 50–200% of

the ice sheet's background winter velocities at timescales from daily to weekly, with such speed-ups often being strongly correlated with daily melt intensities (e.g. Zwally *et al.*, 2002; van der Veen, 2007; Das *et al.*, 2008; Joughin *et al.*, 2008a, 2013; Shepherd *et al.*, 2009; Bartholomew *et al.*, 2010; Palmer *et al.*, 2011; Podrasky *et al.*, 2012; Doyle *et al.*, 2013; Tedesco *et al.*, 2013; Ryser *et al.*, 2014). These velocity increases are sometimes only very short-lived, however, since they are immediately followed by a subsequent slow-down once the drained meltwater pulse has been evacuated, basal water pressure decreases, and the drainage system cannot immediately readjust from its enlarged state following the drainage event (Figure 2.8).

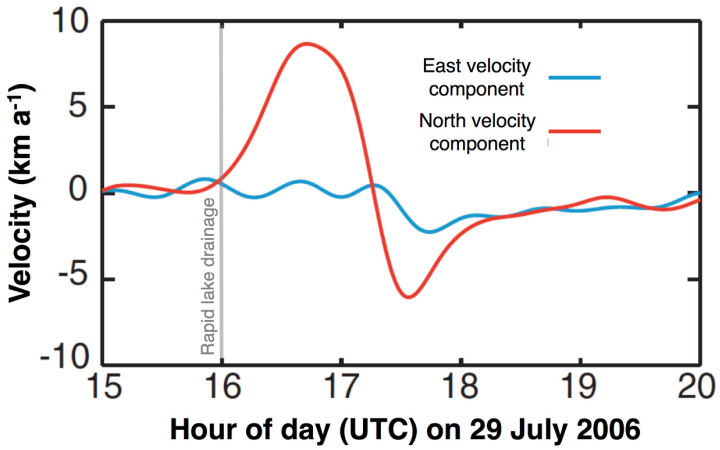



**Figure 2.8:** The effect of rapid lake drainage on short-term ice velocities, showing a rapid increase in ice velocity for ~4 hours following the initiation of lake drainage, and the delivery of a large meltwater pulse to the subglacial system. A decrease in ice velocity then results once rapid drainage has terminated, and basal water pressure decreases while the system remains enlarged from the effect of the drained meltwater pulse. Adapted from Das *et al.* (2008).

## Longer-term impacts of rapid lake drainage on subglacial hydrology

At longer (weekly to seasonal) timescales after lake-drainage events, a slow-down in ice velocity often occurs. This is due to the continued delivery of meltwater to the subglacial system via the moulin opened by drainage, driving the system's evolution to a series of channels that can evacuate meltwater more quickly, and in which there is a direct relationship between effective pressure and discharge (Schoof, 2010; Figure 2.7 (a)). Additionally, the lake-drainage process is important because it is thought to open moulins nearby due to perturbations in the stress field that are associated with the delivery of meltwater to the bed (Christoffersen *et al.*, 2018; Hoffman *et al.*, 2018). These additional moulins can then receive meltwater inputs throughout the ablation season, permitting continued delivery of meltwater to the subglacial system (Bartholomew *et al.*, 2011b),

alongside the moulins opened by individual drainage events. This aids with the transition from inefficient, distributed to efficient, channelised drainage over large portions of the land-terminating margin of the GrIS, inferred from dye-tracing measurements (Chandler *et al.*, 2013; Cowton *et al.*, 2013), and the coincident reductions in ice velocity over seasonal timescales, often observed using direct GPS measurements (Hoffman *et al.*, 2011; Sundal *et al.*, 2011; Fitzpatrick *et al.*, 2013; Cowton *et al.*, 2016; Andrews *et al.*, 2018). Similar evolutions to seasonal ice velocities have been indicated by numerical modelling for ice-marginal regions (de Fleurian *et al.*, 2016). Increases to the efficiency of the non-channelised elements of the subglacial system may also be able to explain late-season velocity slow-downs, which are perhaps due to the leakage of water and lowering of water pressure for weakly-connected regions of the bed (Andrews *et al.*, 2014; Hoffman *et al.*, 2016).

As well as the seasonal implications of an increasing number of lake-drainage events and moulin openings across the GrIS, there are implications over the winter and annually (Colgan *et al.*, 2012; Sole *et al.*, 2013; van de Wal *et al.*, 2015). This is due to channels persisting over winter, rather than closing down, and so being able to drain any subglacial water efficiently, and thus lowering its effect on ice velocities. Finally, the effect of the development of increasingly-efficient drainage seems to be important on inter-annual to decadal timescales: despite increases to surface-melt rates over time, inter-annual to decadal ice-velocity slow-downs have been observed for some marginal areas of the GrIS (van de Wal *et al.*, 2008, 2015; Tedstone *et al.*, 2015; Stevens *et al.*, 2016a). For example, comparing 1985–1994 with 2007–2014, Tedstone *et al.* (2015) document a 12% reduction in annual ice motion despite a 50% increase in surface-meltwater production (Figure 2.9). Similarly, using a static subglacial-hydrological model without any feedbacks on ice flow, Mayaud *et al.* (2014) document an earlier transition from inefficient to efficient drainage when the model is forced with increased future melt volumes. Although Mayaud *et al.*'s (2014) work did not directly couple hydrology with ice flow, the basal water pressures predicted by their model would have produced resultant ice-velocity slow-downs over decadal timescales. These decadal slow-downs are, however, currently not captured in coupled hydrology and ice-flow models, suggesting that further work is needed to constrain the complex nature of subglacial drainage and its feedbacks on ice velocity (Stevens *et al.*, 2016a).

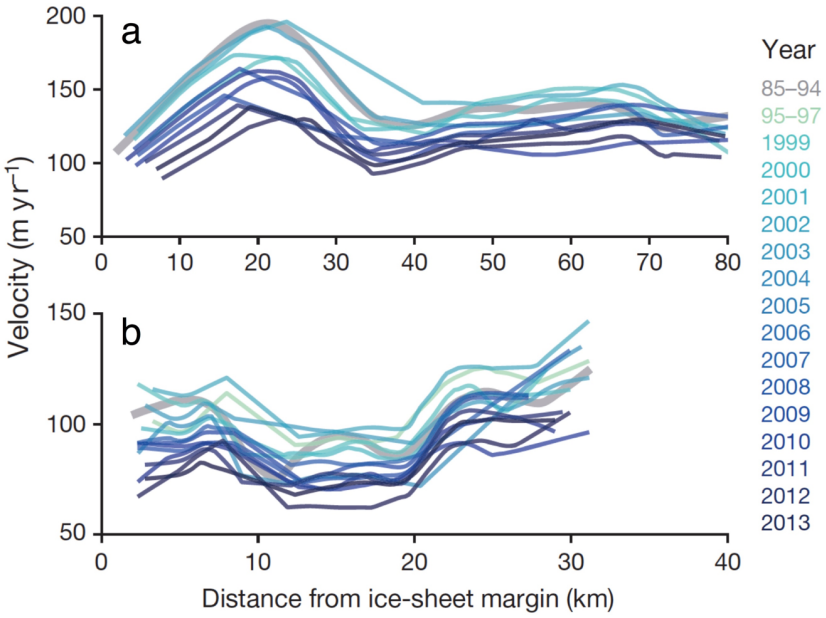



**Figure 2.9:** Decrease in annual ice velocities for two land-terminating transects in west Greenland, showing slow-downs of (a) 19% and (b) 18% in 2013–2014 compared with the 1985–1994 reference period. Adapted from Tedstone *et al.* (2015).

## Impact of rapid lake drainage on inland subglacial hydrology

Despite this decadal-scale slow-down being observed for some of the GrIS's ice-marginal regions, greater uncertainty surrounds the impact of lake drainage, and so greater meltwater volumes reaching the bed, on ice dynamics within interior regions of the ice sheet. This is primarily because fieldwork and modelling have suggested that increased summer velocities do not seem to be offset by subsequent ice-velocity decreases later in the summer, in the winter or in subsequent years (Doyle *et al.*, 2014, 2015; de Fleurian *et al.*, 2016) (Figure 2.10). This creates concern over the future dynamics of the ice sheet. However, predicting the future evolution of the subglacial system inland is particularly difficult given the lack of knowledge regarding the future locations of lakes and how they may drain. Under a warmer future climate, lakes may form and drain at higher elevations earlier in the melt season (e.g. Howat *et al.*, 2013; Leeson *et al.*, 2015; Ignéczi *et al.*, 2016), which may result in meltwater deliveries to a distributed subglacial system that is less able to channelise compared to that beneath thinner ice closer to the margins because the inland ice is thicker (promoting conduit closure) and hydraulic potential gradients are lower with the lower inland ice-surface slopes (inhibiting channel formation downstream) (Meierbachtol *et al.*, 2013; Dow *et al.*, 2014; de Fleurian *et al.*, 2016). This prevention of channelisation may result in continuously higher basal water pressures, and consequently ice velocities, at higher elevations than at present. Alternatively, it has been suggested that there may be a more limited potential in the future for

crevassing at elevations of above ~1600 m a.s.l. on the ice sheet (Poinar *et al.*, 2015). This may limit the likelihood of hydrofracture events, reducing the ability of lakes that form at these elevations to drain and thus to cause melt-induced seasonal acceleration (Poinar *et al.*, 2015). This might be especially true since crevasses may be important for receiving meltwater that can cause transient uplifts or speed-ups of the ice sheet, and thus act as a precursor to hydrofracture (Stevens *et al.*, 2015; Section 2.7). Finally, and by contrast, recent work (Christoffersen *et al.*, 2018) indicates that rapid lake-drainage events close to the ice margin may be able to open surface-to-bed connections as far as 135 km inland, much further than previously thought possible, thus complicating predictions of the future hydrology of the GrIS within interior regions.

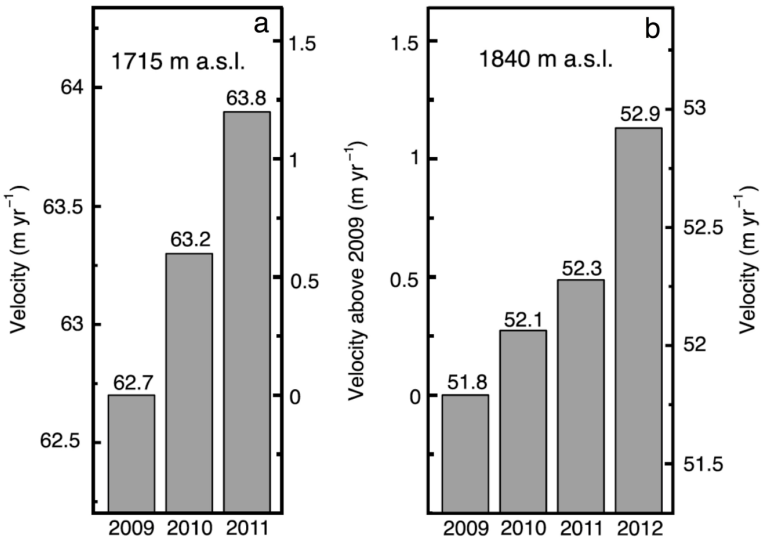



**Figure 2.10:** Persistent flow acceleration after 2009 for two inland sites in the Russell Glacier region of west Greenland (Figure 2.5) at (a) 1715 and (b) 1840 m a.s.l., showing no net annual decrease in velocity following warmer, faster summer flow speeds associated with higher basal meltwater deliveries. Mean winter velocities also did not decrease following the higher summer flow rates. Adapted from Doyle *et al.* (2014).

## Subglacial hydrology of marine-terminating sectors

While the above discussion focuses on land-terminating sectors of the GrIS, the ideas discussed also apply to the grounded portions of marine-terminating sectors. However, hydrology plays an additional role for the floating portions of marine-terminating sectors through its influence on calving rates and its interaction with fjord waters, something that has received comparatively limited research due to the difficulty with making direct observations beneath floating termini (Joughin *et al.*, 2008b; Moon *et al.*, 2015; Voytenko *et al.*, 2015), except perhaps using autonomous underwater vehicles (Stevens *et al.*, 2016b). Research so far has shown that, at the calving front, low-salinity,

less-dense subglacial water emerges and mixes with salty, denser fjord waters, rising towards the surface in buoyant plumes, and creating turbulent eddies that can promote increased calving rates (Jenkins, 2011; Carroll *et al.*, 2016; Slater *et al.*, 2017) (Figure 2.11). The height of the plume depends on the stratification of waters in the fjord and the volume of subglacial discharge, meaning there is concern that, in the future, with higher subglacial discharges from increased melt rates, plume heights may increase, and so a greater portion of the ice front may be impacted by this process; this effect depends on the stratification of fjord waters, however (Slater *et al.*, 2016). Alternatively, subglacial water may promote higher rates of subaqueous melting beneath the calving front, promoting extra undercutting, and thus increasing the likelihood of calving (Fried *et al.*, 2015; Rignot *et al.*, 2015; Moyer *et al.*, 2017). The magnitude of this effect depends on the configuration of subglacial drainage, with a distributed system potentially inducing up to five times more melt than a channelised system (Slater *et al.*, 2015, 2017). A final area of uncertainty for marine-terminating outlets surrounds the degree of longitudinal inland ice coupling associated with iceberg-calving events and its resultant impacts for longer-term ice velocities (Jenkins, 2011; Nick *et al.*, 2009; Hill *et al.*, 2017). There is therefore a need to predict the location, timing and magnitude of water arriving at floating ice tongues to aid with estimates of the future evolution of marine-terminating portions of the GrIS.

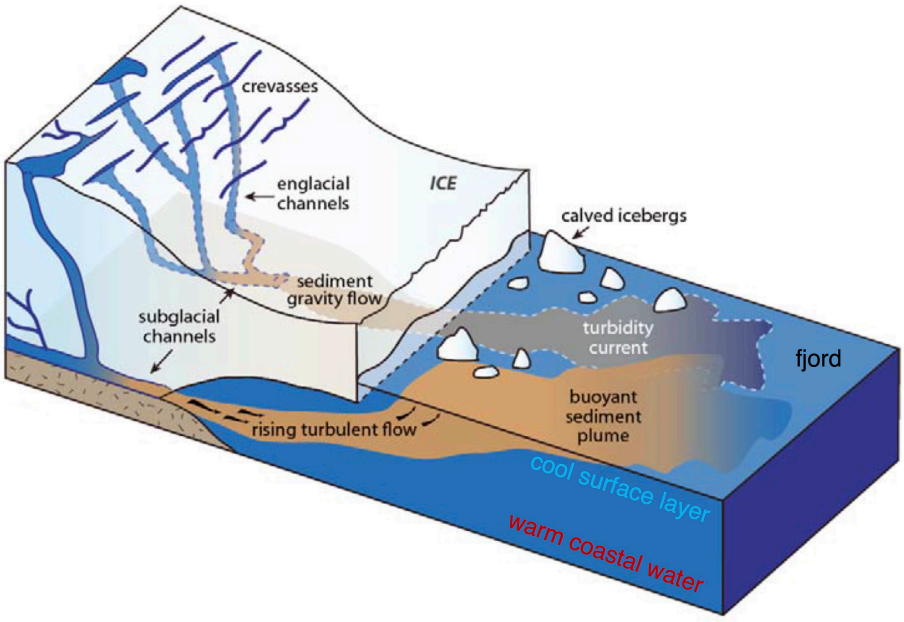



**Figure 2.11:** Schematic of idealised supraglacial, englacial and subglacial hydrology at a marine-terminating outlet of the GrIS, showing a buoyant sediment plume mixing with fjord waters. Submarine melting also occurs beneath the floating tongue. Adapted from Chu (2014).

## Bed configuration of the Greenland Ice Sheet

One final uncertainty relating to the GrIS's subglacial drainage concerns its bed configuration. Most of the current understanding of subglacial hydrology has been derived from modelling work assuming that the GrIS is underlain by a hard bed. This holds true for some areas of the GrIS, such as the Kangerlussuaq sector, where a borehole study revealed the absence of a thick layer of sediment (Harper *et al.*, 2017). Although a hard-bed configuration can explain the relation between melt variations and surface velocity in existing models (Sundal *et al.*, 2009; Bartholomew *et al.*, 2012; Cowton *et al.*, 2013; Hewitt, 2013; Werder *et al.*, 2013; Doyle *et al.*, 2018), a soft bed has now been identified for some regions by observations from boreholes and seismic studies (Clarke and Echelmeyer, 1996; Lüthi *et al.*, 2002; Booth *et al.*, 2012; Dow *et al.*, 2013; Ryser *et al.*, 2014; Walter *et al.*, 2014). These observations have led some workers to include soft beds comprising hydraulically-weak, deformable sediments in their models of ice-sheet hydrology and motion (Bougamont *et al.*, 2014; Aschwanden *et al.*, 2016; Kulessa *et al.*, 2017) since they have different implications for the modelling of subglacial water flow (e.g. Kamb, 1987; Iken *et al.*, 1993; Walder and Fowler, 1994). There is as yet, however, no conclusive evidence to show how widespread these sediments are, and there may be complex, heterogeneous hydrology beneath the GrIS comprising both hard and soft bed components, which can promote the over-winter storage of water (e.g. Chu *et al.*, 2016). Finally, subglacial lakes, which were thought not to exist beneath the GrIS, have also recently been detected and shown to drain (Palmer *et al.*, 2013, 2015; Willis *et al.*, 2015). A detailed examination of radar profiles suggests the existence of 56 subglacial lakes beneath the GrIS (Bowling *et al.*, in preparation). The influence of subglacial lakes, including their drainage, on ice flow may also therefore need incorporating into future modelling work.

## Coupling subglacial hydrology with ice flow

Because of the diverse possibilities regarding the configuration and operation of the subglacial drainage system beneath the GrIS, coupling an ice-flow model to a time-dependent subglacial hydrology model forced with real data has remained elusive. Koziol and Arnold (2018) present the most comprehensive, holistic hydrological model for the GrIS to date. This model incorporates surface-meltwater routing (following Koziol *et al.*, 2017), with Regional Atmospheric Climate-Model Output (RACMO) 2.3 data used to force the model (Noël *et al.*, 2016); the model lacks englacial routing or storage components, and uses Hewitt's (2013) subglacial-hydrology model, which is finally coupled to an ice-flow model using the Schoof sliding law (Schoof, 2005; Gagliardini *et al.*, 2007) and the Budd sliding law (Budd *et al.*, 1979; Hewitt, 2013) – from these two, the Budd sliding law performed best (Koziol and Arnold, 2018). The model was validated using

ice-velocity data from recent years, performing best in 2011, and was then forced into the future with an estimated future climate scenario by multiplying the surface meltwater inputs for summer 2011, defined as an enhanced melt year (Koziol, 2018; Koziol and Arnold, 2018), by four, showing up to a 25% net velocity increase as a result of such extra meltwater inputs to the system (Figure 2.12). The most pronounced speed-ups were at intermediate distances (~30–70 km) from the ice margin (Figure 2.12). However, this was for a static ice-sheet configuration without any dynamic adjustments or changes in the ice-sheet morphology, making it difficult to determine the real impact of extra meltwater reaching the ice-sheet bed inland.

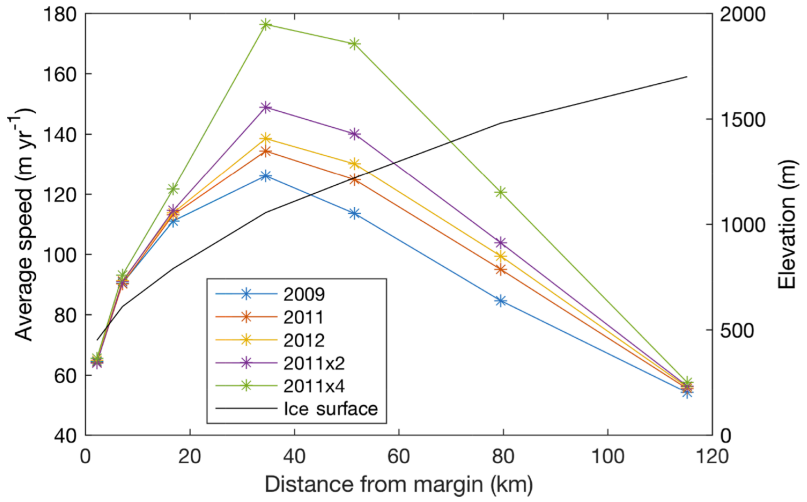



**Figure 2.12:** Sample of modelled land-terminating average seasonal ice velocities for different GPS sites (asterisks) at different elevations in west Greenland, using a coupled hydrology and ice-dynamics model, for different years, including velocities for estimated future melt scenarios (assuming a static ice-sheet configuration, without dynamic adjustments), shown as "2011×2" and "2011×4". Reproduced from Koziol and Arnold (2018).

## 2.7 Controls on rapid supraglacial lake drainage

The above discussion suggests a need to understand the incidence and causes of rapid lake drainage in time and space. However, research to identify the possible drivers of hydrofracture has produced a consensus only on the general controls on rapid lake drainage in terms of its location, timing and magnitude for different regions of the GrIS. Namely, rapid drainage typically occurs at progressively higher elevations over the melt season, with the usually smaller lakes near the ice margin draining before the larger ones further inland (e.g. Chu, 2014; Nienow *et al.*, 2017). Although the hydrofracture mechanism is thought to be responsible for rapid lake drainage, comparatively little attempt has been made to quantify the precise factors responsible for initiating the process for a large

sample of lakes on the GrIS. Instead, most of the insights into the hydrofracture process have been obtained from field studies of individual or groups of lakes (e.g. Das *et al.*, 2008; Tedesco *et al.*, 2013; Doyle *et al.*, 2014; Stevens *et al.*, 2015). These field studies are somewhat limited, however, as they each examine only either single or a few lakes, and so it is unclear whether the findings may apply to different lakes. Consequently, theoretical numerical modelling and remote sensing have attempted to offer further insights into the controls on rapid lake drainage over wider spatial and temporal scales.

## Theoretical insights into hydrofracture

Early theoretical work identified the physical constraints on hydrofracture. This research was based on linear elastic fracture mechanics, which states that a fracture will propagate to the base of an ice mass when the tensile stress of the underlying ice and the water pressure within an initial crack in the ice are sufficient to overcome the fracture toughness of the ice itself (Alley *et al.*, 2005b; van der Veen, 2007; Tsai and Rice, 2010). This indicates that field tensile stresses are the key determinants of crevasse and fracture positions on the ice-sheet surface, and that once these fractures become water-filled, they can work their way to the base of an ice mass due to the difference in density between ice and water at the tip of the crack, as long as the fracture remains water-filled for the entire depth of the crack to offset the process of water refreezing on the crack walls at increased depths (Alley *et al.*, 2005b; van der Veen, 2007; Tsai and Rice, 2010). Lakes are able to provide such a water source. However, the earlier work (Alley *et al.*, 2005b; van der Veen, 2007) simply assumed that there was a constant supply of water, without taking account of the absolute volume necessary to force a crack all the way to the base of an ice mass. Krawczynski *et al.* (2009) therefore advanced this work to calculate the volume of meltwater required within a lake to force a fracture to the base of the ice sheet, finding that lakes at least ~250–800 m in diameter (i.e. with areas of at least 0.0491 to 0.0502 $km^2$ if approximated as perfect circles) and ~2–5 m deep (i.e. with volumes of $9.81 \times 10^4$ $m^3$ to $2.51 \times 10^6$ $m^3$) can hydrofracture through ice 1 km thick. This research suggests that a critical water volume is necessary to ensure that a fracture remains water-filled for the entire depth of the crack from the ice surface to bed; it follows that water volumes would necessarily need to be larger in thicker ice, where cracks must be deeper to penetrate through the full ice thickness.

## Fracture-area thresholds for predicting rapid lake drainage

Because of this suggestion of some relation between ice thickness and a rapidly draining lake's water volume, some studies attempted to incorporate water-volume thresholds into numerical models using the empirically-based concept of a "fracture-area threshold". In this approach, rapid lake drainage is triggered once a lake's water volume exceeds the local ice thickness multiplied by a

prescribed map-plane fracture area (Clason *et al.*, 2012, 2015; Banwell *et al.*, 2013a, 2016; Arnold *et al.*, 2014; Koziol *et al.*, 2017). The predictions of where rapid lake drainage will occur are then compared with observations, adjusting the required fracture values to produce best matches between modelled and observed lake-drainage events. Following the assumptions of Clason *et al.*'s (2012, 2015) model setups, Banwell *et al.* (2013a) found that a fracture area of 1000 $m^2$ times the ice thickness (equivalent to a volume of $1.0 \times 10^6$ $m^3$ for a lake above ice 1 km thick) produced the best matches between modelled and observed results, with 10/44 or 23% of lakes in the Paakitsoq region draining rapidly, comparing favourably with results derived from across the entire GrIS where 13% of lakes drain rapidly (Selmes *et al.*, 2011). However, Banwell *et al.* (2013a) only considered a marginal area of the GrIS. Arnold *et al.* (2014) extended the region of interest further inland; similar to Banwell *et al.* (2013a), they modelled the incidence of hydrofracture, using the fracture-area threshold, over an area of west Greenland for 2001, 2002 and 2005 (Figure 2.13) and found that values of the fracture-area threshold around 4000–7500 $m^2$ times the ice thickness (equivalent to volumes of, respectively, 4.0 and $7.5 \times 10^6$ $m^3$ for lakes above ice 1 km thick) produced the best agreement between satellite-derived (Landsat 7) and modelled lake-water depths across the whole region (Table 2.5). These values are higher than those found by Banwell *et al.* (2013a); this is likely to be because Arnold *et al.*'s (2014) study region included areas of thicker ice, suggesting that the fracture-area threshold and ice thickness do not scale linearly. Arnold *et al.* (2014) were, however, unable to constrain the water volume required for hydrofracture further, which is likely to be because observations have indicated that many lakes with volumes above the critical threshold required for hydrofracture do not drain rapidly, while some with volumes less than this value do drain (Selmes *et al.*, 2013; Fitzpatrick *et al.*, 2014). Thus, fracture-area thresholds are unable to predict the precise locations and timings of rapid lake-drainage events, but they can still replicate the broad statistical patterns of rapid lake drainage across an area of the ice sheet, notably its upglacier progression by elevation band over the season (Figure 2.13).

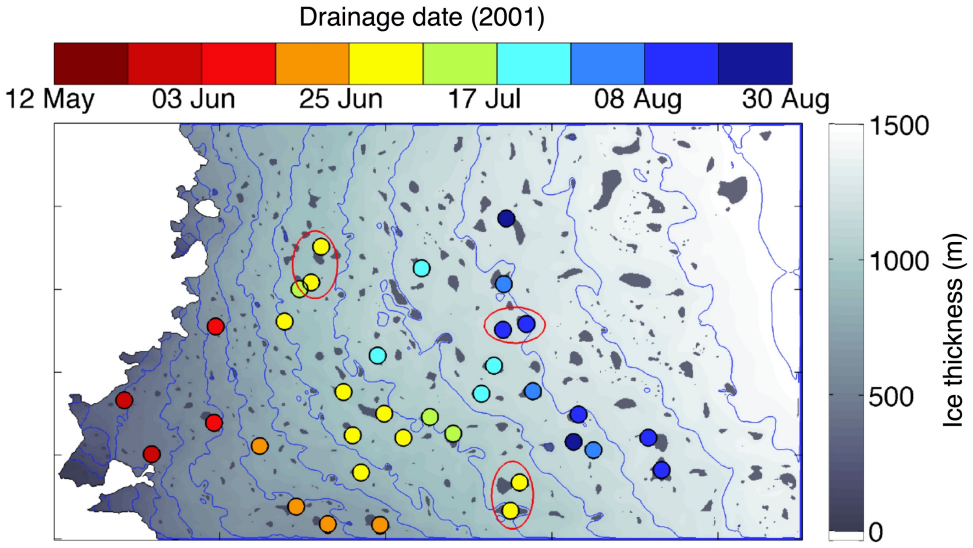



**Figure 2.13:** The modelled seasonal (2001) upglacier progression of the rapid drainage of lakes within the Paakitsoq region of the GrIS, according to a model that includes a simple water-volume threshold linearly related to ice thickness to allow lakes to drain rapidly. This highlights the ability of Arnold *et al.*'s (2014) model to replicate broad-scale statistical patterns of rapid lake drainage. Identified clusters of lake-drainage events are circled in red. Ice-thickness data are from Plummer *et al.* (2008). Adapted from Arnold *et al.* (2014).

## Uncertainties over the distinct characteristics of rapidly draining lakes

Alongside these differences in the fracture-area threshold needed to produce the best matches between modelled and observed lake-drainage events, field and remote-sensing studies have identified a broad range of water volumes prior to rapid lake drainage, leading to uncertainty over the precise volume required for hydrofracture to be initiated (Table 2.5). The idea that there may therefore not be a simple critical water volume, related to the local ice thickness, for rapid lake drainage is further supported by the observations of inter-annual variations in the drainage modes of some lakes: individual lakes can change their drainage behaviour (such as from slow to rapid, or rapid to freezing), and drain with different observed water volumes between different years (Selmes *et al.*, 2013). Observations such as these have led to suggestions that there may be no relationship between a lake's size and its ability to drain rapidly to the GrIS bed (Fitzpatrick *et al.*, 2014), but this requires verification.

In addition to the uncertainty over whether there is a precise water volume required for rapid lake drainage, there is also uncertainty over whether the incidence of lake drainage is affected by the background ice velocity and stress regime beneath or close to a lake basin, and whether this regime

affects the water volume required to trigger hydrofracture. This means that simplifications have to be made in current models of hydrofracture (Carmichael *et al.*, 2015): for example, Alley *et al.* (2005b) assume extension is necessary for hydrofracture, Tsai and Rice's (2010) theoretical considerations are only applicable if the region has moderate extensional or compressional horizontal stresses, and Krawczynski *et al.* (2009) do not consider longitudinal stress in their calculations. Meanwhile, a field study by Stevens *et al.* (2015) observed high transient tensile stresses across the lake basin following the delivery of meltwater to the bed nearby (Figure 2.14). Further work is therefore required to incorporate varying strain regimes into existing models and to collect empirical data to verify these theoretical considerations. Such data will help determine whether rapid lake drainage may be more likely to occur if a lake lies within a relatively more or less tensile area.

It is also possible that a lake's water volume is important in controlling the incidence of hydrofracture but only if one or more additional controls work alongside it. Observations of "clusters" of lake-drainage events, when lakes in similar locations drain at similar times (Figure 2.13) (Arnold *et al.*, 2014; Fitzpatrick *et al.*, 2014; Christoffersen *et al.*, 2018), suggest that factors operating over wider spatial scales, beyond an individual lake basin (or "synoptic" scales), may be important for lake drainage. For example, field data from Stevens *et al.* (2015) show that a local stress perturbation (caused by the delivery of meltwater to the ice-sheet bed via a nearby moulin) was required to initiate hydrofracture, with a certain lake area or volume being only a prerequisite for, rather than the driver of, drainage. Such synoptic-scale factors may be able to influence chain-reaction-style lake drainage whereby surrounding lakes can drain due to the changes in the three-dimensional stress field (Christoffersen *et al.*, 2018). In this way, such observations are not dissimilar to those leading to the disintegration and collapse of the Larsen B Ice Shelf (Banwell *et al.*, 2013b).

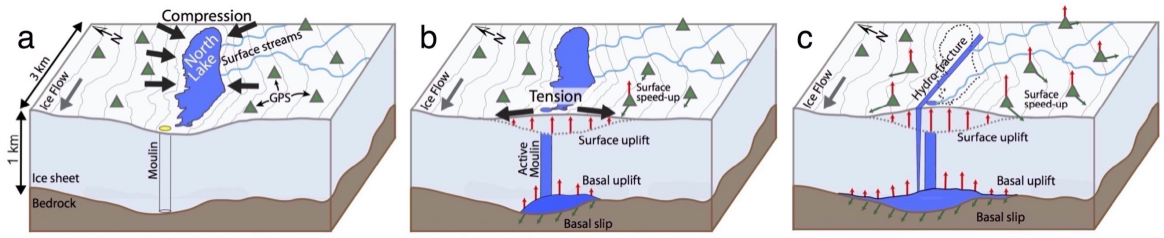



**Figure 2.14:** The hydrofracture process beneath 'North Lake', a rapidly draining lake in west Greenland, including the precursor required for drainage: (a) lake formation within a compressive basin, (b) meltwater is routed into a nearby moulin as one potential synoptic-scale precursor to lake drainage, producing uplift and transient tensile stress across the lake basin, and (c) hydrofracture is initiated beneath the lake, the lake drains in hours, and the moulin opened-up can subsequently route meltwater to the ice-sheet bed. Adapted from Stevens *et al.* (2015).

## Eliciting controls on rapid lake drainage with remote sensing

Because of the range of uncertainties described above regarding the precise hydrological and glaciological controls on rapid lake drainage (Table 2.5), models of GrIS hydrology are presently unable to incorporate a better physical basis for predicting rapid lake drainage, and so cannot be confidently forced into the future. There is a need, therefore, to investigate whether the observations from individual lakes apply more widely, whether additional controls are important in driving lake drainage, and whether the controls are spatiotemporally uniform or variable between sectors of the GrIS and times of the year, including for inland and ice-marginal regions, and land- and marine-terminating sectors. Towards this end, Selmes (2011) examined how ice thickness, ice-surface slope and ice-surface velocity might influence rapid lake drainage identified from MODIS imagery over the entire GrIS in 2005–2009 but found statistically insignificant relationships for all of the controls investigated. This study may have been limited, however, because: (i) the data were of coarse (~5 km) resolution; (ii) it was over the entire GrIS rather than for specific regions, making patterns difficult to distinguish from noise in the data; (iii) the statistical relationships were computed with respect only to lake areas and not lake volumes, and; (iv) the analysis was restricted to linear correlation. A study with finer-resolution data for a suite of other potential controls on drainage in addition to those included by Selmes (2011) would be helpful for ruling out certain possible controls and identifying the importance of others for triggering rapid lake drainage on the GrIS. This is the key focus of Chapter 4.

**Table 2.5:** Hydrological, glaciological and other notable characteristics of rapidly draining lakes on the GrIS identified in previous studies.

| Study | Study type | Lake area ($km^2$) | Lake volume ($10^6 m^3$) | Lake depth (m) | Ice thickness (km) | Ice-stress regime | Other drainage controls |
|---|---|---|---|---|---|---|---|
| Alley *et al.* (2005b) | Theoretical | – | – | – | – | High horizontal tension required | Crack must be connected to water body to offset water refreezing |
| van der Veen (2007) | Theoretical | – | – | – | – | Tension assumed[1] | Crack propagation speed strongly controlled by meltwater inflow rate |
| Krawczynski *et al.* (2009) | Theoretical | 0.0491 | 0.098[2] | 2.0–5.0 | 1.0 | No longitudinal stress | – |
| Boon and Sharp (2003)[3] | Theoretical | – | – | 7.0 | 0.15 | – | – |
| Das *et al.* (2008) | Field | 5.6 | 40.4 | – | – | – | – |
| Doyle *et al.* (2013) | Field | 4.5 | 7.4 | | | Compressive lake basin | – |
| Tedesco *et al.* (2013) | Field | – | 1.6 | 5.0 | – | – | – |
| Stevens *et al.* (2015) | Field | – | 7.0[4] | | – | Extension observed | – |
| Box and Ski (2007)[5] | Remote sensing | 1.4 | 4.1[6] | 6.1 | – | – | – |
| Fitzpatrick *et al.* (2014) | Remote sensing | – | – | – | – | – | Nearby rapid lake drainage can incite other rapid drainage events |
| Miles, K. E. *et al.* (2017) | Remote sensing | 0.0495[7] | – | – | – | – | – |
| Banwell *et al.* (2013a) | Modelling | – | 1.0[8,*] | – | 1.0 | – | – |
| Arnold *et al.* (2014) | Modelling | – | 4.0–7.5[9,*] | – | 1.0 | – | – |
| Clason *et al.* (2015) | Modelling | – | – | – | – | Tensile stress ignored | – |
| Koziol *et al.* (2017) | Modelling | – | 2.0–6.0[10,*] | – | 1.0 | – | – |

[1] Theoretical work was insensitive to assumed tension value.
[2] Calculated by multiplying the study's lower lake-water-depth bound (2 m) by the lower lake-area bound (a 0.25 km-diameter lake approximated as a perfect circle).
[3] Study on John Evans glacier, Ellesmere Island, Canada, rather than the GrIS, but also for cold-based ice (at ~−10 °C).
[4] Study assumes value based on summer 2011 measurements.
[5] Study identifies only 'outburst' events but does not determine the mechanism of 'outburst' (either lake overtopping or hydrofracture).
[6] Smallest value listed in the study, which only presented the 50 largest events.
[7] Lower bound, limited to the smallest lake size (55 × 30 m pixels = 0.0495 $km^2$) tracked in the study.
[8] Value producing best match between modelled and observed proglacial discharge.
[9] Value producing best match between modelled and satellite-observed (Landsat 7) volumes, but volumes were likely to have been overestimated (Pope *et al.*, 2016).
[10] Model sensitivity was tested within this range to show how lakes were partitioned into different drainage types based on adjusting this value.
[*] Value calculated by multiplying the study's fracture-area threshold by an ice thickness of 1 km.

## 2.8 West Greenland study regions

In Chapters 3 and 4, which involve the development, validation and application of a new, fully-automated lake-tracking methodology, the study sites are the Paakitsoq and Store Glacier regions of west Greenland, both of which are ~5600 km$^2$ (Figure 2.15).

The Paakitsoq region (between ~69°15′N and 69°45′N, and ~51°45′W and 48°15′W) is a predominantly land-terminating area of the ice sheet just north of Jakobshavn Isbræ, the site of several previous hydrology-based field (Catania *et al.*, 2008; Das *et al.*, 2008; Tedesco *et al.*, 2013), numerical modelling (Colgan *et al.*, 2011a; Banwell *et al.*, 2012a, 2012b, 2013a, 2016; Arnold *et al.*, 2014; Koziol *et al.*, 2017) and remote-sensing studies (Zwally *et al.*, 2002; Box and Ski, 2007; McMillan *et al.*, 2007; Joughin *et al.*, 2008a; Hoffman *et al.*, 2011; Lampkin, 2011; Banwell *et al.*, 2014). This allows easy comparisons between the results of this thesis and existing work. The Store Glacier region (between ~70°15′N and 70°45′N, and ~51°00′W and 48°15′W) is situated in the Uummannaq district, north of the Paakitsoq region, and includes Store Glacier (Qarassap Sermia), a marine-terminating outlet, which drains into Uummannaq Fjord at 70°N. This study site includes a portion of the catchment of Store Glacier, which drains a total area of ~34,000 km$^2$ (Rignot *et al.*, 2008b). Store Glacier is a heavily crevassed outlet glacier, being the third fastest marine-terminating outlet glacier from the GrIS, with centre-line ice-flow speeds at the terminus of between 4 and 7 km a$^{-1}$ depending on the time interval studied (Ahn and Box, 2010; Joughin *et al.*, 2011; Ryan *et al.*, 2015). Although Store Glacier experiences large seasonal variability in its flow rates, the outlet has remained in a stable configuration for at least four decades, contrasting with most marine-terminating glaciers of the GrIS (Weidick, 1995; Howat *et al.*, 2010). Store Glacier is the subject of extensive field and modelling research into ice dynamics and their interaction with hydrology, and it is hoped that this thesis may be able to inform such work (Xu *et al.*, 2013; Todd and Christoffersen, 2014; Fried *et al.*, 2015; Ryan *et al.*, 2015; Young *et al.*, 2016; Doyle *et al.*, 2018; Hofstede *et al.*, 2018).

In Chapter 5, which adapts the lake-tracking from Chapter 3 for use with high-resolution Sentinel-2 and Landsat 8 imagery, applying it in summers 2016 and 2017, the study region is doubled in size to cover ~12,000 km$^2$ of west Greenland (between ~69°15′N and 70°45′N, and ~51°00′W and 48°15′W) (Figure 2.15 (c)). This larger area is predominantly land-terminating, including almost the entirety of the land-terminating Paakitsoq region and a part of the Store Glacier region analysed in Chapters 3 and 4. This larger area was selected primarily for pragmatic reasons: the Sentinel-2 tiles used in the analysis were distributed with this areal coverage, and to avoid issues associated with mosaicking multiple tiles overlapping different areas of the GrIS, it was decided that this area would

become the central focus of analysis, rather than also including the whole of the Store Glacier region. Using the same study area size as a single Sentinel-2 tile also significantly reduced computational time.

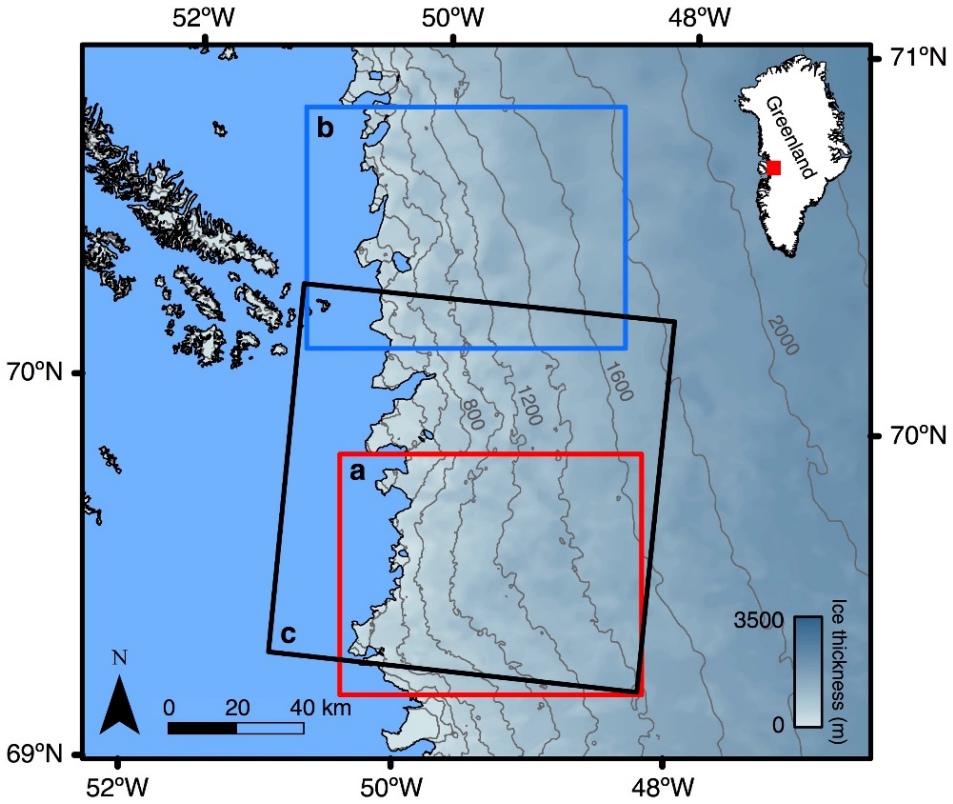



**Figure 2.15:** Study sites for this thesis: (a) the Paakitsoq region, (b) the Store Glacier region, and (c) the large west Greenland region. Location of sites within Greenland is inset. Ice-thickness data (grey shading) are derived from Morlighem *et al.* (2014). Ice-surface elevation contours (in m a.s.l.) are shown as thin grey lines, and the Greenland Ice Mapping Project (GIMP) ice mask is shown as a thick black line, both from Howat *et al.* (2014). Blue shading shows ice-marginal areas.

## 2.9 Summary

- While the remote-sensing discipline has a long history, the present availability of increasing quantities of high-quality remotely-sensed data offers a huge opportunity for environmental scientists. This opportunity has begun to be exploited by the cryospheric community to study processes over larger areas at increasing time frequencies than would be possible with individual field studies, from which it is often difficult to extrapolate patterns to wider scales, particularly over the spatially-extensive Greenland and Antarctic ice sheets.

- Remote sensing has been used to indicate that the GrIS, which contains a global SLE of ~7 m, is losing mass at an accelerating rate, particularly since 2000, with this mass loss now being dominated by the loss due to increased surface melting instead of the loss due to accelerated ice discharge over the grounding line for marine-terminating outlets. The configuration of the ice sheet's hydrological system has been implicated as one means to explain the losses both from increased surface melting and accelerated ice discharge over the grounding line.
- Within the GrIS's supraglacial-hydrological system, lakes can influence surface melt rates due to their lower albedo compared with bare ice and, more importantly, can influence ice dynamics when they drain to the ice-sheet bed, delivering large meltwater pulses to the ice-bed interface and, crucially, opening surface-to-bed connections that can route meltwater into the GrIS interior over the remainder of the season. These lakes form annually in the ablation zone of the GrIS and are known to advance further inland both over the course of a season and over longer inter-annual and decadal timescales. This inland advance is of concern because larger portions of the GrIS may be subjected to the impacts of lake drainage. While the effect of lake drainage on ice dynamics is relatively well understood for ice-marginal regions, it is more poorly constrained within the interior, where the ice is thicker, and for marine-terminating sectors, due to the difficulty of observing processes beneath floating ice tongues, adding uncertainty to future predictions of ice-mass loss from the GrIS. Part of this uncertainty relates to the difficulty in understanding whether the lakes that form further inland in the future will be able to drain rapidly.
- The rapid drainage of lakes is studied with fieldwork, which is limited to one or several lakes, or remote sensing, which can study larger samples of lakes. Remote sensing can therefore potentially offer additional advantages, assuming that lakes can be resolved accurately in such imagery, and that a lake is imaged sufficiently frequently by a satellite or satellites to allow the identification of rapid lake drainage with confidence. For this, there is commonly a trade-off to be made between satellite imagery with high spatial or temporal resolution, although the increasing availability of imagery (such as Landsat 8 and Sentinel-1 or Sentinel-2 imagery) offers the possibility of combining multiple satellite datasets together to provide improved insights into the incidence of rapid lake drainage. These high-resolution satellite data may also allow additional knowledge to be gained for lakes smaller than those which can be identified with lower spatial resolution satellite data like MODIS.
- When remotely sensing lakes, lake areas are normally calculated, but lake volumes are often not, restricting the quantity of information that can be gained on GrIS hydrology. If a method were available to calculate lake volume across wide areas of the GrIS, and this information were combined with the identification of other potential controlling factors on

rapid lake drainage, it may be possible to generate better knowledge of the reasons for which hydrofracture occurs at specific places and times, and not others. Such knowledge could allow improvements either to models of individual aspects of the GrIS's hydrology, such as its supraglacial system, or to coupled hydrology and ice-flow models, which may consequently be able to produce improved estimates of the GrIS's mass balance, presently and in the future.

# Chapter 3

# Developing, testing and applying a fully-automated lake-tracking algorithm for MODIS

## 3.1 Executive summary

While MODIS satellite data are often used to investigate lakes on the GrIS, including calculating changes to their areas through time, no existing method can track changes to lake volume in MODIS imagery over a melt season. In this chapter, such a method is developed. First, this involves testing three automated approaches to derive lake areas from MOD09 images by comparing calculated lake areas with lake areas derived from Landsat 8 images for the Paakitsoq and Store Glacier regions of west Greenland. Second, a physically-based algorithm for calculating lake depth is applied to the pixels within the lake boundaries from the best-performing algorithm for calculating lake area, and the depths calculated from MODIS are compared with those calculated using the same method applied to Landsat 8. The results show that lake areas are most accurately generated using dynamic thresholding of MODIS red-band data: calculated values from MODIS closely resemble those from Landsat 8. There is also close association between the estimated lake depths from the two satellites. The best-performing methods for deriving lake area and depth are then incorporated into a Fully-Automated Supraglacial lake Tracking (FAST) algorithm that tracks individual lakes between successive MODIS images. This chapter presents results from the initial application of the FAST algorithm to two study regions in west Greenland, where it identifies 43 (Paakitsoq) and 19 (Store Glacier) rapidly draining lakes during 2014, representing 21% and 15% of the respective total lake

populations, including some clusters of rapidly draining lakes. The FAST algorithm presented here improves on existing automatic lake-tracking methods because it can calculate both lake areas and volumes over large regions of the GrIS fully automatically.

## 3.2 Objective and aims

The overall objective of this chapter is to develop, apply and evaluate a fully-automated lake-tracking method capable of generating time-dependent lake areas and volumes from a series of MODIS images to help with meeting the overall goal of this thesis to produce improved knowledge of the patterns and causes of lake behaviour on the GrIS. This objective is divided into four main aims that are addressed sequentially, which are to:

1. Extend the limited existing research that assesses and validates algorithms employed to calculate lake areas automatically from MODIS imagery. For this first aim, lake areas are derived using three automatic methods applied to MODIS, and these are then compared with lake areas derived from contemporaneous higher-resolution Landsat 8 imagery. This first step is vital since accurate lake boundaries are required to use as one of the input datasets for the lake depth and volume calculations in (2).
2. Link the best technique for calculating lake areas to a physically-based approach for estimating MODIS lake depths and volumes, and then validate the MODIS lake depths and volumes against values calculated from Landsat 8 images.
3. Incorporate the most effective methods for calculating lake area and depth into the Fully-Automated Supraglacial lake Tracking (FAST) algorithm, which can automatically track the evolution of the areas and volumes of all individual lakes, as well as their totals, within a sequence of MODIS images over a season.
4. Use the FAST algorithm to investigate the incidence of rapid lake-drainage events within two sectors of west Greenland (Figure 3.1): (a) the Paakitsoq region and (b) the region surrounding Store Glacier. The main focus of this aim is to demonstrate the capability of the FAST algorithm for use on the GrIS; in Chapter 4, the FAST algorithm is used alongside other data to investigate the potential causes of rapid lake drainage.

The two study sites in this chapter (Figure 3.1) are used to evaluate the three algorithms for calculating lake area (Section 3.3.3), to validate the physically-based algorithm for calculating lake depth (Section 3.3.4), and to generate the first set of output data from the FAST algorithm (Section 3.3.5). These two regions are selected over other areas of the GrIS since they allow the suitability of the methods to be investigated for both land- and marine-terminating sectors. Moreover, both

regions are the foci of previous and ongoing research on supraglacial and subglacial hydrology, and ice-sheet dynamics, as introduced in Section 2.8.

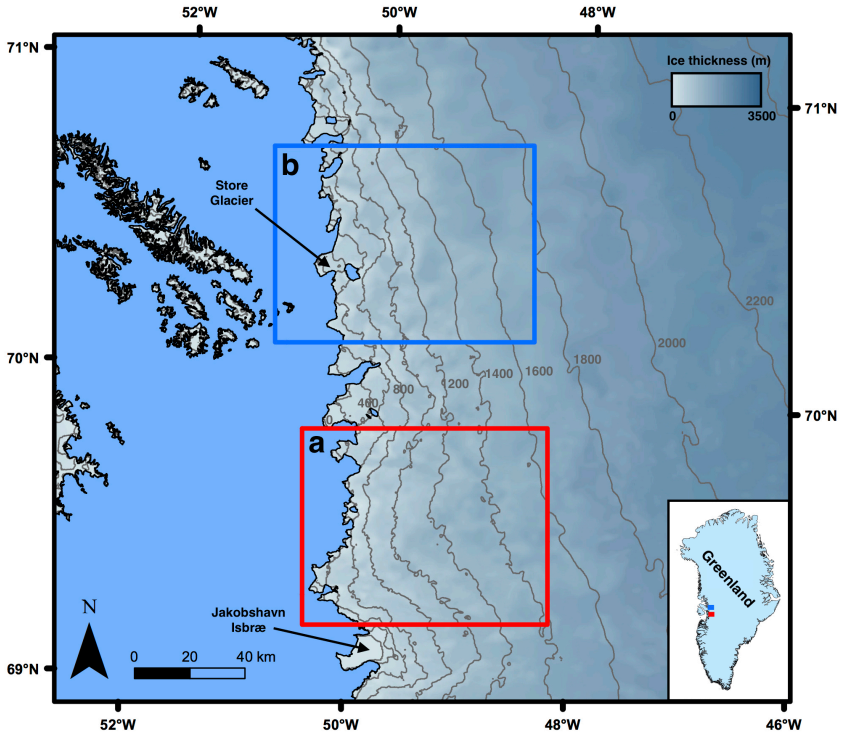



**Figure 3.1:** The study sites in west Greenland on which the analysis in this chapter is focused: (a) the Paakitsoq region delineated by the red box; and (b) the Store Glacier region within the blue box (cf. Figure 2.15). The grey background shading represents ice thickness (m) (Morlighem *et al.*, 2014), and the grey contour lines depict ice-surface elevation (m a.s.l.) (Howat *et al.*, 2014). The thick black lines within the boxes for the study regions delineate the GrIS margin (Howat *et al.*, 2014), and elsewhere they show ice-covered areas. The inset shows the location of sites (a) and (b) within Greenland.

## 3.3 Approach, data and methods

This Section 3.3 describes: (i) the overall approach used to fulfil the overall objective identified at the beginning of Section 3.2 (Section 3.3.1); (ii) the download and pre-processing of the satellite imagery for this chapter's analysis (Section 3.3.2); (iii) how the algorithms for deriving lake areas were chosen, the fundamental principles of the different methods, and the approach used to test these algorithms here (Section 3.3.3); (iv) the same concepts as in (iii) but for the lake-depth algorithm instead (Section 3.3.4), and; (v) the incorporation of the algorithms for calculating lake area and depth into the FAST algorithm, which was developed as the main outcome of this chapter (Section 3.3.5).

### 3.3.1 Approach

The approach in this chapter consisted of five methodological steps that were required to address the four aims identified in Section 3.2 and therefore to accomplish the overall objective of developing and evaluating a fully-automated lake area and volume tracking algorithm for MODIS imagery. These steps were to:

1. Download and pre-process MODIS and Landsat 8 imagery for summer 2014 (Section 3.3.2).
2. Evaluate three methods for generating lake areas from MODIS imagery based on comparing the areas of lakes with those derived from a supervised classification of contemporaneous Landsat 8 images (Section 3.3.3).
3. Use the lake boundaries generated by the most effective algorithm for calculating lake area to subsequently calculate lake depths and volumes from MODIS using a physically-based approach, then validating these measurements against values derived from Landsat 8 (Section 3.3.4).
4. Incorporate the best-performing techniques for calculating lake area and depth into the FAST algorithm, which tracks the formation, evolution and cessation of lakes through a sequence of satellite images during a melt season (Section 3.3.5).
5. Apply the FAST algorithm to the Paakitsoq and Store Glacier regions of west Greenland (introduced in Section 2.8) to investigate lake evolution in summer 2014, including analysing the location, timing and magnitude of rapid lake-drainage events.

### 3.3.2 Satellite image collection and pre-processing

#### MODIS

Level-2 processed MOD09GQ (~250 m resolution) and MOD09GA (~500 m resolution) daily surface-reflectance datasets from 1 May to 30 September 2014 (total = 153 images) were downloaded from the USGS's Land Processes Distributed Archive Center (LP DAAC) data pool (https://lpdaac.usgs.gov/data_access/data_pool). These MODIS products are derived from data collected by the Terra satellite. Because MOD09 images are daily composites and are level-2 processed data (Section 2.4.1), there were no issues with misclassifying shadows as lakes within areas of complex topography (which was an issue for Selmes (2011) and Selmes *et al.* (2011) using MOD02 imagery). Selmes *et al.* (2011) overcame this issue by using an *a priori* distribution of lakes to help derive lake areas more accurately, but this was therefore not required in this work. The level-2

MOD09 data have the same position and source information as level-1 datasets, but have had an atmospheric correction algorithm (for atmospheric gases, cirrus clouds and aerosols) applied to all cloud-free pixels identified within the MOD35 cloud mask.

MODIS surface-reflectance data were used from band 1 (red; 0.620–0.670 μm), band 3 (blue; 0.459–0.479 μm), band 4 (green; 0.545–0.565 μm) and band 6 (SWIR; 1.628–1.652 μm) (Table 2.2). The red, green and blue band data were used to create red-green-blue (RGB) daily composite images. Version 2.2 of the USGS's LP DAAC's MODIS Reprojection Tool Swath (MRTSwath) (https://lpdaac.usgs.gov/tools/modis_reprojection_tool_swath) was used to convert raw datasets distributed as HDF files on MODIS's sinusoidal grid to common projection systems using bilinear interpolation. During the reprojection of pixels to a common grid, the native 231.7 m MODIS pixels were resampled to 250 m and the 463.3 m pixels were resampled to 500 m resolution, consistent with previous MODIS-based research in Greenland (e.g. Selmes *et al.*, 2011; Liang *et al.*, 2012; Morriss *et al.*, 2013; Fitzpatrick *et al.*, 2014). Only red-band data were available at the near-250 m resolution, so the ratio of the red to blue band surface-reflectance values from the MOD09GQ and MOD09GA products was used to sharpen data from the blue and green bands to the red band's native higher resolution (Gumley *et al.*, 2007), a technique used previously (Box and Ski, 2007; Fitzpatrick *et al.*, 2014). When directly comparing MODIS lake areas, depths and volumes against those derived from Landsat 8 imagery for evaluation and validation purposes, entirely cloud-free MODIS images were used. When analysing MODIS imagery for the whole season, a cloud filter was applied to remove pixels with a reflectance value in band 6 that exceeded 0.150 (Box and Ski, 2007; Fitzpatrick *et al.*, 2014). Cloud shadows were also removed by assuming that a pixel contained a cloud shadow when the mean band-6 reflectance in a surrounding 21-by-21-pixel window exceeded 0.150, similar to Selmes' (2011) approach. After Liang *et al.* (2012), an additional filter was included to remove pixels from the analysis that were not classified as water on at least three occasions during the season, following the observation that cloud shadows have spectrally-similar footprints to lakes but are more temporally intermittent. MODIS images were cropped to the chosen study sites (Figure 3.1), and ice-marginal areas were removed with the GIMP ice-sheet mask (Howat *et al.*, 2014).

## Landsat 8

To test and validate the methods for calculating lake area and depth before incorporating them into the FAST algorithm, entirely cloud-free Landsat 8 images from 2014 were used as the training dataset (Table A.1): five images for Paakitsoq (from 3 July, 11 July, 19 July, 4 August and 27 August) and six images for Store Glacier (from 1 July, 3 July, 11 July, 2 August, 11 August and 27 August).

This date range was selected to cover the key period of the melt season when lakes are present on the GrIS. 30 m resolution Landsat 8 data were used from band 2 (blue; 0.45–0.51 μm), band 3 (green; 0.53–0.59 μm) and band 4 (red; 0.64–0.67 μm), and 15 m resolution data from band 8 (panchromatic; 0.50–0.68 μm) (Table 2.3). These data were manually selected and downloaded from the USGS Earth Explorer interface (http://earthexplorer.usgs.gov). The images were reprojected in ArcGIS to a coordinate system common with the MODIS images and were cropped to the regions of interest using the 'Extract by Mask' tool; the GIMP ice-sheet mask (Howat *et al.*, 2014) was used to remove areas peripheral to the GrIS. Following Pope *et al.* (2016), atmospheric correction was not applied to the Landsat 8 scenes since a reliable atmospheric-correction method for the imagery did not exist at the time at the time of the research. Each image's metadata were used to convert digital numbers to TOA reflectance and to correct for solar elevation (USGS, 2013). These TOA reflectance values represent an adequate proxy for surface reflectance on the GrIS, where atmospheric effects are small (Pope *et al.*, 2016).

### 3.3.3 Evaluating algorithms for deriving MODIS lake areas

Lake boundaries are sometimes delimited manually from satellite imagery (e.g. McMillan *et al.*, 2007; Hoffman *et al.*, 2011; Lampkin, 2011; Lampkin and VanderBerg, 2011; Langley *et al.*, 2016; Gledhill and Williamson, 2018) but this is time-consuming and subject to user bias, so automatic methods are frequently preferred. The first aim of this chapter involved testing some of these automatic methods to derive lake areas from satellite imagery. In this sense, this research extended that of Leeson *et al.* (2013), which presented a similar evaluation of some methods to derive lake areas from MODIS images. Three automated methods for identifying lake areas were tested: (i) static red/blue band thresholding; (ii) the Normalised Difference Water Index (NDWI); and (iii) dynamic thresholding of the red band. Methods (i) and (ii) use the same data but calculate lake areas using the measurements in a slightly different numerical way. These methods are described in detail in the sections below, including their theoretical basis, and existing applications of them to studying lakes on the GrIS. In addition to the three methods tested in this chapter, some other methods are also used for automatic lake area calculations, but they are used less frequently, so were not included in this research; these other approaches are therefore described only briefly below.

#### Static red/blue band thresholding

One method that is often used to calculate lake areas was initially proposed by Box and Ski (2007) for MODIS, and uses a ratio of the blue (i.e. MODIS band 3) to red (i.e. MODIS band 1) surface-reflectance values, with a threshold value (which may require lake-by-lake adjustment)

chosen to define the water-covered pixels in a scene. This approach functions on the principle that red wavelengths are attenuated more strongly than blue ones within water columns, reducing the red-band reflectance values compared to the blue ones. Thus, the ratio of blue to red reflectance can help to identify water-covered pixels. This method has been applied successfully to Landsat scenes (e.g. Arnold *et al.*, 2014; Banwell *et al.*, 2014; Pope *et al.*, 2016), and has also informed fuzzy-logic-based image classifications for lake identification (Sundal *et al.*, 2009).

## The Normalised Difference Water Index

The NDWI similarly uses the red and blue bands to derive lake areas, but they are used in a slightly different way. The NDWI is defined as:

$$\text{NDWI} = \frac{(\text{blue-band reflectance} - \text{red-band reflectance})}{(\text{blue-band reflectance} + \text{red-band reflectance})}. \quad (3.1)$$

A threshold NDWI value is needed to define water-covered pixels, with tuning required depending on the site of interest (Huggel *et al.*, 2002; Xu, 2006; Doyle *et al.*, 2013; Morriss *et al.*, 2013; Yang and Smith, 2013; Moussavi *et al.*, 2016; Miles, E. S. *et al.*, 2017; Miles, K. E. *et al.*, 2017). Many glaciological studies, including those aiming to delineate supraglacial ponds on (Himalayan) debris-covered glaciers, use the NDWI (occasionally with modification to include, for example, the NIR and green bands) for MODIS imagery (Doyle *et al.*, 2013; Morriss *et al.*, 2013; Fitzpatrick *et al.*, 2014), and for other sensors, notably Landsat and WorldView-2 (Huggel *et al.*, 2002; Xu, 2006; Gardelle *et al.*, 2011; Yang and Smith, 2013; Moussavi *et al.*, 2016; Miles, E. S. *et al.*, 2017; Miles, K. E. *et al.*, 2017). The NDWI's performance can be improved to minimise lake misclassification through first isolating or filtering image pixels that satisfy certain surface-reflectance criteria, such as a requirement for a high (or low) reflectance value in the blue (or red) band (Fitzpatrick *et al.*, 2014). The NDWI technique is tested in this chapter, but this isolation/filtering was not included in the testing of this technique because this would only be possible if the thresholds were tuned to the study site, meaning that the technique then could not be applied fully automatically.

## Dynamic thresholding of the red band

The third and final approach for deriving lake area tested in this chapter was delineating lake areas using dynamic thresholding of the red band, which was first proposed by Selmes *et al.* (2011). This technique was used subsequently by Selmes *et al.* (2013) across the whole GrIS and Everett *et al.* (2016) for Helheim Glacier, east Greenland. In a similar way to the static red/blue band thresholding and NDWI approaches, this method exploits the pronounced attenuation of red light within a lake's water column, and compares a central pixel's red reflectance against the mean value

for the red reflectance for all 441 pixels within a moving 21-by-21 pixel window surrounding this central pixel. Lakes are defined as any location where the central pixel's reflectance is below a given threshold, such as 0.65 of the mean reflectance within the window (Selmes *et al.*, 2011). This effectively gives this approach a dynamic spatial variability since the background reflectance within the moving window changes spatially across the GrIS according to other factors, such as the broadband albedo. This technique has not been applied to the other optical MODIS bands because they would need sharpening to 250 m resolution, causing loss of fidelity in the original data (Selmes, 2011).

## Other approaches

Various other methods are also used to derive lake areas from remotely-sensed imagery, but they are not tested in this chapter since they have been used less frequently on the GrIS. First, image histograms can be automatically classified with the use of a spatially-dynamic window that moves across images; these histograms display different characteristics based on whether an image has lakes present, in which case a tail of lower reflectance values might be seen on the histogram (Liang *et al.*, 2012; Howat *et al.*, 2013). Second, images can be segmented, with bimodal histograms created based on buffered regions around lakes, which are then examined dynamically to identify lake boundaries accurately (Yang *et al.*, 2015; Yang and Smith, 2016). Third, fuzzy-logic membership can explore the likelihood that an image pixel fits within a specific class (Sundal *et al.*, 2009). Fourth, object-oriented classification can determine descriptive quantities about groups of pixels, assigning them to different categories based on the likelihood that they fit into a specific class (Johansson and Brown, 2013). Finally, textural analysis uses the spectral signatures for satellite scenes and identifies lakes based on a maximum-likelihood algorithm (Lettang *et al.*, 2013).

## Approach for testing the algorithms for deriving lake area

### *Previous appraisals of algorithms for calculating lake area*

Studies calculating lake areas from MODIS imagery normally assess the performance of their methods through validation with higher spatial resolution imagery from another multispectral sensor, typically Landsat or ASTER, or through comparison with manually-delineated lake outlines. Despite several studies conducting independent validations of their lake-area algorithms, only one study (Leeson *et al.*, 2013) evaluates the performance of several techniques for deriving lake area from MODIS imagery by comparing them against a single validation dataset, and no single consensus has emerged regarding the best technique to use, which explains the testing of these methods within this chapter. The only existing study, presented by Leeson *et al.* (2013), evaluated

the methods of Sundal *et al.* (2009), Selmes *et al.* (2011), and Johansson and Brown (2013) for the Russell Glacier region, west Greenland. The performance of the different methods was assessed by comparing the number and size of lakes reported using each algorithm with those delineated manually from MODIS imagery and corresponding ASTER scenes. Each method underestimated the total number of lakes (when compared with the number delimited manually) to a differing degree, leading to the recommendation that all methods should be combined to identify the maximum number of lakes within a specific region (Leeson *et al.*, 2013). Although Selmes *et al.*'s (2011) method reported the fewest lakes overall—only 52% of manually-delineated lakes—it calculated lake area most accurately, with a 0.48 $km^2$ root-mean-square error (RMSE), compared with RMSEs of 0.78 $km^2$ and 0.95 $km^2$ for Sundal *et al.*'s (2009) and Johansson and Brown's (2013) techniques, respectively. Leeson *et al.* (2013) indicated that the low number of lakes derived from Selmes *et al.*'s (2011) approach was likely to be a result of the *a priori* lake distribution required as an input to that technique.

*Technique for appraising lake-area algorithms used in this chapter*

Each of the three automated methods described in detail above were tested for their sensitivity to numerous threshold values, with such a widespread testing of threshold values previously having not been a focus within published literature. For the static red/blue band thresholding and the NDWI technique, spatially fixed thresholds were used rather than adjusting them on a lake-by-lake basis or to the individual study sites, since the aim was to develop a methodology that could be applied to large areas of the GrIS without any 'local' tuning. In the dynamic band thresholding method, a moving window of 25-by-25 pixels was chosen, which was the same size as Liang *et al.*'s (2012), but bigger than Selmes *et al.*'s (2011), to ensure that large lakes were always reported; this would not necessarily have been the case with a smaller window where the overall reflectance would have been affected by the presence of a large lake within it. A different window size could have been chosen – the window size needed to report lakes accurately will be ultimately dependent on the size of the lakes within the region; thus, the size of the window can be regarded as a tuneable parameter within this approach.

When testing these methods, all lakes were excluded that did not reach at least two MODIS pixels (at the 250 m resampled resolution) in area (i.e. 0.125 $km^2$) on at least one occasion in the season; the total amount of water that this procedure omitted from the record was quantified by using the Landsat 8 data for small lakes (i.e. those < 0.125 $km^2$). In addition, the (mean and maximum) areas of the lakes ≥ 0.125 $km^2$ that were excluded from the MODIS record but which were reported in the Landsat 8 data were examined.

Figure 3.2 displays the validation methodology used within this chapter as a flowchart. The performance of the algorithms for calculating lake area was validated on an image-by-image basis, as well as against a single combined dataset containing all of the Landsat 8 images. For the Landsat 8 images, lake areas were calculated using a supervised classification in ArcGIS to ensure independence of the algorithm for the estimates of lake area. Conducting the supervised classification involved manually allocating a few pixels to a known feature class of either 'lake' or 'non-lake' from the background RGB images, and then creating a binary raster automatically based on the knowledge that the program gains from the known properties of the two independent feature classes. The performance of the lake-area algorithms was evaluated for the MODIS imagery by comparing the values from MODIS with the Landsat 8 derived values for total identified lake numbers, total identified lake areas, the Pearson product-moment correlation coefficient ($r$) of lake areas, and the RMSE of lake area for individual lakes. The best-performing threshold for each technique was identified qualitatively based on these four measures of performance, although more weight was usually given to the RMSE to aid with the choice of the threshold.

*Lake-area validation data*

The method of using the higher-resolution Landsat 8 data as the validation dataset was consistent with previous studies that have validated lake areas derived from lower-resolution sensors such as MODIS against higher-resolution ones, including ASTER and Landsat, which were regarded as ground-truth data (Sundal *et al.*, 2009; Selmes *et al.*, 2011; Liang *et al.*, 2012; Leeson *et al.*, 2013; Fitzpatrick *et al.*, 2014; Everett *et al.*, 2016). To verify the reliability of these validation data, the lake outlines from the ArcGIS supervised classification of the Landsat 8 images were qualitatively compared against the lakes present on background Landsat 8 scenes, an approach also used to verify the validity of the training dataset in Pope *et al.* (2016). This indicated that the lakes had been accurately delineated and so it was possible to have high confidence in the validation dataset. Any false positives identified in the Landsat 8 record by the ArcGIS supervised classification were manually removed prior to assessments of the algorithms' performance. Although this approach was time-consuming, it was crucial to ensure that the validation data were reliable, since if they were not, the MODIS-derived values would have been compared against a false dataset.

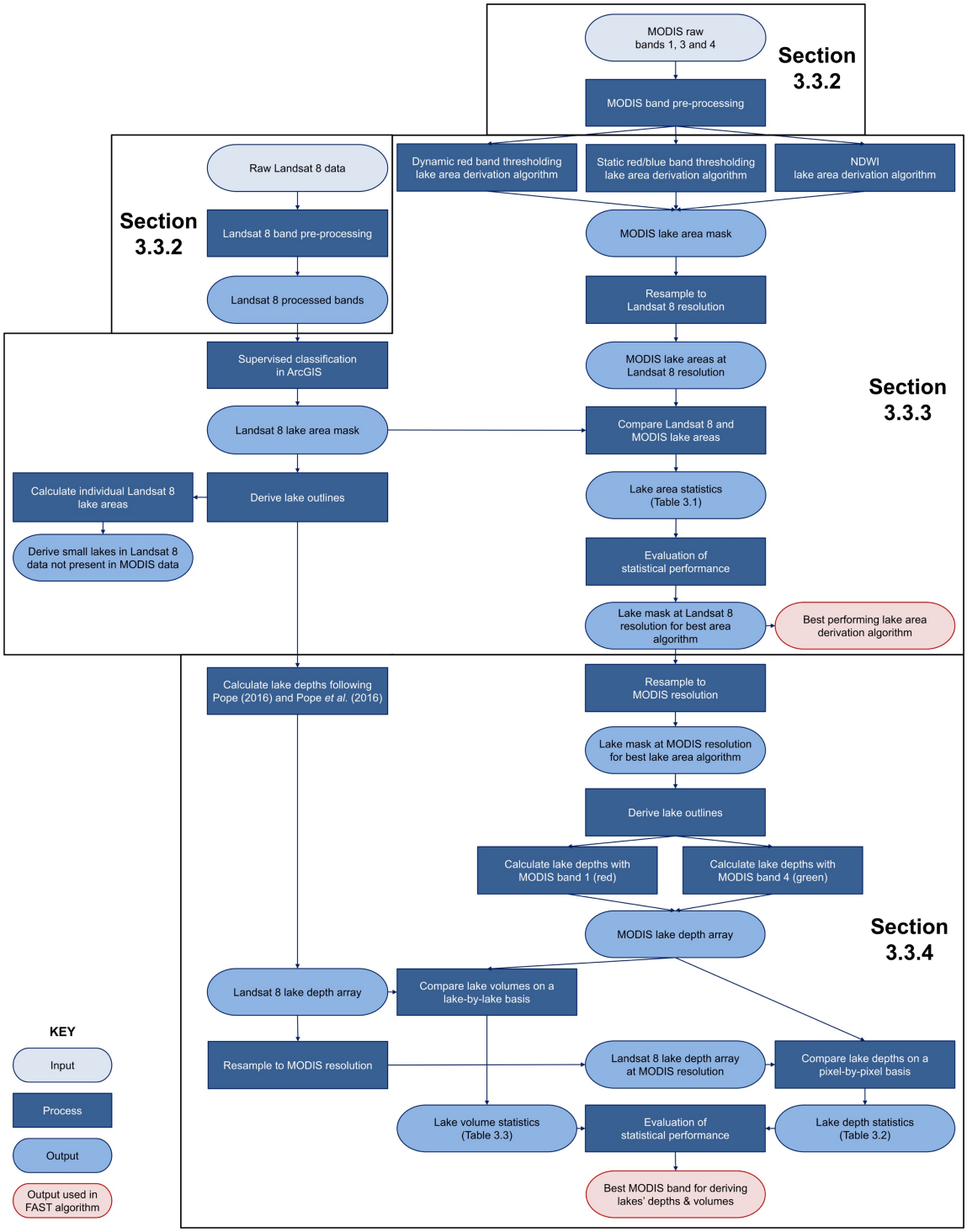



**Figure 3.2:** Flowchart to summarise the techniques used within this chapter to validate MODIS lake areas, depths and volumes against Landsat 8 lake areas, depths and volumes. The statistical performances of the algorithms across all of the images when combined into a single dataset, as well as for each image individually, were assessed.

### 3.3.4 Deriving and validating MODIS lake depths and volumes

Once the best-performing algorithm for automatically calculating lake areas from MODIS imagery was identified, the next aim of this chapter involved deriving a method for automatic calculation of MODIS lake depths and volumes. Although MODIS imagery is widely used to calculate lake areas, it is used far less frequently to calculate lake pixel depths, and thus lake volumes. Two broad methodological approaches were therefore considered for this purpose: one of the several available empirically-based approaches or a physically-based approach. These two contrasting approaches are reviewed briefly below, including how the physically-based approach was adapted and used for the analysis in this chapter.

#### Empirically-based approaches

Among the few studies that calculate lake depths and volumes from MODIS imagery, they normally use empirically-based approaches. These studies conduct this analysis either by employing a first-order relationship between lake areas and volumes by approximating lake basins as cones (Liang *et al.*, 2012), by using lake areas as proxies for volumes (Morriss *et al.*, 2013), or by using empirically-derived depth-reflectance curves from field data to calculate pixel depths, which are then integrated, and multiplied by the pixel size to provide lake volumes (e.g. Box and Ski, 2007; Fitzpatrick *et al.*, 2014). While these techniques are helpful for deriving information on changes to lake volume for specific sectors of the GrIS in individual years, empirical methods lack a physical basis, so they cannot necessarily be applied with confidence to other regions of the GrIS or to different years. This therefore limits their potential for inclusion in a fully-automated lake area and volume tracking algorithm as developed here.

#### A physically-based approach

Sneed and Hamilton (2007), after Philpot (1989), developed the first physically-based water-depth retrieval algorithm for lakes on the GrIS, which they applied to ASTER data. The physical basis of the approach relies on the fundamental principles of radiative transfer through a fluid, and the method is essentially based on the attenuation of light within a water column according to the Beer-Lambert-Bouguer law. The fundamental principle of the method is that deeper water results in higher light attenuation within the column than shallower water. This phenomenon is observed for all wavelengths of visible light, but the attenuation rate (i.e. the degree of attenuation) varies by wavelength, with it being lower for blue wavelengths than red ones, for example. To apply this method to satellite imagery, therefore, the waveband experiencing the greatest change in attenuation over the expected water depth range needs to be selected.

The attenuation rate can be used in the calculation of water depth ($z$, in m) if certain other properties of lakes and the images are known:

$$z = \frac{[\ln\ (A_d - R_\infty) - \ln\ (R_{pix} - R_\infty)]}{g}, \quad (3.2)$$

where $A_d$ is the lake-bottom albedo, $R_\infty$ is the reflectance for optically-deep (> 40 m) water, $R_{pix}$ is the reflectance of a pixel of interest, and $g$ ($m^{-1}$) describes the losses in upward and downward travel in a water column. Since the method is physically based, it does not require site-specific tuning, meaning that it can be widely applied across the GrIS, with the option to test the sensitivity to its physical parameters (e.g. Pope *et al.*, 2016). Pope *et al.* (2016) fully describe the assumptions inherent in this method, but, briefly, these are that: (i) the lake surface is not disturbed by wind (likely not to hold true in Greenland due to the presence of strong katabatic winds, although even such windy conditions are unlikely to significantly affect the pixel brightness and so the lake-depth calculations); (ii) the lake bottom is homogenous and gently sloping; and (iii) sediment is not present within the lake water column. Despite these potential weaknesses, which remain unquantified in the literature, there is presently no alternative physically-based method, and it has been applied successfully in studies for ASTER (Sneed and Hamilton, 2007) and other multispectral sensors (Georgiou *et al.*, 2009; Morriss *et al.*, 2013; Arnold *et al.*, 2014; Banwell *et al.*, 2014; Ignéczi *et al.*, 2016; Langley *et al.*, 2016; Moussavi *et al.*, 2016; Pope *et al.*, 2016; Macdonald *et al.*, 2018), performing well both in Greenland and Antarctica (Banwell *et al.*, 2014).

Currently, only Morriss *et al.* (2013) and Ignéczi *et al.* (2016) have applied this method to MODIS imagery. Ignéczi *et al.* (2016) used it for 24–40 images over each of four melt seasons to derive maximum lake depths for validation of their lake depths derived from digital elevation models (DEMs). Although they used individual daily $R_\infty$ values and $A_d$ calculated for each lake, they did not present evolutions of lake depth and volume across a series of MODIS images. Morriss *et al.* (2013) used the physically-based method to conclude that lake area represents a valid proxy for volume across their study region, but individual lake volumes or their full seasonal changes were not presented. Morriss *et al.*'s (2013) study was also for just one sector of the GrIS and daily $R_\infty$ values were not calculated. Instead, a constant $R_\infty$ value was used, meaning the Beer-Lambert-Bouguer law on which the technique relies was not calibrated for individual scenes. Finally, the $g$ value was calibrated from relatively limited field data, whereas Pope *et al.* (2016) have since presented updated $g$ values for a range of multispectral sensors, including Landsat 8 and MODIS, based on extensive testing of calculated lake water depths (derived with Equation 3.2) against *in situ* lake spectral and bathymetric data.

### Approach for deriving and validating MODIS lake depths and volumes

In this chapter, the second aim involved furthering the limited work described above and including Pope *et al.*'s (2016) developments relating to $g$ values. The physically-based method was applied to MODIS's red and green bands separately, using Pope *et al.*'s (2016) updated $g$ values for MODIS. Depths were multiplied by pixel sizes and integrated over lake areas to provide lake volumes. $R_\infty$ was calculated individually for each scene from deep water in proglacial fjords, rather than specifying static seasonal values. $A_d$ was calculated image-by-image on a lake-by-lake basis by taking the mean reflectance of a ring dilated by one pixel around each lake (Arnold *et al.*, 2014; Banwell *et al.*, 2014), which represents an improvement on previous studies that used region-wide or static values (Sneed and Hamilton, 2007; Morriss *et al.*, 2013).

*Lake-depth and -volume validation data*

The validation data were again derived from the dates on which there were available cloud-free Landsat 8 images in 2014. The lake depths and volumes were then calculated (using Equation 3.2) from the Landsat 8 images within the boundaries of lakes derived from the Landsat 8 supervised classification in ArcGIS. To calculate these depths, the methods of Pope (2016) and Pope *et al.* (2016) were followed, which involved averaging the lake depths derived from Landsat 8's red and panchromatic bands, calculated with their updated $g$ values. The MODIS and Landsat 8 pixel depths were compared at the MODIS resolution, which required resampling of the Landsat 8 depth arrays using a bilinear interpolation regime. This corrected for the finer resolution of Landsat 8 imagery, which often showed deeper values towards the centre of lakes due to Landsat 8's smaller pixel size. By contrast, MODIS and Landsat 8 lake volumes were compared on a lake-by-lake basis by integrating all pixel depth values at the sensor's native resolution without any resampling. This helped to eliminate any smoothing of the results (from the resampling of Landsat 8 data to match the coarser MODIS resolution) when the calculated depths were compared on a pixel-by-basis basis. For both lake depths and volumes, the Pearson product-moment correlation coefficient and the RMSE between the two datasets were used to assess performance.

## 3.3.5 Approach for fully-automated lake tracking

Figure 3.3 summarises the overall approach of the FAST algorithm that was subsequently developed, and which was applied using the best techniques for calculating lake area and depth determined with the methods described in Sections 3.3.3 and 3.3.4. Since the algorithm is fully automated, its only required inputs are (i) a georeferenced mask of the study region and (ii) a set of MODIS MOD09 imagery for a melt season. The FAST algorithm is written in the MATLAB

programming language. Both the mask and the MOD09 images must be georeferenced with the NSIDC Polar Stereographic North projection (EPSG: 3413). The algorithm can then track intra-annual changes to lakes that reach at least two 250 m MODIS pixels (i.e. 0.125 $km^2$) in area at least once in the season, and includes the following steps:

1. The automatic pre-processing stages comprise: (i) cropping MODIS images to the study regions using a georeferenced mask; (ii) sharpening the resolution of MODIS's native 500 m resolution bands to 250 m; (iii) masking ice-marginal areas from the imagery; and (iv) removing clouds and pixels likely to be cloud shadows. (See Section 3.3.2 for full pre-processing details applied to the MODIS imagery.)
2. Create daily stacked RGB composites of the study region. (These RGB images were not used for any quantitative analysis but were used to verify that rapidly draining lakes had been identified correctly.)
3. Run the algorithms for calculating lake area and depth to derive daily lake areas, depths and volumes.
4. Derive the maximum extents of lakes across the season from the aggregated sum of the daily lake area masks.
5. Remove any false positive lakes.
6. Create masks of lakes to track across all images.
7. Track the seasonal evolution of lake area and volume by examining, for each image in the sequence, all of the pixels within the maximum lake extents from step (4).
8. Identify rapidly draining lakes according to critical drainage-duration and volume-loss thresholds.
9. Remove any falsely-identified rapid lake-drainage events.
10. Derive rapidly draining lake locations, drainage dates and their water volumes prior to drainage.

In step (5), false positives are removed by filtering lakes that do not appear at least three times over the season, and which are not observed on more than one occasion during five consecutive cloud-free observations of their basins on their first detection (following Liang *et al.* (2012)). To identify rapid drainage in step (8), it is assumed that a lake drains by hydrofracture if it loses ≥ 80% of its maximum seasonal volume over a period of ≤ 4 days. Although hydrofracture is generally acknowledged to occur in ≤ 2 days (e.g. Das *et al.*, 2008; Tedesco *et al.*, 2013), which is the time adopted by Selmes *et al.* (2011, 2013) in their studies, other workers accounted for uncertainty within satellite observations by relaxing this threshold to four days (Doyle *et al.*, 2013; Fitzpatrick *et al.*,

2014), five days (Liang *et al.*, 2012), or six days (Morriss *et al.*, 2013). The threshold is therefore also relaxed in this chapter.

Under step (9), at least seven cloud-free observations are required of an empty lake basin, with no refilling permitted, following rapid drainage; if this requirement is not met, the rapid event is omitted from any further analysis. To ensure that the FAST algorithm reliably identifies rapid lake drainages within this chapter, all events are manually verified using the RGB composites. This step would not normally be required if the algorithm is applied elsewhere, but it is included here because it is necessary to ensure that the FAST algorithm is performing correctly.

For step (10), the date of lake drainage is identified as the day on which the critical volume loss begins since this is likely to be close to the time when hydrofracture is initiated, and a later focus of this thesis (Chapter 4) is to investigate this occurrence. If required, this date could be adjusted to the date immediately prior to hydrofracture, immediately after hydrofracture occurs, or the midpoint of the two values (as in Chapter 5). In this chapter, preliminary results from the use of the FAST algorithm are presented, which involved investigating simply the relationship between the rapidly draining lake water volumes and the ice thicknesses beneath the rapidly draining lakes; the ice-thickness data were derived from beneath the lake centroids from the GrIS terrain data of Morlighem *et al.* (2014).

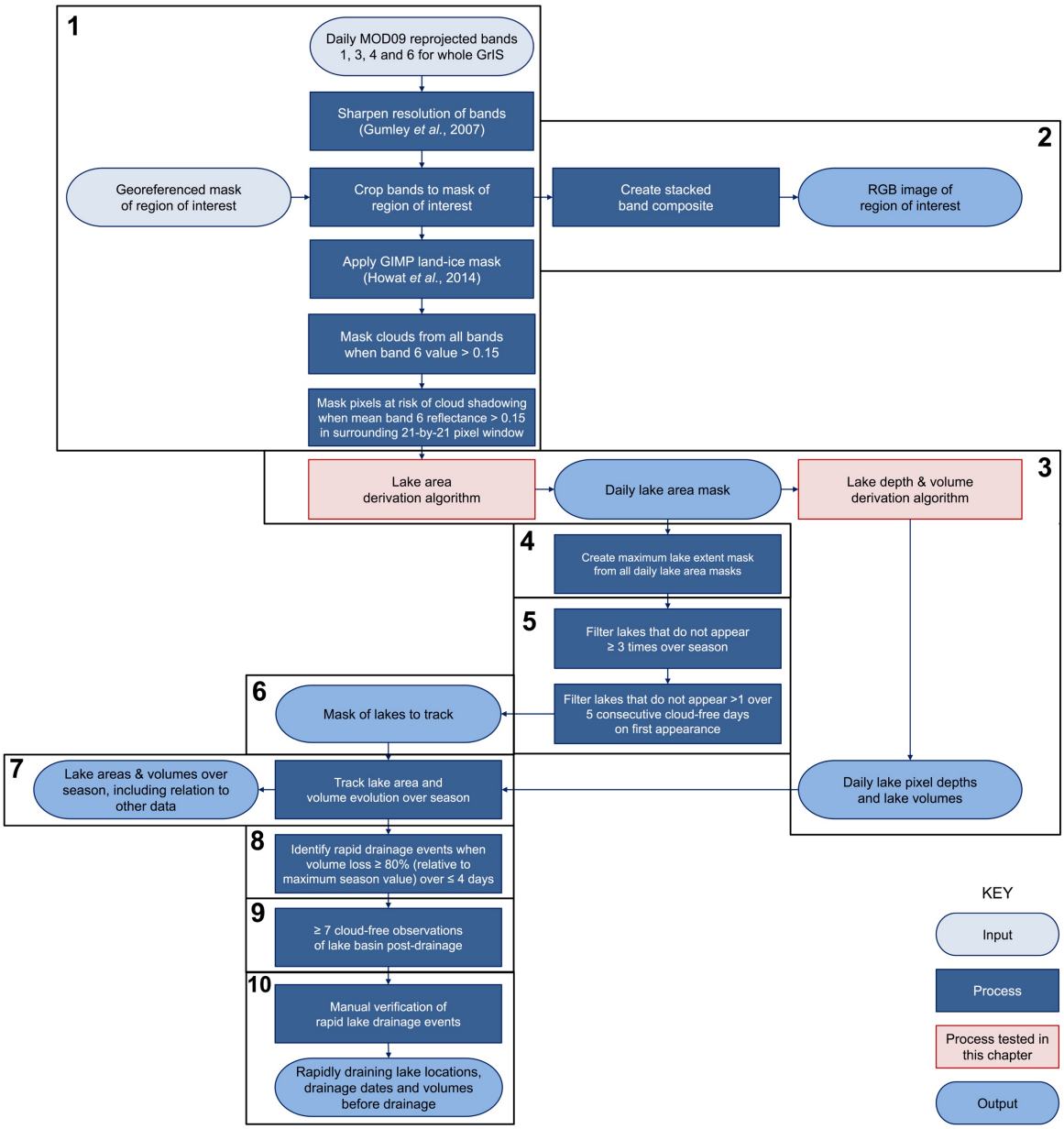



**Figure 3.3:** Flowchart summarising the FAST algorithm, including its key inputs, processes, outputs, and the processes that were evaluated within this chapter. The numbers in the corners of the square black-outlined boxes refer to the steps of the FAST algorithm described in this Section 3.3.5.

# 3.4 Results

## 3.4.1 Calculating lake areas

### Performance of the algorithms for calculating lake area

Initially, the two study regions are considered independently to determine which method for delineating lake area and which threshold is best for each method; the data are then combined into a single dataset for both regions to elicit the best-performing threshold across both of them. Table 3.1 presents the results for lake areas from the MODIS images that overlap (temporally and spatially) with the Landsat 8 images, calculated with the three best-performing thresholds for each algorithm for deriving lake area. Since there is a numerical association between the red/blue band thresholding and NDWI approaches, the thresholds for one technique can be used to infer those required by the other (Tables A.4–A.7). Figure 3.4 shows a comparison of lake areas calculated using the best threshold value with each algorithm at each site. Some false positives are identified by the algorithms for calculating lake area – for example, see the black box labelled "FP" on Figure 3.5 (a). Dynamic thresholding of the red band generally outperforms the other approaches for both regions in terms of the RMSEs and the percentage of lakes reported by MODIS relative to the total number of lakes reported in the Landsat 8 dataset (Table 3.1). While the other methods with specific thresholds occasionally result in higher $r$ values, they are less accurate than the dynamic red band thresholding method in terms of RMSEs and reported percentages of lakes (Table 3.1). Although less accurate than the dynamic red band thresholding method, the NDWI and red/blue band thresholding methods perform better at Paakitsoq than Store Glacier: the RMSEs for the NDWI and red/blue band ratio thresholding approaches are $< 0.40$ km$^2$ at Paakitsoq but $> 0.40$ km$^2$ at Store Glacier (Table 3.1). These results show that dynamic thresholding is the only approach that can be applied with similar threshold values across different regions of the GrIS. The best-performing values for dynamic thresholding are nearly identical between Paakitsoq and Store Glacier, with the threshold value of 0.640 at Store Glacier only marginally outperforming the 0.645 value for Paakitsoq in terms of the number of lakes reported (Table 3.1). This compares with the best-performing threshold values for the NDWI (or red/blue band thresholding) approach, which are 0.125 (or 0.775) in the Paakitsoq region and 0.190 (or 0.710) at Store Glacier, showing the marked differences in them between the two regions. The red/blue band thresholding performs significantly less accurately at Store Glacier, with higher RMSEs, lower $r$ values and lower lake numbers reported. Even though a threshold value of 0.710 performs best, with a RMSE of 0.418 km$^2$ — similar to the RMSEs for the other algorithms — use of this threshold value results in an exceptionally low reporting of lake numbers (only 10.1%) compared with the lakes derived from Landsat 8.

**Table 3.1:** Performance indicators for the best-performing algorithms tested for calculating lake areas at the two study sites. Total numbers of lakes and total lake areas from Landsat 8 for the two regions are: 406 and 173.7 km$^2$ (Paakitsoq) and 298 and 121.3 km$^2$ (Store Glacier). All $r$ values are significant at the 95% confidence interval ($p < 0.05$). The best-performing algorithm and threshold at each site is highlighted in bold italicised text. Full results for all of the thresholds tested for each approach are presented in Tables A.2–A.7.

| Region | Lake area algorithm | Threshold value | Total MODIS lake area (km$^2$) | Difference between MODIS and Landsat 8 lake area (%) | Number of Landsat 8 lakes predicted by MODIS | Detection (%) of Landsat 8 lakes | RMSE (km$^2$) | $r$ |
|---|---|---|---|---|---|---|---|---|
| Paakitsoq | *Dynamic* | 0.640 | 110.1 | 36.6 | 161 | 39.7 | 0.338 | 0.706 |
| | | ***0.645*** | ***114.3*** | ***34.2*** | ***169*** | ***41.6*** | ***0.338*** | ***0.702*** |
| | | 0.650 | 117.6 | 32.3 | 171 | 42.1 | 0.341 | 0.696 |
| | NDWI | 0.120 | 94.7 | 45.5 | 106 | 26.1 | 0.368 | 0.752 |
| | | 0.125 | 82.2 | 52.7 | 95 | 23.4 | 0.369 | 0.762 |
| | | 0.130 | 73.8 | 57.5 | 86 | 21.2 | 0.374 | 0.760 |
| | | 0.770 | 74.1 | 57.3 | 87 | 21.4 | 0.374 | 0.760 |
| | Red/blue band ratio | 0.775 | 79.2 | 54.4 | 90 | 22.2 | 0.371 | 0.760 |
| | | 0.780 | 84.4 | 51.4 | 96 | 23.6 | 0.372 | 0.755 |
| Store Glacier | *Dynamic* | 0.635 | 77.2 | 36.4 | 133 | 44.6 | 0.301 | 0.679 |
| | | ***0.640*** | ***79.1*** | ***34.7*** | ***135*** | ***45.3*** | ***0.301*** | ***0.678*** |
| | | 0.645 | 81.2 | 33.0 | 135 | 45.3 | 0.303 | 0.674 |
| | NDWI | 0.180 | 21.2 | 82.5 | 34 | 11.4 | 0.425 | 0.487 |
| | | 0.190 | 17.2 | 85.8 | 30 | 10.1 | 0.418 | 0.541 |
| | | 0.195 | 15.3 | 87.4 | 29 | 9.7 | 0.419 | 0.563 |
| | Red/blue band ratio | 0.710 | 27.3 | 77.5 | 40 | 13.4 | 0.458 | 0.417 |
| | | 0.750 | 54.8 | 54.8 | 55 | 18.5 | 0.871 | 0.199 |
| | | 0.760 | 63.9 | 47.3 | 63 | 21.1 | 0.942 | 0.196 |

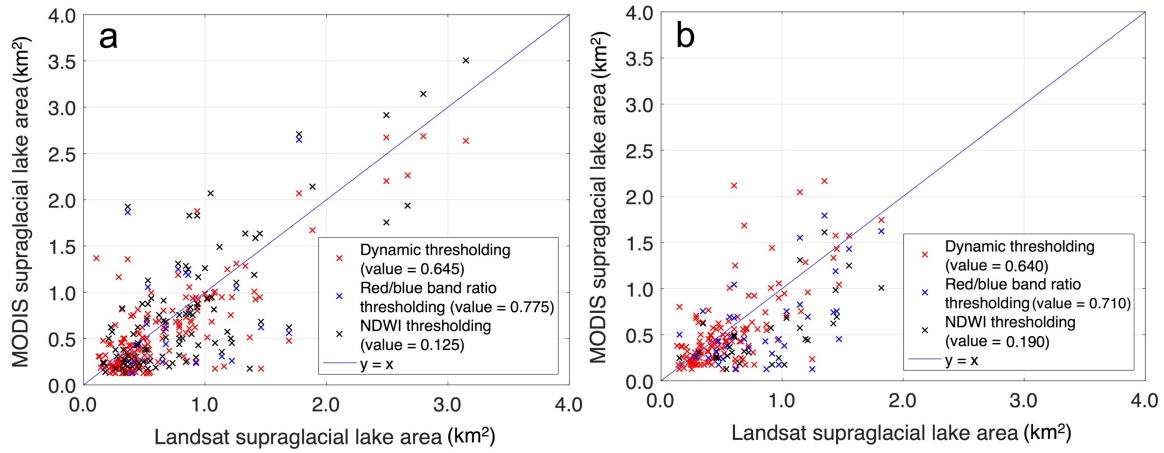



**Figure 3.4:** Lake areas derived from the algorithms applied to MODIS imagery compared with lake areas derived from the Landsat 8 supervised classification for the (a) Paakitsoq and (b) Store Glacier regions. Data shown are for the best-performing threshold value for each technique for calculating lake area. The blue lines on both subplots show $y = x$. Note that only lakes predicted by both the algorithm for calculating MODIS lake and the Landsat 8 supervised classification are plotted.

It is deemed necessary to determine a single uniform threshold value based on the analysis for both regions, which then allows it to be incorporated into a fully-automated approach. Therefore, lake areas derived from MODIS with threshold values in the range 0.640 to 0.645 (i.e. the best-performing thresholds for the two regions) at 0.001 increments are compared with Landsat 8 lake areas. This analysis determines that the 0.640 threshold is best, for which a final RMSE value is obtained for lake area calculations of 0.323 km$^2$, an $r$ of 0.694, and a total of 42% of the Landsat 8 lakes reported (Figure 3.6). Thresholds between 0.641 and 0.645 perform marginally more poorly ($r$ = 0.690–0.693, with all $p$ values < 0.01; RMSE = 0.324 km$^2$; reported Landsat 8 lake number remains at 42%). There is no obvious spatial pattern in terms of lakes that are reported in the Landsat 8 dataset but which are absent from the MODIS record: lakes at all elevation bands and within regions of both dark and bright surrounding ice are reported equally well, but, similarly to Leeson *et al.* (2013), the areas of lakes with partial ice cover are under-estimated (e.g. see outlines on Figure 3.5).

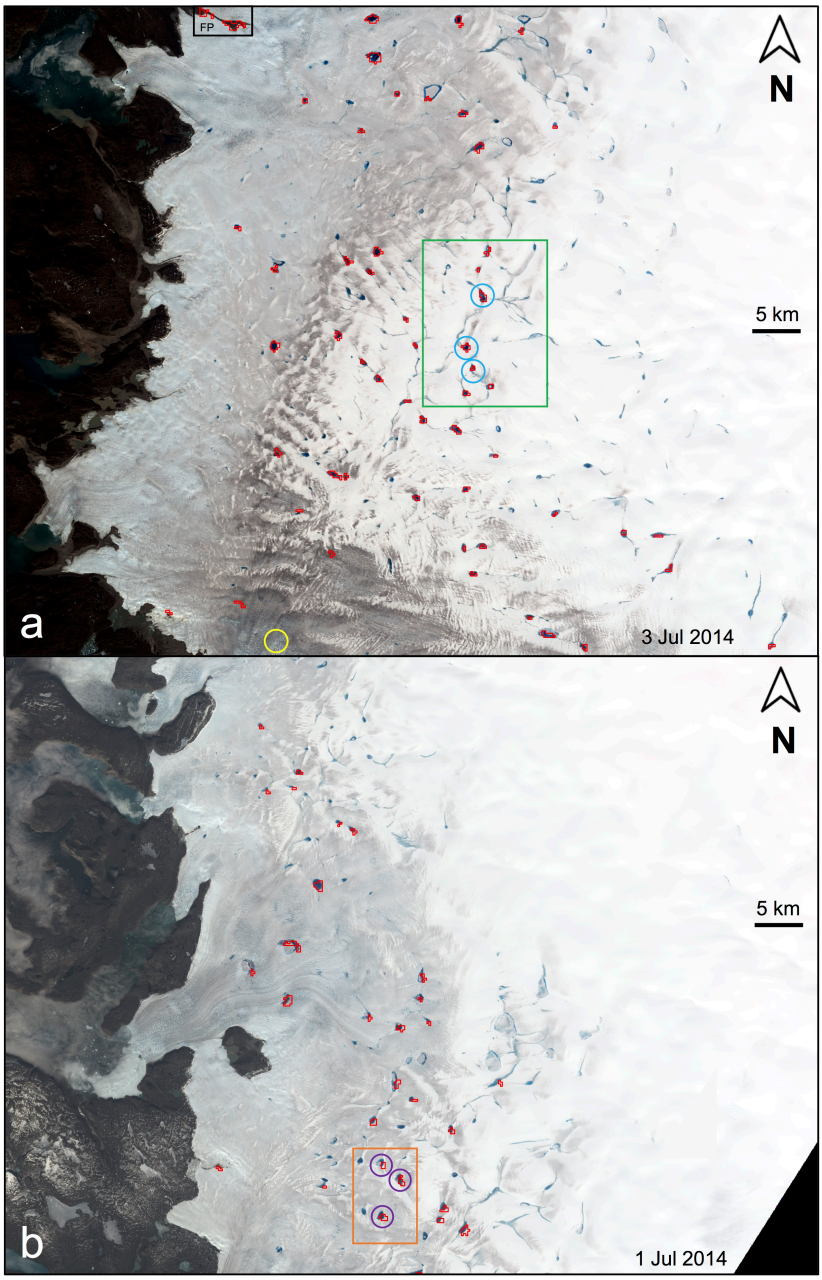



**Figure 3.5:** Lake perimeters (red lines) derived using a dynamic-thresholding approach applied to MODIS's red band with a threshold value of 0.640 for both the (a) Paakitsoq and (b) Store Glacier regions, overlain onto background Landsat 8 images (see Table A.1 for image details). The total areal extents within panels (a) and (b) are equivalent to those shown in Figure 3.1 (a) and (b). A false-positive lake is highlighted in (a) within the black box labelled "FP". The blue circles in (a) and purple circles in (b) indicate lakes that drain rapidly as part of a cluster (Section 3.5.3). The areas within the green box on (a) and orange box on (b) indicate the areas contained within the panels of Figure 3.14. The yellow circle in (a) indicates the area within which a lake drains, refills and then re-drains (Section 3.5.3), although the lake is not shown on this image.

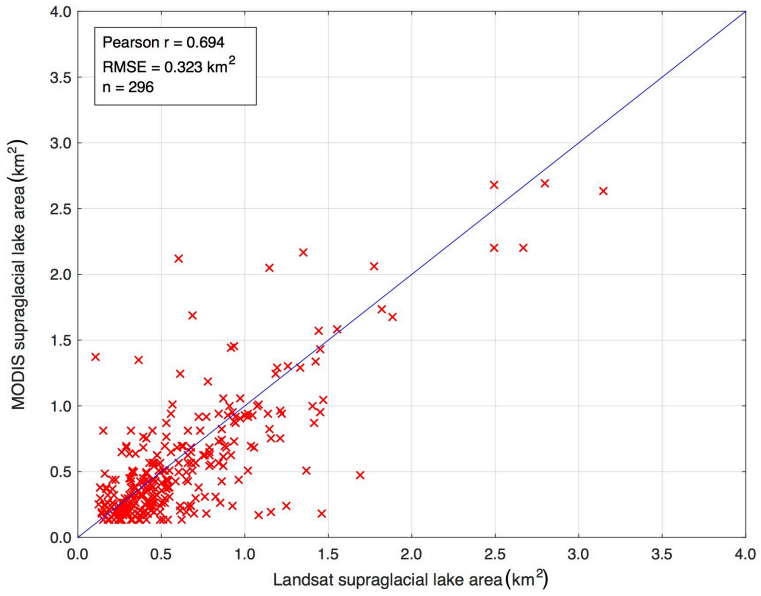



**Figure 3.6:** Lake areas across both study sites derived from MODIS imagery using a dynamic-thresholding approach applied to the red band with a threshold value of 0.640 compared with lake areas ascertained from the Landsat 8 supervised classification. $n$ represents the number of data points on the graph. The blue line shows $y = x$. The $r$ value is significant with a $p$ value of $< 0.01$.

## Lakes omitted from the MODIS record

To quantify the impact of using the coarser-resolution MODIS product on the reporting of total lake areas, the areas classified as water-covered from the Landsat 8 supervised classifications that are less than two MODIS pixels in size are quantified. It is important to note that the values presented here represent all water-covered areas identified from the Landsat 8 supervised classification, so while these numbers will involve some smaller lakes, water contained within larger supraglacial streams/rivers and slush zones, for example, will also be included. Across the Landsat 8 imagery, areas of contiguous water covering < 0.125 km$^2$ in area represent an average total per image of 3.84 km$^2$ (range 0.29–9.61 km$^2$) for Paakitsoq and 1.99 km$^2$ (range 0.11–4.86 km$^2$) for Store Glacier. These compare with the much higher average regional cover by lakes ≥ 0.125 km$^2$ recorded in the MODIS images of 22.02 km$^2$ (Paakitsoq) and 13.18 km$^2$ (Store Glacier). Relative to the sizes of the ice-covered regions, these values for area covered by lakes < 0.125 km$^2$ in size represent coverages of only 0.077% (Paakitsoq) and 0.037% (Store Glacier). Compared with the areas covered by lakes in the MODIS imagery, these other water-covered areas represent only 17.4% (Paakitsoq) and 15.1% (Store Glacier) of the total water-covered areas identified by MODIS. These small lakes have a mean size of 0.006 km$^2$ at both Paakitsoq and Store Glacier.

In addition to the small (< 0.125 km$^2$) lakes that could never be identified in MODIS imagery due to its coarse resolution, the size distribution is examined of lakes ≥ 0.125 km$^2$ (which could theoretically be identified by MODIS) that are present in the Landsat 8 record but which are not identified in the MODIS lake-classification scheme (using a dynamic band threshold value of 0.640). At Paakitsoq, the lakes of this type omitted from the MODIS record have a mean area of 0.26 km$^2$ (maximum 1.20 km$^2$) and at Store Glacier, the lakes of this type have a mean area of 0.27 km$^2$ (maximum 1.08 km$^2$). These are relative to mean lake areas within the MODIS-reported lake populations of 0.69 km$^2$ (Paakitsoq) and 0.59 km$^2$ (Store Glacier). An unpaired Student's $t$-test reveals a statistically significant difference between the lake areas for the populations of lakes reported by Landsat 8 that are absent from the MODIS record and the lakes that are reported by both MODIS and Landsat 8: for Paakitsoq, $t$ = 8.4, with a $p$ value of < 0.01; for Store Glacier, $t$ = 6.4, with a $p$ value of < 0.01. Overall, this analysis indicates that smaller lakes close to MODIS's threshold reporting size (two pixels or 0.125 km$^2$) tend to be omitted from MODIS data while being reported in Landsat 8 data.

## 3.4.2 Calculating lake depths and volumes

### Performance of the algorithm for calculating lake depth

Tables 3.2 and 3.3 present the results of the MODIS-based calculations of lake depth and volume with the green and red bands individually, compared with the corresponding Landsat 8 depths and volumes, which are calculated using Landsat 8's red and panchromatic bands as inputs to the physically-based approach. Depths and volumes calculated with MODIS's red band significantly outperform those from the green band for both sites. For the red band, RMSEs for lake pixel depths are 1.19 m (Paakitsoq) and 1.39 m (Store Glacier), relative to a mean MODIS pixel depth for water-covered pixels of 1.40 m across lakes from all of the images. RMSEs for lake volumes are 6.1 × 10$^7$ m$^3$ (Paakitsoq) and 5.7 × 10$^7$ m$^3$ (Store Glacier), relative to a mean MODIS lake volume of 4.0 × 10$^7$ m$^3$ for lakes from all of the images. Green band RMSEs are always more than double these values (Table 3.2). In general, the MODIS-derived lake depths and volumes are lower than the Landsat 8 ones, particularly for depths < ~4 m, although there is spread in the data (Figures 3.7 and 3.8). There are two dates when this pattern does not obviously apply. The first is 11 July at Paakitsoq, shown on Figures 3.7 (a) and 3.8 (a), where lake pixel depths and volumes tend to be higher in the MODIS than the Landsat 8 images. Further investigation shows that the 11 July Paakitsoq Landsat 8 image includes regions, which are mainly on the ice sheet, that are covered by a light-white banding, interpreted to be very fine high-level clouds, aerosol or dust, which could explain the seemingly low Landsat 8 pixel depths calculated for this image. The second major

anomaly is the sharp positive tail for the lake depths and volumes at Paakitsoq on 4 August (Figure 7 (a)). This may result from the difficulty in accurately resolving water depths > ~4 m when using Landsat 8's red and panchromatic bands for the physically-based calculations (Moussavi *et al.*, 2016). This is therefore likely to indicate a limitation with the validation dataset rather than with the approach applied to the MODIS data. In Figure 8 (a), lake volumes are, however, not similarly overestimated for MODIS lakes compared with Landsat 8 ones, suggesting that bilinearly resampling the Landsat 8 depth arrays to match the MODIS resolution offsets this bias to a degree. For all images, there is no tendency for higher lake-depth errors to be present for specific elevation bands or for given lake sizes (Figures 3.7, 3.8 and 3.9).

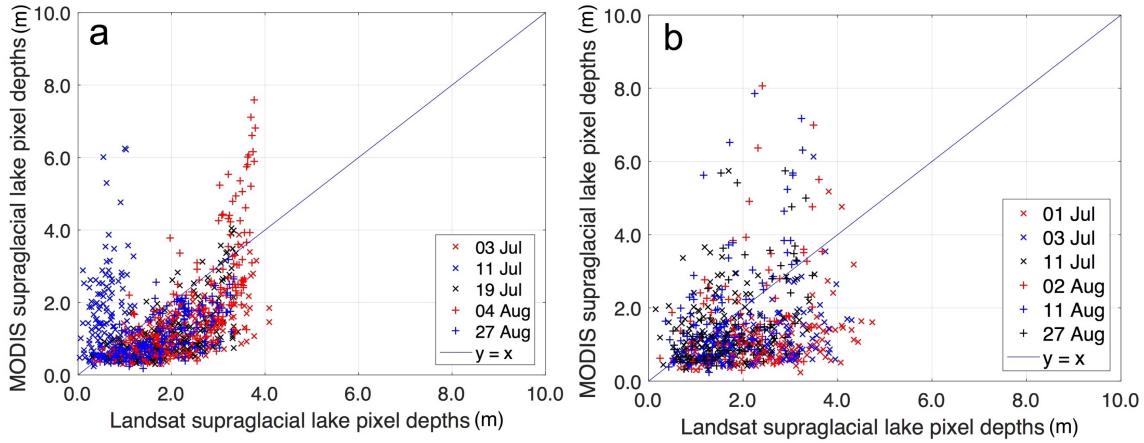



**Figure 3.7:** Lake pixel depths calculated from MODIS's red band for the (a) Paakitsoq and (b) Store Glacier regions, compared with depths calculated from the average of Landsat 8's red and panchromatic bands. The blue lines on both subplots show $y = x$. Note the two anomalous sets of lake pixel depths for Paakitsoq on 11 July and 4 August, where the MODIS values are systematically higher than the Landsat 8 values.

**Table 3.2:** Summary of the performance of MODIS lake depths derived from the red and green bands compared with Landsat 8 depths derived from the average of the red and panchromatic bands across both study sites for each image date. All values of $r$ except the one marked with an asterisk are significant at the 95% confidence interval ($p < 0.05$). Summary data for the best-performing band (i.e. band 1, red) across all days are shown in bold italicised text.

| **Region** | **MODIS band tested** | **Date (2014)** | ***n*** | ***r*** | **RMSE (m)** |
|---|---|---|---|---|---|
| Paakitsoq | Band 1 (red) | 3 Jul | 213 | 0.675 | 1.11 |
| | | 11 Jul | 157 | 0.134* | 1.45 |
| | | 19 Jul | 215 | 0.610 | 1.08 |
| | | 4 Aug | 225 | 0.668 | 1.29 |
| | | 27 Aug | 152 | 0.649 | 0.95 |
| | | ***All*** | ***962*** | ***0.447*** | ***1.19*** |
| Store Glacier | Band 1 (red) | 1 Jul | 121 | 0.427 | 1.88 |
| | | 3 Jul | 137 | 0.388 | 1.49 |
| | | 11 Jul | 161 | 0.221 | 0.94 |
| | | 2 Aug | 101 | 0.419 | 1.35 |
| | | 11 Aug | 111 | 0.575 | 1.30 |
| | | 27 Aug | 72 | 0.497 | 1.21 |
| | | ***All*** | ***703*** | ***0.259*** | ***1.39*** |
| Paakitsoq | Band 4 (green) | 3 Jul | 212 | 0.659 | 6.30 |
| | | 11 Jul | 158 | 0.160 | 10.22 |
| | | 19 Jul | 214 | 0.570 | 6.89 |
| | | 4 Aug | 107 | 0.329 | 3.33 |
| | | 27 Aug | 151 | 0.668 | 6.48 |
| | | All | 842 | 0.298 | 7.11 |
| Store Glacier | Band 4 (green) | 1 Jul | 121 | 0.381 | 4.96 |
| | | 3 Jul | 137 | 0.385 | 5.86 |
| | | 11 Jul | 161 | 0.176 | 7.52 |
| | | 2 Aug | 102 | 0.380 | 10.54 |
| | | 11 Aug | 111 | 0.542 | 11.64 |
| | | 27 Aug | 71 | 0.425 | 11.10 |
| | | All | 703 | 0.233 | 8.59 |

**Table 3.3:** Summary of the performance of MODIS lake volumes derived from the red and green bands compared with Landsat 8 values derived from the average of the red and panchromatic bands across both study sites for each image date. All values of $r$ are significant at the 95% confidence interval ($p < 0.05$). Summary data for the best-performing band (i.e. band 1, red) across all days are shown in bold italicised text.

| **Region** | **MODIS band tested** | **Date (2014)** | ***n*** | ***r*** | **RMSE ($km^3$)** |
|---|---|---|---|---|---|
| Paakitsoq | Band 1 (red) | 3 Jul | 48 | 0.881 | 0.050 |
| | | 11 Jul | 50 | 0.456 | 0.045 |
| | | 19 Jul | 23 | 0.897 | 0.088 |
| | | 4 Aug | 25 | 0.974 | 0.066 |
| | | 27 Aug | 13 | 0.963 | 0.085 |
| | | ***All*** | ***159*** | ***0.777*** | ***0.061*** |
| Store Glacier | Band 1 (red) | 1 Jul | 27 | 0.803 | 0.082 |
| | | 3 Jul | 27 | 0.741 | 0.065 |
| | | 11 Jul | 30 | 0.446 | 0.040 |
| | | 2 Aug | 16 | 0.897 | 0.049 |
| | | 11 Aug | 18 | 0.958 | 0.023 |
| | | 27 Aug | 11 | 0.918 | 0.045 |
| | | ***All*** | ***129*** | ***0.673*** | ***0.057*** |
| Paakitsoq | Band 4 (green) | 3 Jul | 47 | 0.813 | 0.123 |
| | | 11 Jul | 50 | 0.693 | 0.353 |
| | | 19 Jul | 22 | 0.558 | 0.220 |
| | | 4 Aug | 25 | 0.967 | 0.570 |
| | | 27 Aug | 12 | 0.966 | 0.390 |
| | | All | 156 | 0.795 | 0.339 |
| Store Glacier | Band 4 (green) | 1 Jul | 27 | 0.810 | 0.072 |
| | | 3 Jul | 27 | 0.743 | 0.127 |
| | | 11 Jul | 30 | 0.559 | 0.263 |
| | | 2 Aug | 16 | 0.826 | 0.455 |
| | | 11 Aug | 18 | 0.940 | 0.413 |
| | | 27 Aug | 11 | 0.928 | 0.297 |
| | | All | 129 | 0.674 | 0.279 |

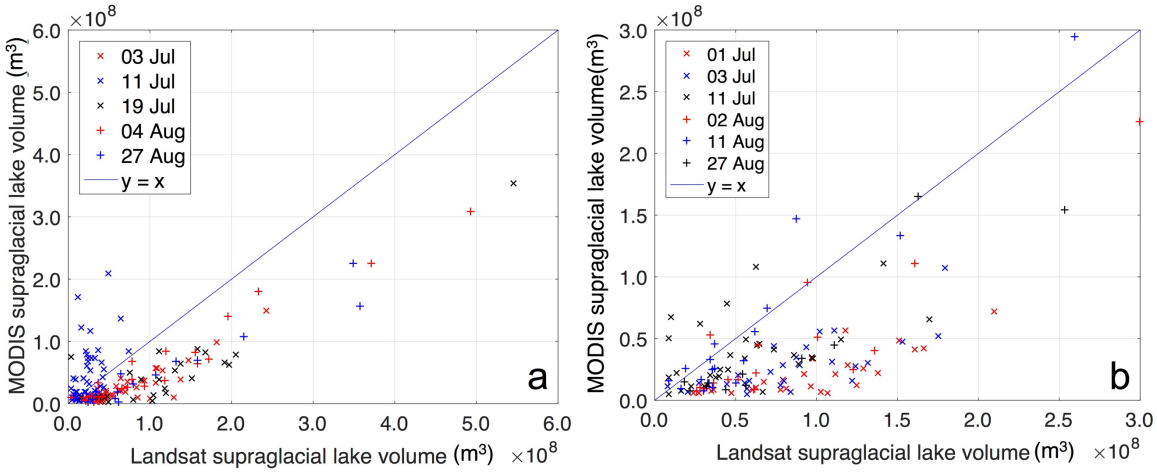



**Figure 3.8:** Lake volumes (calculated by integrating the lake pixel depths, and multiplying this value by the pixel size) derived from MODIS's red band for the (a) Paakitsoq and (b) Store Glacier regions, compared with those calculated from the average of Landsat 8's red and panchromatic bands. The blue lines on both subplots show $y = x$. Note the anomalous set of lake volumes for Paakitsoq on 11 July, where the MODIS values are systematically higher than the Landsat 8 values.

When the differences between MODIS and Landsat 8 depths are averaged across all of the images, the mean differences are small, with the vast majority of lakes displaying errors in the range -0.5 to 0.5 m (Figure 3.9). Errors of ~-3 m (i.e. red values on Figure 3.9), where MODIS depths are higher than Landsat 8 ones, are possibly due the effect described above, where MODIS records deeper water than Landsat 8 due to the limited sensitivity of the Landsat 8 method at higher depths. Errors of ~+3 m (i.e. blue values on Figure 3.9), where Landsat 8 values are consistently higher than MODIS ones, may be the competing effect, which results from the coarse resolution of MODIS, meaning that, on some days, the deepest water pixels within lakes are not recorded accurately within the MODIS surface-reflectance data, and are instead sampled as lighter (and so shallower) water pixels. This possible bias towards the sampling of brighter pixels in MODIS may also result in the derivation of higher $A_d$ values in MODIS than in Landsat 8, which would lead to the reporting of lower lake depths by MODIS than Landsat 8. Combining the red-band MODIS-derived lake pixel depths and volumes to form single samples across both study regions, the final RMSE values are 1.27 m for lake depth and $5.9 \times 10^7$ m$^3$ for lake volume (Figure 3.10). Although both values are statistically significant ($p < 0.01$), the association is better for lake volumes ($r = 0.741$) than depths ($r = 0.365$), due to the fewer data points and lower spread within the lake volume dataset. These errors are applied to the lake depths and volumes calculated by the FAST algorithm for MODIS imagery. These combined data display a similar pattern to the region-specific data, with MODIS values usually underestimated compared with Landsat 8, but with some scatter. This pattern also broadly matches that observed for the Landsat 8 versus MODIS lake-area comparisons (Figure 3.6).

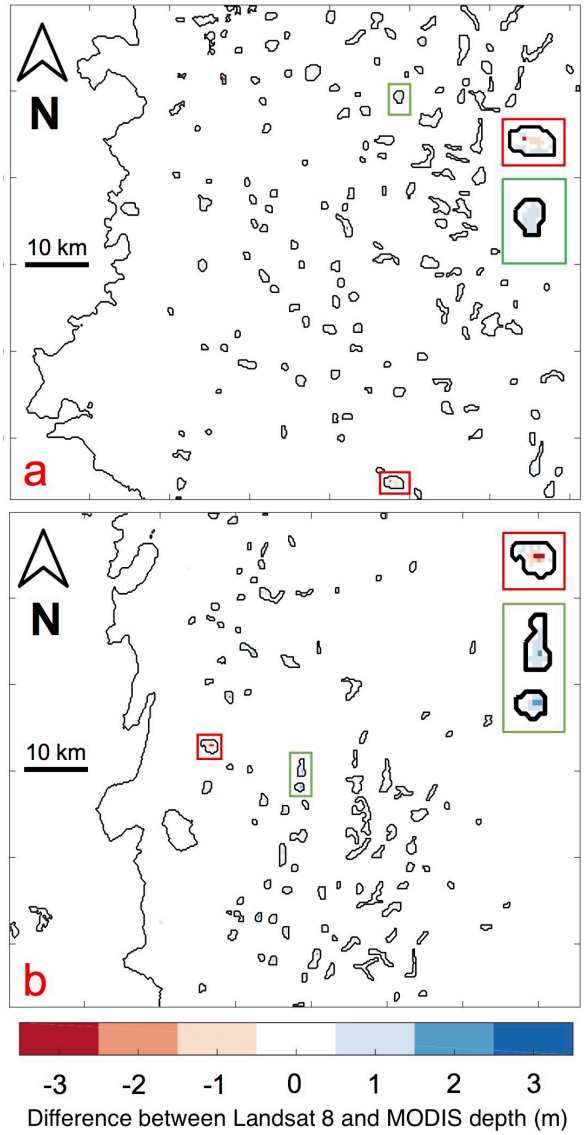



**Figure 3.9:** The mean difference (derived by averaging the difference between pixel water depths across all images) between lake depths for the (a) Paakitsoq and (b) Store Glacier regions, highlighting the lack of spatial or elevation bias in the errors of lake water depth. A positive difference indicates that the MODIS lake depth is underestimated compared with the Landsat 8 depth, and vice versa. To allow these comparisons, the Landsat 8 depths are resampled using a bilinear technique to 250 m resolution and the MODIS depths are retained at their native 250 m resolution. The GrIS margin is shown by the thick black line on both panels, and the areas within the plots are equivalent to those shown within Figure 3.1. The lake boundaries shown are derived from the sum of the lake extents across all of the Landsat 8 images. The green insets on both panels are higher-scale examples of the observation of consistently higher Landsat 8 depths towards lake centres compared with MODIS values. The red insets on both panels are higher-scale examples of where MODIS predicts deeper water than Landsat 8 over lake centres, possibly due to the limited sensitivity of the Landsat 8 method at very high depths.

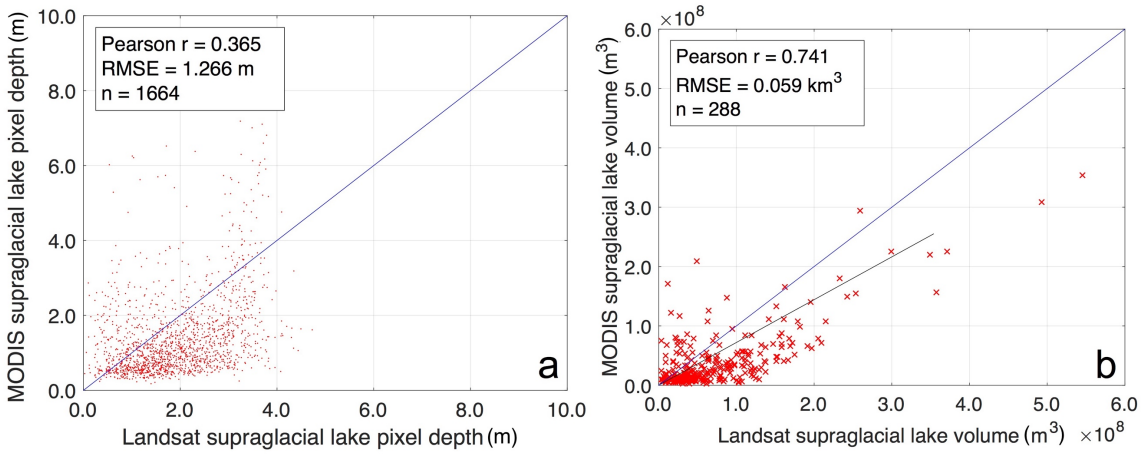



**Figure 3.10:** Lake (a) pixel depths and (b) volumes across both study sites derived using MODIS's red band compared with depths and volumes derived from Landsat 8's red and panchromatic bands. The blue lines on both subplots show $y = x$. The black line on (b) is an ordinary least-squares (OLS) linear regression, with equation $y = 0.721(x)$, which forms the basis of the lake volume scaling relationship described in this section.

Whether there is bias in the errors for the data for lower (or higher) lake depths and volumes is investigated. The errors on MODIS depth measurements show little variation (RMSE mean = 1.16 m; RMSE σ = 0.12 m; RMSE range = 1.00–1.40 m) for water ≤ 4 m deep, but they are almost three times higher (RMSE = 2.99 m) for water > 4 m deep (Table 3.4). A similar pattern exists for lake volumes (Table 3.5), where lakes with volumes < $10.0 \times 10^7$ m$^3$ have lower errors for and variation within their measurements (RMSE mean = $5.6 \times 10^7$ m$^3$; RMSE σ = $1.2 \times 10^7$ m$^3$; RMSE range = $3.9–8.0 \times 10^7$ m$^3$) than lakes exceeding this volume (RMSE = $10.8 \times 10^7$ m$^3$). This pattern of errors may be partially explained by the use of the longer-wavelength red and panchromatic bands from Landsat 8 data to derive the lake depths and volumes within the validation dataset. These longer wavelengths attenuate more quickly within the water column than shorter wavelengths, such as Landsat 8's green band, and this may result in the Landsat 8 data's bias against the deepest (> 4 m) water (Moussavi *et al.*, 2016). This is offset against the sensitive ability of the red wavelength to record measurements more precisely at the lower depths.

**Table 3.4:** Variation in the errors (as measured by the RMSE) for water depths derived from MODIS imagery compared with the Landsat 8 water depths across all images from both study regions. $n$ is the number of data points within each given range.

| Depth range (m) | $n$ | RMSE (m) |
|---|---|---|
| 0.0–0.5 | 169 | 1.08 |
| 0.5–1.0 | 599 | 1.24 |
| 1.0–1.5 | 371 | 1.14 |
| 1.5–2.0 | 220 | 1.07 |
| 2.0–2.5 | 106 | 1.00 |
| 2.5–3.0 | 75 | 1.18 |
| 3.0–3.5 | 40 | 1.17 |
| 3.5–4.0 | 29 | 1.40 |
| > 4.0 | 55 | 2.99 |

**Table 3.5:** Variation in the errors (as measured by the RMSE) for lake volumes derived from MODIS imagery compared with the Landsat 8 lake volumes across all images from both study regions. $n$ is the number of data points within each given range.

| Volume range ($\times 10^7$ m$^3$) | $n$ | RMSE ($\times 10^7$ m$^3$) |
|---|---|---|
| 0.0–0.5 | 8 | 4.0 |
| 0.5–1.0 | 57 | 4.4 |
| 1.0–2.0 | 66 | 3.9 |
| 2.0–2.5 | 19 | 5.7 |
| 2.5–3.0 | 17 | 5.5 |
| 3.0–3.5 | 17 | 5.5 |
| 3.5–4.0 | 11 | 5.2 |
| 4.0–5.0 | 21 | 6.6 |
| 5.0–6.0 | 15 | 5.5 |
| 6.0–7.0 | 12 | 8.0 |
| 7.0–10.0 | 21 | 6.9 |
| > 10.0 | 24 | 10.8 |

## MODIS to Landsat 8 lake-volume scaling

Using the single sample of lake volumes for both regions, a regression of MODIS lake volumes against Landsat 8 lake volumes yields a slope coefficient of 0.721 (Figure 3.10 (b)). Scaling the MODIS lake volumes accordingly (i.e. by dividing them by the slope coefficient of 0.721), and

comparing them with the Landsat 8 values, reduces the RMSE slightly from $5.9 \times 10^7$ $m^3$ to $5.4 \times 10^7$ $m^3$. Depth-based scaling is not attempted because, when the depths were compared, this was done on a pixel-by-pixel basis; whereas for the volumes, comparisons were conducted on a lake-by-lake basis, for which no resampling was required.

### 3.4.3 Lake evolution within the study regions

When applied to the study sites in summer 2014 using the best techniques for calculating lake area and depth, the FAST algorithm tracks individual area and volume changes for 202 lakes at Paakitsoq and 122 lakes at Store Glacier, the first time that an automatic derivation of seasonal changes to lake volume has been possible on the GrIS. For each day of the analysis, individual lake areas and volumes are integrated to obtain the total lake areas and volumes across the regions. Broadly similar patterns are observed for both sites, with gradual increases in lake area and volume in the early melt season, peaks in total stored lake water in mid-July and early August, and then decreasing lake area and water volume from mid-August onwards (Figure 3.11). For both regions, there is a statistically significant correlation (with high $r$ values) between the total number of lakes on an image and the total volume of water contained within lakes for that image (Figure 3.12). However, there is no statistically significant relationship between the total number of lakes on an image and the mean lake volume for the lakes on that image, although the relationship is stronger at Store Glacier ($r$ = 0.469) than Paakitsoq ($r$ = -0.008) (Figure 3.12).

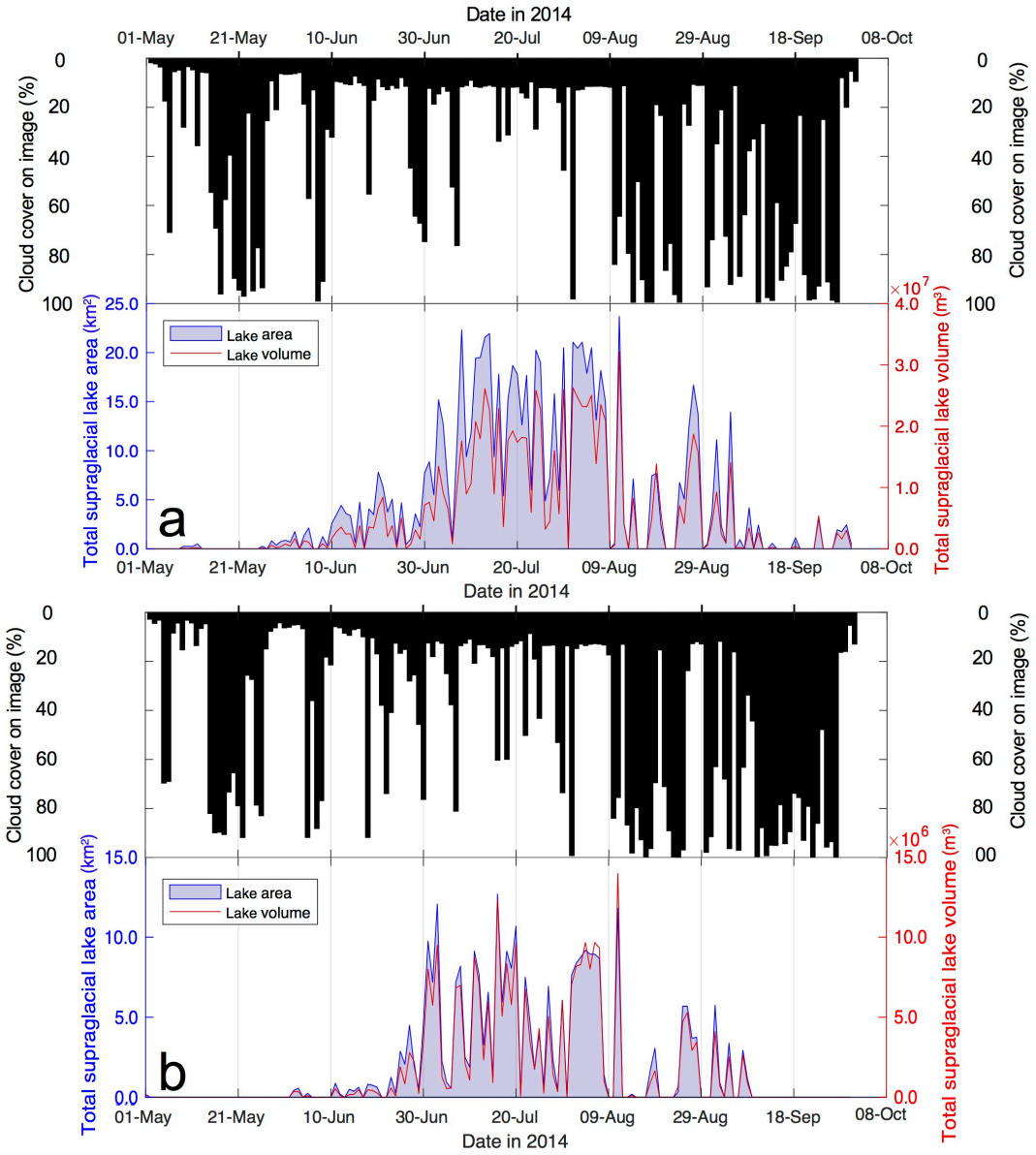



**Figure 3.11:** Total lake area, volume and percentage cloud cover for the (a) Paakitsoq and (b) Store Glacier regions during the 2014 melt season. The large mid-season decreases in total lake area and volume to values that are at or close to zero correspond with high regional cover by clouds (top panels of (a) and (b)), explaining the seasonal pattern of seeming anomalies in total lake area and volume evolution.

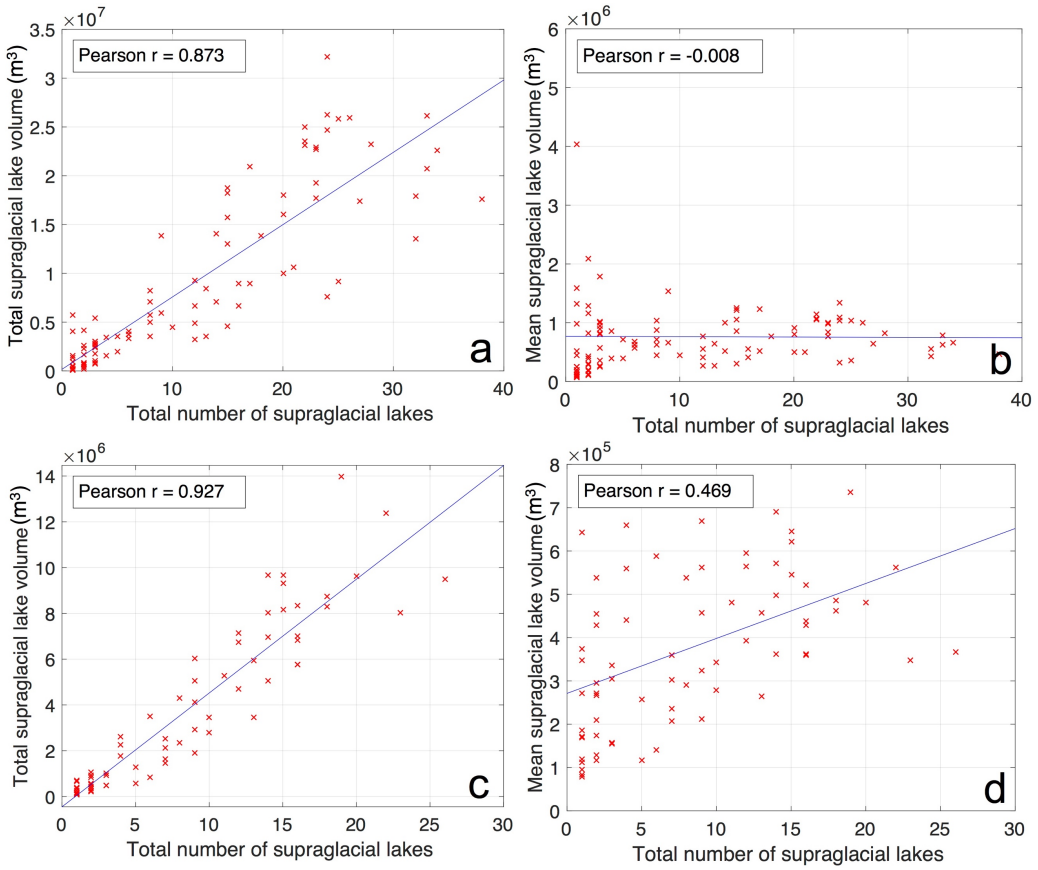



**Figure 3.12:** The relationship between the total number of lakes on each individual MODIS image in the season and the total and mean lake water volume for each individual MODIS image. Note that images on which no lakes are identified are not plotted. Subplots (a) and (b) show relationships for the Paakitsoq region, with (c) and (d) being for the Store Glacier region. The blue lines on all subplots display OLS linear regressions. $r$ values are significant ($p < 0.01$) at the 99% confidence interval for subplots (a) and (c), but are not significant at the 95% confidence interval for subplots (b) and (d).

Table 3.6 summarises results from the identification of rapid lake-drainage events using the FAST algorithm. The mean surface elevation (derived from Howat *et al.*, 2014) at which rapid lake-drainage events occur is ~1050 m a.s.l. in both regions, and both regions also exhibit similar median dates of rapid-drainage initiation: 12 July (Paakitsoq) and 7 July (Store Glacier). However, the modal dates of rapid drainage vary more between the two regions: 13 July (Paakitsoq) and 3 July (Store Glacier). There is an obvious upglacier, seasonal progression of rapid lake drainage in both regions, and 37% of rapid events occur from 9–18 July (Figure 3.13). The fewer late-season (i.e. post-18 July) rapid drainage events may result from increasing regional cloud cover during this later period (cf. Figure 3.11), meaning that rapid lake drainage could not be identified with certainty.

**Table 3.6:** Summary of the results from the FAST algorithm applied to the two study sites. Tables A.8 and A.9 present full details for all of the rapid lake-drainage events identified within the two regions.

| Property | Paakitsoq region | Store Glacier region |
|---|---|---|
| Number of rapid drainage events | 43 | 19 |
| Percentage of lakes draining rapidly | 21 | 15 |
| Median date of rapid drainage | 12 July | 7 July |
| Modal date of rapid drainage | 13 July | 3 July |
| Total water drained during rapid drainage ($m^3$) | $1.9 \times 10^7$ | $6.6 \times 10^6$ |
| Mean water drained per rapid drainage event ($m^3$) | $4.3 \times 10^5$ | $3.5 \times 10^5$ |

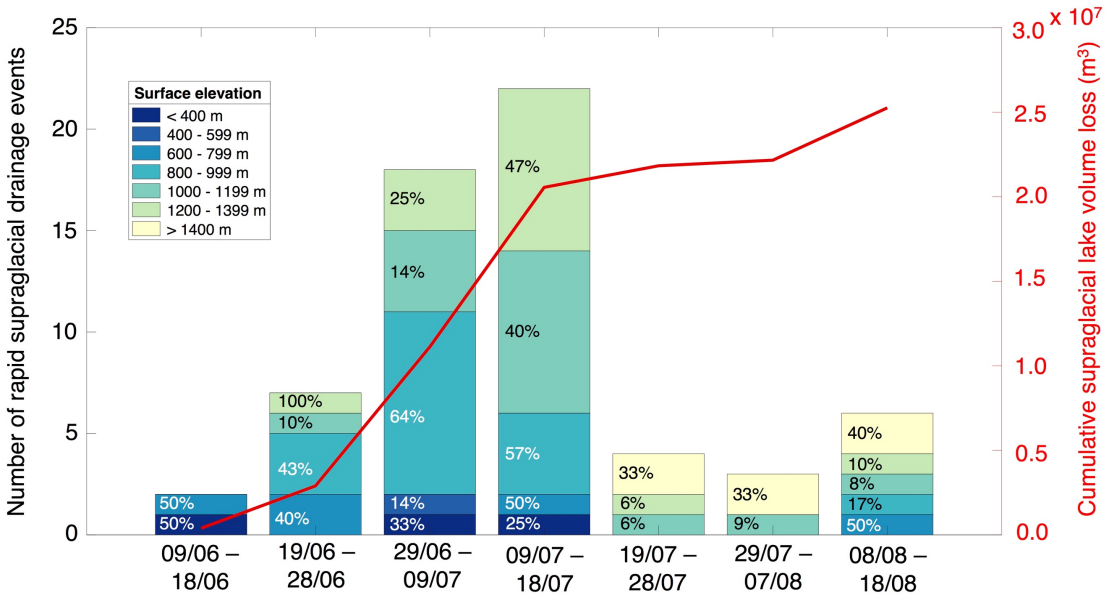



**Figure 3.13:** The number of rapid lake-drainage events across both study sites, binned by initiation dates and stacked by the surface elevation of lakes within that category. Cumulative lake-volume loss from all rapid events in 2014 is shown by the solid red line. The percentage figures give the percentage of lakes that drain within each elevation band relative to the maximum number of observed lakes within that elevation band over the corresponding dates.

# 3.5 Discussion

## 3.5.1 Performance of the algorithms for calculating lake area

The first aim of this chapter was to evaluate a variety of methods that are commonly used to automatically classify lake areas from MODIS imagery since a consensus on the best method to use has not yet emerged. In doing this, this thesis complemented Leeson *et al.*'s (2013) testing of numerous algorithms for deriving lake area, but built on that work by also testing a range of threshold values for the different methods. The results showed that a dynamic-thresholding technique applied to MODIS's red band with a threshold value of 0.640 performed best among the algorithms tested. The RMSE of 0.32 $km^2$ for this method is higher than values reported in some other studies (e.g. 0.14 $km^2$ in Fitzpatrick *et al.* (2014); 0.20 $km^2$ in Liang *et al.* (2012); 0.11 $km^2$ in Selmes *et al.* (2011); 0.22 $km^2$ in Sundal *et al.* (2009); 0.08 $km^2$ in Everett *et al.* (2016)), but is lower than Leeson *et al.*'s (2013) value of 0.48 $km^2$ for dynamic thresholding of the red band. However, these studies used a range of validation data derived from different techniques for different regions and areal extents of the GrIS, which is likely to explain the differences in performance compared with that in this chapter. For example, the MODIS lake areas in this work were compared against Landsat 8 lake areas from a supervised classification, while previous research validated them against manually-derived lakes (e.g. Leeson *et al.*, 2013; Everett *et al.*, 2016) or other validation data. In addition, the higher RMSE observed here may be because the earlier studies only compared specific-sized lakes or subsets of a complete population: for example, Liang *et al.* (2012) included only 63 lakes in their sample rather than a complete lake dataset as used here. This use of the entire lake population allowed for more robust comparisons than if a subset of lakes had been used. This research identified a similar percentage of the total number of lakes present within the validation dataset as other studies (e.g. Leeson *et al.*, 2013). Using dynamic thresholding of the red band without an *a priori* distribution of lakes appears to have had only a minor impact on the overall percentage of lake numbers reported compared with Leeson *et al.*'s (2013) value. However, it is feasible that omitting this pre-defined distribution led to the lower accuracy (in terms of the RMSE) of lake areas compared with lake areas calculated in other studies (Selmes *et al.*, 2011; Everett *et al.*, 2016).

Dynamic thresholding of the red band was sensitive to the chosen threshold value, with values of 0.635–0.650 performing the best depending on the region investigated (Table 3.1). Using this method, the marginally higher performance (based on the RMSE and $r$ values) for a threshold of 0.645 for the Paakitsoq region can likely be attributed to the large areas of dark ice, and so low albedo, present within this region compared with Store Glacier (e.g. see the differing ice darkness

on Figures 3.5 (a) and (b)). Whether this difference in background albedo is meaningful is investigated by comparing surface-reflectance values for all visible spectral bands across all of the ice-covered areas of the two regions. To ensure similar illumination, this is conducted for the Landsat 8 tiles that were obtained from the same pass of the Landsat 8 satellite across both study regions (i.e. for the passes on 3 July, 11 July and 27 August; Table A.1). Since albedo is a measure of diffuse reflection and here surface-reflectance values (i.e. directional-hemispherical reflection) are being compared, it is important to note that these values represent only a first-order approximation. This analysis reveals a mean directional-hemispherical reflection for all bands of 0.64 ($\sigma$ = 0.078) for Paakitsoq and 0.67 ($\sigma$ = 0.097) for Store Glacier, with a similar pattern for the red band: a directional-hemispherical reflectance of 0.61 ($\sigma$ = 0.072) for Paakitsoq and 0.66 ($\sigma$ = 0.092) for Store Glacier. With the darker background ice at Paakitsoq, the mean overall reflectance in the moving window used for dynamic thresholding is lower than at Store Glacier, and so a slightly higher threshold is needed to define a lake at Store Glacier than at Paakitsoq. Even with this effect represented at these sites, the performance of the dynamic-thresholding technique was not markedly affected by differing thresholds, and at Paakitsoq a value of 0.640 performed nearly as well as the threshold value of 0.645. Overall, this indicates that there is a broad peak in performance for threshold values in the 0.635–0.650 range across the GrIS, also justifying Selmes *et al.*'s (2011) use of a 0.650 threshold.

Although the NDWI and red/blue band thresholding approaches performed relatively poorly compared to the dynamic red-band thresholding method, once the thresholds for these methods were tuned for the specific study regions, their RMSEs for lake area (Table 3.1) were lower than those for some other lake-area algorithms examined by Leeson *et al.* (2013): they found RMSEs of 0.78 km$^2$ (using Sundal *et al.*'s (2009) method) and 0.95 km$^2$ (using Johansson and Brown's (2013) method) when comparing automatically- versus manually-derived MODIS lakes. Thus, applying the red/blue band thresholding and NDWI approaches to specific regions of the GrIS can be defended, but only with adjustment of thresholds either on a site-by-site basis (Fitzpatrick *et al.*, 2014) or even on a lake-by-lake basis (Box and Ski, 2007). However, this would be problematic for applying thresholds across larger areas of the GrIS and for their incorporation into automated methodologies of lake detection and tracking, such as that developed in this chapter. Finally, lower performances for the NDWI and red/blue band thresholding methods compared to dynamic thresholding of the red band may also have resulted from the sharpening of MODIS's 500 m native resolution blue band to match that of the 250 m red band, meaning blue-band values were smoothed and the ratio between the highly-attenuating red and the lower-attenuating blue bands became diminished (Selmes, 2011).

## Lakes omitted from MODIS imagery

Part of this chapter's first aim involved quantifying the impact of using MODIS imagery on the reporting of total lake numbers on the GrIS, particularly to determine whether the use of coarser-resolution imagery represents a sufficient trade-off in terms of spatial resolution to exploit its higher temporal resolution. The results indicated that using coarse-resolution MODIS imagery results in the omission of numerous lakes in two main ways. The first category of lakes omitted from the MODIS record were those < 0.125 km$^2$ (as measured by Landsat 8) and therefore which could never have been resolved within the MODIS record because they were below MODIS's threshold reporting area of two pixels. The results showed that these small lakes represented only a small percentage relative to the regional coverage by lakes ≥ 0.125 km$^2$, which were identified by MODIS. Although these values were low, use of MODIS imagery alone potentially misses lakes within this category that may be capable of hydrofracture: Krawczynski *et al.* (2009) indicate lakes ≥ 0.25 km in diameter (i.e. with areas ≥ 0.0491 km$^2$ when approximated as perfect circles (Section 2.7)) can fracture through subfreezing ice 1 km thick in low-tension regions of the GrIS (since their work did not account for large longitudinal stresses). The data are therefore investigated further to determine the number of lakes in the regions that meet this criterion (i.e. with sizes of 0.0491–0.125 km$^2$); this involves creating a maximum lake extent mask from the Landsat 8 images. This shows that 189 (or 89) lakes grow to within this size range but do not grow beyond it at least once in the season in the Paakitsoq (or Store Glacier) region. The second category of lakes omitted from the MODIS record were those which were theoretically large enough to be identified by MODIS (i.e. ≥ 0.125 km$^2$), but which were not identified as part of the algorithm for calculating lake area. The algorithm for deriving lake area used in this chapter resulted in the reporting of only 42% of all of the Landsat 8 lakes ≥ 0.125 km$^2$ in area. By investigating the area of the lakes ≥ 0.125 km$^2$ reported by Landsat 8 but not by MODIS, the results showed that these unreported lakes tended to be smaller than the mean size of the MODIS-reported lakes within both regions (Section 3.4.1). This indicated that MODIS can more reliably identify larger lakes than those that lie closer to its threshold reporting area of 0.125 km$^2$. This under-reporting by MODIS replicates Leeson *et al.*'s (2013) findings for the Russell Glacier region.

Overall, the results suggest that using the MODIS record in isolation from spatially finer records is unlikely to introduce significant loss of information on the hydrology of the GrIS since a high percentage of lakes are included in the MODIS record. To be able to capture the drainage of these small lakes, which may be capable of hydrofracture (Krawczynski *et al.*, 2009), a dataset with the spatial resolution of (at least) the Landsat 8 sensor but with MODIS's near-daily temporal resolution

is required. Combined records of lake observations from Landsat 8 and Sentinel-1 (Miles, K. E. *et al.*, 2017) or Landsat 8 and Sentinel-2 (Chapter 5) hold promise in this regard.

### 3.5.2 Performance of the algorithm for calculating lake depth

This chapter's second aim was to apply a physically-based algorithm for calculating lake depth to the areas within the lake boundaries derived from the best-performing technique for calculating lake area. The application of Sneed and Hamilton's (2007) physically-based algorithm for calculating lake depth to MODIS's red band predicted lake depths and volumes in west Greenland with errors comparable to those in other studies (e.g. Pope *et al.*, 2016). Using MODIS's red band instead of its green band produced significantly better results. There are two possible reasons for these results. First, red light attenuates more strongly in the water column than green light, and can reproduce a range of water depths more reliably (Pope *et al.*, 2016), particularly at shallower depths. Second, the resolution sharpening applied to MODIS's green band (which is not required for the red band) is likely to have resulted in loss of accuracy in the surface-reflectance values, which then carry through into the lake-depth calculations. Although the lake depths and volumes calculated with MODIS's red band were dispersed around a linear regression line, producing low $r$ values (Figure 3.10; Tables 3.2 and 3.3), the derived RMSE values were low compared to the RMSE values for depths and volumes generated from the green band (Tables 3.2 and 3.3). The RMSE of 1.27 m for lake depth was higher than those for lake depths derived for Landsat 8's higher-resolution red (RMSE = 0.28 m) and panchromatic (RMSE = 0.63 m) bands (Pope *et al.*, 2016), but is lower than values from other studies using empirically-based depth-reflectance techniques for MODIS imagery (e.g. RMSE = 1.47 m in Fitzpatrick *et al.* (2014)).

#### Underestimated MODIS lake depths and volumes

Despite the better performance of the physically-based algorithm for calculating lake depth using the red over the green band, using the red band still tended to produce lower MODIS lake depths and volumes than those calculated from the Landsat 8 data. This is likely to be due to the different spatial resolutions of the two datasets. Landsat 8's higher resolution means that deep water towards lake centres is reliably sampled as dark pixels. Similarly-deep water will not be reliably sampled with MODIS's coarser resolution data if the shallower water depths away from the lake centres bias the sampling within MODIS pixels towards those shallower depths, which would then appear as relatively bright pixels. This work involved attempting to correct for this when comparing Landsat 8 and MODIS-derived lake pixel depths by resampling the Landsat 8 depth arrays (Section 3.3.4), but it is probable that this effect cannot be eliminated entirely. Furthermore, the lower MODIS lake

depths and volumes may also have been explained by the error associated with the lake outlines to which the algorithm for calculating lake depth was applied. If the algorithm for deriving lake area resulted in inaccurately-resolved lake perimeters, it is probable that (i) shallow water at the edges of lakes will have been omitted from the MODIS lake volume calculations; and (ii) $A_d$, which was taken as the mean of the reflectance of the ring of pixels surrounding the lake outline, will have been lower than it should have been, since this ring may have included some shallow water when it was intended to contain only bare ice. This error may have been especially influential since the algorithm for calculating lake depth is particularly sensitive to $A_d$ values (Georgiou *et al.*, 2009; Pope *et al.*, 2016). Finally, the lake depth and volume validation data derived from Landsat 8 had errors associated with them since they were also derived from the same physically-based lake depth retrieval algorithm. For example, Landsat 8's red and panchromatic bands may not be able to resolve the deepest (> 4 m) water accurately (Moussavi *et al.*, 2016), which may explain the pattern of higher RMSEs with higher water depths (Table 3.4). Comparing the MODIS-derived depths with field data or very high-resolution DEM data (similar to Pope *et al.* (2016) or Moussavi *et al.* (2016)) would provide additional tests of the algorithm's performance beyond those reported here, and would be a valuable future study, particularly given the now freely-available, high-resolution Arctic DEM data from the Polar Geospatial Center (http://pgc.umn.edu/arcticdem).

Finally, scaling the MODIS lake volumes using the slope coefficient from the linear regression line for the MODIS and Landsat 8 volume data produced only a marginal improvement to the lake-volume estimates, and given that this relationship was derived from a limited number of data points ($n$ = 288), this MODIS-Landsat 8 scaling relationship was not carried forward into the FAST algorithm.

### 3.5.3 Lake evolution within the study regions

The third aim of this chapter was to incorporate the best-performing techniques for calculating lake area and depth into a fully-automated lake-tracking algorithm, allowing automatic lake depth and volume calculations across large regions of the GrIS. The FAST algorithm permits additional insights into the GrIS's surface hydrology to be made compared with many previous studies in which only lake areas were tracked between images. As might be expected, the results indicated that total lake volume scales with the number of lakes on an image (Figure 3.12 (a) and (c)). However, the results also showed that the mean lake size across an individual image does not change alongside the total number of lakes present on the image (Figure 3.12 (b) and (d)). This suggests that as the melt season progresses, with more lakes forming on the ice sheet, the total lake water volume on an image increases by the presence of increasingly numerous lakes instead of through increases to the

dimensions of individual lakes. This might suggest an overall region-wide control on lake volume, such as limits to the size of ice-surface topographic depressions, preventing the formation of larger lakes, or perhaps a critical threshold that initiates lake drainage before lakes reach a certain size. However, the slightly stronger relationship between mean lake volume and the total number of lakes on an image (Figure 3.12 (d)) at Store Glacier could indicate that this control is less dominant here than at Paakitsoq. These and other controls are investigated fully in Chapter 4.

## Rapid lake drainage-event identification

The final aim of this chapter was to use the FAST algorithm to examine the incidence of rapid lake drainage across the two study regions in west Greenland. The numbers of rapidly draining lakes, as a proportion of the total lake population, identified by the FAST algorithm within the study regions (21% and 15% of the total lake populations at Paakitsoq and Store Glacier, respectively) are similar to results from other ice-marginal (i.e. < 80 km inland) areas of west Greenland (e.g. the 28% at Russell Glacier reported by Fitzpatrick *et al.* (2014)). As the melt season progresses, there are increasing numbers of rapid drainage events at higher elevations (Figure 3.13). This might be expected due to an upglacier increase in total meltwater production over the season, causing the filling of progressively higher lakes to reach the water volume required to drain, assuming there is a relation between this value and the initiation of hydrofracture (tested in Chapter 4). Alternatively, another control, such as those analysed in Chapter 4, may be able to explain the upglacier progression of lake drainage. The lack of early-season rapid drainage events at high elevations is because there are few lakes there. For example, during the 19 June to 28 June period, the single lake within the 1200–1399 m a.s.l. elevation band drained rapidly; by the 8 August to 18 August period, only 10% of the lakes within the elevation band drained rapidly (Figure 3.13). Fewer rapid events occur at lower surface elevations (< 600 m a.s.l.) later in the season because most lakes that could drain here would have done so earlier in the season.

Among the rapidly draining lakes identified by the FAST algorithm, clusters of drainage events are detected (which are defined as events that occurred within four days and 10 km of each other), as was also observed by Fitzpatrick *et al.* (2014) at Russell Glacier. In the Paakitsoq region, three lakes drain in mid-July at a similar elevation band and with comparable ice thicknesses beneath them; a similar pattern is observed for a lake cluster in early July at Store Glacier (Figures 3.5 and 3.14). In addition, one lake at Paakitsoq drains twice within the season: once on 12 June and then again on 10 July (Figure 3.5, yellow circle). This observation of the filling, drainage, refilling and re-drainage of a lake is a phenomenon that has been reported only once previously in a remote-sensing study (Fitzpatrick *et al.*, 2014) and once in a field-based study (Bryzgis and Box, 2005). It is encouraging that the FAST algorithm is able to automatically detect similar phenomena.

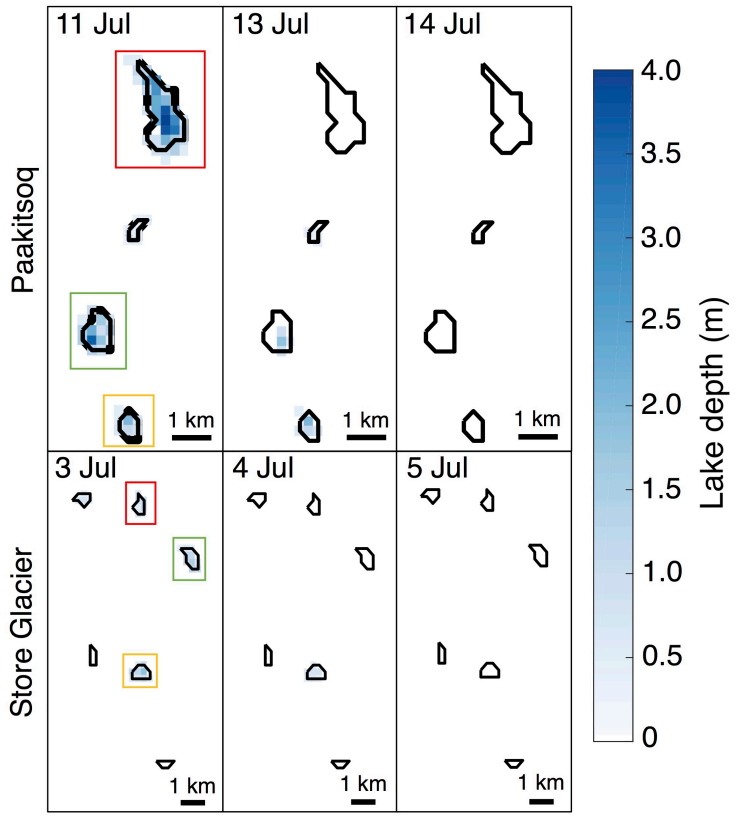



**Figure 3.14:** Clusters of rapidly draining lakes at Paakitsoq (top three panels) and Store Glacier (bottom three panels) identified by the FAST algorithm from MODIS imagery. The black outlines show the maximum extent of lakes and represent the areas within which the FAST algorithm tracked changes to lake area and volume over the full 2014 season. The area for Paakitsoq is equivalent to the area shown within the green box on Figure 3.5 (a) and the area for Store Glacier is equivalent to the area shown within the orange box on Figure 3.5 (b). For Paakitsoq, the lake contained within the large red box drains entirely between 11 July (coincident with its maximum water volume) and 13 July; the lakes within the smaller green and orange boxes drain entirely between 11 July (when they contain their maximum water volumes) and 14 July. For Store Glacier, the lakes within the red and green rectangular boxes drain entirely between 3 July and 4 July, and the lake within the square orange box drains rapidly between 3 July and 5 July; these three lakes all contain their maximum water volumes on 3 July.

Given that the twice-draining lake is found to reach a similar water volume before draining rapidly on two occasions ($2.2 \times 10^5 \pm 5.6 \times 10^7$ m$^3$ and $2.1 \times 10^5 \pm 5.6 \times 10^7$ m$^3$), a brief investigation is conducted into whether a critical water volume threshold related to local ice thickness can explain rapid drainage. However, no relationship is found between the lake water volume immediately prior to rapid drainage and the local ice thickness (Figure 3.15), suggesting that a universal critical water volume threshold required to initiate hydrofracture, which is dependent solely on the local ice thickness, does not exist across the GrIS. This is in line with the suggestion of previous workers that

factors other than simply local ice thickness will determine the lake water volume required to initiate hydrofracture and thus the rapid lake-drainage process (Banwell *et al.*, 2013a, 2016; Arnold *et al.*, 2014; Fitzpatrick *et al.*, 2014; Stevens *et al.*, 2015). The water volumes immediately prior to rapid lake drainage within the study regions are compared against the water volume that is required to initiate rapid hydrofracture beneath lakes identified by Krawczynski *et al.* (2009). They indicate that lakes with diameters ≥ 0.25 km (equivalent to areas ≥ 0.0491 km$^2$ if approximated as perfect circles) overlying sub-freezing ice of 1000 m thickness can initiate hydrofracture. This critical lake area value is scaled to lake volume using the area-to-volume scaling relationships identified for the two regions below. At Paakitsoq, all lakes meet or exceed this threshold, but at Store Glacier, many lakes drain with water volumes that are considerably below this threshold (Figure 3.15). This again indicates that the application of a universal critical water-volume threshold across the two regions is unlikely to be a robust explanatory variable for the prediction of hydrofracture, suggesting that one or several other factors may also be important. This finding led to the comprehensive investigation of a range of these possible factors in Chapter 4.

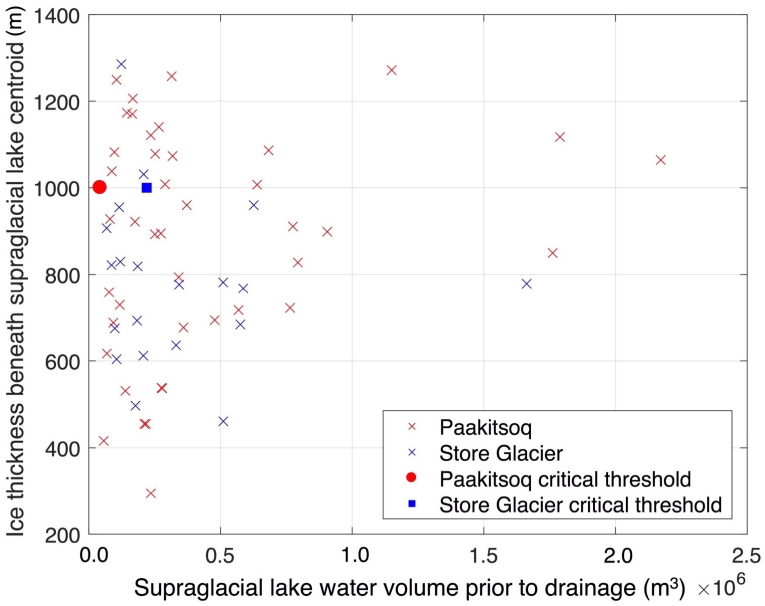



**Figure 3.15:** Scatterplot of lake water volumes immediately prior to drainage, and the ice thickness beneath lake centroids, for the two study sites. For Paakitsoq: $R^2 = 0.03$; for Store Glacier: $R^2 = 0.00$. Both $R^2$ values are not significant at the 95% confidence interval. The critical lake water volume thresholds required to initiate hydrofracture from Krawczynski *et al.* (2009) are also shown for the two regions.

## Lake area-to-volume scaling

Various studies assume that lake volume is strongly correlated with lake area in MODIS images and establish empirically-based lake area to volume scaling relationships, either by using area as a proxy for volume (Box and Ski, 2007; Morriss *et al.*, 2013), or by approximating lake basins as cones, with lake area as the independent variable within a non-linear relationship (Liang *et al.*, 2012). However, these studies lack a high number of data points: for example, Box and Ski's (2007) area-to-volume scaling relationship ($R^2 = 0.620$; $p < 0.01$) is based on only 31 data points. The results of this chapter permit lake area-to-volume scaling factors to be derived across the full melt season for the two regions of the GrIS, allowing the validity of the relationships established in previous work to be tested. For Paakitsoq, a lake area ($A_{SGL}$, km$^2$) to volume ($V_{SGL}$, m$^3$) scaling relationship ($n = 1114$) is established using a quadratic least-squares regression (Figure 3.16):

$$V_{SGL} = 575341\left(A_{SGL}{}^2\right) + 271187(A_{SGL}) + 89617. \quad (3.3)$$

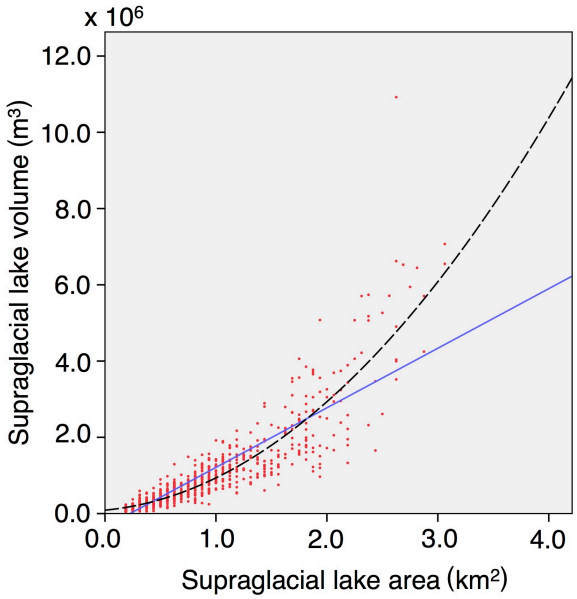



**Figure 3.16:** The Paakitsoq region lake area-to-volume scaling relationship. The black dashed line shows a quadratic least-squares regression, $y = 575341(x^2) + 271187(x) + 89617$, which is used for the lake area-to-volume scaling. The blue solid line shows an OLS linear regression, which is deemed inappropriate for lake area-to-volume scaling.

This quadratic least-squares lake area-to-volume scaling basis is stronger ($R^2 = 0.827$; $p < 0.01$; RMSE = $0.420 \times 10^6$ m$^3$) than an OLS linear regression relationship.

At Store Glacier, a similarly strong relationship ($n$ = 558) is obtained using an OLS linear regression (Figure 3.17):

$$V_{SGL} = 1191332(A_{SGL}) - 161311. \quad (3.4)$$

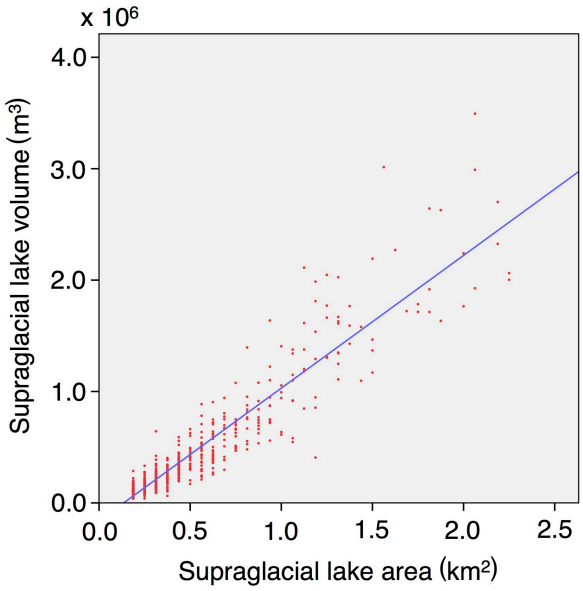



**Figure 3.17:** The Store Glacier region lake area-to-volume scaling relationship. The blue solid line shows an OLS linear regression, with equation $y = 1191332(x) - 161311$, which is used for the lake area-to-volume scaling.

Again, a strong relationship ($R^2$ = 0.869; $p < 0.01$; RMSE = 0.184 × $10^6$ $m^3$) is observed. Using a quadratic least-squares regression does not significantly improve the $R^2$ at Store Glacier, so the linear model is chosen.

This difference in the required regression model for the two regions is likely to be a result of the presence of shallower lakes at Store Glacier, perhaps due to a regional surface-topography control that limits lake depth. This could mean that for lakes with larger areas (i.e. > 2.5 $km^2$) at Store Glacier, the shallower depths can be better described with a linear relationship, whereas, at Paakitsoq, there is more scatter in the volume data for these higher lake area values since the lakes can become deeper. The low RMSE values for both regions are particularly encouraging given that lake area can only be resolved to within 0.0625 $km^2$ (i.e. one MODIS pixel) across the two regions, yet the lake volumes show relatively little spread for similar lake area values. Overall, these relationships indicate that lake area derived from MODIS imagery represents a valid proxy for volume, matching the findings of Morriss *et al.* (2013) who obtained a similarly high $R^2$. As an alternative to the polynomial regressions fitted here, a power-law regression may be able to explain

as much or more of the variance in the data, thus representing a possible avenue of future investigation.

## 3.6 Summary and conclusions

- Lakes on the GrIS are commonly investigated with satellite imagery, with the fine temporal-resolution MODIS record providing a valuable dataset since it has the potential to resolve dynamic changes to lake areas and volumes over daily to weekly timescales. Many MODIS-based studies have derived lake areas using semi- or fully-automated approaches and then tracked the evolution of lake areas across images; however, there has been little evaluation of the automatic methods used. Moreover, of the few studies that calculate both lake depths and volumes from MODIS data, none have tracked volumes between images, and so no previous studies have systematically identified the locations, timings and quantified the volumes of water entering the GrIS's internal hydrological system via rapidly draining lakes.
- In this chapter, the limitations of previous research identified above have been addressed through the development of the FAST algorithm, which is capable of tracking lake areas and volumes between MODIS images; this represents one of the most comprehensive lake-tracking algorithms to date. The FAST algorithm incorporates fully automatic (i) lake-area calculations and (ii) physically-based lake-depth calculations. Both of these approaches do not rely on field data for calibration, allowing for the widespread application of the FAST algorithm across the GrIS.
- To select the best approach for calculating lake areas, and to address the first aim of the chapter, three existing methods for deriving lake areas were evaluated, finding that dynamic thresholding applied to the MODIS red-band MOD09 surface-reflectance data, with a threshold value of 0.640, significantly outperformed other methods for calculating lake area, and could reproduce lake areas with high accuracy when compared with Landsat 8 lake areas and without threshold adjustment on a site- or lake-specific basis. Although lakes $< 0.125$ km$^2$ cannot be resolved with MODIS imagery, they accounted for $< 18\%$ of the total water-covered areas (as measured by MODIS) within both of the study regions, justifying the exploitation of MODIS's high temporal resolution to investigate GrIS hydrology.
- To incorporate fully-automated lake-depth calculations, and to address the second aim of this chapter, the physically-based methods of Sneed and Hamilton (2007), with updated physical parameters from Pope *et al.* (2016), were tested for MODIS, finding that the application of their method to the red-band data produced accurate lake depths and volumes

when compared with Landsat 8 values (RMSE for depth: 1.27 m; RMSE for volume: $5.9 \times 10^7$ $m^3$). These errors were comparable to those produced using empirically-based depth-retrieval methods applied to MODIS imagery (Fitzpatrick *et al.*, 2014). Moreover, the lake-depth calculations were only slightly less accurate than those derived using the same physically-based algorithm applied to higher-resolution sensors, such as Landsat 8: when comparing the RMSE for MODIS lake depth against Pope *et al.*'s (2016) RMSEs for Landsat 8 lake depths, the difference is < 1 m.

- For the third and fourth aims of this chapter, the best methods identified from the first two aims were incorporated into a new FAST algorithm, which was then applied to two study regions. In these regions, it successfully reproduced the expected patterns of lake evolution, including the identification of 62 rapid lake-drainage events, some drainage-event clustering across both regions, and the drainage, refilling and re-drainage of one lake in the Paakitsoq region. There was no statistically significant relationship between the rapidly draining lake water volumes identified by the FAST algorithm and the local ice thickness beneath the lakes. This indicated that factors other than the local ice thickness are likely to be important in controlling the lake water volume required to initiate hydrofracture, in line with previous research (Arnold *et al.*, 2014; Fitzpatrick *et al.*, 2014; Stevens *et al.*, 2015). This provides the context for the further research in Chapter 4.
- The FAST algorithm's main improvement on previous lake-tracking methods (e.g. Selmes *et al.*, 2011; Liang *et al.*, 2012) is its ability to calculate lake volumes automatically and then to track them across wide swathes of the GrIS. Given this, the high temporal resolution of the MODIS record can now be fully exploited to offer significant extensions to previous remotely-based calculations of lake depth and volume. Future work could focus on generating outputs from the FAST algorithm to investigate the locations, timings and water volumes of rapid lake-drainage events at the whole GrIS scale. Furthermore, the application of the FAST algorithm across large areas of the GrIS could allow water volumes reaching the subglacial drainage system across different regions, and in different years, to be calculated more effectively, which could help to offer better explanations for the observed patterns of intra- and inter-annual ice-velocity variations, and also form a valuable additional input dataset for coupled hydrology and ice-dynamic models.

# Chapter 4

# Controls on rapid supraglacial lake drainage on the Greenland Ice Sheet

## 4.1 Executive summary

The controls on rapid lake drainage on the GrIS remain uncertain, making it challenging to incorporate lake drainage into models of GrIS hydrology, and so to determine the ice-dynamic impact of meltwater reaching the ice-sheet bed. In this chapter, first the lake area and volume tracking algorithm presented in Chapter 3 is used to identify rapidly draining lakes and their water volumes prior to drainage within two land- and marine-terminating sectors of west Greenland during summer 2014. Second, hydrological, morphological, glaciological and SMB data are derived for various potential factors that may influence the incidence of rapid lake drainage. Third, these factors are used within an Exploratory Data Analysis statistical methodology to examine some of the existing hypotheses used to explain rapid lake drainage, as well as new ideas. This approach involves testing for statistical differences between the rapidly and non-rapidly draining lake types, as well as examining statistical associations between lake size and the various potential controlling factors. This analysis shows that the two lake types are statistically indistinguishable for almost all of the factors investigated, except lake area, where non-rapidly draining lakes are larger than rapidly draining ones. This adds support to the idea that the concept of a fracture-area threshold cannot be used as a reliable predictor of rapid lake drainage within models of GrIS surface hydrology. However, the results of this chapter also do not allow for the recommendation of an empirically-supported, deterministic alternative to the fracture-area threshold parameter.

## 4.2 Objective and aims

Following the development of a fully-automated method for lake tracking with MODIS, the overall objective of this chapter is to combine the outputs from the analysis in Chapter 3 with an examination of the potential controls on hydrofracture. These include hydrological and glaciological controls on rapid lake drainage suggested by previous research (Section 2.7; Table 2.5), as well a variety of other factors perceived as being potential controls on the location, timing and magnitude of rapid lake-drainage events. This objective is motivated by a lack of agreement within published literature on the causes of rapid lake drainage on the GrIS, stemming from the reasons outlined in Chapter 2 for the need to understand this process. The overall objective of this chapter is addressed using a rigorous, regional-scale statistical Exploratory Data Analysis (EDA), which is a technique to explore existing hypotheses, to re-evaluate them with new data, and perhaps to propose new hypotheses or to suggest future research directions (Tukey, 1977). The EDA focuses on two locations: the land-terminating Paakitsoq and the marine-terminating Store Glacier regions of west Greenland (Figures 2.15, 3.1 and 4.1), for the 2014 melt season. The analysis is conducted for a large sample of 213 lakes to determine whether the insights gained from previous field studies for individual lakes (e.g. Doyle *et al.*, 2013; Tedesco *et al.*, 2013; Stevens *et al.*, 2015) more widely apply. The EDA aims to:

1. Identify the distribution of rapidly and non-rapidly draining lake types within the two regions, including their areas, volumes and their drainage dates or the dates when they reach their maximum extent.
2. Derive data for a variety of potential controlling factors that may explain the observed distributions of the lake types within the regions.
3. Analyse whether there are statistically significant differences between the two lake types in terms of the potential controlling factors.
4. Analyse whether statistically significant correlations exist between the potential controlling factors and both lake areas or volumes for the two lake types.

Collectively, it is hoped that the analysis within this chapter might be capable of indicating links between one or multiple factors and the incidence of hydrofracture on the GrIS. If this were the case, existing models of the GrIS's surface hydrology, which include empirical methods to predict rapid lake drainage (based on fracture-area thresholds; Section 2.7), could be improved to include a more deterministic basis for predicting the incidence of hydrofracture.

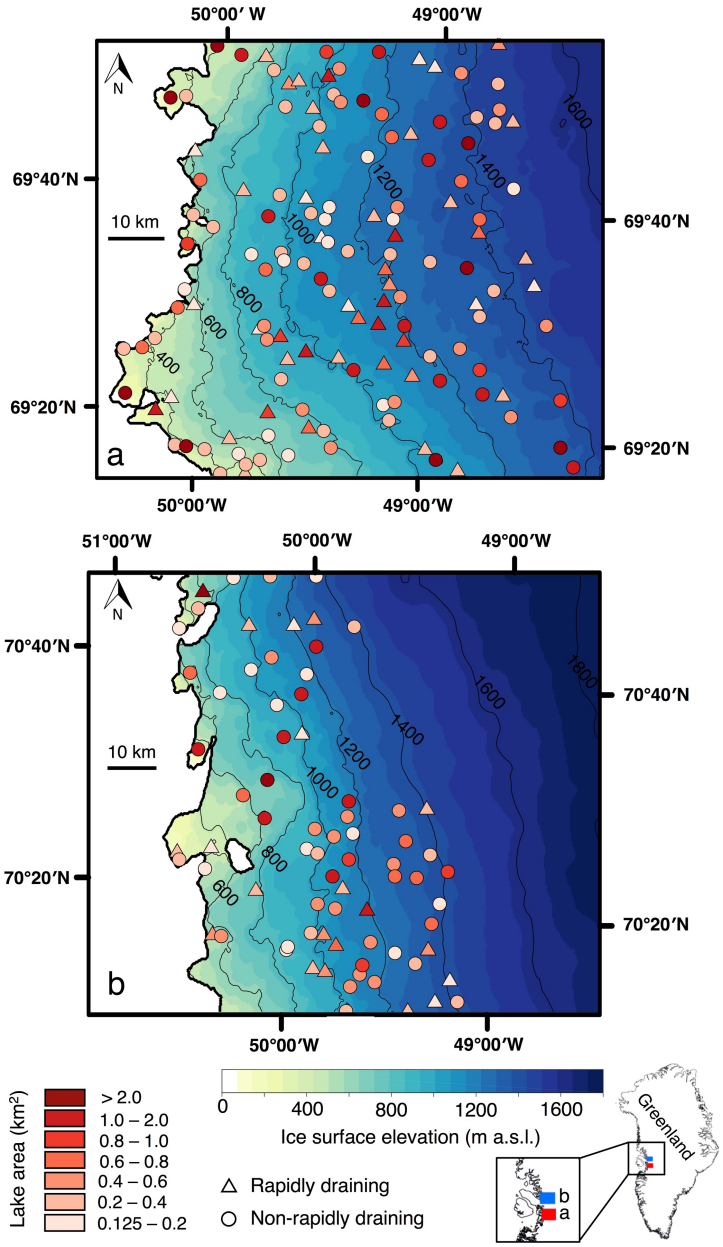



**Figure 4.1:** The (a) Paakitsoq and (b) Store Glacier regions of west Greenland (inset). Note the difference in horizontal scale between the two panels. Polygons indicate whether lakes observed in 2014 MODIS imagery drain rapidly (triangles; in ≤ 4 days) or not (circles; in > 4 days), colour-coded according to their area immediately prior to drainage for rapidly draining lakes and their area when reaching their maximum seasonal extents for non-rapidly draining lakes (Section 4.3.1). The GrIS margin (thick black line) and ice-surface elevation contours (thin black lines) from Howat *et al.* (2014) are shown.

# 4.3 Data and methods

This section describes: (i) the methods used to identify rapidly and non-rapidly draining lakes (Section 4.3.1); (ii) the original datasets used in the EDA, and the derivation of various factors from these data that may control the spatiotemporal patterns of rapid lake drainage, including the justification for including them (Section 4.3.2); (iii) the statistical techniques for the EDA (Section 4.3.3); and, (iv) the rationale for choosing the study sites (Section 4.3.4).

## 4.3.1 Identifying rapidly and non-rapidly draining lakes

For the first aim of this chapter, involving detecting rapid lake-drainage events and thus the distribution of rapidly draining and non-rapidly draining lakes, the FAST algorithm presented in Chapter 3 was used. For the purpose of this chapter, there were no specific adaptations to the algorithm compared with that in Chapter 3. As in Chapter 3, images derived from the MODIS MOD09 surface-reflectance product from 1 May to 30 September 2014 were chosen, totalling 153 images. Bands 1 (red; 0.620–0.670 μm) and 6 (1.628–1.652 μm) were required; band-1 data are distributed at native ~250 m resolution, while band-6 data have ~500 m resolution (Table 2.2). MODIS imagery was chosen to exploit the daily temporal resolution of the record, crucial for identifying rapid lake drainage since hydrofracture occurs in hours to days, although it was recognised that there was a trade-off with MODIS's lower spatial resolution (Leeson *et al.*, 2013; Miles, K. E. *et al.*, 2017; Chapter 3). Two lake types were recognised by the use of the FAST algorithm: lakes that drained rapidly at least once in the season, and non-rapidly draining lakes, which included lakes that: (i) drained slowly (losing ≤ 80% of their maximum seasonal water volume over ≤ 4 days or losing any water volume over ≥ 4 days); (ii) did not drain but simply froze towards the end of the melt season, and; (iii) were falsely classified as non-rapidly draining by the FAST algorithm due to cloud cover or false negatives within the MODIS record. Since Chapter 3 presents the extensive validation of the outputs from the FAST algorithm applied to MODIS imagery against Landsat 8 imagery (regarded as ground-truth data) for 2014 in the study regions, there was very high confidence in the data used here, including in the correct identification of rapid lake drainage.

## 4.3.2 Deriving potential controlling factors on rapid lake drainage

For the second aim of the chapter, various other datasets were acquired to calculate 21 additional factors that may potentially control rapid lake drainage, besides just lake areas and volumes (Table

4.1). The 23 factors were separated into four categories: (i) hydrological, (ii) morphological, (iii) glaciological, and (iv) SMB. Time-dependent factors were derived for the day of hydrofracture initiation for the rapidly draining lakes and for the day when the lake reached its maximum seasonal extent for the non-rapidly draining lakes. The motivations for exploring these factors, along with the methods for their derivation, are outlined in the following sections.

## Hydrological factors

Six hydrological factors (Table 4.1) were derived with the FAST algorithm (Section 4.3.1). The rationale for including these factors in the analysis was that previous research suggests a possible link between rapid lake drainage and the lake's area, volume, depth, or some combination thereof (Section 2.7). The standard deviation of lake water depth (in space) was included to investigate whether lakes with a more uniform depth were more likely to fracture and drain rapidly than those containing more variable depths (such as having a few locations with very deep water). The lake's mean filling rate was included due to the potential link between the rate of increase in the hydrostatic pressure head and the timing and/or occurrence of hydrofracture (e.g. van der Veen, 2007). For example, Tedesco *et al.* (2013) showed that a lake drained rapidly following an increased filling rate due to an overflowing lake upstream, although it is plausible that the lake's drainage simply resulted from the increased water volume within it.

## Morphological factors

Two morphological factors, lake eccentricity and orientation (Table 4.1), were derived using MATLAB's 'regionprops' function, which involved best-fitting an ellipse to the lake outline, as described in Banwell *et al.* (2014) (Figure 4.2). The eccentricity is a ratio that describes how closely a lake resembles a circle, and the orientation is the angle of the lake's long axis relative to the orientation of the average ice flow (ascertained with the ice-velocity dataset described below). These morphological properties were investigated since different patterns of normal stress at the lake bottom (induced by the water) with respect to the surface horizontal stress field of the ice (induced by ice flow) might make it more or less likely for hydrofracture to be initiated.

**Table 4.1:** Potential controlling factors on hydrofracture investigated in this chapter. Hydrological and morphological data are at the individual lake scale (i.e. up to several kilometres), glaciological data are at the scale of the ice underlying or adjacent to lakes (i.e. up to tens of kilometres), while SMB data cover synoptic-scale processes typically operating across the entire regions (i.e. tens of kilometres).

| Data category | Potential controlling factor | Dimensions | Data source or method | Notes |
|---|---|---|---|---|
| Hydrological | Lake area | $km^2$ | Chapter 3 | RMSE: 0.323 $km^2$ |
| Hydrological | Lake volume | $m^3$ | Chapter 3 | RMSE: $5.9 \times 10^7$ $m^3$ |
| Hydrological | Mean lake water depth | m | Chapter 3 | RMSE: 0.29 m |
| Hydrological | Maximum lake water depth | m | Chapter 3 | RMSE: 0.29 m |
| Hydrological | Standard deviation of lake water depth (in space) | m | Chapter 3 | |
| Hydrological | Lake mean filling rate | $m^3 s^{-1}$ | Chapter 3 | Over previous 5 days |
| Morphological | Lake eccentricity | – | Banwell *et al.* (2014) | |
| Morphological | Lake orientation | ° | Banwell *et al.* (2014) | W.r.t. ice-flow direction[1] |
| Glaciological | Ice-surface elevation | m a.s.l. | Howat *et al.* (2014) | At lake's centroid |
| Glaciological | Ice-bed elevation | m a.s.l. | Morlighem *et al.* (2014) | At lake's centroid |
| Glaciological | Ice-sheet thickness | m | Ice surface minus bed elevation | At lake's centroid |
| Glaciological | Ice-surface slope[2] | ° | ArcGIS 'Slope' tool | Across lake basin[3] |
| Glaciological | Background winter ice velocity | $m\ a^{-1}$ | Joughin *et al.* (2010, 2016) | Across lake basin |
| Glaciological | Principal ice-surface strain rate | $a^{-1}$ | Poinar *et al.* (2015) | Across lake basin |
| Glaciological | von Mises yield criterion | Pa | Clason *et al.* (2015) | Across lake basin |
| SMB | Melt within catchment[4] on day | $m^3$ w.e. | Noël *et al.* (2016) | |
| SMB | Melt within catchment on previous day | $m^3$ w.e. | Noël *et al.* (2016) | |
| SMB | Rain within catchment on day | $m^3$ w.e. | Noël *et al.* (2016) | |
| SMB | Rain within catchment on previous day | $m^3$ w.e. | Noël *et al.* (2016) | |
| SMB | Cumulative melt in catchment | $m^3$ w.e. | Noël *et al.* (2016) | |
| SMB | Cumulative rain in catchment | $m^3$ w.e. | Noël *et al.* (2016) | |
| SMB | Cumulative runoff in catchment | $m^3$ w.e. | Noël *et al.* (2016) | Melt plus rain |
| SMB | Difference between cumulative catchment runoff and lake volume | $m^3$ w.e. | | Runoff minus volume |

[1] Average ice flow derived from *x* and *y* components of MEaSUREs winter ice-velocity data.
[2] Derived from ice-surface elevation data, which were first coarsened to 1 km resolution to ensure slopes were derived across rather than within lake basins, then interpolated (using a nearest-neighbour technique) to 250 m resolution for consistency with the other data.
[3] Lake basin is defined as the lake area at the lake's maximum extent (for non-rapidly draining lakes) or on the day prior to hydrofracture (for rapidly draining lakes).
[4] Catchment refers to a lake's ice-surface catchment, determined with MATLAB's 'watershed' function (using a default eight-connected neighbourhood).

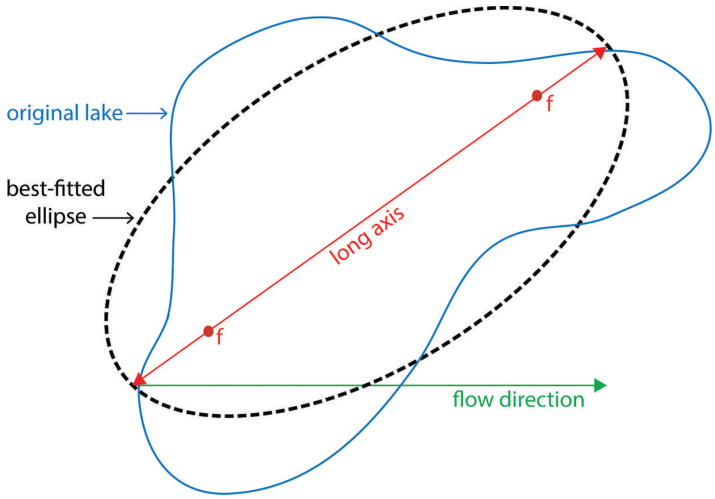



**Figure 4.2:** A best-fitted ellipse using the MATLAB 'regionprops' function for a lake outline ("f" = foci), with the lake outline determined from the maximum lake extent over the summer season. The function ensures that the ellipse and the original lake are of the same area. The eccentricity then measures how closely the lake outline resembles a circle. The orientation of the lake is derived by comparing the lake's long axis (red line) against the average flow direction (green line) derived from the $x$ and $y$ components of the Making Earth System data records for Use in Research Environments (MEaSUREs) winter velocity data. Reproduced from Banwell *et al.* (2014).

## Glaciological factors

Seven glaciological factors (Table 4.1) were included to investigate how the properties of the ice, including the horizontal velocity field around a lake (used to calculate the local stress and strain rates), and the local ice-sheet topography, might influence lake-drainage potential. Since high temporal resolution velocity data were unavailable for summer 2014, the background (long-term, steady-state) winter ice-velocity data were used from the MEaSUREs multi-year mosaic (Joughin *et al.*, 2010, 2016) to calculate the principal ice-surface strain rate ($\dot{\varepsilon}$) and the von Mises yield criterion ($\sigma_V$).

To calculate the ice-surface principal strain rate, $\dot{\varepsilon}$, the methods of Poinar *et al.* (2015) were used; these involved differencing the 250 m resolution ice-velocity data to derive the strain rate tensor ($\dot{\varepsilon}_{ij}$), and then calculating $\dot{\varepsilon}$ following Cuffey and Paterson (2010):

$$\dot{\varepsilon} = \frac{\partial u}{\partial x}\cos^2\theta + \frac{\partial v}{\partial y}\sin^2\theta, \tag{4.1}$$

with $\theta$ derived by:

$$\theta = \frac{1}{2}\tan^{-1}\left(\frac{\frac{\partial u}{\partial y}+\frac{\partial v}{\partial x}}{\frac{\partial u}{\partial x}+\frac{\partial v}{\partial y}}\right). \quad (4.2)$$

To calculate the von Mises yield criterion, $\sigma_V$, the methods of Clason *et al.* (2015) were followed. The strain-rate tensor was first derived as above, and from this, the second invariant or the effective strain rate ($\dot{\mathcal{E}}_E$) was calculated, which measures the total magnitude of the tensor's diagonal components (Cuffey and Paterson, 2010). These values were then used to derive the stress tensors ($\sigma_{ij}$) using Nye's (1957) constitutive relation:

$$\sigma_{ij} = A^{[-1/N]}\dot{\mathcal{E}}_E^{(1-N)/N}\dot{\mathcal{E}}_{ij}, \quad (4.3)$$

where $A$ is the creep factor, which was assigned as $9.3 \times 10^{-16}$ $s^{-1}$ $kPa^{-3}$, consistent with ice at -5 °C for a creep exponent ($N$) that was set at 3 (Cuffey and Paterson, 2010). The stress tensors were then used to derive $\sigma_V$:

$$\sigma_V = (\sigma_1\sigma_1) + (\sigma_3\sigma_3) - (\sigma_1\sigma_3), \quad (4.4)$$

where $\sigma_1$ and $\sigma_3$ represented the maximum and minimum principal stresses, respectively. These were calculated with:

$$\sigma_1 = \sigma_{max} = \frac{1}{2}\left(\sigma_{xx} + \sigma_{yy}\right) + \sqrt{\left[\frac{1}{2}(\sigma_{xx} - \sigma_{yy})\right] + \tau_{xy}^2} \quad (4.5)$$

and

$$\sigma_3 = \sigma_{min} = \frac{1}{2}\left(\sigma_{xx} + \sigma_{yy}\right) + \sqrt{\left[\frac{1}{2}(\sigma_{xx} - \sigma_{yy})\right] + \tau_{xy}^2}, \quad (4.6)$$

where $\sigma_{xx}$, $\sigma_{yy}$ and $\tau_{xy}$ were the longitudinal, transverse and shear stresses, respectively.

In this analysis, positive $\dot{\mathcal{E}}$ values indicated areas of extension, while negative ones indicated areas of compression; higher $\sigma_V$ values indicated areas undergoing the most tension or where two surface parallel principal stresses were both compressive (Vaughan, 1993; Clason *et al.*, 2015).

### Surface-mass-balance factors

To investigate the relation of rapid lake drainage to SMB processes, Noël *et al.*'s (2016) downscaled daily 1 km resolution RACMO2.3 climate-model output data for the GrIS from summer 2014 were used to derive eight potential SMB controlling factors (Table 4.1). These data were used to explore whether the quantity of melt and precipitation within a lake's ice-surface catchment influence rapid drainage. This may be important because, for example, Stevens *et al.* (2015) provide evidence that water input through crevasses to the ice-sheet bed at a location proximal to a rapidly draining lake's site is an important precursor to drainage (Section 2.7). Melt, rain and runoff data were assembled for lake catchments on the day of drainage for rapidly draining lakes and on the day of the lake's maximum extent for non-rapidly draining lakes. In addition, these data were assembled for the day previously, as well as the cumulative seasonal totals up to that point. Finally, calculations were made of the difference between a lake's volume at its maximum extent (for non-rapidly draining lakes) or on the day prior to its drainage (for rapidly draining lakes) and the cumulative total runoff volume (i.e. melt plus rain) within the ice-surface catchment up to those dates. The rationale here was that a big discrepancy between these two volumes would imply that large amounts of water might have previously entered the GrIS via crevasses or pre-existing moulins near to the lake, which could have reached the ice-sheet bed, initiating basal uplift or sliding, and thereby increasing the propensity for hydrofracture (e.g. Stevens *et al.*, 2015).

## 4.3.3 Exploratory Data Analysis techniques

For the third and fourth aims of the research, the EDA branch of statistical analysis was used (Tukey, 1977) to explore the existing hypotheses of rapid lake drainage, to re-evaluate them in the context of the new datasets, and perhaps to suggest new ones that better explain the observations (Tukey, 1977). EDA contrasts with confirmatory analysis, which involves testing only specific hypotheses, and deterministic analysis, which involves formulating statistical models. EDA is thus an important analytical step to help determine whether statistical models might be devised from the data, which, in this context, could assist in the formulation of better physically-based models for predicting rapid lake drainage on the GrIS. Here, EDA was used to test for statistical differences and associations as described in the following two sections.

## Statistical tests for difference

For the third aim of this chapter, the analysis involved testing for statistically-significant differences between the rapidly draining and non-rapidly draining lake types to determine if the lakes were drawn from the same population. This was partly used to examine whether the potential controls on hydrofracture were able to account for the observed regional distributions of the two lake types. First, a univariate parametric analysis was conducted: this involved a series of unpaired Student's two-sample *t*-tests for each of the potential controlling factors for the two data samples (i.e. rapidly draining and non-rapidly draining lakes), with significance tested at the 95% confidence interval ($p < 0.05$) in view of the many data points (213) involved. None of the data were normally distributed (verified using the Kolmogorov-Smirnov test with 95% confidence) but since the sample size was high (> 50) for both the rapidly draining and non-rapidly draining lake samples, the Student's two-sample *t*-test could be used.

The second stage involved multivariate principal component analysis (PCA). PCA was used to determine whether the rapidly draining and non-rapidly draining lake types could be distinguished based on a combination of the potential controlling factors (Table 4.1). PCA involves removing collinearity between variables in a dataset, collapsing the data into a set of components that show the maximum amount of variance within the data (Jolliffe, 2002). This technique has been used previously in glaciology, for example, to pre-process different spectral bands of satellite imagery prior to glacier-surface classification (Pope and Rees, 2014a, 2014b), to map ice flow (Fahnestock *et al.*, 2016), or to examine the metrics of palaeo-subglacial channels in Antarctica (Kirkham, 2017). It is also widely used in other geosciences disciplines for collapsing complex data into simpler components, commonly with satellite imagery (e.g. de Almeida *et al.*, 2015; Dronova *et al.*, 2015; Luo *et al.*, 2016; Zhao *et al.*, 2016; Licciardi and Chanussot, 2018). The first three principal components (PCs) were examined, with each subsequent PC accounting for progressively decreasing data variance, and positioned orthogonal to the previous PC (Ringnér, 2008). Since the potential controlling variables were measured at different scales and had different dimensions, the data were first normalised and rendered dimensionless using the inverse variable variances as weights. PCA involved two stages: first, it was undertaken separately for each category of factor from Table 4.1 (i.e. hydrological, morphological, glaciological and SMB) and, second, it was conducted for all the potential controlling factors listed in Table 4.1 at once. During the first step, the morphological factors were grouped with the hydrological factors because there were only two morphological variables and, if they had not been included within another category, they could not have been incorporated into the PCA; it was also most obvious to group these two categories of

controlling factor together since they both represented data collected at the local lake scale. For each stage of analysis, once the individual PCs were identified, the scores for the first three PCs for each lake were determined and projected in the new coordinate space; if the two lake types were statistically different based on the groups of controlling factors, they would visibly cluster within specific areas of the PCA plots. Finally, for each stage of PCA, this clustering was also assessed quantitatively for the rapidly draining and non-rapidly draining lakes by testing for statistical differences between the first three PCs using unpaired two-sample Student's $t$-tests (again, verified at the 95% confidence interval).

### Statistical tests for association

The next part of the EDA, and the fourth aim of this chapter, comprised formulating bivariate linear correlation relationships to determine whether there were statistically-significant associations between the lake areas or volumes of rapidly and non-rapidly draining lakes and the other factors, and how these associations differed between the lake types. The objectives here included determining whether a critical lake area or volume was needed for hydrofracture that scaled with any of the other potential controlling factors, and therefore also identifying any linear regression relationships between the various controlling factors, for example to see if greater lake volumes need to be reached for thicker ice or for more compressive ice flow. Since the data were not normally distributed, the relationships were assessed using the Spearman's rank correlation coefficient ($\rho$), rather than the Pearson product-moment correlation coefficient, with statistical significance checked with 95% confidence (Weisberg, 2005).

## 4.3.4 Study sites

As in Chapter 3, the analysis was conducted for two sites in west Greenland (Figures 2.15 and 4.1): (a) the Paakitsoq land-terminating region, and (b) the marine-terminating region surrounding Store Glacier. The 213-lake sample across these two regions in 2014 represented just under 20% of the 1126 lakes mapped with MODIS across the whole of south-west Greenland in 2005–2009 (Selmes *et al.*, 2011). This led to confidence that the sample represented the wider population of lakes. Both regions were similarly sized, extending ~70 km latitudinally, and ~80 km inland, to ensure that the highest-elevation lakes were included in the record. Because the data were from 2014, which was regarded a climatically normal year (van den Broeke *et al.*, 2016) without extreme weather, the results should apply to other years too.

## 4.4 Results

### 4.4.1 Distribution of rapidly and non-rapidly draining lakes

The first aim of this chapter was to identify the distribution of rapidly and non-rapidly draining lakes within the two regions, including their areas, volumes and their drainage dates or the dates when they reach their maximum extent. These results are shown in Figures 4.1, 4.3 and 4.4, respectively. Within Paakitsoq, 48 rapidly draining and 90 non-rapidly draining lakes are identified, and at Store Glacier, 21 rapidly draining and 54 non-rapidly draining lakes are identified. There is no obvious variation in lake area or volume by elevation band. However, non-rapidly draining lakes seem to have, on average, larger areas than rapidly draining lakes (Figure 4.1), even though the volumes appear more similar (Figure 4.3); these patterns are verified statistically later (Section 4.4.2). Figure 4.4 shows, as in previous studies (e.g. Doyle *et al.*, 2013; Fitzpatrick *et al.*, 2014; Miles, K. E. *et al.*, 2017), an upglacier progression of rapid lake drainage over the season within both study regions although there are exceptions, with some lower-elevation lakes draining uncharacteristically late in the season.

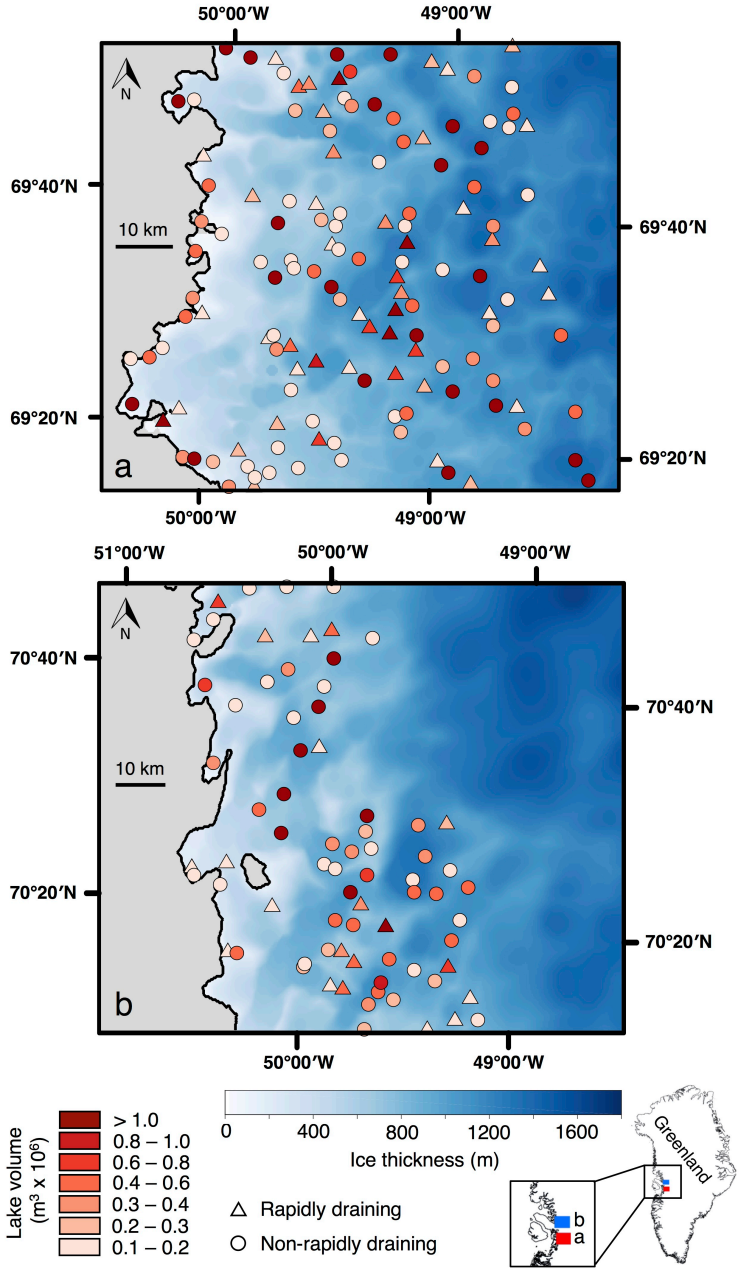



**Figure 4.3:** The locations of rapidly draining (triangles) and non-rapidly draining (circles) lakes within the (a) Paakitsoq and (b) Store Glacier regions of west Greenland (inset) overlying the background ice thickness (m) from Morlighem *et al.* (2014). Note the difference in horizontal scale between the two panels. Colour-coding shows lake water volumes immediately prior to drainage for rapidly draining lakes and the water volumes when lakes reached their maximum extent for non-rapidly draining lakes. The thick black lines on both panels delineate the GrIS margin from Howat *et al.* (2014).

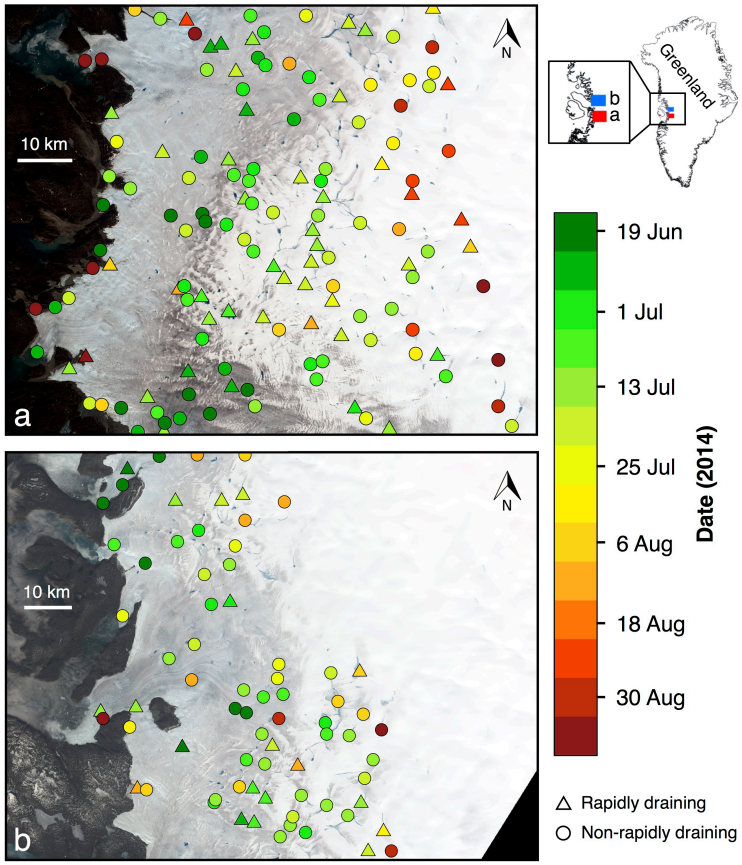



**Figure 4.4:** The dates on which rapidly draining lakes (triangles) drain and the dates on which non-rapidly draining lakes (circles) reach their maximum extents in the (a) Paakitsoq and (b) Store Glacier regions within west Greenland (inset), highlighting the similarity between the two sets of dates. Note the difference in horizontal scale between the two panels. Panels are equivalent to those in Figures 4.1, 4.3, 4.10 and 4.11. The extreme early and late colourbar values include dates outside of those shown (i.e. from 1 May to 18 June, and from 6 September to 30 September, respectively). Note that most of the lakes shown on the images are included in the analysis, but that some of the smaller lakes are omitted, particularly at Paakitsoq; for further details, see Chapter 3. The backgrounds are true-colour Landsat 8 images from (a) 3 July 2014 and (b) 1 July 2014 (see Table A.1 for image details).

The data from both regions are grouped to form a single large sample of 69 rapidly draining lakes and 144 non-rapidly draining lakes, in order to represent a sample of the entire population of lakes in west Greenland (Selmes *et al.*, 2011). Tables 4.2 and 4.3 and Figures 4.5–4.8 show that, in the case of both ice-surface-elevation and ice-thickness bands for lakes grouped by area and volume, more lakes drain rapidly at a given elevation or for a specific ice thickness simply because the total number of lakes in that band is greater. This demonstrates that there is no bias towards rapid lake drainage occurring above certain ice thicknesses or at specific ice-surface elevations. Furthermore,

Tables 4.2 and 4.3 suggest that there is no association between ice thickness or ice-surface elevation and the area or volume of lakes for both the rapidly and non-rapidly draining types, which is verified statistically later (Section 4.4.3).

**Table 4.2:** The distribution of rapidly draining (RD) and non-rapidly draining (NRD) lakes by ice-surface-elevation and ice-thickness bands, with lakes grouped according to their areas. These data are presented as grouped bar charts in Figures 4.5 and 4.6.

| | **Lake area (km$^2$)** | | | | | | | | | | | | | | |
|---|---|---|---|---|---|---|---|---|---|---|---|---|---|---|---|
| | 0.125–0.2 | | 0.2–0.4 | | 0.4–0.6 | | 0.6–0.8 | | 0.8–1.0 | | 1.0–2.0 | | > 2.0 | | *Total* |
| **Ice-surface elevation (m a.s.l.)** | RD | NRD | RD | NRD | RD | NRD | RD | NRD | RD | NRD | RD | NRD | RD | NRD | |
| < 400 | 1 | 2 | 4 | 7 | – | – | – | 2 | – | 1 | 1 | 1 | – | 3 | *22* |
| 400–600 | 2 | 2 | 1 | 4 | 1 | 1 | – | 3 | – | – | – | 2 | 1 | 1 | *18* |
| 600–800 | 1 | 3 | 1 | 3 | – | 1 | – | 1 | 1 | – | – | – | – | 1 | *12* |
| 800–1000 | 2 | 8 | 8 | 11 | 3 | 6 | – | 1 | 1 | 1 | 2 | 3 | – | – | *46* |
| 1000–1200 | 3 | 7 | 3 | 7 | 2 | 11 | 4 | 1 | 1 | 2 | 3 | 7 | – | 2 | *53* |
| 1200–1400 | 5 | 4 | 5 | 6 | 2 | 6 | 1 | 7 | – | 2 | 1 | 5 | – | 3 | *47* |
| > 1400 | 2 | 1 | 3 | 5 | 1 | 2 | – | – | – | 1 | – | – | – | – | *15* |
| *Total* | *16* | *27* | *25* | *43* | *9* | *27* | *5* | *15* | *3* | *7* | *7* | *18* | *1* | *10* | *213* |
| | **Lake area (km$^2$)** | | | | | | | | | | | | | | |
| | 0.125–0.2 | | 0.2–0.4 | | 0.4–0.6 | | 0.6–0.8 | | 0.8–1.0 | | 1.0–2.0 | | > 2.0 | | *Total* |
| **Ice thickness (m)** | RD | NRD | RD | NRD | RD | NRD | RD | NRD | RD | NRD | RD | NRD | RD | NRD | |
| < 200 | 3 | 3 | 3 | 6 | 1 | 1 | – | 2 | – | 2 | 1 | 2 | – | 2 | *26* |
| 200–400 | 1 | 1 | 4 | 6 | – | – | – | 1 | – | – | – | – | – | 2 | *15* |
| 400–600 | 1 | 1 | 2 | 2 | – | 1 | – | 2 | 1 | – | – | 2 | 1 | – | *13* |
| 600–800 | 3 | 11 | 6 | 10 | 4 | 6 | 2 | 1 | 1 | 1 | 1 | 3 | – | 1 | *50* |
| 800–1000 | 4 | 8 | 6 | 8 | 1 | 11 | 1 | 1 | 1 | 1 | 2 | 6 | – | 1 | *51* |
| 1000–1200 | 2 | 2 | 6 | 7 | 3 | 4 | 2 | 3 | – | 4 | 2 | 3 | – | 1 | *39* |
| > 1200 | 2 | 1 | – | 2 | – | 4 | 1 | 4 | – | – | 1 | 2 | – | 3 | *20* |
| *Total* | *16* | *27* | *27* | *41* | *9* | *27* | *6* | *14* | *3* | *8* | *7* | *18* | *1* | *10* | *213* |

**Table 4.3:** The distribution of RD and NRD lakes by ice-surface-elevation and ice-thickness bands, with lakes grouped according to their water volumes. These data are presented as grouped bar charts in Figures 4.7 and 4.8.

| | **Lake volume (× $10^6$ $m^3$)** | | | | | | | | | | | | | | |
|---|---|---|---|---|---|---|---|---|---|---|---|---|---|---|---|
| **Ice-surface elevation (m a.s.l.)** | 0.1–0.2 | | 0.2–0.3 | | 0.3–0.4 | | 0.4–0.6 | | 0.6–0.8 | | 0.8–1.0 | | > 1.0 | | *Total* |
| | RD | NRD | RD | NRD | RD | NRD | RD | NRD | RD | NRD | RD | NRD | RD | NRD | |
| < 400 | 3 | 6 | 2 | – | – | 4 | – | 3 | – | – | 1 | 1 | 1 | 3 | *24* |
| 400–600 | 4 | 4 | – | 1 | – | 1 | – | 3 | 1 | 1 | – | – | – | 3 | *18* |
| 600–800 | 3 | 5 | 2 | – | – | – | – | – | 1 | – | – | – | – | 1 | *12* |
| 800–1000 | 6 | 15 | 3 | 6 | 2 | 3 | 3 | 1 | – | – | 1 | – | 1 | 5 | *46* |
| 1000–1200 | 3 | 9 | 2 | 5 | 3 | 3 | 1 | 8 | 4 | 2 | – | 1 | 3 | 9 | *53* |
| 1200–1400 | 7 | 9 | 2 | 2 | 2 | 7 | 1 | 7 | 1 | – | – | – | 1 | 8 | *47* |
| > 1400 | 4 | 6 | – | – | – | – | – | 3 | – | – | – | – | – | – | *13* |
| *Total* | *30* | *54* | *11* | *14* | *7* | *18* | *5* | *25* | *7* | *3* | *2* | *2* | *6* | *29* | *213* |

| | **Lake volume (× $10^6$ $m^3$)** | | | | | | | | | | | | | | |
|---|---|---|---|---|---|---|---|---|---|---|---|---|---|---|---|
| **Ice thickness (m)** | 0.1–0.2 | | 0.2–0.3 | | 0.3–0.4 | | 0.4–0.6 | | 0.6–0.8 | | 0.8–1.0 | | > 1.0 | | *Total* |
| | RD | NRD | RD | NRD | RD | NRD | RD | NRD | RD | NRD | RD | NRD | RD | NRD | |
| < 200 | 7 | 5 | – | – | – | 5 | – | 4 | – | – | – | – | 1 | 3 | *25* |
| 200–400 | 2 | 6 | 3 | 1 | – | – | – | 1 | – | – | – | – | – | 2 | *15* |
| 400–600 | 2 | 4 | 2 | – | – | – | – | 1 | 1 | 1 | – | – | – | 2 | *13* |
| 600–800 | 6 | 18 | 1 | 5 | 3 | 2 | 5 | 2 | 1 | 1 | – | – | 1 | 5 | *50* |
| 800–1000 | 6 | 11 | 2 | 5 | 2 | 5 | – | 6 | 3 | 1 | 1 | – | 1 | 8 | *51* |
| 1000–1200 | 5 | 6 | 5 | 3 | 1 | 3 | – | 7 | 2 | – | – | 1 | 2 | 4 | *39* |
| > 1200 | 2 | 4 | – | – | 1 | 3 | – | 4 | – | – | – | – | 1 | 5 | *20* |
| *Total* | *30* | *54* | *13* | *14* | *7* | *18* | *5* | *25* | *7* | *3* | *1* | *1* | *6* | *29* | *213* |

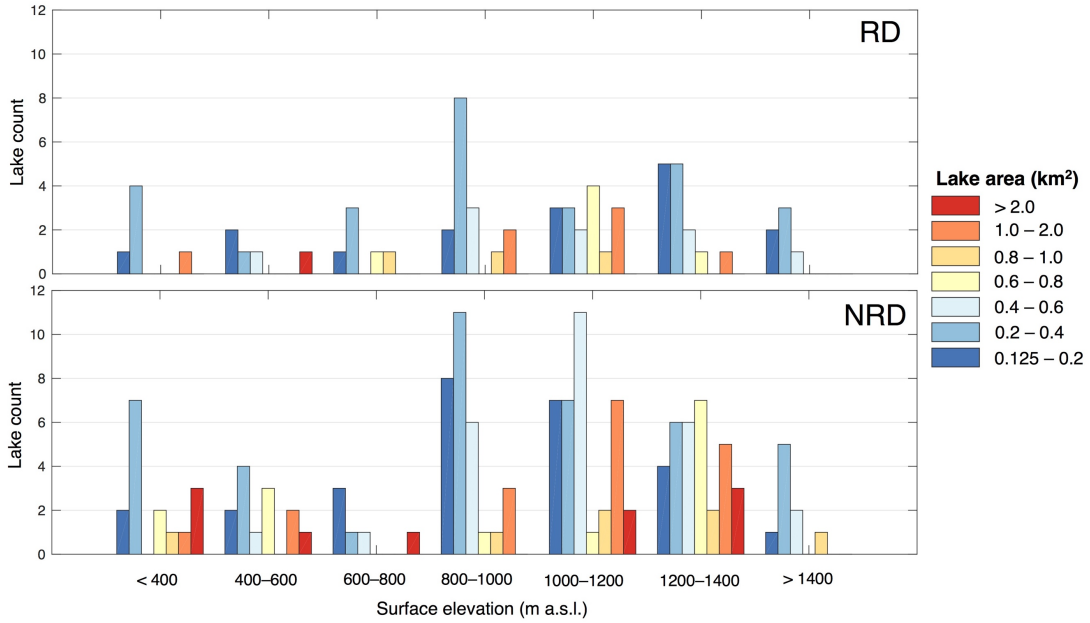



**Figure 4.5:** The distribution of RD and NRD lakes by surface-elevation band (from Howat *et al.*, 2014), colour-coded by lake area immediately prior to drainage for the RD lakes and by lake area when lakes reach their maximum extent for the NRD lakes.

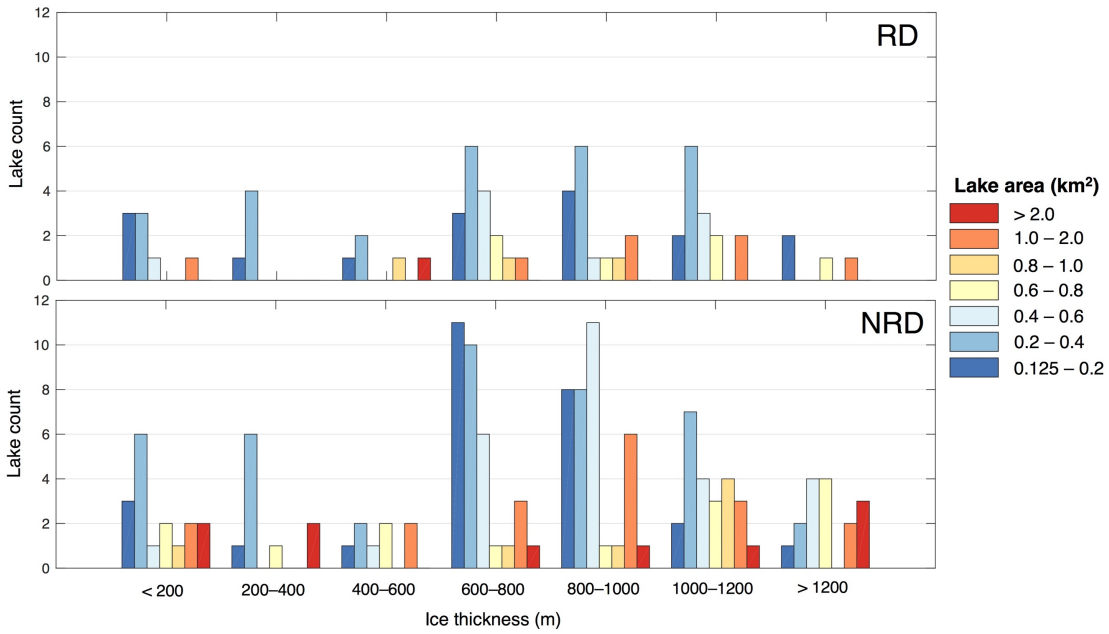



**Figure 4.6:** The distribution of RD and NRD lakes by ice-thickness band (from Morlighem *et al.*, 2014), colour-coded by lake area immediately prior to drainage for RD lakes and by lake area when lakes reach their maximum extent for NRD lakes.

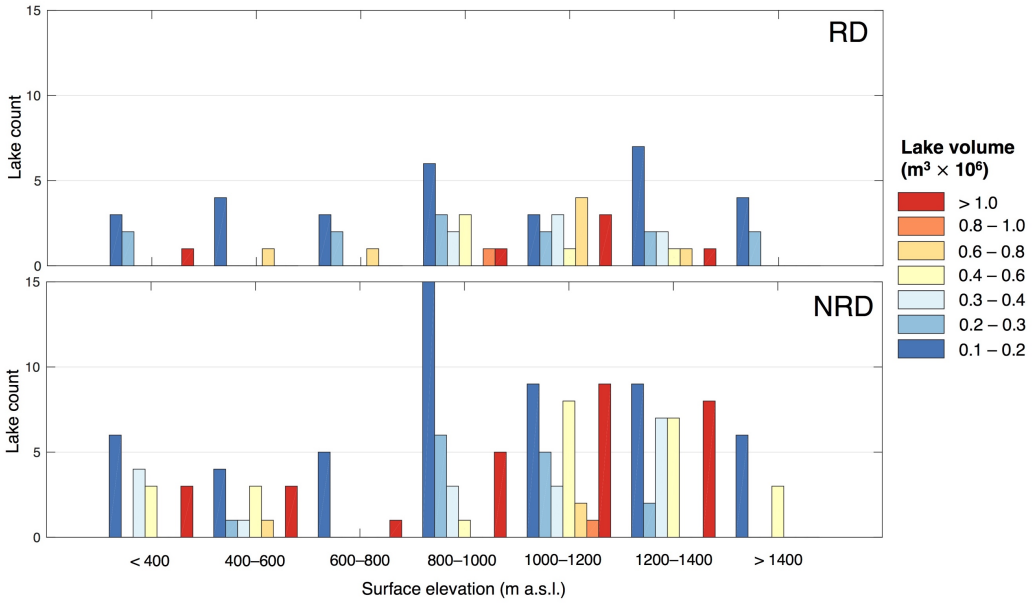



**Figure 4.7:** The distribution of RD and NRD lakes by surface-elevation band (from Howat *et al.*, 2014), colour-coded by lake volume prior to drainage for the RD lakes and by lake volume when lakes reach their maximum extent for the NRD lakes.

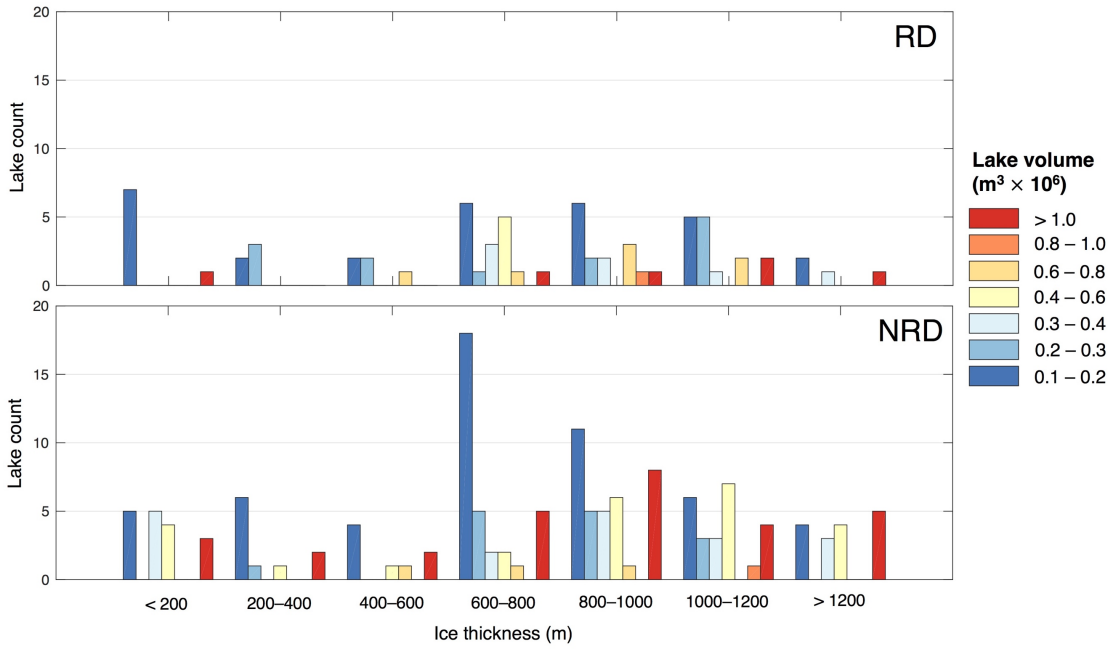



**Figure 4.8:** The distribution of RD and NRD lakes by ice-thickness band (from Morlighem *et al.*, 2014), colour-coded by the lake volume immediately prior to drainage for RD lakes and by lake volume when lakes reach their maximum extent for NRD lakes.

### 4.4.2 Differences in potential controlling factors between rapidly and non-rapidly draining lakes

The second aim of this chapter was gathering data for other potentially controlling factors on hydrofracture (Table 4.1) and the third aim was to analyse whether these factors could explain the distributions of rapidly draining and non-rapidly draining lakes, and so to examine the differences in the factors between the lake types. First, the two lake types are compared qualitatively using boxplots (Figure 4.9) and statistically using unpaired Student's *t*-tests (Table 4.4).

**Table 4.4:** Results of unpaired two-sample Student's *t*-tests (degrees of freedom = 211) for the potential controlling factors for the RD and NRD lake types. *t*-test results that are statistically significant at above the 95% confidence interval (i.e. $p < 0.05$) are highlighted in bold text; *p* value marked with an asterisk narrowly misses the 95% confidence interval, being significant at only the 94.6% confidence interval. Refer to Table 4.1 for dimensions of variables.

| Potential controlling factor | RD lake mean | NRD lake mean | *t* value | *p* value |
|---|---|---|---|---|
| Lake volume | $4.1 \times 10^5$ | $7.4 \times 10^5$ | -1.934 | 0.054* |
| Lake area | **0.47** | **0.69** | **-2.261** | **0.025** |
| Ice thickness | 752 | 764 | -0.234 | 0.815 |
| Ice-surface elevation | 978 | 964 | 0.271 | 0.786 |
| Ice-bed elevation | 226 | 200 | 1.104 | 0.271 |
| Lake eccentricity | 0.74 | 0.73 | 0.215 | 0.830 |
| Lake orientation | 41 | 38 | 0.595 | 0.553 |
| Maximum lake water depth | 1.29 | 1.35 | -0.432 | 0.666 |
| Mean lake water depth | 0.77 | 0.80 | -0.449 | 0.654 |
| Standard deviation of lake water depth | 0.31 | 0.32 | -0.225 | 0.822 |
| Lake mean filling rate | 3.66 | 3.99 | -0.271 | 0.787 |
| Ice-surface slope | 1.40 | 1.61 | -1.001 | 0.318 |
| Background winter ice velocity | 346 | 240 | 1.300 | 0.195 |
| Principal strain rate | 0.04 | 0.00 | 1.510 | 0.132 |
| von Mises yield criterion | $4.3 \times 10^4$ | $4.4 \times 10^4$ | -0.075 | 0.940 |
| Melt within catchment† on day | $1.4 \times 10^6$ | $1.9 \times 10^6$ | -0.792 | 0.429 |
| Rain within catchment† on day | $1.9 \times 10^5$ | $2.9 \times 10^4$ | 1.440 | 0.151 |
| Melt within catchment† on previous day | $1.4 \times 10^6$ | $1.8 \times 10^6$ | -0.697 | 0.487 |
| Rain within catchment† on previous day | $4.4 \times 10^5$ | $7.5 \times 10^4$ | 1.545 | 0.124 |
| Cumulative melt within catchment† | $7.5 \times 10^7$ | $8.8 \times 10^7$ | -0.472 | 0.637 |
| Cumulative rain within catchment† | $6.3 \times 10^6$ | $7.5 \times 10^6$ | -0.310 | 0.757 |
| Cumulative runoff within catchment† | $4.1 \times 10^9$ | $4.7 \times 10^9$ | -0.333 | 0.740 |
| Difference between cumulative catchment† runoff and lake volume | $6.5 \times 10^7$ | $7.4 \times 10^7$ | -0.321 | 0.749 |

† Mean catchment sizes are 13.0 $km^2$ and 14.6 $km^2$ for RD and NRD lakes, respectively.

The analysis reveals that the two lake types are indistinguishable for the majority of potential controlling factors. Some factors show a wide spread of values with, in some cases, a high proportion of data falling outside 2.7 $\sigma$ of the arithmetic mean (for example, lake area, lake volume or the principal strain rate) (Figure 4.9), but this pattern is usually observed for both the rapidly draining and non-rapidly draining lake types. For the hydrological factors (Table 4.1), Figure 4.9 (a) and Table 4.4 show that the lake types are statistically similar in all cases, except lake area (Figure 4.1), where non-rapidly lakes (mean = 0.69 $km^2$) are statistically larger ($t$ = -2.261; $p$ = 0.025) than rapidly draining lakes (mean = 0.47 $km^2$). For lake volume (Figure 4.3), a similar pattern is observed, with non-rapidly draining lakes containing higher volumes (mean = $7.4 \times 10^5$ $m^3$) than rapidly draining lakes (mean = $4.1 \times 10^5$ $m^3$), with lake volume only narrowly missing the 95% interval required for statistical confidence ($t$ = -1.934; $p$ = 0.054; Table 4.4). The two lake types are also statistically indistinguishable for the morphological factors (Figures 4.9 (b) and 4.10; Table 4.4). Among the glaciological factors, including the ice-surface elevation (Figure 4.1), the ice-surface slopes (Figure 4.10), the ice-bed elevation (Figure 4.11), the ice thickness (Figure 4.3), the ice-surface principal strain rate (Figure 4.12) and the von Mises yield criterion (Figure 4.13), the lake types are also indistinguishable (Figure 4.9 (c); Table 4.4). Thus, there is no evidence for rapidly draining lakes to be located preferentially over thinner or thicker ice (Figure 4.3), or within areas undergoing notably high extension or compression (Figures 4.12 and 4.13), with an approximately equal distribution of rapidly draining and non-rapidly draining lakes within these areas. For example, the mean principal strain rate is nearly identical for the two lake types: 0.04 (i.e. slightly compressional) for rapidly-draining lakes and 0.00 for non-rapidly draining lakes (Table 4.4); this indicates that they are situated within areas of similar surface-strain regimes. Finally, the SMB factors are statistically similar between the two lake types (Figure 4.9 (d); Table 4.4), with both showing similar patterns of melt, rain, runoff, and differences between the cumulative runoff within their catchments and their water volumes (Figure 4.11).

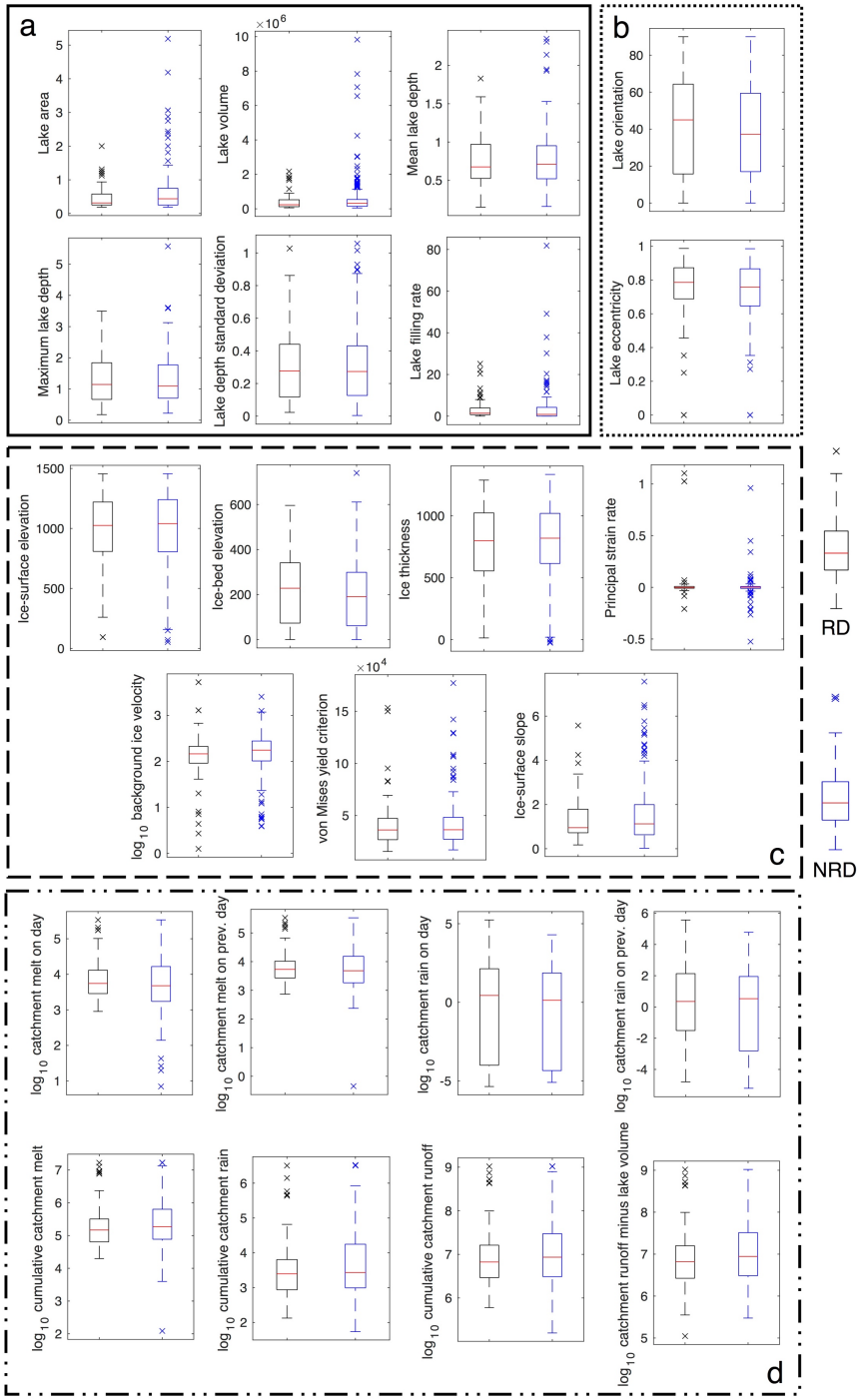



**Figure 4.9:** Boxplots highlighting the similarity of the potential controlling factors on hydrofracture for RD and NRD lakes for each category of potential control (Table 4.1): (a) hydrological, (b) morphological, (c) glaciological, and (d) SMB. On each boxplot, the red solid line shows the median, the box's upper and lower edges show, respectively, the upper and lower quartiles, the whisker lengths show ± 2.7 $\sigma$ from the arithmetic mean, and the crosses show values outside of this range. Some data are log-transformed (to the base 10) for presentation purposes only, indicated on the $y$ axis where relevant.

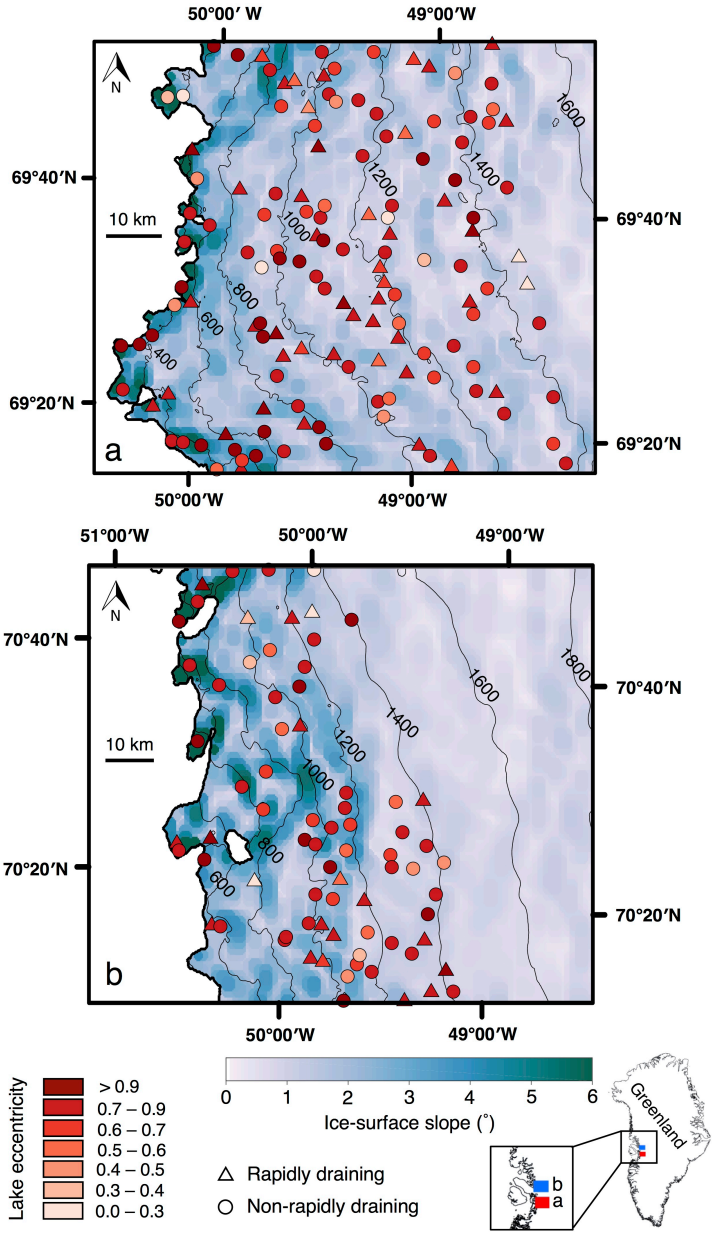



**Figure 4.10:** The locations of rapidly draining (triangles) and non-rapidly draining (circles) lakes within the (a) Paakitsoq and (b) Store Glacier regions of west Greenland (inset) overlying the ice-surface slopes, showing steeper slopes towards the ice margin. Note the difference in horizontal scale between the two panels. Colour-coding shows the lake eccentricity on the day of drainage for rapidly draining lakes and on the day when lakes reached their maximum extent for non-rapidly draining lakes. A lake eccentricity value of 0 would indicate a perfect circle and a value of 1 would indicate a line segment. The thick black lines on both panels delineate the GrIS margin from Howat *et al.* (2014).

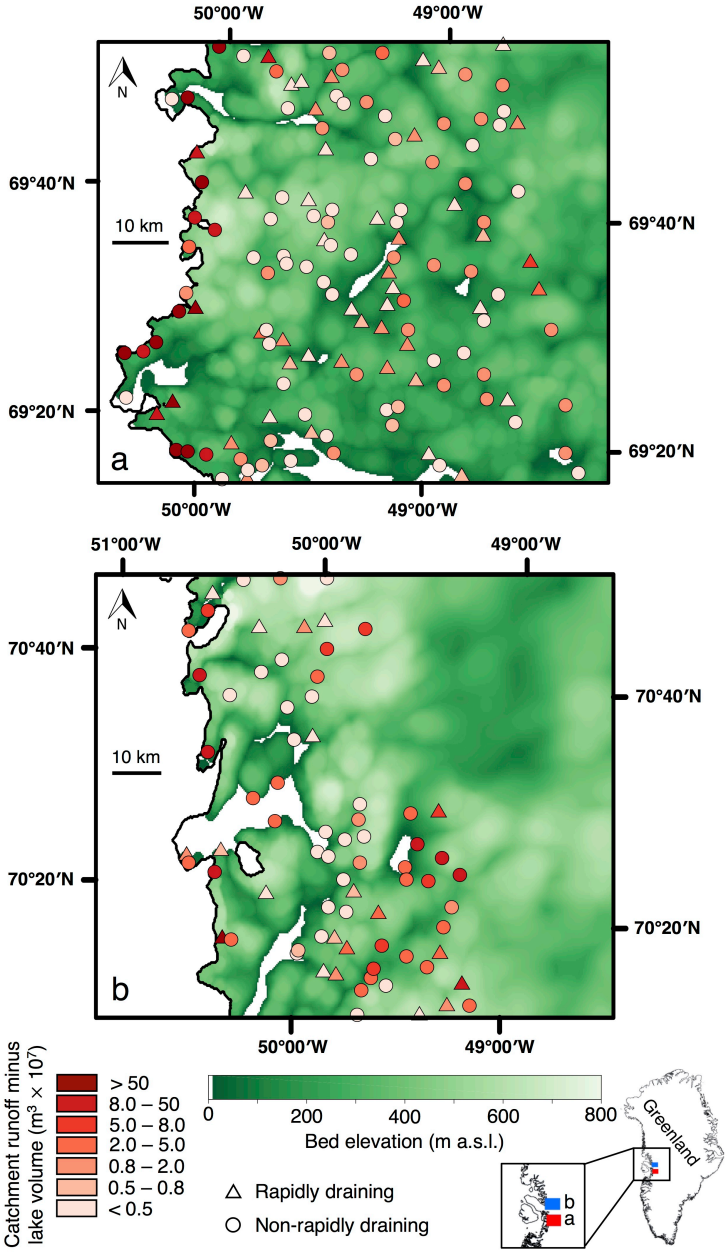



**Figure 4.11:** The locations of rapidly draining (triangles) and non-rapidly draining (circles) lakes within the (a) Paakitsoq and (b) Store Glacier regions of west Greenland (inset) overlying the ice-sheet bed elevation derived from Morlighem *et al.* (2014). Note the difference in horizontal scale between the two panels. Colour-coding shows the difference between the cumulative runoff in the catchment, derived from Noël *et al.* (2016), and the lake volume, derived as described in Section 4.3.1, on the date of drainage for rapidly draining lakes and on the date when lakes reached their maximum extent for non-rapidly draining lakes. The thick black lines on both panels delineate the GrIS margin from Howat *et al.* (2014), and white areas within the ice-sheet area show regions that are at or below global mean sea level (i.e. ≤ 0 m a.s.l.).

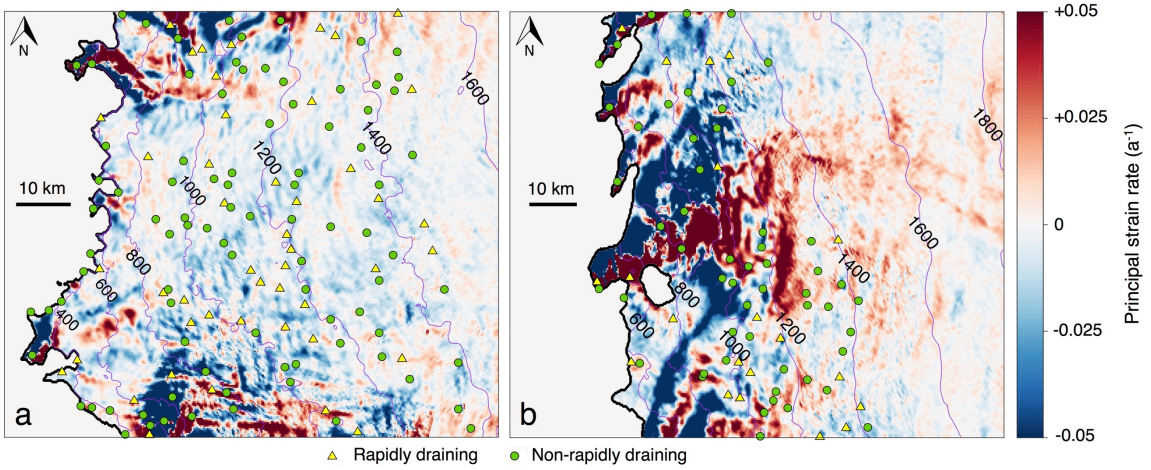



**Figure 4.12:** The variation in the ice-surface principal strain rate across the (a) Paakitsoq and (b) Store Glacier regions, with the locations of rapidly draining (yellow triangles) and non-rapidly draining (green circles) lakes shown. Note the difference in horizontal scale between the two panels. Panels are equivalent to those in Figures 4.1, 4.3, 4.10 and 4.11. Positive principal strain rates indicate extension and negative ones indicate compression. The thick black lines on both panels delineate the ice-sheet edge and the purple contour lines show ice-surface elevations (m a.s.l.) from Howat *et al.* (2014). The high principal strain rates observed close to central portion of the ice margin in (b) result from the fast flow rates of the floating tongue of the marine-terminating Store Glacier.

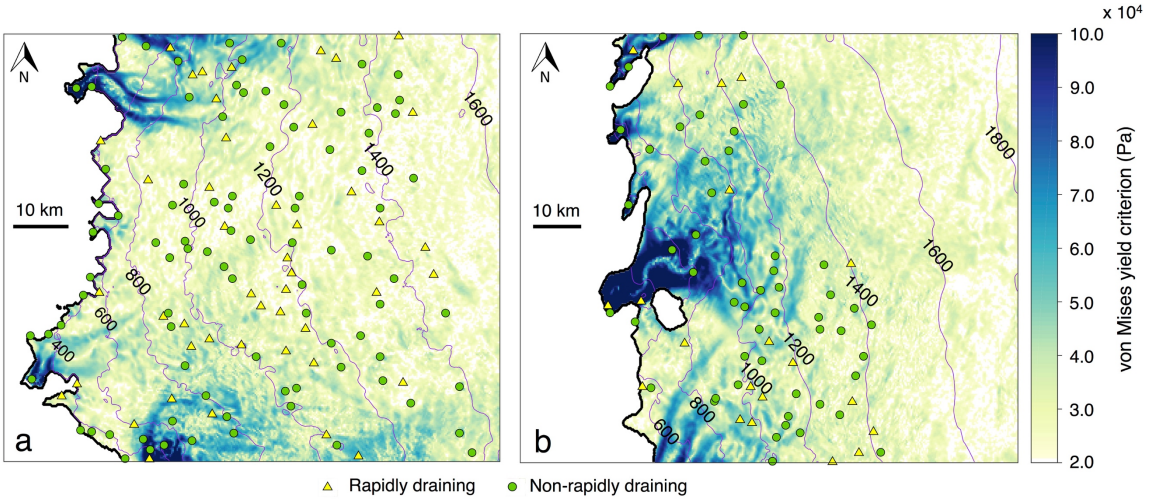



**Figure 4.13:** The variation in the von Mises yield criterion across the (a) Paakitsoq and (b) Store Glacier regions, with the locations of rapidly draining (yellow triangles) and non-rapidly draining (green circles) lakes shown. Note the difference in horizontal scale between the two panels. Panels are equivalent to those in Figures 4.1, 4.3, 4.10 and 4.11. The thick black lines on both panels delineate the ice-sheet edge and the purple contours show ice-surface elevations (m a.s.l.) from Howat *et al.* (2014).

## Principal Component Analysis

Figures 4.14–4.16 show the results of the first step of the PCA, where each category of variable (Table 4.1) is analysed separately; Figure 4.17 shows the second step of the PCA, which is performed for all of the 23 variables simultaneously. In every case, the two lake types do not cluster within specific areas of the PCA plots, suggesting that they are not statistically distinguishable. The results of unpaired two-sample Student's *t*-tests for the first three PCs verify the statistically indistinguishable nature of the lake types (Table 4.5). This shows that the rapidly draining and non-rapidly draining lakes are statistically similar in terms of all of the properties examined; they can thus be regarded as having been drawn from the same statistical population.

**Table 4.5:** Results of unpaired Student's *t*-tests (for each category of controlling factor from Table 4.1, as well as for all of the 23 potential controlling factors simultaneously, shown within the 'All' category) for the rapidly draining and non-rapidly draining lakes scored for the first three PCs. None of the results are significant at above the 95% confidence interval ($p < 0.05$). See Table A.10 for the eigenvectors for the first three PCs.

| Potential controlling factor category | PC number | *t* statistic | *p* value |
|---|---|---|---|
| Hydro-morphological | 1 | -0.388 | 0.698 |
| | 2 | -0.220 | 0.826 |
| | 3 | -0.068 | 0.946 |
| Glaciological | 1 | -1.294 | 0.197 |
| | 2 | 0.056 | 0.956 |
| | 3 | 0.945 | 0.346 |
| SMB | 1 | -0.935 | 0.926 |
| | 2 | 0.257 | 0.798 |
| | 3 | 0.416 | 0.678 |
| All | 1 | -1.342 | 0.181 |
| | 2 | 0.082 | 0.935 |
| | 3 | 0.638 | 0.524 |

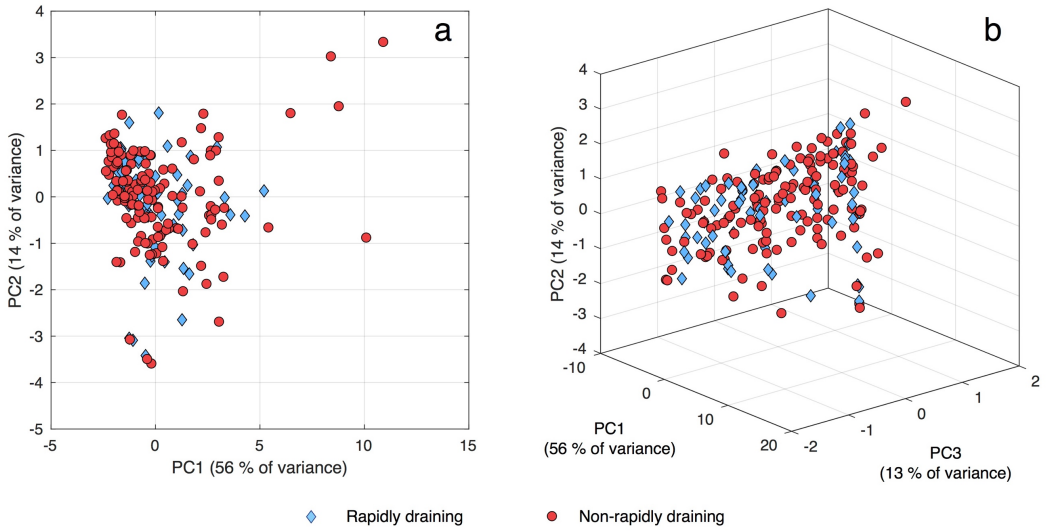



**Figure 4.14:** Scores for (a) PCs 1 and 2, and (b) PCs 1–3 for rapidly draining lakes (blue diamonds) and non-rapidly draining (red circles) lakes for variables within the hydro-morphological category of analysis (see Table 4.1). The percentage figures indicate the amount of variance in the data explained by the PC. The tight clustering of the rapidly draining and non-rapidly draining lake PC scores shows the statistical similarity of the potential controlling factors for the two lake types.

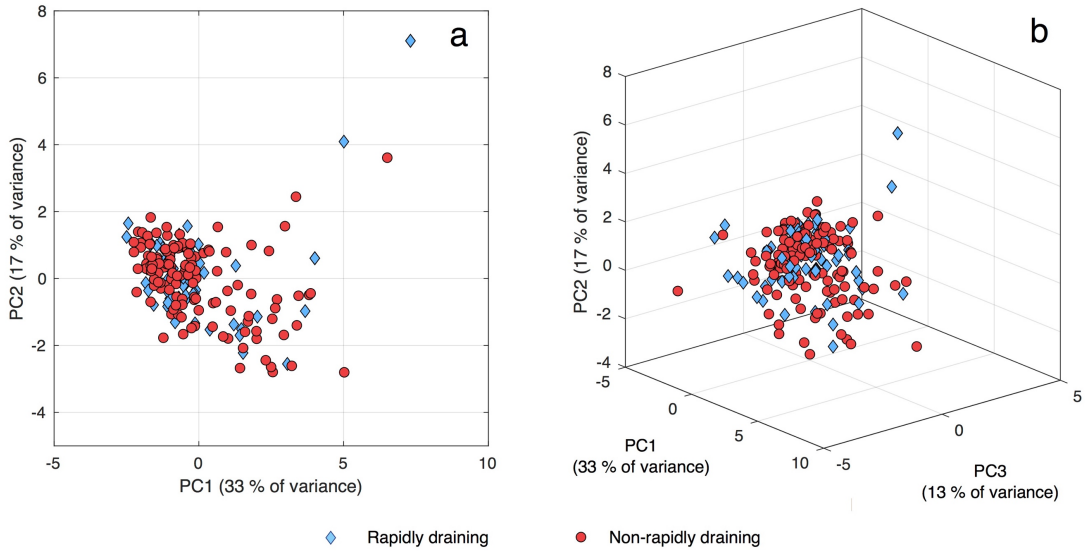



**Figure 4.15:** Scores for (a) PCs 1 and 2, and (b) PCs 1–3 for rapidly draining (blue diamonds) and non-rapidly draining (red circles) lakes for variables within the glaciological category of analysis (see Table 4.1). The percentage figures indicate the amount of variance in the data explained by the PC. The tight clustering of the rapidly draining and non-rapidly draining lake PC scores shows the statistical similarity of the potential controlling factors for the two lake types.

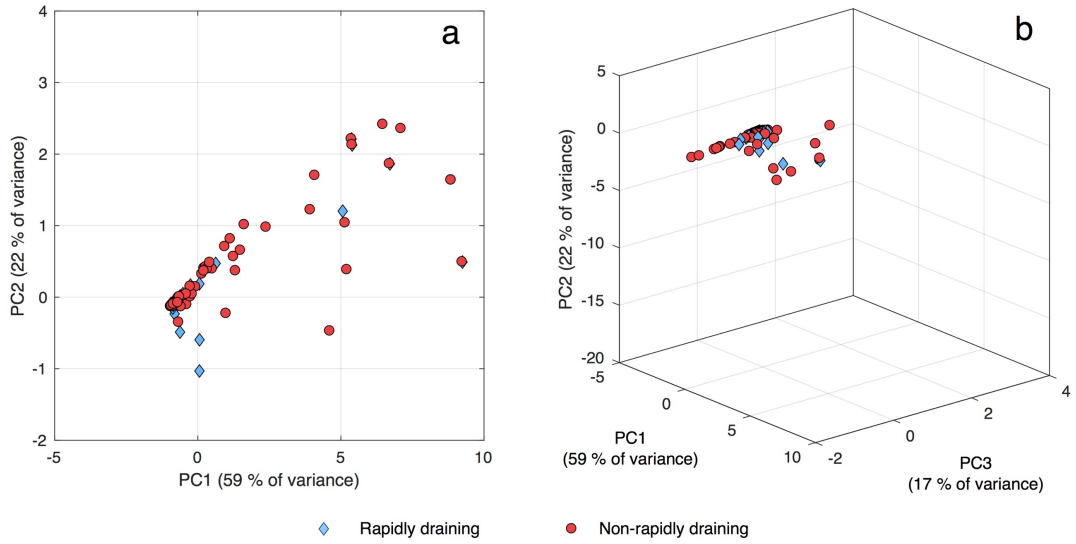



**Figure 4.16:** Scores for (a) PCs 1 and 2, and (b) PCs 1–3 for rapidly draining (blue diamonds) and non-rapidly draining (red circles) lakes for variables within the SMB category of analysis (see Table 4.1). The percentage figures indicate the amount of variance in the data explained by the PC. The tight clustering of the rapidly draining and non-rapidly draining lake PC scores shows the statistical similarity of the potential controlling factors for the two lake types.

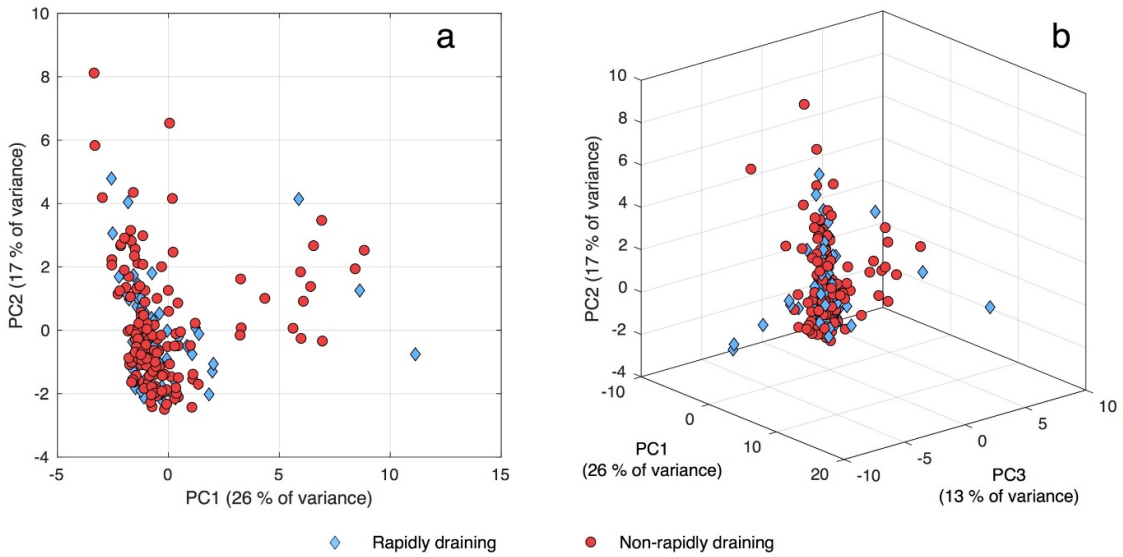



**Figure 4.17:** Scores for (a) PCs 1 and 2, and (b) PCs 1–3 for rapidly draining (blue diamonds) and non-rapidly draining (red circles) lakes for PCA for all of the potential controlling factors included in the analysis (see Table 4.1). The percentage values labelled on the axes indicate the amount of variance in the data explained by each PC. The tight clustering of the rapidly draining and non-rapidly draining lake PC scores shows the statistical similarity of the potential controlling factors for the two lake types.

### 4.4.3 Associations between lake area or volume and the potential controlling factors

The fourth and final aim of the study was to determine whether there were differences in the associations between lake area or volume and the potential controlling factors for the two lake types, and whether there was a critical threshold for rapid lake drainage that could be linked to one of the other potential controlling factors. Existing modelling studies have only considered this possibility with regards to lake area or volume and the local ice thickness, but have found similar model performance for a range of thresholds (Banwell *et al.*, 2013a, 2016; Arnold *et al.*, 2014; Koziol *et al.*, 2017). It is plausible, however, that a lake area or volume threshold exists with respect to a factor other than local ice thickness. For example, hydrofracture might occur if a certain lake size is reached and a certain strain pattern exists (Figure 4.12), with larger (or smaller) sizes required in more compressive (or more tensile) regions. Alternatively, perhaps rapid lake drainage is initiated once a certain lake size is attained and a particular volume of melt has already been lost from the catchment (Figure 4.11), with larger (or smaller) lake sizes required in catchments where less (or more) melt has been lost into the GrIS, for example. Bivariate correlations are examined between both lake areas (Table 4.6) and lake volumes (Table 4.7) and the other factors potentially controlling hydrofracture. The results in Tables 4.6 and 4.7 show that the majority of the correlations are statistically insignificant, indicating no link between these variables and lake area and volume. However, a few of the correlations are statistically significant at above the 95% confidence interval. For rapidly draining lakes, the only significant correlation is between lake area and ice-bed elevation, but for the non-rapidly draining lakes there are more numerous significant correlations (Tables 4.6 and 4.7). Tables 4.6 and 4.7 also show strong correlations between lake areas or volumes (for both rapidly draining and non-rapidly draining lakes) and the other hydrological factors, notably the maximum, mean and standard deviation of lake depth, and the lake filling rate, but it seems obvious that these variables should be correlated with lake area or volume since they are highly co-variant.

**Table 4.6:** Results of bivariate correlation analyses of lake area against other potential controlling factors for RD and NRD lake types. $\rho$ is the Spearman's rank correlation coefficient. Correlations significant at above the 95% confidence interval (i.e. $p < 0.05$) are highlighted in bold text. Negative correlations are shown in red text. Refer to Table 4.1 for dimensions of variables.

| **Potential controlling factor** | **RD $\rho$** | **RD $p$** | **NRD $\rho$** | **NRD $p$** |
|---|---|---|---|---|
| Ice thickness | 0.132 | 0.279 | 0.185 | **0.026** |
| Ice-surface elevation | -0.021 | 0.861 | 0.075 | 0.375 |
| Ice-bed elevation | -0.249 | **0.039** | -0.208 | **0.012** |
| Lake eccentricity | 0.079 | 0.517 | -0.102 | 0.224 |
| Lake orientation | 0.121 | 0.321 | 0.106 | 0.205 |
| Maximum lake water depth | 0.588 | **0.000** | 0.673 | **0.000** |
| Mean lake water depth | 0.379 | **0.001** | 0.584 | **0.000** |
| Standard deviation of lake water depth | 0.570 | **0.000** | 0.646 | **0.000** |
| Lake mean filling rate | 0.617 | **0.000** | 0.687 | **0.000** |
| Ice-surface slope | 0.088 | 0.473 | -0.117 | 0.162 |
| Background winter ice velocity | 0.064 | 0.599 | 0.119 | 0.154 |
| Principal strain rate | -0.058 | 0.645 | 0.007 | 0.937 |
| von Mises yield criterion | 0.200 | 0.107 | 0.132 | 0.123 |
| Melt within catchment on day | -0.025 | 0.841 | -0.008 | 0.922 |
| Rain within catchment on day | -0.156 | 0.200 | 0.067 | 0.427 |
| Melt within catchment on previous day | 0.094 | 0.444 | 0.015 | 0.857 |
| Rain within catchment on previous day | -0.043 | 0.723 | 0.116 | 0.167 |
| Cumulative melt within catchment | -0.024 | 0.846 | 0.216 | **0.009** |
| Cumulative rain within catchment | -0.019 | 0.877 | 0.219 | **0.008** |
| Cumulative runoff within catchment | -0.024 | 0.844 | 0.262 | **0.002** |
| Difference between cumulative catchment runoff and lake volume | -0.060 | 0.627 | 0.167 | **0.045** |

**Table 4.7:** Results of bivariate correlation analyses of lake volume against other potential controlling factors for RD and NRD lake types. $\rho$ is the Spearman's rank correlation coefficient. Correlations significant at above the 95% confidence interval (i.e. $p < 0.05$) are highlighted in bold text. Negative correlations are shown in red text. Refer to Table 4.1 for dimensions of variables.

| **Potential controlling factor** | **RD $\rho$** | **RD $p$** | **NRD $\rho$** | **NRD $p$** |
|---|---|---|---|---|
| Ice thickness | 0.176 | 0.149 | 0.203 | **0.015** |
| Ice-surface elevation | 0.032 | 0.797 | 0.109 | 0.195 |
| Ice-bed elevation | -0.231 | 0.056 | -0.162 | 0.052 |
| Lake eccentricity | -0.108 | 0.376 | -0.176 | **0.035** |
| Lake orientation | 0.116 | 0.344 | 0.038 | 0.652 |
| Maximum lake water depth | 0.889 | **0.000** | 0.888 | **0.000** |
| Mean lake water depth | 0.773 | **0.000** | 0.844 | **0.000** |
| Standard deviation of lake water depth | 0.847 | **0.000** | 0.833 | **0.000** |
| Lake mean filling rate | 0.741 | **0.000** | 0.724 | **0.000** |
| Ice-surface slope | -0.044 | 0.723 | -0.184 | **0.027** |
| Background winter ice velocity | -0.053 | 0.668 | 0.036 | 0.665 |
| Principal strain rate | -0.135 | 0.279 | 0.031 | 0.719 |
| von Mises yield criterion | 0.078 | 0.536 | 0.065 | 0.445 |
| Melt within catchment on day | -0.078 | 0.521 | -0.024 | 0.773 |
| Rain within catchment on day | -0.185 | 0.129 | 0.049 | 0.557 |
| Melt within catchment on previous day | 0.021 | 0.863 | -0.005 | 0.950 |
| Rain within catchment on previous day | -0.169 | 0.164 | 0.024 | 0.772 |
| Cumulative melt within catchment | -0.084 | 0.490 | 0.176 | **0.035** |
| Cumulative rain within catchment | -0.098 | 0.421 | 0.198 | **0.017** |
| Cumulative runoff within catchment | -0.078 | 0.522 | 0.219 | **0.008** |
| Difference between cumulative catchment runoff and lake volume | -0.113 | 0.353 | 0.126 | 0.131 |

# 4.5 Discussion

Collectively, the results showed that rapidly draining and non-rapidly draining lakes for these two regions of the GrIS were largely indistinguishable in terms of the potential hydrofracture controlling factors examined here (Sections 4.4.1 and 4.4.2). This suggests that, in statistical terms, the lakes were drawn from the same population. Moreover, when the lakes were categorised according to their mode of drainage, the correlation analyses were able to explain almost none of the variability of lake area or volume for the rapidly draining lakes (except when ice-bed elevation was the independent variable), but they could explain some of the variability for non-rapidly draining lakes (Section 4.4.3). In this Section 4.5, first the likely reasons for the results of the correlation analyses are discussed (Section 4.5.1); second, the results of the statistical tests for difference for each category of potential controlling factor are examined, with reference to existing hypotheses for rapid lake drainage (Section 4.5.2), and; finally, potential reasons for the negative results of this chapter are offered, with suggestions for where future research should be directed to verify or refute these findings for other sectors of the GrIS and for different years (Section 4.5.3).

## 4.5.1 Associations between lake area or volume and the potential controlling factors

When all of the lakes within both study regions were categorised according to their drainage mode, and then examined using a series of tests for correlation, the results indicated that, for rapidly draining lakes, the lakes normally drained before any of the controls were influential, whereas some of the controls were influential for the non-rapidly draining lakes. The negative weak correlation (Table 4.6) for both lake types between ice-bed elevation and lake area suggests that larger lakes tend to form in areas of lower ice-bed elevation, likely to be a result of the bed tending to be lower inland where the larger area lakes are present (Figures 4.1 and 4.10). The weak positive correlation (Tables 4.6 and 4.7) between ice thickness and non-rapidly draining lake area and volume can be explained because non-rapidly draining lakes grow bigger inland where the ice is thicker. This observation is also supported by the weak negative correlation (Table 4.7) between ice-surface slopes and non-rapidly draining lake volume since ice-surface slopes are lower inland (Figure 4.10), meaning non-rapidly draining lakes can reach higher volumes here than closer to the coast, where the steeper ice-surface slopes prevent the formation of the largest lakes. These correlation results might also be because lakes tend to form over areas of bed topography that are low relative to their surroundings (Lampkin and VanderBerg, 2011; Sergienko, 2013). The lack of similar correlations between rapidly

draining lake areas or volumes and the same factors indicate that ice thickness is not important in determining the size of the rapidly draining lakes prior to their drainage, instead suggesting that another factor may drive their rapid drainage. Non-rapidly draining lake volume also decreases as lakes become more eccentric (i.e. less circular and more linear; Figure 4.10), and so the lakes will contain lower total water volumes, possibly because the more linear features occur higher on the ice sheet where lakes are bigger (Figure 4.1), which could include some areas of slush rather than water contained within lakes. Finally, the correlation analysis showed that the cumulative totals of melt, rain and runoff in non-rapidly draining lake catchments were important in controlling the size of these lakes (Tables 4.6 and 4.7), as would be expected. However, the lack of a similar relationship between these SMB factors and rapidly draining lakes may be because these factors are not important for affecting the size of these lakes.

### 4.5.2 Statistically similar rapidly and non-rapidly draining lakes

This section discusses the results of the tests for statistical difference for each category of potential controlling variable separately.

#### Hydrological factors

Amongst all factors examined, this category was the only one for which any difference between the two lake types was identified: non-rapidly draining lakes were, on average, more expansive than rapidly draining lakes ($p < 0.05$); with slightly reduced confidence ($p = 0.054$), they also contained larger water volumes. Existing models of the GrIS's surface hydrology use a critical threshold for lake area or volume, scaled with local ice thickness, to predict hydrofracture (Banwell *et al.*, 2013a, 2016; Arnold *et al.*, 2014; Clason *et al.*, 2015; Koziol *et al.*, 2017) (Section 2.7). However, the results showed that, in many places, non-rapidly draining lakes were able to expand without causing hydrofracture to a size that was larger than that which caused hydrofracture elsewhere. Thus, while these current models assume a certain lake area or volume triggers hydrofracture, which could indicate that rapidly draining lakes would be larger than non-rapidly draining lakes, these results point towards the opposite, showing that cause and effect may have been reversed. In addition, no correlation was identified between rapidly draining lake area or volume and local ice thickness (although this correlation did exist for non-rapidly draining lakes), suggesting that rapidly draining lake area and volume do not scale according to ice thickness, but that the incidence of hydrofracture (presumably driven by a different control altogether) limits rapidly draining lake areas and volumes.

These results agree with the lack of a direct relationship between the lake volume for rapidly draining lakes and the local ice thickness identified in Chapter 3 (Figure 3.15).

To examine this relationship further, the "fracture areas", defined as the individual lake water volume divided by the local ice thickness, are calculated following Banwell *et al.* (2013a, 2016) and Arnold *et al.* (2014) (Section 2.7). These calculations show that the fracture areas are higher for non-rapidly draining lakes than rapidly draining lakes: at Paakitsoq, the mean fracture area for rapidly draining lakes is 600 $m^2$ ($\sigma$ = 572 $m^2$) compared with the mean fracture area for non-rapidly draining lakes of 2002 $m^2$ ($\sigma$ = 5084 $m^2$); at Store Glacier, the mean fracture area for rapidly draining lakes is 663 $m^2$ ($\sigma$ = 594 $m^2$) compared with a mean fracture area for non-rapidly draining lakes of 734 $m^2$ ($\sigma$ = 919 $m^2$). The high standard deviation values indicate that there is wide scatter across and between the study regions, supporting the idea that including a fracture-area threshold within models of the GrIS's surface hydrology is unlikely to be able to reproduce the precise locations and timings of rapid lake-drainage events, just their broad-scale patterns across the ice sheet (Arnold *et al.*, 2014).

While there was a difference between the rapidly draining and non-rapidly draining lake areas ($p < 0.05$) and volumes ($p = 0.054$) for the reasons explained above, the two lake types were statistically similar for the other hydrological factors (either individually or when combined into PCs). This indicates that the local, hydrological factors of individual lakes are unimportant in hydrofracture initiation. The fact that lake areas were significantly different between the two lake types, but lake volumes and depths were not (with 95% statistical confidence), may be due to the greater uncertainties associated with calculating lake water depth compared with lake area from MODIS imagery, possibly an effect of MODIS's coarse resolution (Section 3.5.1). The FAST algorithm's depth-calculation method tends to report smaller values for the highest water depths compared with those derived from Landsat 8 imagery (Section 3.5.1). This might have resulted in the two lake types appearing statistically similar even though they were not. To attempt to overcome this resolution-related problem, a finer-spatial resolution satellite record (like that from Sentinel-2) might be useful, such as that presented in Chapter 5. Use of such a record in the future alongside other high spatial resolution datasets might allow a clearer conclusion to be reached on whether non-rapidly draining lakes, as well as covering larger areas and containing higher water volumes, also contain deeper water than rapidly draining lakes.

## Morphological factors

The rapidly draining and non-rapidly draining lakes were similar in terms of their shapes and orientations, showing no link between these properties and the propensity for rapid lake drainage. This indicates that the distribution of the water load on the ice surface (i.e. whether it is more elongate or circular, and/or whether it is aligned more or less perpendicular or parallel to average ice-flow direction), is unimportant for hydrofracture initiation. This may be because the variation in load distribution is too small relative to the ice thickness to affect the hydrostatic-pressure potential, which also possibly explains the reason for which no statistically significant difference was identified between the mean filling rates and the likelihood of hydrofracture.

## Glaciological factors

The results showed that rapidly draining and non-rapidly draining lakes were similar in terms of the glaciological factors investigated. The long-term average winter stress field was included as a potential control on hydrofracture since higher temporal-resolution summer ice-velocity or strain-rate data were critically unavailable in this research. However, while this was useful for defining the long-term average strain regime across each lake basin (which was hypothesised to be a potential first-order control on hydrofracture), no evidence was found to indicate that hydrofracture is controlled by the background winter stress or strain field. Existing research has only shown the degree of compression across a lake basin (e.g. Doyle *et al.*, 2013), but has not considered whether the magnitude of the tensor affects the lake's likelihood of drainage. Here, no support was found for this idea either. Moreover, the background strain or velocity data did not scale with the rapidly draining lake areas or volumes (Section 4.4.3), suggesting that a threshold for rapidly draining lake area or volume cannot be linked to the local strain rate or ice velocity derived from background winter velocity data. Recent research, also in the Paakitsoq region, using high spatial resolution, summer strain-rate data has also indicated no apparent link between strain rates and the incidence of rapid lake drainage (Poinar *et al.*, 2017c). There is thus no evidence that including the background stress regime in GrIS surface-hydrology models will improve their ability to predict rapid lake drainage accurately. However, perhaps it is only the deviation from this long-term stress field that is important, resulting, for example, from surface meltwater reaching the bed via a nearby crevasse or moulin, perturbing the horizontal or vertical velocity or stress field beneath a lake basin (Stevens *et al.*, 2015). This process was also investigated within this chapter by including the difference between the cumulative runoff in the lake's catchment and the lake's water volume, but negative results were also found (Section 4.4.2).

### Surface-mass-balance factors

Finally, the two lake types cannot be distinguished statistically on the basis of the SMB factors examined: there was no tendency for rapidly draining lakes to have different meltwater, rain and runoff quantities within their ice-surface catchments. The key rationale for including these factors was because previous work had found that water input to the ice-sheet bed nearby to a single lake initiated hydrofracture (Stevens *et al.*, 2015), so these SMB data were used as proxies for this process. Moreover, to measure the input of water to the bed near to a lake, the total melt in a lake's catchment was calculated, from which the individual lake volume was subtracted, but no support was found within this chapter for the importance of the hypothesis of Stevens *et al.* (2015) for driving lake drainage for a larger sample of lakes. However, a weak positive correlation was observed between the melt, rain and runoff quantities and non-rapidly draining lake area and volume, even though the same correlations did not apply to rapidly draining lakes. This indicates that, for rapidly draining lakes, lake area and volume may not be dependent on these factors, or perhaps that they drain before the controls become manifest.

Even though the findings of Stevens *et al.* (2015) could not be corroborated, that the input of water to the ice-sheet bed close to a lake was a precursor to hydrofracture, for a greater lake sample across the GrIS, this may reflect the coarse resolution of the MODIS imagery (250 m) and the RACMO2.3 gridded data (1 km) used in this chapter. The important meltwater-generation and surface-routing processes within lakes' catchments may therefore operate at too fine a scale to be resolved with these data. Further studies that model or observe surface-meltwater production and its routing at spatial resolutions of metres to tens of metres and combine this information with ice-surface strain rates measured at hourly to daily temporal resolutions would be helpful for examining the influence of water delivery to the ice-sheet bed close to lakes in better detail. This objective could potentially be addressed using either higher-resolution remote-sensing imagery (e.g. WorldView, Sentinel-1 or Sentinel-2) or more field studies monitoring individual lakes and their catchments, which would generate data at a spatial resolution comparable to that of the width of a fracture (metres to tens of metres) formed by rapid lake drainage.

## 4.5.3 Reasons for the negative results and suggestions for future work

Here, four explanations are offered for which causal links between the potential controlling factors and hydrofracture were not identified within this chapter; in addition, suggestions are presented for how this study might be continued with further research. First, although the EDA included many

of the factors that might be important in controlling hydrofracture (with the choice guided by previous research), other potential controls may have been overlooked. It is conceivable, therefore, that there is a control on hydrofracture that could be detected using the approach in this chapter, but that its potential was not identified at the outset. Second, it is possible that a control is important but that it was not in summer 2014 within the study regions; further investigations for other sectors of the GrIS and in additional years would therefore help to validate whether the negative results apply more widely in space and time. Third, the interplay between some of the controls that were identified may be too complex to be elicited at the spatial and temporal scales used for the analysis in this thesis. Remote sensing and SMB model outputs over finer grids and time steps may overcome this problem, or perhaps the control(s) might only be found from more field-based studies of individual or groups of lakes (Das *et al.*, 2008; Doyle *et al.*, 2013; Tedesco *et al.*, 2013; Stevens *et al.*, 2015). With continuing improvements to the availability and resolution of remotely-sensed data (such as ice-bed topography (e.g. Morlighem *et al.*, 2017) or ice-velocity data (e.g. Joughin *et al.*, 2018)), future studies that use a similar EDA approach to this one alongside these new datasets might be better able to reveal the control(s) on hydrofracture. Fourth, there may be a strong stochastic element to rapid lake drainage, which would explain the statistical similarity between the lake types observed in this chapter and which may help to explain the reason why some lakes change their mode of drainage inter-annually (Selmes *et al.*, 2013; Fitzpatrick *et al.*, 2014). For example, hydrofracture might only be possible if pre-existing weaknesses exist in the ice beneath a lake basin, which can then be exploited by a water load on the ice surface (Catania *et al.*, 2008). This would consequently make rapid lake drainage appear random. Without being able to include these very site-specific processes and ice-sheet features, which relate to the complex strain history upglacier of a lake, it may be difficult to predict rapid lake drainage with confidence. A more detailed examination of such features as well as the strain history upglacier of a lake would therefore be helpful.

## 4.6 Summary and conclusions

- The precise controls on rapid lake drainage, which is important for the GrIS's mass balance, remain uncertain, having not been examined comprehensively within existing research. The aim in this chapter was therefore to address this shortfall by conducting a comprehensive, statistically-robust EDA of various potential controls on hydrofracture for a large sample of rapidly draining and non-rapidly draining lakes in west Greenland, using the FAST algorithm presented in Chapter 3 and combining it with other potential explanatory environmental variables.

- The results did not indicate any clear links between the incidence of hydrofracture and the potential controlling factors examined for the two study regions in summer 2014. This means that an empirically-supported, deterministic alternative cannot be recommended to the fracture-area threshold parameter in use within current surface-hydrology models of the GrIS (Banwell *et al.*, 2013a, 2016; Arnold *et al.*, 2014; Clason *et al.*, 2015; Koziol *et al.*, 2017).
- However, the results also did not provide evidence to support the use of a fracture-area threshold parameter in future surface-hydrology models. This is because it was indicated that rapid lake drainage seems to control lake size, and not the reverse, which directly contradicts the use of a fracture-area threshold in models of the GrIS's surface hydrology. Using a deterministic basis to predict precisely when and where rapid lake drainage will occur on the GrIS therefore remains one of the weaker components of GrIS hydrology models, despite recent work showing the importance of the lake-drainage process, and particularly the opening of moulins, for the evolution of subglacial drainage (Banwell *et al.*, 2016).
- Based on the results of this chapter, future work might focus on incorporating some or all of the potential controls identified here into supraglacial-hydrology models of the GrIS and testing the models' ability to reproduce empirical observations with these controls included. These improvements to surface-hydrology models are necessary to provide more realistic inputs to SMB models (requiring knowledge of lake locations and their duration on the GrIS surface to determine the amount of enhanced surface ablation) (Section 2.6.1), and to coupled subglacial hydrology-ice flow models (requiring knowledge of the location, timing and magnitude of meltwater deliveries to the ice-sheet bed to determine ice-dynamic impacts) (Section 2.6.3).

# Chapter 5

# Fully-automated lake tracking with a dual-satellite (Sentinel-2 and Landsat 8) record

## 5.1 Executive summary

Although remote sensing is commonly used to monitor lakes on the GrIS surface, most satellite records must trade-off high spatial resolution for high temporal resolution (e.g. MODIS) or vice versa (e.g. Landsat). Here, this issue is overcome by developing and applying a dual-sensor method that can monitor changes to lake areas and volumes at high spatial resolution (10–30 m) with a frequent revisit time (~3 days). This is achieved by mosaicking imagery from the Landsat 8 with imagery from the recently-launched Sentinel-2 for a ~12,000 km$^2$ area of west Greenland in summer 2016. First, a physically-based method for calculating lake depths with Sentinel-2 is validated by comparing measurements against those derived from the available contemporaneous Landsat 8 imagery; this validation produces close correspondence between the two sets of values. This provides the methodological basis for automatically calculating lake areas, depths and volumes from all available Landsat 8 and Sentinel-2 images. These automatic methods are incorporated into an algorithm for Fully-Automated Supraglacial lake Tracking at Enhanced Resolution (FASTER). The FASTER algorithm produces time series showing lake evolution during the 2016 melt season, including automated rapid (≤ 4 day) lake-drainage identification. With the dual Sentinel-2–Landsat 8 record, 184 rapidly draining lakes are identified, many more than identified with either imagery

collection alone (93 with Sentinel-2; 66 with Landsat 8), due to their inferior temporal resolution, or more than would be possible with MODIS, due to its omission of small lakes < 0.125 km$^2$. The water volumes drained into the GrIS by rapid lake-drainage events are identified and, by using downscaled regional climate-model (RACMO2.3p2) runoff data, the water quantity is determined that enters the GrIS via the moulins opened by such events. During the lake-drainage events alone, the water drained by small lakes (< 0.125 km$^2$) is only 5.1% of the total water volume drained by all lakes. However, considering the total water volume entering the GrIS after lake drainage, the moulins opened by small lakes deliver 61.5% of the total water volume delivered via all moulins (i.e. opened by large and small lakes). These findings suggest that small lakes should be included in future remote sensing and modelling work. Finally, Sentinel-2 imagery is used alone in 2017 to determine whether Landsat 8 data are additionally needed to provide a high temporal resolution record of lake behaviour. Using these data, marked differences in lake behaviour are observed between the years, with lakes containing lower water volumes and draining later in 2017, which is related to the regional, inter-annual differences in runoff. The analysis suggests that a dual-satellite record from these two satellites is necessary to provide sufficiently high temporal resolution to identify rapid lake drainage confidently.

## 5.2 Objective and aims

Following the successful development of a fully-automated method for tracking changes to lake areas and volumes with MODIS imagery (Chapter 3), the overall objective of this chapter is to present an automatic method for monitoring the evolution and drainage of lakes on the GrIS using a combination of Sentinel-2 and Landsat 8 imagery, which will allow the mosaicking of a high spatial resolution (10–30 m) record with a frequent revisit time (approaching that of MODIS), something only possible by using the two sets of imagery simultaneously. The objective is addressed using five aims, which are to:

1. Trial new methods for calculating lake areas, depths and volumes from Sentinel-2 imagery and assess their accuracy against Landsat 8 for two overlapping dates in summer 2016.
2. Apply the best methods for Sentinel-2 from (1), alongside existing methods for calculating lake areas, depths and volumes for Landsat 8, to all of the available summer 2016 and 2017 (May–October) imagery for a large study site (~12,000 km$^2$) in west Greenland. These methods are applied within a fully-automated lake-tracking algorithm to produce time series of water-volume measurements for each lake in the study region to show their seasonal evolution.

3. Identify lakes that drain rapidly using the automatic algorithm, separating these lakes into small (< 0.125 $km^2$) and large (≥ 0.125 $km^2$) categories, based on whether they could be identified with MODIS, in summer 2016 and 2017.
4. Quantify the runoff volumes routed into the GrIS both during the lake-drainage events themselves, and afterwards via moulins opened by hydrofracture, for the small and large lakes in summer 2016.
5. Investigate inter-annual changes in lake behaviour in the study region by comparing the numbers of rapidly draining lakes, their drainage dates and water volumes, between summer 2016 and 2017, and relate these changes to inter-annual differences in runoff within the region.

It is hoped that improved insights into GrIS hydrology will be offered by using the dual-satellite record, and that it may be able to overcome some of the issues associated with using the coarse-resolution MODIS record (Chapter 3), such as the relatively high errors associated with lake-depth calculations or its omission of lakes close to its threshold reporting size.

## 5.3 Data and methods

This section describes the expansion of the study region from the earlier chapters (Section 5.3.1), the collection and pre-processing of the Landsat 8 and Sentinel-2 imagery (Section 5.3.2), the technique for delineating lake area (Section 5.3.3), the methods used to calculate lake depth and volume (Section 5.3.4), the approaches for automatically tracking lakes and identifying rapid lake drainage (Section 5.3.5), and the methods used to determine the runoff volumes, including the quantity routed into the GrIS interior following the opening of moulins by hydrofracture (Section 5.3.6).

### 5.3.1 Study region

The analysis in this chapter focuses on a ~12,000 $km^2$ area of west Greenland, extending ~110 km latitudinally and ~90 km from the ice margin (Figures 2.15 and 5.1). It is primarily a land-terminating sector of the ice sheet, extending from just north of Jakobshavn Isbræ, near Ilulissat, to just south of Store Glacier in the Uummannaq district. This study location was chosen because it is an area of high lake activity (Section 2.8), having been the focus of many previous remote-sensing studies with which the results can be compared (e.g. Box and Ski, 2007; Selmes *et al.*, 2011; Fitzpatrick *et al.*, 2014; Cooley and Christoffersen, 2017; Miles, K. E. *et al.*, 2017).

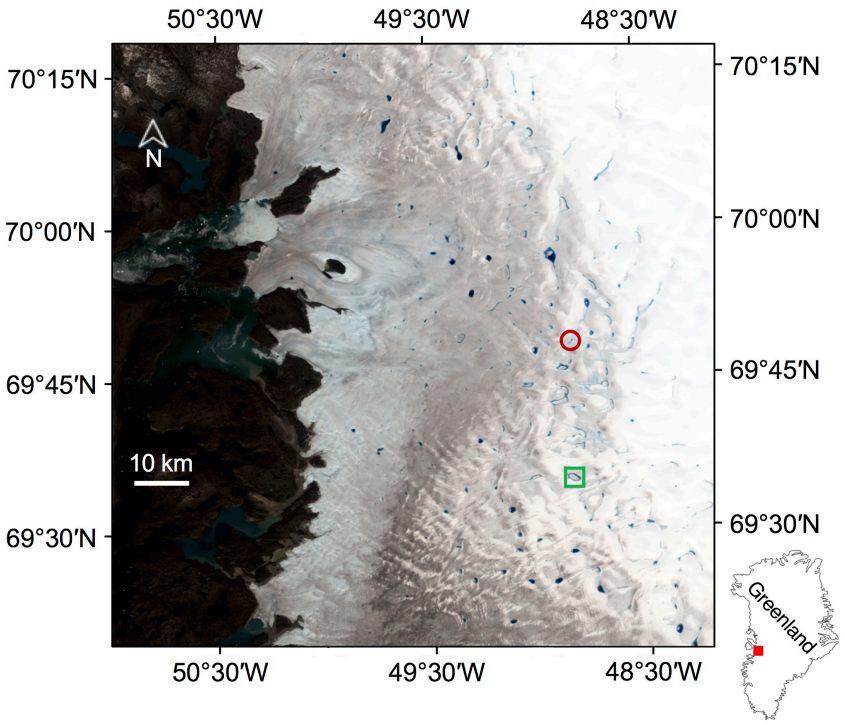



**Figure 5.1:** The ~12,000 km$^2$ study site within Greenland (inset). The background image is a Sentinel-2 RGB image from 11 July 2016 (see Table A.11 for image details). Green box shows the location of a rapidly draining lake and red circle shows the location of a non-rapidly draining lake (cf. Figure 5.8).

## 5.3.2 Satellite imagery collection and pre-processing

### Landsat 8

17 Landsat 8 images from May to October (Table A.12) were downloaded from the USGS Earth Explorer interface (http://earthexplorer.usgs.gov). These were level-1T, radiometrically- and geometrically-corrected images, which were distributed as raw digital numbers (Section 2.4.2). The 30 m resolution data were required from bands 2 (blue; 0.452–0.512 µm), 3 (green; 0.533–0.590 µm), 4 (red; 0.636–0.673 µm) and 6 (SWIR; 1.566–1.651 µm), as well as the 15 m resolution data from band 8 (panchromatic; 0.503–0.676 µm) (Table 2.3). All of the available 2016 imagery that covered at least a portion of the study site was used, regardless of cloud cover. Since Landsat 8 images cover greater spatial areas than Sentinel-2 images (due to their lower spatial resolution), the Landsat 8 images were batch cropped to the extent of the Sentinel-2 images using ArcGIS's 'Extract by Mask' tool. All of the tiles were reprojected to the WGS 84 UTM zone 22N geographic coordinate system (EPSG: 32622) for consistency with the Sentinel-2 images, and ice-marginal areas were removed with the GIMP ice-sheet mask (Howat *et al.*, 2014). The raw digital numbers were converted to TOA

reflectance using the image metadata and the USGS Landsat 8 equations (available at: https://landsat.usgs.gov/landsat-8-l8-data-users-handbook-section-5). Landsat 8 TOA values adequately represent surface reflectance in Greenland (Pope *et al.*, 2016) and have been used previously for studying GrIS hydrology (Pope *et al.*, 2016; Miles, K. E. *et al.*, 2017; Macdonald *et al.*, 2018). The cloud-masking procedure involved marking pixels as 'no data' when their band-6 (SWIR) TOA reflectance value exceeded 0.100 (Figure 5.2), similar to the method used in Chapter 3 for MODIS imagery albeit requiring a higher threshold value of 0.150. This lower threshold was chosen based on manual inspection of the pixels marked as cloudy against clouds visible on the original images. To reduce any uncertainty in the cloud-filtering technique, the cloud mask was dilated by 200 m (just over six Landsat 8 pixels), so that there was high confidence that all clouds had been marked as 'no data' and would not affect the subsequent analyses. Images were manually checked for cloud shadowing and shadows were filtered if present.

## Sentinel-2

Sentinel-2 images were required for both summer 2016 and 2017. For summer 2016, 39 Sentinel-2A level-1C images from May to October (Table A.11) were downloaded from the Amazon S3 Sentinel-2 database (http://sentinel-s2-l1c.s3-website.eu-central-1.amazonaws.com). In summer 2017, both Sentinel-2A and Sentinel-2B level-1C images were downloaded from May to October from the same database. In total, 54 Sentinel-2A and 27 Sentinel-2B images were used (Table A.11). The Sentinel-2 data were distributed as TOA reflectance values that were radiometrically- and geometrically- corrected, including orthorectification and spatial registration to a global reference system with sub-pixel accuracy. All Sentinel-2 images were downloaded from 2016 that had ≥ 20% data cover of the study region and ≤ 75% cloud cover. In 2017, all images of the study region, except those with > 95% cloud cover, were included. These image-filtering thresholds resulted in the exclusion of 38 (27) images from the 77 (108) in total available in 2016 (2017), reducing the average temporal resolution from 2.0 (1.4) to 3.9 (1.9) days in 2016 (2017). Sentinel-2 data were downloaded for the satellite's 10 m resolution bands 2 (blue; 0.460–0.520 μm), 3 (green; 0.534–0.582 μm) and 4 (red; 0.655–0.684 μm), and 20 m resolution data from band 11 (SWIR; 1.570–1.660 μm) (Table 2.4). Ice-marginal areas were removed using the GIMP ice-sheet mask (Howat *et al.*, 2014). A cloud-masking procedure similar to that for Landsat 8 was used, where pixels were assumed to be clouds and were marked as 'no data' when the TOA value exceeded a threshold of 0.140 in band 11, after the band-11 data had been interpolated (using nearest-neighbour resampling) to 10 m resolution for consistency with the optical bands (Figure 5.2). This threshold was chosen by manually comparing the pixels identified as clouds against the background RGB images. As with

the Landsat 8 images, the cloud mask was dilated by 200 m (ten Sentinel-2 pixels) to account for any uncertainty in the cloud-masking procedure.

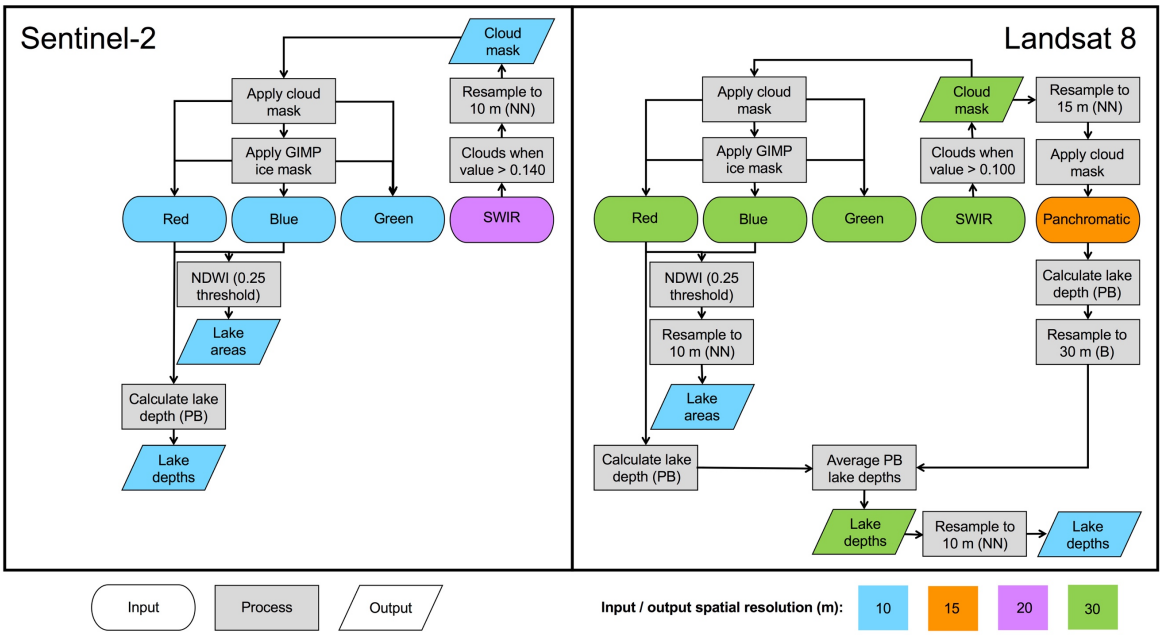



**Figure 5.2:** Summary of the methods applied to the Sentinel-2 and Landsat 8 input data to calculate lake areas using the NDWI and depths using the physically-based ("PB" in this figure) method. The interpolation techniques used are indicated by "NN" for nearest neighbour or "B" for bilinear. The lake-area outputs are compared between the two datasets as described in Section 5.3.3, and the physically-based lake-depth outputs are compared as outlined in Section 5.3.4. When the empirical lake depth method for calculating Sentinel-2 lake depths was also evaluated, the final Landsat 8 depths at 10 m resolution were directly compared against the original Sentinel-2 input band data (at native 10 m resolution) within the lake outlines defined from the NDWI.

## 5.3.3 Lake area delineation

Figure 5.2 summarises the overall method used to calculate lake areas and depths for the Landsat 8 and Sentinel-2 imagery, including the cloud-masking procedure described above, and the resampling required because the data were distributed at different spatial resolutions. These comparisons were only conducted for an image pair in summer 2016, and not in summer 2017, since Sentinel-2 data were used in isolation of Landsat 8 data in summer 2017. Since the Landsat 8 optical band data were at 30 m native resolution, they were first resampled to 10 m resolution (using nearest-neighbour resampling) for consistency with the resolution of the Sentinel-2 data (Figure 5.2). Once complete, lake areas were derived for the two sets of imagery using the NDWI approach (Section 3.3.3), which

has been widely used previously for medium- to high-resolution imagery of the GrIS (e.g. Moussavi *et al.*, 2016; Miles, K. E. *et al.*, 2017), although it was deemed to perform more poorly than other techniques for the lower-resolution MODIS imagery analysed earlier in this thesis (Section 3.4.1). There were two stages involved here. First, various NDWI thresholds were applied to the Sentinel-2 and Landsat 8 images and the delineated lake boundaries were compared against the lake perimeters in the background RGB images. A supervised classification was alternatively considered here, but it performed poorly at identifying the lake areas reliably (cf. Chapter 3). The NDWI threshold was qualitatively selected for each type of imagery based on the threshold that produced the closest match between the lake outlines and the perimeters of the lakes in the RGB images. Based on this qualitative analysis, NDWI thresholds of 0.25 were chosen for both types of imagery (Figure 5.2). By varying the thresholds in increments of ± 0.01 from these values, the total lake area calculated across the whole image only changed by < 2%. The second stage involved comparing the areas of 594 lakes defined using the NDWI for the contemporaneous Landsat 8 and Sentinel-2 images from 1 July (collected in < 90 minutes of each other) and 31 July (collected in < 45 minutes of each other). This gave an extremely close agreement between the two sets of lake areas ($R^2$ = 0.999; RMSE = 0.007 $km^2$, equivalent to seven Sentinel-2 pixels) without any bias, producing confidence that the NDWI approach applied to the two types of imagery reproduced the same lake areas (Figure 5.3). Using these NDWI thresholds, binary (lake and non-lake) masks were created for each day of imagery for the two satellites for both summers. From the binary images, groups of < 5 pixels in total and linear features < 2 pixels wide were filtered, since these were likely to represent areas of mixed slush or supraglacial streams, as opposed to lakes (Pope, 2016; Pope *et al.*, 2016).

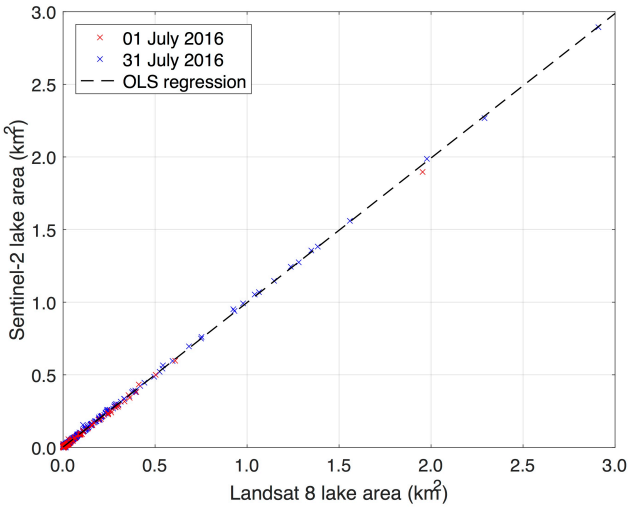



**Figure 5.3:** The very strong relationship between Landsat 8 and Sentinel-2 lake areas for the days of overlapping imagery (1 July and 31 July) in 2016 (Tables A.11 and A.12). The 594 lake areas used for comparisons were derived using the NDWI approach with threshold values of 0.25 for both types of imagery. The black dashed line shows an OLS linear regression, which can explain 99.9% ($R^2$ = 0.999; $p$ = 0.000) of the variance in the data. The RMSE of 0.007 km$^2$ (i.e. seven Sentinel-2 pixels) between the two sets of lake areas is remarkably small.

## 5.3.4 Lake depth and volume estimates

### Landsat 8

For each Landsat 8 image, the lake depths and volumes were calculated using the physically-based method of Pope (2016) and Pope *et al.* (2016), based on Sneed and Hamilton's (2007) original method for ASTER imagery, as introduced in Chapter 3. This approach is based on the premise that there is a measurable change in the reflectance of a pixel within a lake according to its depth, since deeper water causes higher attenuation of the optical wavelengths within the water column. Lake depth ($z$) can therefore be calculated based on the satellite-measured reflectance for a pixel of interest ($R_{pix}$) and other lake properties:

$$z = \frac{[\ln\ (A_d - R_\infty) - \ln\ (R_{pix} - R_\infty)]}{g}, \tag{5.1}$$

where $A_d$ is the lake-bottom albedo, $R_\infty$ is the reflectance for optically-deep (> 40 m) water, and $g$ is the coefficient for the losses in upward and downward travel through a water column. For Landsat 8, Pope *et al.*'s (2016) recommendations were again followed as in Chapter 3, taking an average of the depths calculated using the red and panchromatic band TOA reflectance data within the boundaries of the lakes (before they had been resampled to 10 m resolution for comparing the

Sentinel-2 and Landsat 8 lake areas; Section 5.3.3) defined by the method described in Section 5.3.3. Since the panchromatic-band data were at 15 m resolution, they were resampled using bilinear interpolation to match the 30 m red-band resolution (Figure 5.2). $A_d$ was calculated as the average reflectance in the relevant band for the ring of pixels immediately surrounding a lake, $R_\infty$ was determined from optically-deep water in proglacial fjords on a scene-by-scene basis for each band, and $g$ values for the relevant Landsat 8 bands were taken from Pope *et al.* (2016). Lake volume was calculated as the sum of lake depths, multiplied by the pixel area, within the lake outlines. As in Chapter 3, these Landsat 8 depths and volumes as were regarded as ground-truth data for the validation of the Sentinel-2 lake-depth measurements.

## Sentinel-2

Since no existing work has derived lake depths using Sentinel-2, it was necessary to formulate a new method. For this purpose, the Landsat 8 lake depths were used as the validation dataset, with the validation being conducted on the two dates (1 July and 31 July) with contemporaneous Landsat 8 and Sentinel-2 images (as described in Section 5.3.3). It was decided to test both physically-based and empirically-based techniques to derive Sentinel-2 lake depths, noting at the outset that physical techniques are generally thought to be preferable over empirical ones since they do not require site- or time-specific tuning.

For the physically-based technique, the same method as applied to Landsat 8 (Equation 5.1) was tested for its use on the Sentinel-2 TOA reflectance data. However, since Sentinel-2 does not collect panchromatic-band measurements, only Sentinel-2's red band could be used to calculate lake depths (Figure 5.2). So, this physically-based technique was applied to the red-band data within the lake outlines defined with the NDWI (Section 5.3.3). The value for $R_\infty$ was derived as described above for Landsat 8, but for $A_d$, the lake was dilated by a ring of two pixels, and not one, to ensure that shallow water was not included due to the finer pixel resolution. A new $g$ value for Sentinel-2's red band needed to be calculated using Pope *et al.*'s (2016) methods. For this purpose, the relationship from Smith and Baker (1981; their Equation 5) states that:

$$K_d = a + \frac{1}{2}b, \tag{5.2}$$

where $K_d$ is the diffuse attenuation coefficient for the clearest natural freshwaters, $a$ is the absorption coefficient for pure water, and $b$ is the backscattering coefficient for molecular (Rayleigh) scattering in freshwater. The relationship from Sneed and Hamilton (2007; their Equation 3) was then used, which indicates that:

$$g \approx K_d + aD_u, \tag{5.3}$$

where $D_u$ is an upwelling light distribution or the reciprocal of the upwelling average cosine (Mobley, 1994). Since $K_d \approx aD_u$ (Maritorena *et al.*, 1994), $g$ could simply be calculated (using measured values of $a$ and $b$) with the following:

$$g = 2(K_d), \tag{5.4}$$

meaning that Equation 5.2 could then be used to derive the following relationship:

$$g = 2(a + \tfrac{1}{2}b). \tag{5.5}$$

For $a$, the value was taken from Pope and Fry (1997; their Table 3) to replace that from Smith and Baker (1981; their Table 1), and, for $b$, the value from Buiteveld *et al.* (1994; their Table 1) was taken for each wavelength of Sentinel-2's red band. This allowed a preliminary $g$ value to be calculated for Sentinel-2's red band by using Equation 5.5 for each wavelength of the red band (from 646–684 nm in 1 nm increments). To derive a final value, following Pope *et al.* (2016), Sentinel-2's spectral response function (ESA, 2017) was used (akin to the data available for Landsat 8 (Barsi *et al.*, 2014)), and an average weighted value was calculated according to the spectral response for each wavelength of the red band. This produced a final $g$ value for Sentinel-2's red band of 0.8304 $m^{-1}$, which compares with the lower $g$ value for Landsat 8's red band of 0.7507 $m^{-1}$ (Pope *et al.*, 2016).

The empirically-based approach involved deriving various lake depth-reflectance regression relationships (to determine which explained most variance in the data) using the Landsat 8 lake depth data (dependent variable) and the Sentinel-2 TOA reflectance data for the three optical bands (independent variables) for each pixel within the lake outlines predicted in both sets of imagery to determine which band and relationship produced the best match between the two datasets. To compare these values, the Landsat 8 depth arrays were first resampled (using nearest-neighbour interpolation) from 30 m to 10 m to match the resolution of the Sentinel-2 TOA reflectance data (Figure 5.2). To evaluate the performance of the empirical versus physical techniques, goodness-of-fit indicators were calculated for the Sentinel-2 and Landsat 8 measurements derived from the empirically-based technique (applied to all optical bands) and physically-based method (applied to the red band).

As for Landsat 8, Sentinel-2 lake volumes were calculated as the sum of the individual lake depths, multiplied by the pixel areas, within the lake boundaries.

### 5.3.5 Lake evolution and rapid lake-drainage identification

#### Time series of lake water volumes

Once validated, the new techniques to calculate lake areas, depths and volumes from Sentinel-2, as well as the existing methods for Landsat 8 (Sections 5.3.3 and 5.3.4), were applied to the satellite imagery within the Fully-Automated Supraglacial lake Tracking at Enhanced Resolution (FASTER) algorithm to produce cloud- and ice-marginal-free 10 m resolution lake area and depth arrays for each day of the 2016 melt season for which either a Landsat 8 or Sentinel-2 image was available, or for each day of the 2017 melt season with a Sentinel-2 image available (Figure 5.2). In 2016, for the days (1 July and 31 July) when both Landsat 8 and Sentinel-2 imagery was available (as used for the comparisons above), in the FASTER algorithm, only the higher-resolution Sentinel-2 images were used. The FASTER algorithm is an adapted version of the FAST algorithm presented in Chapter 3 for MODIS imagery. Similar to the FAST algorithm, the FASTER algorithm involves creating an array mask to show the maximum extent of lakes within the region in summers 2016 and 2017, by superimposing the lake areas from each image. Within this maximum lake-extent mask, changes to lake areas and volumes were tracked between each consecutive image pair, with any lakes that were obscured (even partially) by cloud marked as 'no data'. While a 2-pixel minimum threshold lake size was required for MODIS, for the analysis in this chapter, only lakes that grew to ≥ 495 pixels (i.e. 0.0495 $km^2$) at least once in the season were tracked, which is identical to the minimum threshold used by Miles, K. E. *et al.* (2017), and is based on the minimum estimated lake size (approximated as a circle) required to force a fracture to the ice-sheet bed (Krawczynski *et al.*, 2009) (Section 2.7). It is encouraging that this minimum threshold size for lake tracking was over seven times larger than the error (0.007 $km^2$) associated with calculating lake area (Section 5.3.3; Figure 5.3). While a lower tracking threshold could have been used, it would have significantly increased computational time and power required, alongside adding uncertainty to whether the groups of pixels being tracked actually represented lakes. This tracking procedure produced time series for all lakes to show their evolution over the whole 2016 and 2017 melt seasons.

#### Rapid lake-drainage identification

From the time series, a lake was classified as draining rapidly if two criteria were met: (i) it lost > 80% of its maximum seasonal volume in ≤ 4 days (following Doyle *et al.*, 2013; Fitzpatrick *et al.*, 2014; Miles, K. E. *et al.*, 2017; Chapter 3); and (ii) it did not then refill on the subsequent day of cloud-free imagery by > 20% of the total water volume lost during the previous time period, following Miles, K. E. *et al.* (2017); the aim here was to filter false positives from the record.

However, the sensitivity of the rapid lake-drainage identification methodology to these thresholds was tested for summer 2016 by varying the threshold by ± 10% (i.e. 70–90%) for the critical-volume-loss threshold, ± 10% (i.e. 10–30%) for the critical-refilling threshold, and ± 1 day (i.e. 3–5 days) for the critical-timing threshold.

To determine how much extra information could be obtained from the finer spatial resolution satellite record, the number of rapidly draining lakes identified that grew to ≥ 0.125 $km^2$ (which would theoretically be resolvable by MODIS) was compared with the number that never grew to this size (which would not be resolvable by MODIS) at least once in the season. The drainage date was defined as the midpoint between the date of drainage initiation and cessation (cf. Section 3.3.5), and the error on the drainage date was defined as half of this value. In 2016, three sets of analyses were conducted: one for each set of imagery individually, and a third for both sets together; the intention here was to quantify how mosaicking the dual-satellite record improved the identification of lake-drainage events compared with using either record alone. In 2017, only a single set of analysis was conducted for Sentinel-2 imagery alone, because of the improved temporal resolution when using both Sentinel-2A and Sentinel-2B imagery; a secondary aim was to determine whether Sentinel-2 data could be used in isolation of Landsat 8 data, which would be preferable since it would reduce the need for any resampling, and therefore the consequent introduction of errors. The water volumes reaching the GrIS interior from the small and large lakes during the drainage events themselves were determined using the lake volume measurements on the day of drainage.

The difference in lake behaviour between 2016 and 2017 was investigated in terms of the difference in the drainage dates and the water volumes contained in the lakes prior to rapid drainage.

### 5.3.6 Meltwater deliveries after moulin opening and inter-annual runoff

To quantify the extra runoff entering the GrIS via the moulins opened in 2016, using the dual Sentinel-2 and Landsat 8 record, the locations and timings of moulin openings by large and small rapidly draining lakes were identified. Then, at these moulin locations, the meltwater volumes that subsequently entered the ice sheet were determined using statistically-downscaled, daily 1 km resolution RACMO2.3p2 runoff data (Noël *et al.*, 2018). Here, "runoff" was defined as melt plus rainfall minus any refreezing in snow (Noël *et al.*, 2018). These data were reprojected from Polar Stereographic (EPSG: 3413) to WGS 84 UTM zone 22N (EPSG: 32622) for consistency with the other data, and upsampled to 100 m resolution using bilinear resampling. Then, the ice-surface catchment for each rapidly draining lake was delineated using MATLAB's 'watershed' function,

applied to the GIMP ice-surface-elevation data (Howat *et al.*, 2014). The elevation data were first coarsened using bilinear resampling to 100 m resolution from 30 m native resolution. For each of the days after rapid lake drainage had finished, it was assumed that all of the runoff within a lake's catchment reached the moulin in that catchment instantaneously (i.e. no flow-delay algorithm was applied) and entered the GrIS. This allowed first-order comparisons between cumulative runoff into the GrIS via the moulins opened by small and large lake-drainage events. In 2017, the RACMO2.3p2 runoff data (Noël *et al.*, 2018), which were only available until the end of August, were used to assess whether differences in the timing and quantity of surface melt between 2016 and 2017 could explain any differences in lake behaviour between the years, such as the drainage dates or water volumes contained within lakes prior to drainage.

# 5.4 Results

## 5.4.1 Sentinel-2 lake-depth estimates

Table 5.1 shows the results of the lake-depth calculations using the physically- and empirically-based techniques. The physically-based method (Figure 5.4) performs slightly less well ($R^2$ = 0.841; RMSE = 0.555 m) than the best empirical method (Figure 5.5) when a power-law regression is applied to the red-band data ($R^2$ = 0.889; RMSE = 0.447 m). Figures 5.6 and 5.7, respectively, show the data for the empirical technique applied to the Sentinel-2 TOA reflectance values and Landsat 8 lake depths for the more poorly-performing Sentinel-2 green and blue bands (Table 5.1). The physically-based method performs better on 1 July 2016, when the relationship between Sentinel-2 depths and Landsat 8 depths is more linear (Figure 5.4, blue circles) than on 31 July 2016 (Figure 5.4, red squares), when the relationship is more curvilinear. This is because the depths calculated with Sentinel-2 on 31 July are limited to ~3 m, while higher depths (> 4 m) are reported on 1 July 2016 (Figure 5.4). Although less distinct, the best empirical relationship for the red band also differs slightly in performance between the two dates (Figure 5.5). Section 5.5.1 discusses the possible reasons for the under-measured lake depths w Sentinel-2 on 31 July 2016 compared with 1 July 2016.

Although the physically-based method performs slightly more poorly than the empirical techniques, the physical method is preferable because it can be applied across wide areas of the GrIS and in different years without site- or time-specific tuning; it is likely that a different empirical relationship would have better represented the data for a different area of the GrIS or in a different year. The physically-based method is therefore carried forward into the lake-tracking approach, with the error defined on all of the subsequently calculated lake-depth (and therefore lake-volume) measurements

for Sentinel-2 using the RMSE of 0.555 m, and, in summer 2016, treating the Landsat 8 measurements as ground-truth data, meaning they do not have errors associated with them.

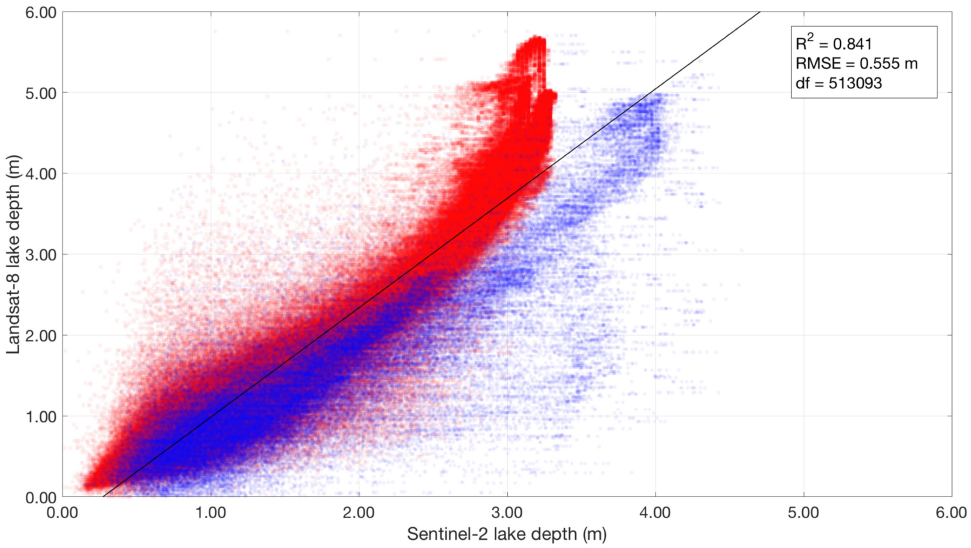



**Figure 5.4:** Comparison between lake depths calculated using the physically-based method for Sentinel-2 (with the red band) and for Landsat 8 (with the average depths from the red and panchromatic bands). Degrees of freedom ("df") = 513,093 (blue circles = 1 July 2016; red squares = 31 July 2016). The solid black line shows an OLS linear regression. The $R^2$ value indicates that the regression explains 84.1% of the variance in the data. The RMSE of 0.555 m shows the error associated with calculating the Sentinel-2 lake depths using this relationship.

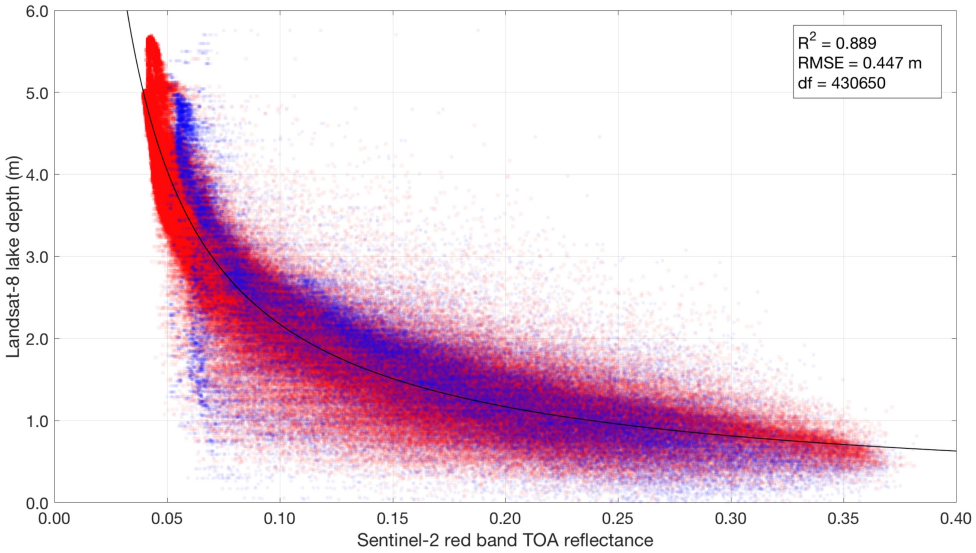



**Figure 5.5:** The empirical power law regression (solid black curve, equation $y = 0.2764x^{-0.8952}$) between Sentinel-2 red-band TOA reflectance and Landsat 8 lake depth. Degrees of freedom ("df") = 430,650 (blue circles = 1 July 2016; red squares = 31 July 2016). The $R^2$ value indicates that the regression explains 88.9% of the variance in the data. The RMSE of 0.447 m shows the error associated with calculating the Sentinel-2 lake depths using this relationship.

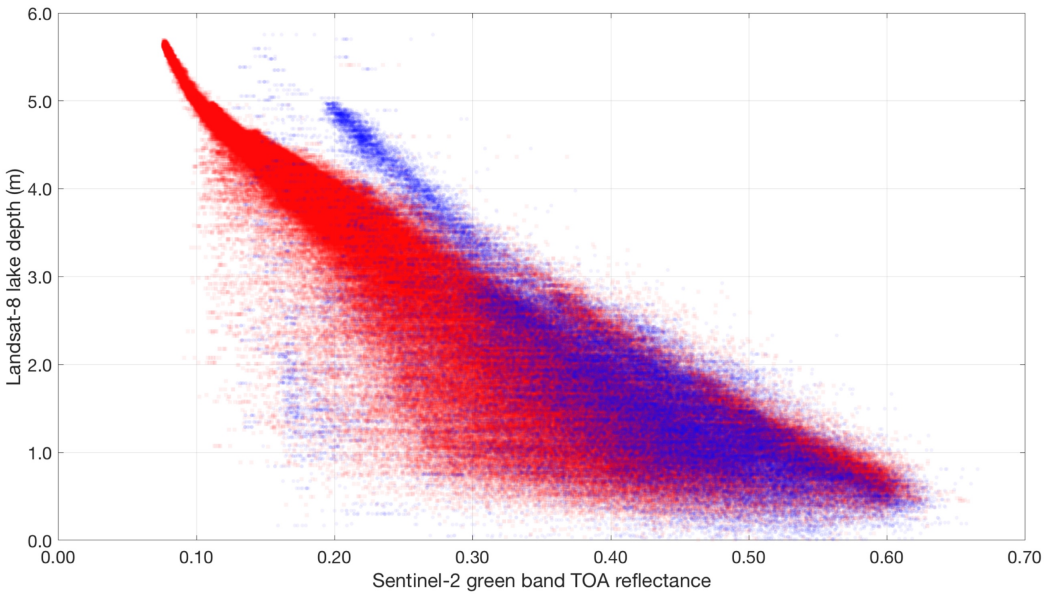



**Figure 5.6:** Scatter plot to show the relationship between Sentinel-2 green-band TOA reflectance and Landsat 8 lake depth for 430,650 data points (blue circles = 1 July 2016; red squares = 31 July 2016).

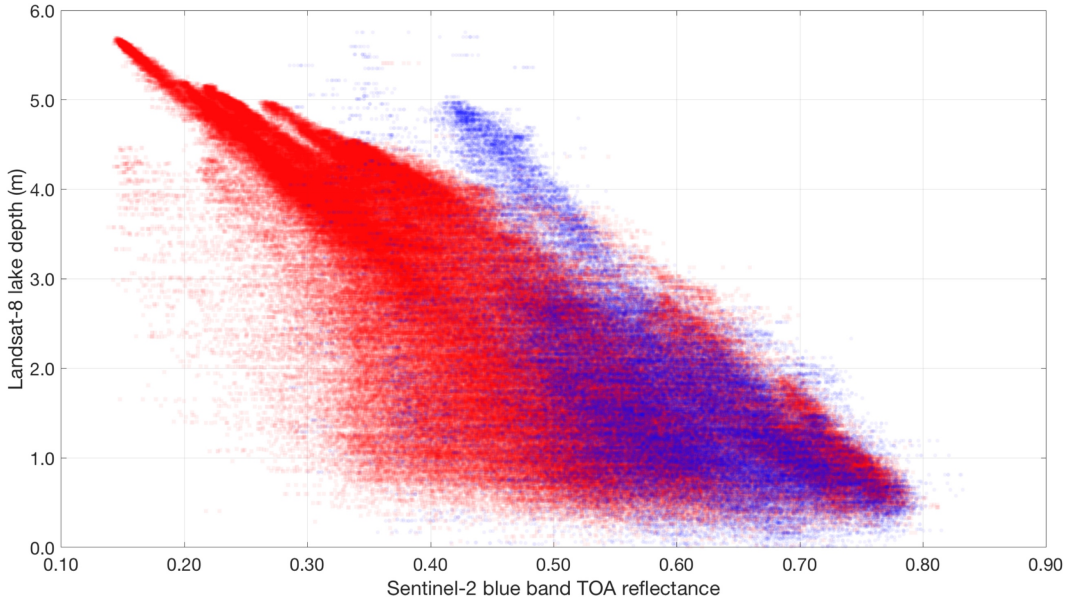



**Figure 5.7:** Scatter plot to show the relationship between Sentinel-2 blue-band TOA reflectance and Landsat 8 lake depth for 430,650 data points (blue circles = 1 July 2016; red squares = 31 July 2016).

**Table 5.1:** Goodness-of-fit indicators for the empirical and physical techniques tested in this chapter for deriving Sentinel-2 lake depths, with validation against the Landsat 8 lake depths. SSE is the sum of squares due to error. The best-performing (red-band) regression relationship (i.e. the one with highest $R^2$, and lowest RMSE and SSE) among the empirical techniques is shown in bold italicised text.

| **Sentinel-2 band (technique)** | **Goodness-of-fit indicator** | **OLS regression** | **Power-law regression** | **Exponential regression** |
|---|---|---|---|---|
| Red (empirical) | $R^2$ | 0.702 | ***0.889*** | 0.842 |
| | RMSE | 0.734 | ***0.448*** | 0.534 |
| | SSE ($m^3$) | $2.39 \times 10^5$ | ***$8.62 \times 10^4$*** | $1.23 \times 10^5$ |
| Green (empirical) | $R^2$ | 0.782 | 0.768 | 0.829 |
| | RMSE | 0.627 | 0.647 | 0.556 |
| | SSE ($m^3$) | $1.69 \times 10^5$ | $1.80 \times 10^5$ | $1.33 \times 10^5$ |
| Blue (empirical) | $R^2$ | 0.647 | 0.622 | 0.673 |
| | RMSE | 0.799 | 0.826 | 0.768 |
| | SSE ($m^3$) | $2.75 \times 10^5$ | $2.94 \times 10^5$ | $2.54 \times 10^5$ |
| Red (physical) | $R^2$ | 0.841 | – | – |
| | RMSE | 0.555 | | |
| | SSE ($m^3$) | $1.58 \times 10^5$ | | |

### 5.4.2 Lake evolution in summer 2016

Having verified the reliability of the lake area and depth techniques for both Sentinel-2 and Landsat 8, the automatic calculation methods are included in the FASTER algorithm to derive seasonal changes to lake areas and depths, and therefore volumes, in summer 2016. The FASTER algorithm is applied to the Landsat 8 and Sentinel-2 image batches individually, as well as to both sets when combined into a dual record. In 2016, using the dual-satellite image collection produces an improvement to the temporal resolution of the dataset over the summer season (1 May to 30 September) from averages of 9.0 days (for Landsat 8) and 3.9 days (for Sentinel-2) to 2.8 days (for the dual record). The months of June and July have the most imagery available (both with 14 images) within the dual-satellite analysis. For the Landsat 8 individual analysis, the algorithm tracks changes to 453 lakes that grow to $\geq 0.0495$ km$^2$ once in the season; equivalent numbers are 599 lakes for the Sentinel-2 analysis, and 690 lakes for the dual-satellite analysis. Using the dual-satellite record therefore involves tracking an additional 237 (91) lakes over the season than is possible with Landsat 8 (Sentinel-2) alone.

The largest lake size varies between the analyses: 4.0 km$^2$ for Landsat 8 (recorded on 16 July 2016), and 8.6 km$^2$ for Sentinel-2 (recorded on 21 July 2016), which may be because there are no Landsat 8 images close to 21 July 2016. The maximum lake volumes recorded also vary between the two platforms: $1.1 \times 10^7$ m$^3$ for Landsat 8 (recorded on 15 July 2016) and $1.2 \times 10^7$ m$^3$ for Sentinel-2 (recorded on 14 July 2016). The mean and median lake sizes across all of the images from the dual Sentinel-2–Landsat 8 record are 0.09 km$^2$ and 0.02 km$^2$, respectively. Both values are well below (by 0.035 km$^2$ and 0.105 km$^2$, respectively) the threshold reporting size of MODIS, assuming two 250 m MODIS pixels are required to confidently classify lakes (Fitzpatrick *et al.*, 2014; Chapter 3). Unpaired Student's *t*-tests between Sentinel-2 and Landsat 8 lake areas and volumes (from all of the imagery) confirm that they are not significantly different with > 99% confidence ($t = 6.5$, degrees of freedom = 9503 for areas; $t = 11.4$, degrees of freedom = 6859 for volumes), justifying using the two imagery types together despite their resolution difference (10 m versus 30 m).

Using the full Sentinel-2–Landsat 8 dataset, the FASTER algorithm produces time series that document changes to individual lake volumes over the season, samples of which are shown in Figure 5.8. Total areal and volumetric changes across the whole region are also calculated by summing the values for all lakes in the region. However, it is noted that cloud cover (which was masked from the images) often affects the observational record, and there are time periods, such as the end of August and early July, with a lot of missing data (Figure 5.9). Figure 5.10 is therefore produced to normalise total lake areas and volumes against the proportion of the region visible, and this shows the

estimated pattern of lake evolution on the GrIS. There is virtually no water in lakes before June, steady increases in total lake area and volume until the middle of July, and then a gradual decrease in total lake area and volume through the remainder of the season, with most lakes emptying or freezing by early September (Figures 5.9 and 5.10). Dates with seemingly low total lake areas and volumes are explained by the low portion of the whole region visible in those images (Figures 5.9 and 5.10). Finally, as in previous studies (e.g. Box and Ski, 2007; Georgiou *et al.*, 2009) and Chapter 3, there is a very close correspondence between lake areas and volumes: comparing lake area and volume values from all dates produced an $R^2$ value of 0.73 ($p$ = 0.00).

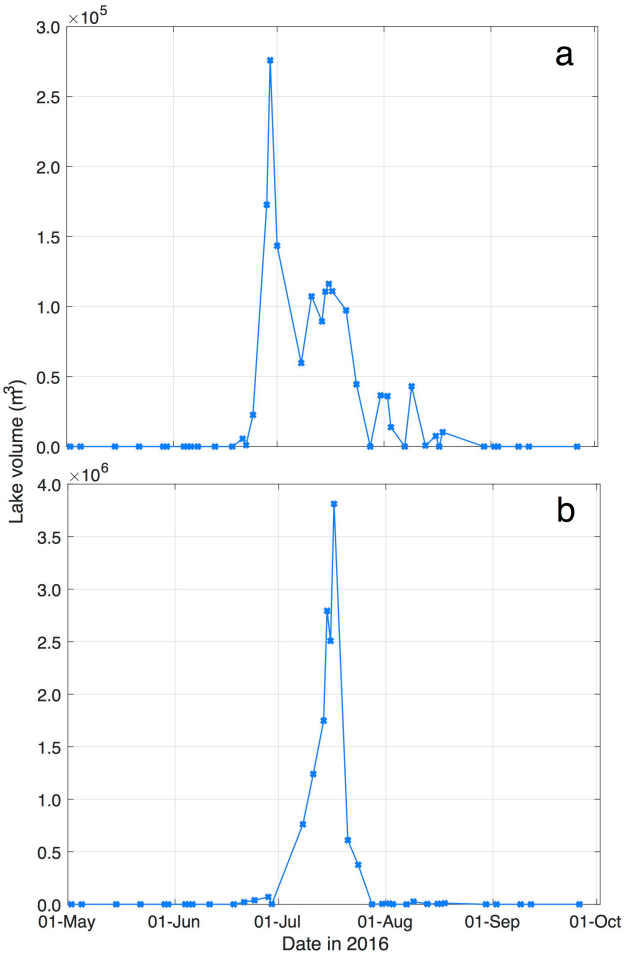



**Figure 5.8:** Sample time series of lake volume to show seasonal changes for (a) a non-rapidly draining lake (Figure 5.1, red circle) and (b) a rapidly draining lake (Figure 5.1, green box). Lines connect points without any data smoothing.

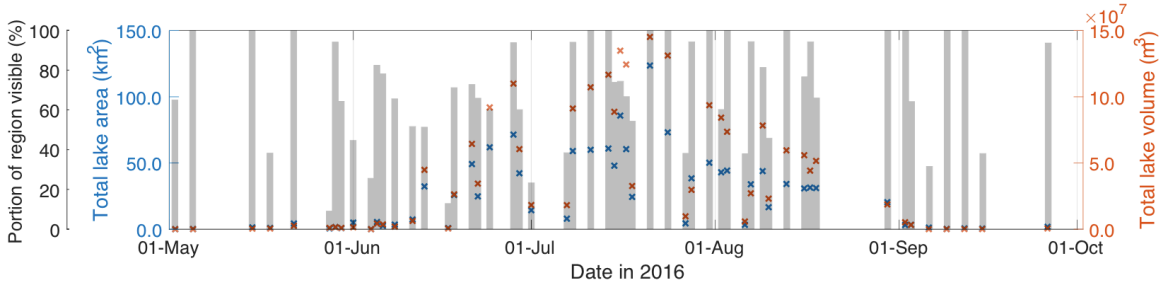



**Figure 5.9:** Evolution to total lake area and volume across the whole study region during the 2016 melt season. "Portion of region visible" measures the percentage of all pixels within the entire region that are visible in the satellite image, i.e. which are not obscured either by cloud (or cloud shadows) or which are not missing data values. Figure 5.10 presents total lake area and volume after normalising for the portion of the region visible.

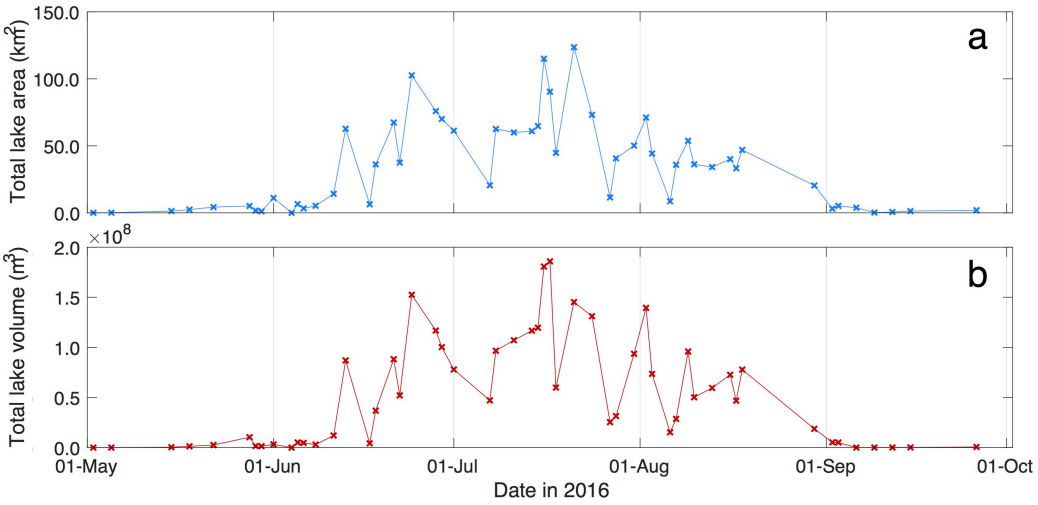



**Figure 5.10:** Estimates of evolution to total lake (a) area and (b) volume across the whole study region during the 2016 melt season after daily values were normalised against the proportion of the region visible on that day (i.e. not obscured by cloud, cloud shadows or missing data). Values are derived by dividing the daily total lake area and volume by the portion of the region visible on that day (cf. Figure 5.9).

### 5.4.3 Rapid lake drainage in summer 2016

Table 5.2 shows the results of the identification of rapidly draining lakes using the three different datasets, and indicates that the dual-satellite record is better for identifying rapidly draining lakes than the individual records. This was for two main reasons. First, the dual-satellite record identifies 118 (91) more rapidly draining lakes than the Landsat 8 (Sentinel-2) record in isolation (Table 5.2). When either record is used alone, Sentinel-2 (Landsat 8) performs better (worse), identifying 50.5%

(35.9%) of the total number of rapidly draining lakes identified by the dual-satellite record. Second, with the dual-satellite dataset, drainage dates are identified with lower error (i.e. half of the number of days between the date of drainage initiation and cessation) than with the Sentinel-2 analysis (Table 5.2). However, the errors appear lower for the Landsat 8 analysis than either the dual-satellite or Sentinel-2 analysis, and this is because nearly all Landsat 8 lake-drainage events occur on two occasions when an image pair is only separated by a day, on 8–9 July (small lakes) and 13–14 July (large lakes) (Table 5.2).

The dual-satellite record also identifies the rapid drainage of many small lakes (< 0.125 $km^2$) that would not be visible with MODIS imagery due to the lower limit of its reporting size (Table 5.2), thus presenting an advantage of the dual-satellite record over the MODIS record of GrIS surface hydrology. These smaller lakes tend to drain rapidly earlier in the season (mean date = 8 July for the dual-satellite record) than the larger lakes (mean date = 11 July for the dual-satellite record), although the difference in dates is small, with most draining in early to mid-July (Table 5.2; Figure 5.11). In general, lakes closer to the ice margin tend to drain earlier than those inland (Figure 5.11).

Finally, the impacts of adjusting the thresholds used to define rapidly draining lakes on rapid lake-drainage identification are investigated. Changing the critical volume loss required for a lake to be identified as having drained from 80% to 70% and 90% results in the identification of only six more and four fewer rapid drainage events, respectively. Similarly, changing the critical-refilling threshold from 20% to 10% and 30% results in identifying only eight fewer and five more rapidly draining lakes. However, adjusting the timing over which the volume loss is required has a larger impact, with adjustments from 4 to 3 and 5 days producing 37 fewer and 65 more rapid lake-drainage events, respectively.

**Table 5.2:** Properties of rapid lake-drainage events identified using the satellite datasets individually and when as part of a dual-satellite dataset. Large lakes are ≥ 0.125 km$^2$ (identifiable by MODIS), while small lakes are < 0.125 km$^2$ (omitted by MODIS). "DoY" refers to day of year in 2016.

| Analysis type | Property | Large lakes | Small lakes | Total/ overall |
|---|---|---|---|---|
| Sentinel-2 | Number of drainage events | 45 | 48 | 93 |
| | Percentage of total lakes | 7.5 | 8.0 | 15.5 |
| | Mean drainage date (DoY) ± mean error | 193.4 ± 1.8 | 188.2 ± 1.6 | 190.7 ± 1.7 |
| | Minimum drainage volume ($10^5$ m$^3$) | 0.02 | 0.006 | 0.006 |
| | Maximum drainage volume ($10^5$ m$^3$) | 90.1 | 2.1 | 90.1 |
| | Mean drainage volume ($10^5$ m$^3$) | 7.5 | 0.2 | 3.7 |
| | Median drainage volume ($10^5$ m$^3$) | 1.3 | 0.2 | 0.3 |
| | Total drainage volume ($10^5$ m$^3$) | 337.3 | 11.7 | 349.0 |
| Landsat 8 | Number of drainage events | 30 | 36 | 66 |
| | Percentage of total lakes | 6.6 | 7.9 | 14.6 |
| | Mean drainage date (DoY) ± mean error | 196.8 ± 0.6 | 190.5 ± 0.5 | 193.4 ± 0.5 |
| | Minimum drainage volume ($10^5$ m$^3$) | 0.1 | 0.05 | 0.05 |
| | Maximum drainage volume ($10^5$ m$^3$) | 19.8 | 1.1 | 19.8 |
| | Mean drainage volume ($10^5$ m$^3$) | 4.2 | 0.4 | 2.1 |
| | Median drainage volume ($10^5$ m$^3$) | 1.6 | 0.4 | 0.6 |
| | Total drainage volume ($10^5$ m$^3$) | 126.8 | 14.1 | 140.9 |
| Dual Sentinel-2 and Landsat 8 | Number of drainage events | 79 | 105 | 184 |
| | Percentage of total lakes | 11.4 | 15.2 | 26.7 |
| | Mean drainage date (DoY) ± mean error | 193.1 ± 1.1 | 190.1 ± 1.0 | 191.4 ± 1.1 |
| | Minimum drainage volume ($10^5$ m$^3$) | 0.006 | 0.007 | 0.006 |
| | Maximum drainage volume ($10^5$ m$^3$) | 91.0 | 1.6 | 91.0 |
| | Mean drainage volume ($10^5$ m$^3$) | 7.4 | 0.3 | 3.4 |
| | Median drainage volume ($10^5$ m$^3$) | 1.8 | 0.2 | 3.9 |
| | Total drainage volume ($10^5$ m$^3$) | 586.1 | 31.2 | 617.3 |

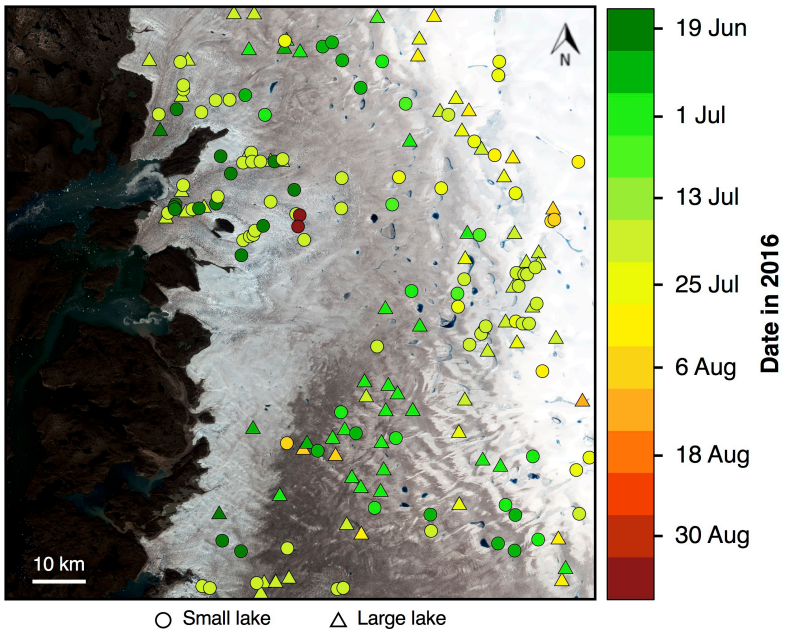



**Figure 5.11:** Dates of rapid drainage events for small (circles) and large (triangles) lakes in 2016. The panel coverage and background are the same as that shown in Figure 5.1. The extreme colourbar values include those dates outside of the range shown (i.e. before 19 June and after 5 September, respectively).

### 5.4.4 Meltwater deliveries and moulin opening by rapid lake drainage

Each rapid lake-drainage event from the dual-satellite record delivers a mean water volume of $3.4 \times 10^5$ m$^3$ (range = 0.006–$91.0 \times 10^5$ m$^3$; $\sigma = 10.2 \times 10^5$ m$^3$) into the ice sheet (Table 5.2; Figure 5.12). Figure 5.12 shows the patterns of meltwater delivery across the region, suggesting that small ($< 0.125$ km$^2$) and large ($\geq 0.125$ km$^2$) rapidly draining lakes are randomly distributed across the region. Figure 5.13 shows that large lakes generally contain more water than small lakes, as might be expected, but also shows that large lakes contain a higher range of water volumes than small lakes, producing an overlap between the lake types for the lower water volume values. Thus, although large lakes each cover a higher area, some large lakes must be relatively shallow, as also suggested by the red to yellow coloured triangles on Figure 5.12.

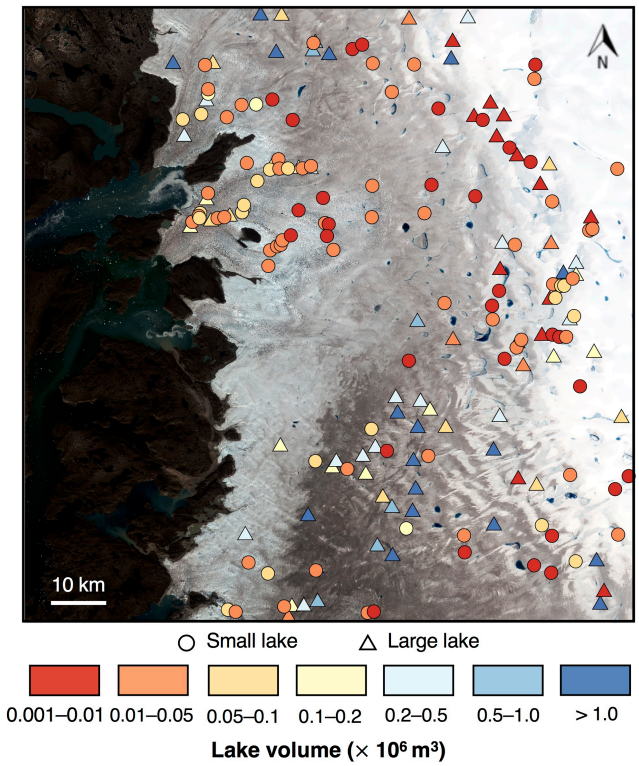



**Figure 5.12:** Lake water volumes measured using the physically-based technique on the days prior to lake drainage, categorised into small (< 0.125 km$^2$ in area; circles) and large lakes (≥ 0.125 km$^2$ in area; triangles). Each point shown is also assumed to represent the location at which a moulin is opened by hydrofracture during rapid lake drainage. The panel coverage and background are the same as that in Figure 5.1.

Using the data from the dual-satellite record, and considering just the water volumes delivered into the GrIS during lake-drainage events (and not subsequently via the moulins opened), the drainage of small (< 0.125 km$^2$) lakes delivers a total meltwater volume of 31.2 × 10$^5$ m$^3$, which is just 5.1% of the total volume (617.3 × 10$^5$ m$^3$) delivered into the GrIS during the drainage of all lakes across the region (Table 5.2). Although this volume is low, small lake-drainage events, like large lake-drainage events, are additionally important because they are associated with the opening of moulins that transport surface meltwater into the GrIS, and perhaps to the bed, for the remainder of the season (Banwell *et al.*, 2016; Koziol *et al.*, 2017). Associating lake drainages with moulin opening in this way means that the dual-satellite record finds an additional 105 moulins (Table 5.2) that would not have been identified by MODIS; this is greater than the total number of moulins associated with large lake-drainage events (79) that could have been identified by MODIS, assuming MODIS can identify all lakes > 0.125 km$^2$, which itself is unlikely (Leeson *et al.*, 2013). For example, Chapter 3 showed that only 42% of the lakes from Landsat 8 were identified by MODIS. Figure

5.14 shows that the moulins opened by the rapid drainage of small lakes allow a higher total volume of meltwater to enter the GrIS than that routed via moulins opened by rapidly draining large lakes; in total, moulins opened by small (large) lakes channel $1.61 \times 10^{11}$ ($1.04 \times 10^{11}$) $m^3$ water equivalent (w.e.) of meltwater into the GrIS interior. Thus, moulins opened by small (large) lakes deliver 61.5% (38.5%) of the total runoff into the GrIS after they were opened. Moreover, moulins opened by small lakes deliver more meltwater into the GrIS than those opened by large lakes across all ice-elevation bands, although this finding is more pronounced at lower elevations than higher elevations, i.e. below and above 800 m a.s.l. respectively (Figure 5.14). The runoff into the moulins opened by small lakes also tends to reach the GrIS interior earlier in the season than that delivered into the moulins opened by large lakes, because these lakes tend to drain earlier (Figure 5.14).

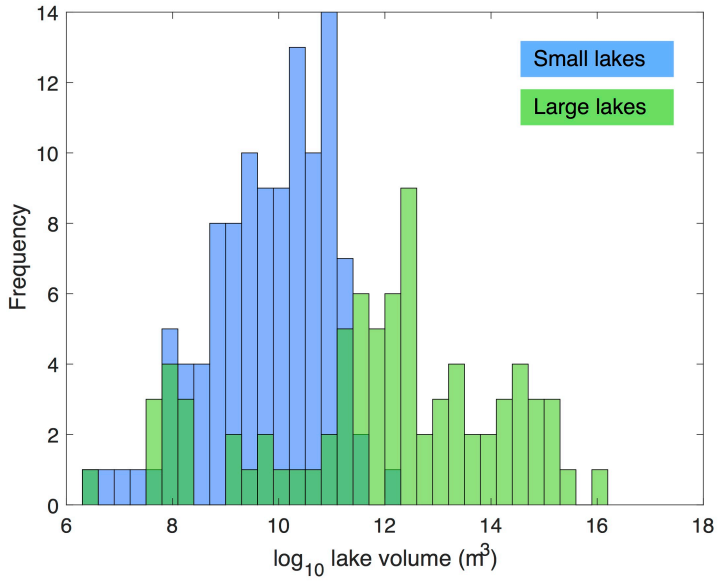



**Figure 5.13:** Frequency distribution of water volumes prior to rapid drainage for small and large lakes to show the lower and more tightly clustered water volumes contained within small lakes compared with large lakes. Water volumes were log-normalised (to the base 10) for presentation.

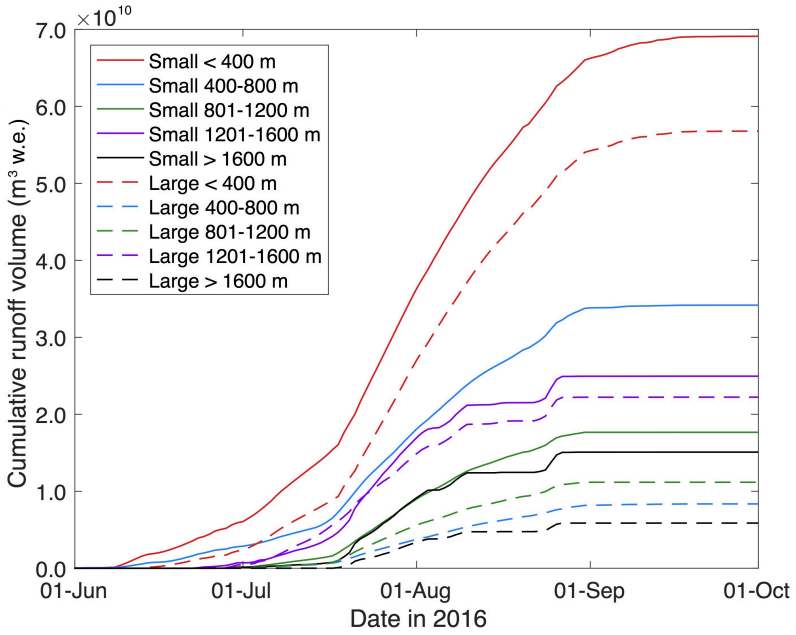



**Figure 5.14:** Cumulative runoff volume (from RACMO2.3p2 data (Noël *et al.*, 2018)) entering the GrIS over the remainder of the melt season via the moulins opened by lake drainage for small (< 0.125 km$^2$) and large (≥ 0.125 km$^2$) lakes for different ice-surface-elevation bands (derived from Howat *et al.* (2014)) shown in m a.s.l. in the legend. Runoff volume is derived within lakes' ice-surface catchments and is assumed to reach the moulin instantaneously on each day, without any flow delay (Section 5.3.6).

## 5.4.5 Inter-annual differences in lake behaviour

### Lake evolution

Inter-annual differences in lake behaviour are assessed between 2016 and 2017. Using Sentinel-2 imagery alone in summer 2017 identifies 512 lakes that grow to at least 0.0495 km$^2$ in size at least once in the season, 87 fewer lakes than with the Sentinel-2 analysis alone in summer 2016. The largest lake size recorded in 2017 is 2.4 km$^2$ (recorded on 2 August 2017), which is some 6.2 km$^2$ smaller than the largest lake size recorded by Sentinel-2 in 2016 (recorded on 21 July 2016). The largest lake volume recorded in 2017 is 8.2 × 10$^6$ m$^3$ (recorded on 27 July 2017), being 3.8 × 10$^6$ m$^3$ smaller than the value from 2016 (recorded on 14 July 2016). The mean lake size across all of the images is 0.04 km$^2$, 0.085 km$^2$ below the threshold reporting size of MODIS (0.125 km$^2$, i.e. two pixels). As for 2016, the FASTER algorithm produces time series to show seasonal volume changes for all lakes in summer 2017 (Figure 5.15). These individual hydrographs are summed to produce values for total lake area and volume change during the whole summer, normalised against the proportion of the region visible, as for 2016 (Figure 5.16). Figure 5.16 shows a similar pattern to that

observed in 2016, with no water in lakes until the beginning of June, then small increases during June, and pronounced increases throughout July, with steady decreases from a peak in early August until the end of the melt season, with most lakes emptying or freezing by the end of September. However, compared with 2016, the maximum total area and volume of lakes is reached later in the season (at the end of July compared with the middle of July). The magnitude of the maximum values is similar between the two years (Figures 5.10 and 5.16).

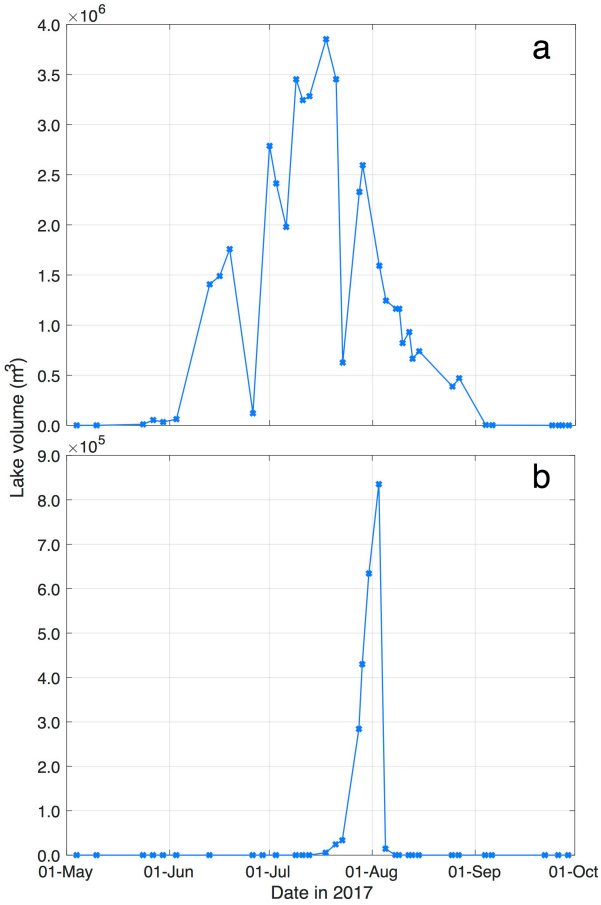



**Figure 5.15:** Sample time series to show 2017 seasonal changes for (a) a non-rapidly draining lake and (b) a rapidly draining lake. Lines connect points without any data smoothing.

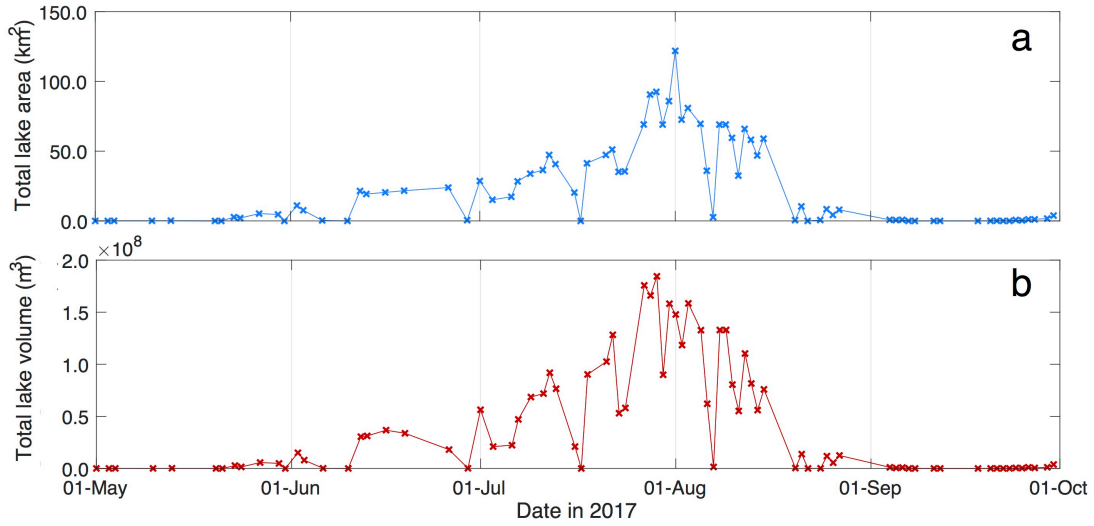



**Figure 5.16:** Estimates of evolution to total lake (a) area and (b) volume across the whole study region during the 2017 melt season after daily values were normalised against the proportion of the region visible on that day (i.e. not obscured by cloud or missing data). Values are derived by dividing the daily total lake area and volume by the portion of the region visible on that day (cf. Figure 5.10 for summer 2016).

## Rapid lake drainage

Table 5.3 shows the results of the identification of rapidly draining lakes in summer 2017 using the Sentinel-2 dataset, and Table 5.4 compares the numbers and properties of rapidly draining lakes in 2017 with the results from 2016 using the Sentinel-2 data alone, rather than the dual-satellite record (Section 5.4.3). A similar total number of rapidly draining lakes is identified (92 in 2017 versus 93 in 2016), although the distribution of this total between small and large lakes differs, with more (fewer) small (large) lake-drainage events identified in 2017 compared with 2016: 58 versus 48 for small lakes and 34 versus 45 for large lakes (Tables 5.2 and 5.3). As in 2016, the Sentinel-2 record in 2017 is able to identify 58 additional small lake-drainage events than would be identified with MODIS (Table 5.3; Figure 5.17). Lakes drain later in 2017 than 2016: Figure 5.17 shows that the drainage dates of many lakes are biased towards the later dates compared with the drainage dates of lakes in 2016 (Figure 5.11). Moreover, rapidly draining lakes in 2017 deliver lower quantities of meltwater into the GrIS interior (both in terms of the total and mean water volumes) during the drainage events themselves than in 2016 (Table 5.4; Figures 5.12 and 5.18).

The error on lake-drainage dates in 2017 is lower than in 2016, most likely resulting from including the Sentinel-2B images in 2017 in addition to the Sentinel-2A images in 2016. Compared with the dual-satellite (Sentinel-2 and Landsat 8) record in 2016, the Sentinel-2 record in 2017 identifies 91 fewer rapidly draining lakes, thus performing similarly to the Sentinel-2 record in isolation in 2016.

Figure 5.18 also highlights this pattern, showing many fewer lake-drainage events identified using the Sentinel-2 data alone compared with the dual-satellite record identification shown on Figures 5.11 and 5.12. The drainage-date errors from the Sentinel-2 record alone in 2017 are also higher (by 0.2 days) than the errors for the dual-satellite record in 2016, suggesting a dual-satellite record holds more potential than Sentinel-2 data used alone.

**Table 5.3:** Properties of rapid lake-drainage events identified using Sentinel-2 in summer 2017. Large lakes are ≥ 0.125 km$^2$ (identifiable by MODIS), while small lakes are < 0.125 km$^2$ (omitted by MODIS). "DoY" refers to day of year in 2017.

| Property | Large lakes | Small lakes | Total/overall |
|---|---|---|---|
| Number of drainage events | 34 | 58 | 92 |
| Percentage of total lakes | 6.6 | 11.3 | 18.0 |
| Mean drainage date (DoY) ± mean error | 199.7 ± 1.3 | 200.9 ± 1.3 | 200.4 ± 1.3 |
| Minimum drainage volume ($10^5$ m$^3$) | 0.2 | 0.2 | 0.2 |
| Maximum drainage volume ($10^5$ m$^3$) | 41.1 | 2.5 | 41.1 |
| Mean drainage volume ($10^5$ m$^3$) | 6.0 | 0.4 | 2.4 |
| Median drainage volume ($10^5$ m$^3$) | 2.8 | 0.2 | 0.4 |
| Total drainage volume ($10^5$ m$^3$) | 204.2 | 20.1 | 224.3 |

**Table 5.4:** Differences in properties of rapid lake-drainage events between 2016 and 2017. Red (black) text indicates values that are lower (higher) in 2017 compared with 2016. Large lakes are ≥ 0.125 km$^2$ (identifiable by MODIS), while small lakes are < 0.125 km$^2$ (omitted by MODIS). "DoY" refers to day of year in 2017.

| Property | Large lakes | Small lakes | Total/overall |
|---|---|---|---|
| Number of drainage events | 11 | 10 | 1 |
| Percentage of total lakes | 0.9 | 3.3 | 2.5 |
| Mean drainage date (DoY) ± mean error | 6.3 ± 0.5 | 12.7 ± 0.3 | 9.7 ± 0.4 |
| Minimum drainage volume ($10^5$ m$^3$) | 0.18 | 0.194 | 0.194 |
| Maximum drainage volume ($10^5$ m$^3$) | 49 | 0.4 | 49 |
| Mean drainage volume ($10^5$ m$^3$) | 1.5 | 0.2 | 1.3 |
| Median drainage volume ($10^5$ m$^3$) | 1.5 | 0 | 0.1 |
| Total drainage volume ($10^5$ m$^3$) | 133.1 | 8.4 | 124.7 |

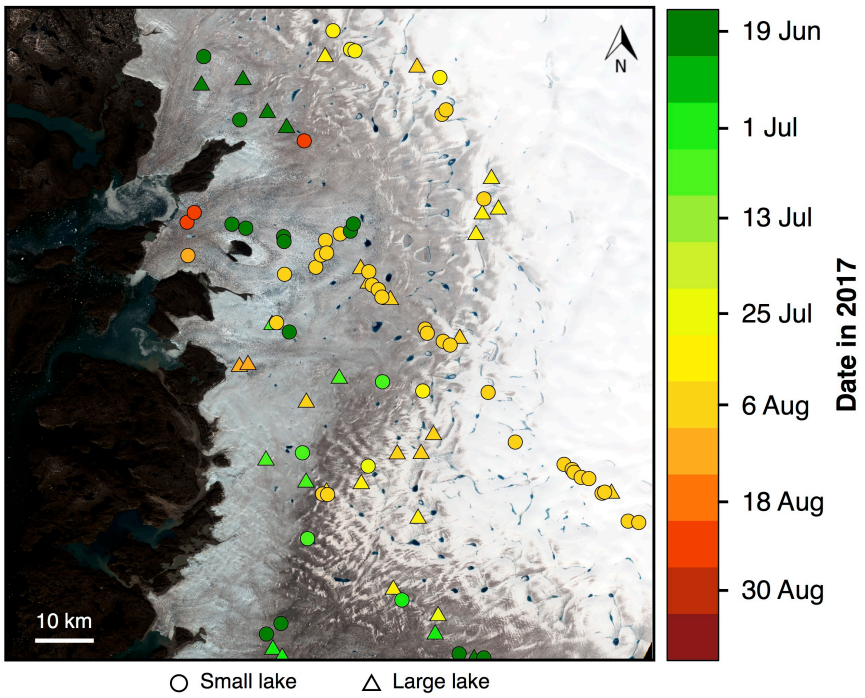



**Figure 5.17:** Dates of rapid drainage events for small (circles) and large (triangles) lakes in 2017. The panel coverage is the same as that shown in Figure 5.1, and the background is a Sentinel-2 RGB image from 3 August 2017 (see Table A.11 for image details). The extreme colourbar values include those dates outside of the range shown (i.e. before 19 June and after 5 September, respectively).

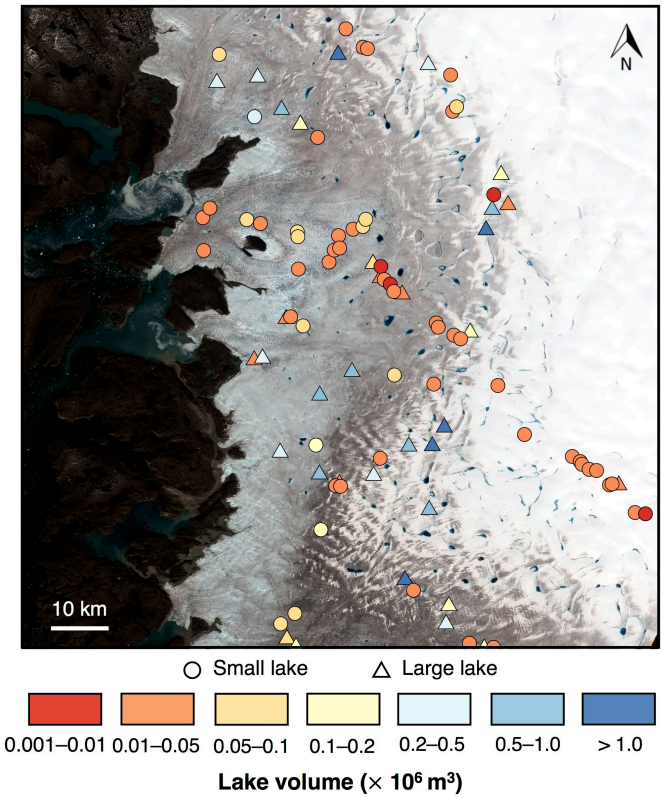



**Figure 5.18:** Lake water volumes measured on the days prior to lake drainage, categorised into small (< 0.125 km$^2$ in area; circles) and large lakes (≥ 0.125 km$^2$ in area; triangles). The panel coverage is the same as that in Figure 5.1 and the background is the same as that in Figure 5.17.

## Relating inter-annual changes in lake behaviour to runoff volumes

RACMO2.3p2 data (Noël *et al.*, 2018) show that, for each day of the season, in 2016 there is nearly always higher runoff than in 2017 (Figure 5.19 (a)); this produces a higher cumulative total in 2016 than 2017 (Figure 5.19 (b)). By the end of August 2016, across the whole region, runoff amounts to 13.0 × 10$^9$ m$^3$ w.e., compared with the lower total of 7.4 × 10$^9$ m$^3$ w.e. by the end of August 2017, meaning 2017 runoff was only 56.9% of the 2016 total. Figure 5.19 also shows that melting is higher earlier in the season in 2016 than 2017, particularly during the middle and end of July. The implications of these differences for lake behaviour are discussed in Section 5.5.4.

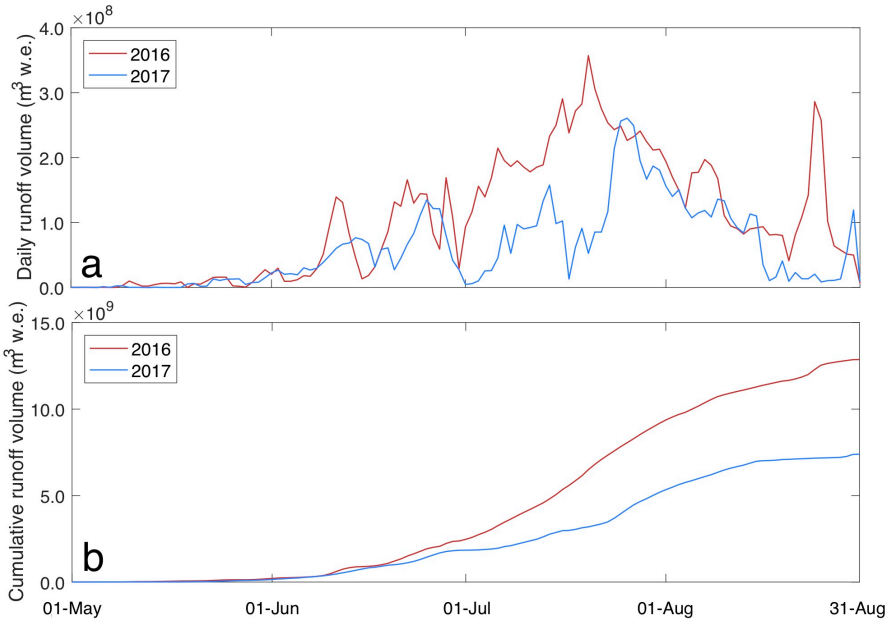



**Figure 5.19:** Comparison of (a) daily and (b) cumulative runoff volumes in the study region, derived from RACMO2.3p2 data (Noël *et al.*, 2018), highlighting the discrepancies between the years.

## 5.5 Discussion

### 5.5.1 Sentinel-2 lake-depth estimates

The first and second aims of this chapter involved trialling and then applying a new method for calculating lake depths from Sentinel-2 imagery. This derived a RMSE of 0.555 m on lake depths calculated with the physically-based method applied to Sentinel-2's red band when compared with lake depths calculated from Landsat 8 using similar physically-based methods (Pope *et al.*, 2016). The physical method was chosen over the empirical one because the empirical method cannot be applied without the site- or time-specific adjustments suggested in previous research (e.g. Sneed and Hamilton, 2007; Pope *et al.*, 2016), and might therefore perform more poorly in other years and/or for other regions of the GrIS. Given that the performance of the two methods was very similar, it therefore seemed most sensible to use the more robust physically-based technique. In addition, the RMSE value obtained here for Sentinel-2 is only slightly higher than the error on lake-depth calculations using the physical method for similar-resolution Landsat 8 data (0.28 m for the red band and 0.63 m for the panchromatic band; Pope *et al.*, 2016). However, the RMSE on Sentinel-2 lake depths is less than half both that produced using the physically-based method applied to coarser-resolution (250 m) MODIS red band data (1.27 m; Chapter 3) and that produced using an empirical depth-reflectance relationship for MODIS (1.47 m; Fitzpatrick *et al.*, 2014). Therefore,

using this record over MODIS imagery produces a much more reliable measure of lake water depths on the GrIS because of the improved spatial resolution. The dual-satellite record is even further strengthened by its high temporal resolution, which approaches that of MODIS (Section 5.5.2).

Despite the low overall error for the physically-based lake-depth calculations from Sentinel-2, different performances were observed for the two validation dates (1 July and 31 July; Section 5.4.1): the depths calculated for Sentinel-2 and Landsat 8 showed closer agreement on 1 July than on 31 July (Figure 5.4). This is likely to be because clouds obscured a large portion of the image from 1 July. Although the lakes used for comparison were cloud-free, there were probable adjacency effects associated with the cloud, which had more of an impact for Sentinel-2 than for Landsat 8. For example, the pixel brightness might have been reduced in locations close to the clouds, consequently producing higher lake depths with the seemingly darker water (Figure 5.4). Similar cloud adjacency effects have been recorded with other satellites, such as MODIS (Feng and Hu, 2016), and Landsat 8 and RapidEye (Houborg and McCabe, 2017). The depths calculated with the physical method on 31 July (Figure 5.4), when there was less cloud cover, are therefore more likely to be true depths than the depths from 1 July when the image was affected by the cloud, even though the 1 July depths appear to be more correct. Assuming this is the case, the results indicate that Sentinel-2 may not entirely accurately record deeper water (> ~3.5 m; Figure 5.4) using the physical method applied to the red band. This is perhaps because the red wavelengths become saturated (i.e. fully attenuated) within the water column at higher depths, a result similar to that observed for lake-depth measurements from WorldView-2 and Landsat 8, and as reported in Chapter 3 (Moussavi *et al.*, 2016; Pope *et al.*, 2016). Alternatively, the presence of clouds on the 1 July image might be indicative of a difference in the atmospheric composition on that day, which could have affected the lake-depth calculations with Sentinel-2, but not to the same degree with Landsat 8. This might be because of the difference in bandwidths between the satellites, or because Landsat 8's panchromatic band (used for calculating lake depths) is less sensitive to the presence of clouds in an image, therefore producing more reliable lake-depth measurements. The effect of clouds on the atmosphere could have been better accounted for if the Sentinel-2 TOA reflectance data had been first converted to BOA (i.e. surface-reflectance) measurements. However, while surface-reflectance data are available for Landsat 8's optical bands, they are not for its panchromatic band, meaning that the lake-depth calculation method used here could not have been applied to generate reliable ground-truth data. It was therefore intentionally decided not to perform this correction on the Sentinel-2 TOA data to allow direct comparisons between the measurements from the two satellites.

### 5.5.2 Lake evolution in summer 2016

The second aim of this chapter was to apply the new methods for calculating lake areas, depths and volumes from Sentinel-2 imagery, alongside existing methods for Landsat 8, within the FASTER algorithm to produce time series for the evolution of all lakes. Applying this algorithm to the dual-satellite record allowed the tracking of the evolution of 690 lakes. The mean and median lake sizes (0.09 $km^2$ and 0.02 $km^2$) were well below the threshold (0.125 $km^2$) of lake size that MODIS can identify. Using a dual-satellite record, it was therefore possible to achieve both high temporal (2.8 days) and spatial resolution (10–30 m). Previous studies (e.g. Selmes *et al.*, 2011, 2013; Fitzpatrick *et al.*, 2014; Miles, K. E. *et al.*, 2017) have acknowledged that MODIS is useful because it can provide very high temporal resolution (up to sub-daily repeat site imaging) since the GrIS's surface hydrology can change quickly. However, because of the coarse spatial resolution, lake area and depth can only be calculated with large errors: for example, Chapter 3 shows that the errors on MODIS lake areas are 0.323 $km^2$ (six times larger than the value derived in this chapter) and the errors on MODIS lake depths are 1.27 m (twice that obtained in this chapter). The minor loss of temporal resolution (i.e. a reduction from daily to 2.8 days) by using the dual-satellite record rather than MODIS therefore seems to be offset by the record's improved accuracy in resolving lake areas and depths.

### 5.5.3 Rapid lake drainage in summer 2016

The third and fourth aims of the chapter were to identify the lakes tracked by the FASTER algorithm that drained rapidly, and to investigate the quantity of runoff reaching the GrIS interior both during the drainage events themselves and subsequently via the moulins opened by rapid lake drainage. This was because recent work (Banwell *et al.*, 2016; Koziol *et al.*, 2017) has shown that the moulins opened by rapid lake-drainage events allow much greater meltwater volumes to reach the subglacial system than the actual drainage events themselves. Most research to date has used MODIS imagery to identify rapidly draining lakes because the high temporal resolution is required to separate rapidly draining lakes from those draining slowly. Although this MODIS-based research has been helpful for quantifying the characteristics of relatively large lakes ($\geq$ 0.125 $km^2$) and the potential controls on their rapid drainage (Box and Ski, 2007; Morriss *et al.*, 2013; Fitzpatrick *et al.*, 2014; Chapters 3 and 4), such work has been unable to study smaller (< 0.125 $km^2$) lakes.

Rapid drainage of both large and small lakes can be identified using the FASTER algorithm with the dual-satellite record. Although the water volumes associated with the drainage of small lakes into the GrIS amount to just 5.1% of the total water volume associated with the drainage of all lakes

across the region, rapid drainage of small lakes is important because, like large lakes, they open-up moulins that can direct surface meltwater into the GrIS interior over the remainder of the season (Banwell *et al.*, 2016; Koziol *et al.*, 2017). With the dual-satellite record, 105 small rapid lake-drainage events were identified, thus providing 105 additional inputs for surface meltwater to reach the ice-sheet interior than would be identified by MODIS; this also assumes all moulin-opening locations would be identified, which they would not, due to the under-reporting of lake numbers by MODIS (Leeson *et al.*, 2013; Chapter 3). The moulins opened by small lake-drainage events are particularly important because in total they deliver over half (61.5%) of the total meltwater delivered via all moulins into the GrIS interior. This is because the small lakes tend to drain earlier in the melt season, meaning that the moulins they create are open for a greater proportion of the melt season, and because smaller lakes tend to be at lower elevations than the larger lakes, where surface melting is higher. In addition, the moulins opened by small lake-drainage events tend to result in higher volumes of runoff reaching the GrIS interior earlier rather than later in the season (Figure 5.14), which may be important because the subglacial system is likely to be less hydraulically efficient at this time (Bartholomew *et al.*, 2010; Sundal *et al.*, 2011; Banwell *et al.*, 2013a, 2016; Chandler *et al.*, 2013; Sole *et al.*, 2013; Andrews *et al.*, 2014). Therefore, by including these rapidly draining small lakes, the FASTER algorithm with the dual-satellite record could be used to provide a better dataset than previously for the testing of lake filling and draining models (e.g. Banwell *et al.*, 2012b, 2013a; Arnold *et al.*, 2014), or alternatively to specify the input locations and water volumes for the forcing of subglacial-hydrology models with much greater confidence than would be possible with MODIS alone. Further work is still required, however, to determine whether the water volumes delivered by these small lakes during the drainage process are capable of temporarily pressurising the subglacial drainage system, such that ice velocity speed-up events may occur, and to determine whether the associated deviations from background stresses in the far field would be enough to open moulins outside the basins of small lakes (Hoffman *et al.*, 2018).

Over the 2016 summer, 27% of all lakes detected in the region drained rapidly, compared with 21% that drained rapidly in 2014 across the slightly smaller but also predominantly land-terminating Paakitsoq region analysed in Chapters 3 and 4. However, since Chapters 3 and 4 used MODIS imagery, they omitted the rapid drainage of small lakes, which could explain the lower percentage if it is assumed that these small lakes are more likely to drain rapidly than the large ones, relative to the total numbers of lakes in each category. The 27% value in this chapter compares well with that of 22% from Miles, K. E. *et al.* (2017), who also tracked changes to small lakes using a similar tracking threshold to that used here, albeit for a different combination of satellite platforms (Landsat 8 and Sentinel-1), and for a larger region of west Greenland in summer 2015. Finally, the error on rapid drainage dates in this chapter (± 1.1 days) is smaller than that identified by Miles, K. E. *et al.*

(2017) (± 4.0 days); this is likely to be a result of the different temporal resolution of Sentinel-1 compared with Sentinel-2, and because Miles, K. E. *et al.* (2017) were forced to discard some images before conducting their analysis, reducing the average temporal resolution possible with that satellite combination and so the ability to identify rapid lake drainage dates confidently. Thus, although Sentinel-1 can image through clouds, the Sentinel-1 record suffers from separate issues that offset this advantage. The dual-satellite record in this chapter therefore offers an additional advance over their dual-satellite method since it can calculate the water volumes delivered into the GrIS by rapid lake drainage (because of using optical satellite data), whereas Miles, K. E. *et al.*'s (2017) study could only identify lake-area changes using the Landsat 8 and Sentinel-1 combination.

### 5.5.4 Inter-annual differences in lake behaviour

The final aim of this chapter involved applying the FASTER algorithm to the Sentinel-2 imagery alone in 2017 without using Landsat 8 imagery. There were two reasons for this: first, it allowed a conclusion to be reached on whether Sentinel-2 by itself in 2017 (when Sentinel-2B as well as Sentinel-2A imagery were available) produces a suitable record of lakes on the GrIS; second, it permitted inter-annual comparisons of lake behaviour in the study region. The results showed that, despite adding Sentinel-2B imagery to yield an improved temporal resolution record compared with Sentinel-2A alone in 2016 (1.9 days in 2017 versus 3.9 days if just using Sentinel-2 data or 2.8 days for the dual-satellite record in 2016), the Sentinel-2 record by itself performed similarly to the Sentinel-2A record alone in 2016. Additionally, despite the improved temporal resolution of Sentinel-2 data in 2017, only a minor improvement (in terms of the error on drainage dates) was found, reducing the error from ± 1.7 days to ± 1.3 days (Tables 5.2 and 5.3). This suggests that future studies of GrIS hydrology using high-resolution satellite data should aim to mosaic a record from Landsat 8 and Sentinel-2 rather than simply using Sentinel-2 alone, as greater insights can be provided by using the two datasets together. This is likely to be because of the different satellite pass times of Landsat 8 and Sentinel-2.

The results also showed marked inter-annual differences in the behaviour of lakes, with lakes reaching smaller sizes (both in terms of their areas and volumes) in 2017 compared with 2016, and tending to drain later in the season (Table 5.3; Figure 5.17). Lower total volumes of meltwater were also delivered into the GrIS during the drainage events themselves in 2017 compared with 2016 (Table 5.4; Figure 5.18). These differences can possibly be explained by differences in the runoff quantities within the study region between the two years (Figure 5.19). Most lake-drainage events, in both years, tend to occur around the time of peak melt. During this time, water may have been

able to reach the ice-sheet bed, so perturbing ice velocities from steady-state values, and increasing the propensity for rapid lake drainage (Stevens *et al.*, 2015).

## 5.6 Summary and conclusions

- This chapter presented the results of the first approach to combine two optical satellite datasets (from Sentinel-2 and Landsat 8) to generate the highest spatial- and temporal-resolution record of lake area and volume evolution on the GrIS to date. To achieve this, the increasing availability of medium- to high-resolution satellite imagery was exploited, and then combined with newly-available data and an adapted version of the fully-automated lake-tracking algorithm from Chapter 3.
- The resultant FASTER algorithm allows lake areas and volumes to be calculated with high accuracy from Sentinel-2. For lake area, the RMSE is 0.007 $km^2$ when compared with that derived from Landsat 8 data, which is nearly fifty times lower than the error associated with MODIS derived in Chapter 3. For lake depth, the RMSE is 0.555 m, under half that associated with MODIS derived in Chapter 3.
- The techniques for lake area and depth calculation from Sentinel-2, when combined with similar techniques applied to Landsat 8 data, yielded a dual-satellite record with comparable temporal resolution (2.8 days) to that of MODIS (daily). Thus, the FASTER algorithm applied here reduces the large errors associated with calculating lake depth and, to a lesser extent, lake area using the FAST algorithm for MODIS imagery in Chapter 3. In addition, the FASTER algorithm provides a similarly frequent site revisit time as MODIS, allowing rapid lake drainage to be identified with low error (± 1.1 days). This chapter shows that using both sets of high-resolution satellite imagery together provides better insights into lake filling and drainage than using either one in isolation, and that this was the case even in 2017 when Sentinel-2B as well as Sentinel-2A data were available. In the future, the dual-satellite record presented here is therefore likely to be able to replace, or at least supplement, the MODIS record used to investigate lakes on the GrIS.
- This chapter also took advantage of new, and increasingly reliable, downscaled regional climate-model (RACMO2.3p2) output data (Noël *et al.*, 2018) to provide insights into the volumes of surface meltwater entering the GrIS's englacial or subglacial hydrological systems after moulin opening was identified using the FASTER algorithm. The results show that the water volumes released into the GrIS by small lakes during the lake-drainage events themselves are small (only 5.1%) relative to the volumes released by all lake-drainage events, suggesting small lakes are not important in this sense. However, of the total water volume that subsequently reaches the GrIS interior via all moulins opened-up by lake drainage (from

both large and small lakes), moulins opened-up by small lakes deliver 61.5% of the total water volume. This suggests that small lakes are important to include in future remote-sensing and modelling studies.

- The RACMO2.3p2 runoff data (Noël *et al.*, 2018) were also used to investigate the influence of runoff on inter-annual patterns of lake drainage. In 2017 compared with 2016, lakes reached lower sizes (in terms of their areas and volumes) and drained later. The runoff data showed that these results are likely to be caused by differing total runoff quantities produced in the two years, with the runoff volumes being much higher in 2016 than 2017. This suggests that there may be some relationship between rapid lake-drainage dates and melt volume, such as potentially greater volumes of meltwater reaching the ice-sheet bed in 2016 compared with 2017, and so increasing the propensity for hydrofracture by impacting basal sliding and uplift rates (Stevens *et al.*, 2015).
- In summary, the FASTER algorithm holds great potential for generating novel insights into lake behaviour on the GrIS from remote sensing, including for small lakes that change quickly (cf. Miles, K. E. *et al.*, 2017). Future work should focus on applying the FASTER algorithm to wider areas of the GrIS and comparing the results with increasingly available and reliable high temporal resolution ice-velocity data (e.g. Joughin *et al.*, 2018) to investigate the influence of lake drainage on the observed patterns of intra- and inter-annual velocity variations across the GrIS. Moreover, the high spatial resolution record could be used to identify the potential controls on the initiation of rapid lake drainage, something that was impossible with MODIS data, perhaps due to the data's coarse spatial resolution (Chapter 4). Finally, the water volumes delivered into the GrIS during the rapid lake-drainage events identified with this record, the moulins that are assumed to open during such events, and the subsequent runoff that enters the GrIS via these moulins, could be used as forcing or testing data for subglacial-hydrology models (e.g. Hewitt, 2013; Banwell *et al.*, 2016) and linked hydrology-ice dynamics models (Koziol and Arnold, 2018).

# Chapter 6

# Conclusions

For almost two decades, rapidly draining lakes on the surface of the GrIS have been the subject of intense research because they can influence both the SMB and dynamic ice loss from the ice sheet. This thesis has built on this research through developing and using new tools to better quantify the volumes of water that accumulate in lakes, to identify more precisely if, when and where lakes drain, and to investigate the causes of rapid lake drainage across the GrIS. This thesis took advantage of existing and newly-available satellite datasets, notably those from MODIS, Landsat 8 and Sentinel-2, combined these data with recent developments in satellite-imagery analysis and techniques for tracking lakes, and analysed the results alongside other remotely-sensed, gridded data products. The knowledge acquired and the techniques developed in this study will help to constrain models of the GrIS's supraglacial-hydrological system and coupled models that simulate the effect of hydrology on ice flow, and therefore the ice sheet's mass balance, in the present and future.

## 6.1 Outcomes of research aims

In Chapter 1, an overall research objective was identified for this thesis, which was divided into three aims forming the basis of Chapters 3–5. This section presents a summary of the outcomes and implications of the results from each of these aims.

### 6.1.1 Aim 1 – Develop, test and apply a fully-automated method for tracking lake area and volume changes with MODIS (Chapter 3)

To develop an improved understanding of the behaviour of rapidly draining lakes on the GrIS, a new method was needed to track changes to lake areas and volumes at high temporal frequency.

MODIS imagery was initially selected because its high temporal resolution, offset against its lower spatial resolution (250 m), allowed rapid lake drainage (occurring in hours to days) to be detected with confidence. Previous work with MODIS had automatically monitored only changes to lake areas, and not lake depths or therefore volumes, for sequences of imagery, which restricted the quantity of information that could be generated from the satellite's imagery. To overcome this shortfall, a fully-automated method for tracking changes to lake areas, depths and volumes (the FAST algorithm) was successfully developed, validated and applied to two sections of the GrIS, and this was reported in Chapter 3. The initial stage of this work involved a comprehensive appraisal of different methods for calculating lake areas from MODIS imagery by comparing the different calculated areas against those generated from higher-resolution Landsat 8 imagery; this work found that dynamic thresholding of the red band produced the closest statistical agreement between the two datasets (RMSE = 0.323 $km^2$). This method for calculating lake areas was successfully combined with a physically-based lake-depth calculation technique, developed originally for ASTER imagery (Sneed and Hamilton, 2007), and subsequently applied to Landsat 7 (Arnold *et al.*, 2014; Banwell *et al.*, 2014) and Landsat 8 imagery (Pope *et al.*, 2016). Statistical comparisons of depths calculated with MODIS and Landsat 8 showed that lake depths and volumes could be calculated accurately with MODIS (RMSE = 1.27 m), justifying the inclusion of the physically-based technique in the FAST algorithm, which can be applied over wide areas of the GrIS and in multiple years without site- or time-specific adjustments.

Having verified the accuracy of the MODIS-derived lake area, depth and volume calculations, the automatic methods were incorporated into the new FAST algorithm, which is a comprehensive, fully-automated lake-tracking method that was developed, as part of this work, to document intra-seasonal lake area and volume changes, and to identify the location, timing and magnitude (in terms of water volumes) of rapid lake-drainage events. A set of outputs was generated by applying the FAST algorithm to the Paakitsoq and Store Glacier regions of west Greenland in summer 2014, showing the algorithm's potential for investigating supraglacial processes on both land- and marine-terminating sectors of the GrIS. For example, while existing surface-hydrology models of the GrIS (e.g. Banwell *et al.*, 2013a, 2016; Arnold *et al.*, 2014; Koziol *et al.*, 2017) prescribe an empirically-based "fracture-area threshold" parameter (when a critical lake water volume is divided by the ice thickness beneath a lake) to predict the location, timing and magnitude of rapid lake drainage, the results presented in Chapter 3 provided evidence against the use of such a method. More specifically, the water volumes contained within lakes prior to rapid drainage showed no statistical relation to the underlying ice thickness ($R^2$ = 0.03 for Paakitsoq and $R^2$ = 0.00 for Store Glacier). This suggested that a more thorough investigation was needed of whether factors other

than water volume explain the incidence of rapid lake drainage, leading to the conception of the research in Chapter 4.

In summary, the development and initial applications of the FAST algorithm presented in Chapter 3 showed that it holds great potential for generating new information on the supraglacial hydrology of the GrIS, which will be useful for constraining models of lake filling and drainage (e.g. Banwell *et al.*, 2012b, 2013a, 2016; Arnold *et al.*, 2014; Koziol *et al.*, 2017).

### 6.1.2 Aim 2 – Investigate the controls on rapid lake drainage on the Greenland Ice Sheet (Chapter 4)

The second aim of this thesis involved another application of the FAST algorithm to derive information on the potential controls on the incidence of rapid lake drainage, an area of study that had previously received only limited attention. The FAST algorithm outputs from Chapter 3, notably the location, timing and magnitude of rapid lake-drainage events in summer 2014 for the Paakitsoq and Store Glacier regions, were analysed alongside 23 factors that were perceived to act as potential controls on rapid lake drainage. These factors were carefully chosen based either on new or existing hypotheses surrounding the triggering of rapid lake drainage, such as the role of water inputs to moulins located proximal to lakes prior to hydrofracture and rapid drainage (Stevens *et al.*, 2015). Lakes were classified into two types using the FAST algorithm: those which drained rapidly and those which did not (i.e. which drained slowly or froze over) and then each potential control was analysed using an EDA statistical framework (comprising bivariate and multivariate analyses), for each of the lake types.

Among the potential controls investigated, non-rapidly draining and rapidly draining lakes were identified as being statistically indistinguishable in all cases, except in terms of their areas and, with slightly lower statistical confidence, their volumes. This suggested that both lake types were drawn from the same statistical population. In the latter cases, non-rapidly draining lakes were, on average, larger in area and volume than rapidly draining lakes. This adds further support to the finding from Chapter 3 that the use of the empirical fracture-area threshold method for predicting rapid lake drainage in modelling studies may not be effective. However, because of the statistical similarity of the other potential controls between the two lake categories, no support was found for the inclusion of an alternative, deterministic, statistically-supported method for predicting rapid lake drainage in such models.

The results regarding the statistical similarity of the two lake types have several possible explanations. First, it is plausible that there is indeed a control on rapid lake drainage but that it was

simply not identified using the approach and method described in Chapter 4, perhaps because the control's potential was not identified at the outset, and so it was omitted from the EDA. If this were the case, a search for other potential controls would be useful. Second, it is conceivable that a control was included in the EDA but was simply not important in summer 2014 in the study regions. If this were the case, a wider geographical and temporal exploration of the controls on rapid lake drainage for different regions of the GrIS and in different years would be helpful (Section 6.3.5). Third, the interplay of the controls may have been too difficult to elicit at the spatial and temporal scales of the data used in Chapter 4: for example, the ice-surface strain rates were derived using the background winter ice-velocity (MEaSUREs) dataset (30–90 m resolution, depending on data availability), and the runoff data were derived from the RACMO2.3 climate model (1 km resolution). Therefore, a future study that conduced a similar investigation using newer, higher spatial and temporal resolution datasets may be able to reveal the controls on rapid lake drainage more successfully, if they exist. In such work, the inclusion of high spatial and temporal resolution ice-velocity data would be critical. Alternatively, more field studies of individual or groups of lakes, including detailed monitoring of the processes in their supraglacial and subglacial catchments, may help identify possible controls. Finally, it is possible that rapid lake drainage has a strong stochastic element, bearing no relation to the controls that were investigated in Chapter 4 or to other, similar, untested controls. This could perhaps help to explain why some lakes are observed to change their drainage modes inter-annually on the GrIS (Selmes *et al.*, 2013; Fitzpatrick *et al.*, 2014).

In summary, Chapter 4 presented a comprehensive examination of the controls on rapid lake drainage on the GrIS, but was unable to find any statistically significant drivers of the process. Thus, although a step forward has been made towards research that seeks to elicit the controls on rapid lake drainage in this study, further work is still required.

### 6.1.3 Aim 3 – Develop and apply a method for fully-automated, dual-satellite (Sentinel-2 and Landsat 8) lake tracking (Chapter 5)

The results of Chapters 3 and 4 suggested that greater knowledge of rapidly draining lakes on the GrIS may be gained if a remote-sensing record were capable of imaging the GrIS surface at both higher spatial and temporal resolutions than previously. For example, the controls on rapid lake drainage in Chapter 4 may have been unidentifiable because of the coarse spatial resolution dataset offered by MODIS, notwithstanding the satellite's high temporal resolution that allowed rapid lake drainage dates to be identified with confidence. The final aim of this thesis was therefore to develop and use an approach involving a dual-satellite record, notably with Landsat 8 and Sentinel-2 data, to monitor lakes in fine spatial detail (10–30 m) and at high frequency (average ~2.8 days site revisit

time), overcoming a common issue in satellite remote sensing whereby high spatial resolution must be traded-off for low spatial resolution, or vice versa.

The first stage of this analysis involved deriving a new method for automatically calculating lake depth and therefore volume using Sentinel-2 images, and both physically- and empirically-based methods were tested for this purpose. The same physically-based method for calculating lake depth that was incorporated into the FAST algorithm using MODIS (Section 6.1.1) was found to reliably estimate lake depths using Sentinel-2, when depths were compared with contemporaneous Landsat 8 measurements (RMSE = 0.56 m). Although the physically-based method was slightly less accurate than the best-performing empirically-based method, it is more suitable since it does not require site- or time-specific tuning. This method for calculating lake depth from Sentinel-2 and Landsat 8 data, together with the NDWI technique for deriving lake areas, were included in a new iteration of the FAST algorithm called the FASTER algorithm, which allows automatic lake tracking and rapid lake-drainage identification using the dual-satellite record.

The FASTER algorithm using the dual-satellite record presents numerous additional advantages over previous automatic lake-tracking methods for lakes on the GrIS. First, it can calculate lake areas, depths and volumes more accurately than MODIS. Second, it can identify many more lake-drainage events, with lower errors on the dates of drainage, than would have been possible with either of the Landsat 8 or Sentinel-2 satellite records in isolation, due to their lower temporal resolution, or with MODIS, due to its inferior spatial resolution. Third, because of the high spatial resolution of the dual-satellite record, the drainage of small lakes (i.e. < 0.125 $km^2$, not identifiable by MODIS) can also be identified; moreover, assuming moulins are opened at these locations by hydrofracture during rapid lake drainage, more input locations for water to enter the GrIS can be recognised than with MODIS.

In a similar way to the FAST algorithm, the FASTER algorithm can be used automatically to investigate intra- and inter-annual patterns of lake evolution on the GrIS, with the output data being useful for combining with other remotely-sensed datasets, including ice-velocity data, to investigate the relation between lake drainage and ice dynamics over different timescales. To demonstrate the potential of the FASTER algorithm, in Chapter 5, it was applied to a large, predominantly land-terminating region of west Greenland in summers 2016 and 2017, and the outputs from this application were combined with downscaled climate-model (RACMO2.3p2) output data. For summer 2016, this analysis showed that the total water volume drained by small (< 0.125 $km^2$) lakes is only a small fraction (5.1%) of the total water volume drained by all lakes during the times of drainage. However, over half (61.5%) of the subsequent water entering the GrIS via the moulins opened by rapidly draining lakes enters via the moulins opened by small lakes. This suggests that

small lakes should be included in future remote-sensing and numerical modelling studies. Finally, inter-annual (2016 versus 2017) changes in lake behaviour (i.e. lake drainage dates and lake volumes prior to drainage) identified by the FASTER algorithm were explained by combining outputs from the FASTER algorithm with the climate-model data, showing that the timing and quantity of runoff across the whole region affects the incidence of lake drainage.

The development of the FASTER algorithm, and its initial applications in Chapter 5, show its value and potential for investigating the complex supraglacial hydrology of the GrIS in finer detail and over single or multiple seasons, which was not possible with previously existing remote-sensing techniques.

## 6.2 Synthesis of conclusions

The outcomes described above show the success of this thesis at achieving the overall objective of improving knowledge of the behaviour of rapidly draining lakes in west Greenland in recent years, as well as developing a better understanding of the potential causes of such behaviour. Collectively, this research underlines the high value of remote sensing within glaciology since the insights in this study have only been possible through the investigation of patterns and processes operating over much wider spatial and temporal scales, and for much larger samples of lakes, than can be identified or investigated with fieldwork. This work has added to a growing number of studies that show the complexity of the GrIS's supraglacial hydrology, both temporally and spatially. For example, while the approach was capable of identifying the potential control(s) on rapid lake drainage on the GrIS, it failed to find evidence that such controls actually caused hydrofracture and rapid lake drainage, suggesting that the supraglacial system may behave in an unpredictable, stochastic manner. As a consequence, precisely where and when rapid lake drainage occurs remains one of the weaker components of models of the GrIS's surface hydrology. The reliability and predictive power of numerical modelling is therefore being restricted by the lack of specific process-based understanding of hydrofracture. Looking ahead, however, the new fully-automated FAST and FASTER algorithms presented in Chapters 3 and 5 provide robust, physically-based methods to understand the dynamic supraglacial-hydrological system of the GrIS in better detail within and between years for different sectors of the GrIS. Consequently, with further applications of the techniques presented in this thesis and the resultant developments to the theoretical understanding of lakes on the GrIS, novel insights will be offered into surface hydrology, which will ultimately allow improved estimates of water runoff and dynamic ice discharge from the GrIS over the coming decades and centuries.

## 6.3 Future directions of research

This research suggests that the future directions described below may significantly improve knowledge of both the supraglacial hydrology of the GrIS and other ice masses.

### 6.3.1 Improving the calculations of lake depth and volume

While the physically-based technique for calculating lake depth, which was incorporated into the FAST and FASTER algorithms, provides reliable estimates of lake depth using MODIS and Sentinel-2 imagery (with Landsat 8 imagery used as ground-truth data), there are several limitations in this method. These relate to the effect of dissolved matter in the water column and the disturbance of a lake's surface by wind, both of which are ignored, and differences between the albedo at the lake bottom and that of the surrounding ice, which are assumed to be identical (Pope *et al.*, 2016). Although these effects are likely to be small in Greenland (Pope *et al.*, 2016), they require more careful quantification, especially if the same technique were to be used elsewhere, such as on Himalayan debris-covered glaciers. In addition, while Landsat 8 data were used in this study as ground-truth measurements for the MODIS and Sentinel-2 lake-depth calculations, future work could employ higher-resolution WorldView imagery (Moussavi *et al.*, 2016) or high-resolution DEM measurements from the Arctic DEM to test lake-depth measurements.

### 6.3.2 Developing the lake-tracking algorithms

Although the FAST and FASTER algorithms are among the most comprehensive methods for tracking changes to lake areas, and the only methods for continuous tracking of lake volumes, from optical imagery, further improvements are possible. One such improvement would involve separating non-rapidly draining lakes into those that drain slowly and those that freeze-over. However, no automatic method for such separation exists; current methods instead use climate data (Selmes *et al.*, 2013) or manual methods (Miles, K. E. *et al.*, 2017) for such classification. Thus, future work on developing a technique for this purpose would be valuable.

Additionally, while the analysis here focused solely on optical satellite data, a combination of Sentinel-1 and Sentinel-2 imagery would be likely to produce significantly improved temporal resolution because of Sentinel-1's ability to image through clouds, which visible/NIR sensors cannot (Chapters 3 and 5; Selmes, 2011; Selmes *et al.*, 2011; Johansson and Brown, 2012). If such a dual-satellite approach were used, Sentinel-1 lake-volume estimates could be derived using an area-to-volume scaling relationship from the Sentinel-2 data, particularly because of the strong

association between lake areas and volumes identified in this thesis (Chapters 3 and 5). This would build on the work of Miles, K. E. *et al.* (2017) by offering lake-volume estimates and improved temporal resolution over the optical data when used in isolation. However, this would also require an automated method for calculating lake areas from Sentinel-1, rather than using the optical imagery to guide the radar-based lake area classifications, as in Miles, K. E. *et al.* (2017). Moreover, with the increasing availability of data from other optical satellites, such as Landsat 9 and Landsat 10 (with planned launch dates of December 2020 and 2027 or 2028, respectively), there is great potential for remote sensing to offer even greater insights into changes to lake behaviour on the GrIS. Finally, since many satellite data are now distributed at near-real time frequency, it would be possible to adapt the algorithms for real-time tracking of lakes on the GrIS. Then, assuming the controls on rapid lake drainage could be determined by future studies (Section 6.3.5), it would be possible to combine the tracking of lakes with the mechanism that initiates rapid lake drainage to produce a predictive, deterministic, real-time model for rapid lake drainage.

### 6.3.3 Applying the lake-tracking algorithms elsewhere in Greenland

This thesis involved applying the FAST and FASTER algorithms to regions of west Greenland in the summers of 2014, 2016 and 2017, since west Greenland has been the focus of many previous remote-sensing studies, with which the results of this thesis could be compared. However, recent hydrological research has begun to examine other areas of the GrIS, specifically the north-west (Gledhill and Williamson, 2018; Macdonald *et al.*, 2018) and south-east (Everett *et al.*, 2016), which is necessary as these areas are likely to see particularly extensive inland progression of lakes in the future (Leeson *et al.*, 2015; Ignéczi *et al.*, 2016). Thus, examining recent behaviour of lakes in these regions, including inter-annual changes to rapid lake drainage, would help with first-order projections of whether lakes forming further inland in the future would be able to drain (e.g. Poinar *et al.*, 2015), perhaps helping to determine the influence of these inland lakes on ice dynamics.

The algorithms developed in this study were applied only to grounded portions of the GrIS. However, lake behaviour on Greenland's ten floating ice tongues (Moon *et al.*, 2012) could be investigated using the fully-automated methods presented here, reducing the time required compared with manual studies, and so helping to verify whether recent results from a study on Petermann Glacier, north-west Greenland (Macdonald *et al.*, 2018), apply more widely. The FAST and FASTER algorithms could also be used across the entire ablation zone of the GrIS, assuming sufficient time and computational power, with such uses perhaps generating valuable testing data for the processes of lake filling and drainage included in GrIS surface-hydrology models (e.g. Banwell *et al.*, 2013a, 2016; Arnold *et al.*, 2014; Koziol *et al.*, 2017). Finally, this thesis did not

specifically consider the influence of lakes on the GrIS's velocity structure; however, with increasingly reliable, high-resolution velocity maps becoming available (e.g. Joughin *et al.*, 2018), research using FAST and FASTER could focus more comprehensively on assessing the impact of lake drainage on the patterns of intra- and inter-annual velocity variations across the GrIS.

### 6.3.4 Applying the lake-tracking algorithms to other ice masses

Outside Greenland, the FAST and FASTER algorithms could be used for monitoring lakes on other ice masses. For example, lakes are now known to form on the surface of the grounded Antarctic Ice Sheet and many of its buttressing ice shelves, with implications for ice-shelf instability and break-up (e.g. Banwell *et al.*, 2013b, 2014; Banwell and MacAyeal, 2015; Langley *et al.*, 2016; Banwell, 2017; Bell *et al.*, 2017; Kingslake *et al.*, 2017). If a sufficient quantity of cloud-free imagery were available in Antarctica, or if optical imagery could be combined with radar imagery that images through clouds (Section 6.3.2), the algorithms will be valuable for automatically tracking changes to lakes there. Finally, since lakes form and drain periodically on Himalayan debris-covered glaciers (e.g. Benn *et al.*, 2001, 2017; Miles, E. S. *et al.*, 2017), even though they are smaller than those on the GrIS, high spatial resolution satellite imagery could be used, such as WorldView or Planet Labs data, to track lake filling and drainage, and subsequently to generate improved knowledge of debris-covered glacier hydrology.

### 6.3.5 Investigating the controls on rapid lake drainage

Despite the capability of FAST and FASTER for identifying rapid lake drainage, no single control on the triggering of lake drainage was identified. Future work should verify whether these results apply for multiple years and for other areas of the GrIS. Alternatively, remote-sensing studies might attempt to include higher spatial and temporal resolution data in the analysis: for example, summer strain-rate data should be included rather than background winter ice-velocity data (and strain rates derived therefrom) as used here, or climate-model output data distributed on finer spatial grids could be incorporated. Detailed field studies monitoring processes both at lakes (such as lake filling and two- or three-dimensional strain rates), as well as in lake catchments (such as the routing of water into crevasses nearby), might reveal whether controls on lake drainage can only be discovered at spatial resolutions comparable to that of the width of the fracture formed by the lake-drainage process (metres to tens of metres). Such fieldwork should be directed towards a lake that changes its drainage mode inter-annually, to determine how local and synoptic inter-annual changes affect the timing and magnitude of lake drainage (Selmes *et al.*, 2013; Fitzpatrick *et al.*, 2014).

### 6.3.6 Improving understanding of Greenland Ice Sheet hydrology

The discussion above in Section 6.3 has highlighted future-research avenues to build on the new methods and results offered by this thesis. In particular, they have shown that there remains still an urgent need for better knowledge about the precise behaviour of the GrIS's supraglacial system, whether lakes will be able to drain inland in the future, and, if so, how water delivery through the ice and to the bed will impact subglacial-drainage development (e.g. Bartholomew *et al.*, 2011a; Doyle *et al.*, 2014; Meierbachtol *et al.*, 2016; Andrews *et al.*, 2018), cryo-hydrologic warming (Phillips *et al.*, 2010, 2013; Poinar *et al.*, 2017b) and viscous heat dissipation (Mankoff and Tulaczyk, 2017). The drainage of inland lakes may also have implications for the evacuation of subglacial solutes and sediments to the ocean, with potential consequences for ocean fertilisation and productivity (e.g. Hawkings *et al.*, 2015, 2016).

To understand such processes, more complex, three-dimensional models need to be developed for the whole of the GrIS's hydrological system, including for both land- and marine-terminating systems, with their markedly different velocities of ~100 m $a^{-1}$ and > 1000 m $a^{-1}$ (Nienow *et al.*, 2017). This is because it is theoretically conceivable (e.g. Kamb, 1987) that there are variations in the response of these two systems to the input of large volumes of surface meltwater during lake drainage, but this requires verification using further observations and modelling (e.g. Moon *et al.*, 2014). These holistic ice-sheet-wide hydrological models should include components to fully replicate the complete seasonal and inter-annual evolution of lakes from snow and ice (e.g. Law, 2018). The fully-automated methods developed in this thesis, particularly in the case of the FASTER algorithm with its low errors on lake areas, depths and volumes, hold the potential to provide valuable testing data (i.e. for lake filling and drainage) and driving data (i.e. the locations and timings of meltwater deliveries) for such hydrological models in the present day. Ultimately, if contemporary hydrological observations can be reproduced using such models, greater confidence would be afforded in the ability of these models to predict future changes to the GrIS's hydrology and, assuming this knowledge can be coupled with models for basal sliding (e.g. Koziol and Arnold, 2018), future ice-sheet dynamics, runoff and thus sea-level change.

## 6.4 Concluding remarks

With an ongoing and accelerating mass loss from the GrIS, it is crucial to constrain the processes responsible for the ice loss in the present day, in order to improve estimates of future runoff and calving from the ice sheet. While fundamental developments have been made towards understanding the contemporary drivers of the loss, and it is now recognised that hydrology plays

an important role, significant uncertainties still surround the way in which rapidly draining lakes on the GrIS affect the mass loss both today and in the future. A part of this uncertainty surrounds precisely why lakes drain in the present day, thus making it difficult to predict when and where lakes are likely to drain in the future. This means that the future locations of rapid lake drainage cannot be incorporated into predictive models of GrIS hydrology and its coupling with ice dynamics, limiting their ability to be forced confidently into the future. Therefore, if extra knowledge can be developed of the processes operating in the GrIS's supraglacial system, alongside coincident improvements to other aspects of the GrIS's hydrology, such as the configuration of basal drainage, particularly beneath marine-terminating sectors, such predictive models could be improved.

This thesis, through its development of two novel analytical techniques, the FAST and FASTER algorithms, which were used alongside other remotely-sensed datasets, has provided significant advances in our understanding of the recent behaviour of lakes in west Greenland. This research has emphasised the complexity of the GrIS's supraglacial hydrology by showing that a precise control on the initiation of rapid lake drainage could not be identified using remote sensing. However, the methodological approaches and automatic techniques presented in this thesis have provided the means for future studies to analyse rapidly draining lakes within other sectors of the GrIS and over longer timescales. In addition, the FAST and FASTER algorithms will be useful for monitoring changes to surface lakes within and between years on other ice masses, including the grounded Antarctic Ice Sheet and its ice shelves, and Himalayan debris-covered glaciers. With applications such as these, improved knowledge of supraglacial-hydrological systems across different components of the global cryosphere will ultimately help reduce the uncertainties in future SLR projections, and their implications for society.

# References


Abdalati, W. and Steffen, K. (2001). Greenland Ice Sheet melt extent: 1979–1999. *Journal of Geophysical Research: Atmospheres*, 106, 33983–33988, https://doi.org/10.1029/2001JD900181.

Ahlstrøm, A. P., Andersen, S. B., Andersen, M. L., Machguth, H., Nick, F. M., Joughin, I., Reijmer, C. H., van de Wal, R. S. W., Merryman Boncori, J. P., Box, J. E., Citterio, M., van As, D., Fausto, R. S., and Hubbard, A. (2013). Seasonal velocities of eight major marine-terminating outlet glaciers of the Greenland ice sheet from continuous in situ GPS instruments. *Earth System Science Data*, 5, 277–287, https://doi.org/10.5194/essd-5-277-2013.

Ahn, Y. and Box, J. E. (2010). Glacier velocities from time-lapse photos: technique development and first results from the Extreme Ice Survey (EIS) in Greenland. *Journal of Glaciology*, 56(198), 723–734, https://doi.org/10.3189/002214310793146313.

Alley, R. B., Clark, P. U., Huybrechts, P., and Joughin, I. (2005a). Ice-sheet and sea-level changes. *Science*, 310(5747), 456–460, https://doi.org/10.1126/science.1114613.

Alley, R. B., Dupont, T. K., Parizek, B. R., and Anandakrishnan, S. (2005b). Access of surface meltwater to beds of sub-freezing glaciers: preliminary insights. *Annals of Glaciology*, 40, 8–14, https://doi.org/10.3189/172756405781813483.

Andrews, L. C., Catania, G. A., Hoffman, M. J., Gulley, J. D., Lüthi, M. P., Ryser, C., Hawley, R. L., and Neumann, T. A. (2014). Direct observations of evolving subglacial drainage beneath the Greenland Ice Sheet. *Nature*, 514, 80–83, https://doi.org/10.1038/nature13796.

Andrews, L. C., Hoffman, M. J., Neumann, T. A., Catania, G. A., Lüthi, M. P., Hawley, R. L., Schild, K. M., Ryser, C., and Morriss, B. F. (2018). Seasonal evolution of the subglacial hydrologic system modified by supraglacial lake drainage in western Greenland. *Journal of Geophysical Research: Earth Surface*, 123, https://doi.org/10.1029/2017JF004585.

Arnold, N. S., Banwell, A. F., and Willis, I. C. (2014). High-resolution modelling of the seasonal evolution of surface water storage on the Greenland Ice Sheet. *The Cryosphere*, 8, 1149–1160, https://doi.org/10.5194/tc-8-1149-2014.

Aschwanden, A., Fahnestock, M. A., and Truffer, M. (2016). Complex Greenland outlet glacier flow captured. *Nature Communications*, 7, 10524, https://doi.org/10.1038/ncomms10524.

Bamber, J. and Aspinall, W. O. (2013). An expert judgement assessment of future sea-level rise from the ice sheets. *Nature Climate Change*, 3, 424–427, https://doi.org/10.1038/nclimate1778.

Bamber, J. L., Hardy, R. J., and Joughin, I. (2000). An analysis of balance velocities over the Greenland ice sheet and comparison with synthetic aperture radar interferometry. *Journal of Glaciology*, 46(152), 67–74, https://doi.org/10.3189/172756500781833412.

Banwell, A. (2017). Glaciology: ice-shelf stability questioned. *Nature*, 544, 306–307, https://doi.org/10.1038/544306a.

Banwell, A. F. and MacAyeal, D. R. (2015). Ice-shelf fracture due to viscoelastic flexure stress induced by fill/drain cycles of supraglacial lakes. *Antarctic Science*, 27(6), 587–597, https://doi.org/10.1017/S0954102015000292.

Banwell, A. F., Willis, I. C., Arnold, N. S., Messerli, A., Rye, C. J., Tedesco, M., and Ahlstrøm, A. P. (2012a). Calibration and evaluation of a high-resolution surface mass-balance model for Paakitsoq, west Greenland. *Journal of Glaciology*, 58(212), 1047–1062, https://doi.org/10.3189/2012JoG12j034.

Banwell, A. F., Arnold, N. S., Willis, I. C., Tedesco, M., and Ahlstrøm, A. P. (2012b). Modeling supraglacial water routing and lake filling on the Greenland Ice Sheet. *Journal of Geophysical Research: Earth Surface*, 117, F04012, https://doi.org/10.1029/2012JF002393.

Banwell, A. F., Willis, I. C., and Arnold, N. S. (2013a). Modeling subglacial water routing at Paakitsoq, W Greenland. *Journal of Geophysical Research: Earth Surface*, 118, 1282–1295, https://doi.org/10.1002/jgrf.20093.

Banwell, A. F., MacAyeal, D. R., and Sergienko, O. V. (2013b). Breakup of the Larsen B Ice Shelf triggered by chain reaction drainage of supraglacial lakes. *Geophysical Research Letters*, 40, 5872–5876, https://doi.org/10.1002/2013GL057694.

Banwell, A. F., Caballero, M., Arnold, N. S., Glasser, N. F., Cathles, L. M., and MacAyeal, D. R. (2014). Supraglacial lakes on the Larsen B ice shelf, Antarctica, and at Paakitsoq, west Greenland: a comparative study. *Annals of Glaciology*, 55, 1–8, https://doi.org/10.3189/2014AoG66A049.

Banwell, A., Hewitt, I., Willis, I., and Arnold, N. (2016). Moulin density controls drainage development beneath the Greenland ice sheet. *Journal of Geophysical Research: Earth Surface*, 121, 2248–2269, https://doi.org/10.1002/2015jf003801.

Barsi, J. A., Lee, K., Kvaran, G., Markham, B. L., and Pedelty, J. A. (2014). The spectral response of the Landsat-8 Operational Land Imager. *Remote Sensing*, 6, 10232–10251, https://doi.org/10.3390/rs61010232.

Bartholomew, I., Nienow, P., Mair, D., Hubbard, A., King, M. A., and Sole, A. (2010). Seasonal evolution of subglacial drainage and acceleration in a Greenland outlet glacier. *Nature Geoscience*, 3, 408–411, https://doi.org/10.1038/ngeo863.

Bartholomew, I. D., Nienow, P., Sole, A., Mair, D., Cowton, T., King, M. A., and Palmer, S. (2011a). Seasonal variations in Greenland Ice Sheet motion: inland extent and behaviour at higher elevations. *Earth and Planetary Science Letters*, 307, 271–278, https://doi.org/10.1016/j.epsl.2011.04.014.

Bartholomew, I., Nienow, P., Sole, A., Mair, D., Cowton, T., Palmer, S., and Wadham, J. (2011b). Supraglacial forcing of subglacial drainage in the ablation zone of the Greenland ice sheet. *Geophysical Research Letters*, 38, L08502, https://doi.org/10.1029/2011GL047063.

Bartholomew, I., Nienow, P., Sole, A., Mair, D., Cowton, T., and King, M. A. (2012). Short-term variability in Greenland Ice Sheet motion forced by time-varying meltwater drainage: implications for the relationship between subglacial drainage system behavior and ice velocity. *Journal of Geophysical Research: Earth Surface*, 117, F03002, https://doi.org/10.1029/2011jf002220.

Bell, R. E. (2008). The role of subglacial water in ice-sheet mass balance. *Nature Geoscience*, 1, 297–304, https://doi.org/10.1038/ngeo186.

Bell, R. E., Chu, W., Kingslake, J., Das, I., Tedesco, M., Tinto, K. J., Zappa, C. J., Frezzotti, M., Boghosian, A., and Lee, W. S. (2017). Antarctic ice shelf potentially stabilized by export of meltwater in surface river. *Nature*, 544, 344–348, https://doi.org/10.1038/nature22048.

Benn, D. I. and Evans, D. J. A. (2010). *Glaciers and glaciation*. 2nd ed. London: Hodder Education.

Benn, D. I., Wiseman, S., and Hands, K. A. (2001). Growth and drainage of supraglacial lakes on debris-mantled Ngozumpa Glacier, Khumbu Himal, Nepal. *Journal of Glaciology*, 47(159), 626–638, https://doi.org/10.3189/172756501781831729.

Benn, D. I., Thompson, S., Gulley, J., Mertes, J., Luckman, A., and Nicholson, L. (2017). Structure and evolution of the drainage system of a Himalayan debris-covered glacier, and its relationship with patterns of mass loss. *The Cryosphere*, 11, 2247–2264, https://doi.org/10.5194/tc-11-2247-2017.

Boon, S. and Sharp, M. (2003). The role of hydrologically-driven ice fracture in drainage system evolution on an Arctic glacier. *Geophysical Research Letters*, 30, L018034, https://doi.org/10.1029/2003GL018034.

Booth, A. D., Clark, R. A., Kulessa, B., Murray, T., Carter, J., Doyle, S., and Hubbard, A. (2012). Thin-layer effects in glaciological seismic amplitude-versus-angle (AVA) analysis: implications for characterising a subglacial till unit, Russell Glacier, west Greenland. *The Cryosphere*, 6, 909–922, https://doi.org/10.5194/tc-6-909-2012.

Bougamont, M., Christoffersen, P., Hubbard, A. L., Fitzpatrick, A. A., Doyle, S. H., and Carter, S. P. (2014). Sensitive response of the Greenland Ice Sheet to surface melt drainage over a soft bed. *Nature Communications*, 5, 5052, https://doi.org/10.1038/ncomms6052.

Bowling, J. S., Livingstone, S. J., Sole, A. J., and Chu, W. (in preparation). Discovery of 56 subglacial lakes beneath the Greenland Ice Sheet.

Box, J. E. and Ski, K. (2007). Remote sounding of Greenland supraglacial melt lakes: implications for subglacial hydraulics. *Journal of Glaciology*, 53, 257–265, https://doi.org/10.3189/172756507782202883.

Box, J. E., Bromwich, D. H., Veenhuis, B. A., Bai, L.-S., Stroeve, J. C., Rogers, J. C., Steffen, K., Haran, T., and Wang, S.-H. (2006). Greenland Ice Sheet surface mass balance variability (1988–2004) from calibrated polar MM5 output. *Journal of Climate*, 19(12), 2783–2800, https://doi.org/10.1175/JCLI3738.1.

Box, J. E., Fettweis, X., Stroeve, J. C., Tedesco, M., Hall, D. K., and Steffen, K. (2012). Greenland ice sheet albedo feedback: thermodynamics and atmospheric drivers. *The Cryosphere*, 6, 821–839, https://doi.org/10.5194/tc-6-821-2012.

Bryzgis, G. and Box, J. E. (2005). West Greenland ice sheet melt lake observations and modeling. *American Geophysical Union Fall Meeting, abstract C41A-07*. San Francisco: December 2005.

Budd, W., Keage, P., and Blundy, N. (1979). Empirical studies of ice sliding. *Journal of Glaciology*, 23(89), 157–170, https://doi.org/10.1017/S0022143000029804.

Campbell, J. B. and Wynne, R. (2011). *Introduction to remote sensing*. 5th ed. New York: Guildford Press.

Carmichael, J. D., Joughin, I., Behn, M. D., Das, S., King, M. A., Stevens, L., and Lizarralde, D. (2015). Seismicity on the western Greenland Ice Sheet: surface fracture in the vicinity of active moulins. *Journal of Geophysical Research: Earth Surface*, 120, 1082–1106, https://doi.org/10.1002/2014JF003398.

Carroll, D., Sutherland, D. A., Hudson, B., Moon, T., Catania, G. A., Shroyer, E. L., Nash, J. D., Bartholomaus, T. C., Felikson, D., Stearns, L. A., Noël, B. P. Y., and van den Broeke, M. R. (2016). The impact of glacier geometry on meltwater plume structure and submarine melt in Greenland fjords. *Geophysical Research Letters*, 43(18), 9739–9748, https://doi.org/10.1002/2016GL070170.

Catania, G. A. and Neumann, T. A. (2010). Persistent englacial drainage features in the Greenland Ice Sheet. *Geophysical Research Letters*, 37, L02501, https://doi.org/10.1029/2009GL041108.

Catania, G. A., Neumann, T. A., and Price, S. F. (2008). Characterizing englacial drainage in the ablation zone of the Greenland ice sheet. *Journal of Glaciology*, 54(187), 567–578, https://doi.org/10.3189/002214308786570854.

Chandler, D. M., Wadham, J. L., Lis, G. P., Cowton, T., Sole, A., Bartholomew, I., Telling, J., Nienow, P., Bagshaw, E. B., Mair, D., Vinen, S., and Hubbard, A. (2013). Evolution of the subglacial drainage system beneath the Greenland Ice Sheet revealed by tracers. *Nature Geoscience*, 6(3), 195–198, https://doi.org/10.1038/ngeo1737.

Chandler, D. M., Alcock, J. D., Wadham, J. L., Mackie, S. L., and Telling, J. (2015). Seasonal changes of ice surface characteristics and productivity in the ablation zone of the Greenland Ice Sheet. *The Cryosphere*, 9, 487–504, https://doi.org/10.5194/tc-9-487-2015.

Chen, C., Howat, I. M., and de la Peña, S. (2017). Formation and development of supraglacial lakes in the percolation zone of the Greenland ice sheet. *Journal of Glaciology*, 63, 847–853, https://doi.org/10.1017/jog.2017.50.

Christoffersen, P., Mugford, R. I., Heywood, K. J., Joughin, I., Dowdeswell, J. A., Syvitski, J. P. M., Luckman, A., and Benham, T. J. (2011). Warming of waters in an East Greenland fjord prior to glacier retreat: mechanisms and connection to large-scale atmospheric conditions. *The Cryosphere*, 5, 701–714, https://doi.org/10.5194/tc-5-701-2011.

Christoffersen, P., Bougamont, M., Hubbard, A., Doyle, S. H., Grigsby, S., and Pettersson, R. (2018). Cascading lake drainage on the Greenland Ice Sheet triggered by tensile shock and fracture. *Nature Communications*, 9, 1064, https://doi.org/10.1038/s41467-018-03420-8.

Chu, V. W. (2014). Greenland ice sheet hydrology: a review. *Progress in Physical Geography*, 38(1), 19–54, https://doi.org/10.1177/0309133313507075.

Chu, V. W., Smith, L. C., Rennermalm, A. K., Forster, R. R., Box, J. E., and Reeh, N. (2009). Sediment plume response to surface melting and supraglacial lake drainages on the Greenland ice sheet. *Journal of Glaciology*, 55(194), 1072–1082, https://doi.org/10.3189/002214309790794904.

Chu, W., Schroeder, D. M., Seroussi, H., Creyts, T. T., Palmer, S. J., and Bell, R. E. (2016). Extensive winter subglacial water storage beneath the Greenland Ice Sheet. *Geophysical Research Letters*, 43(24), 12484–12492, https://doi.org/10.1002/2016GL071538.

Church, J. A. and White, N. J. (2006). A 20th century acceleration in global sea-level rise. *Geophysical Research Letters*, 33(1), L01602, https://doi.org/10.1029/2005GL024826.

Church, J. A., Clark, P. U., Cazenave, A., Gregory, J. M., Jevrejeva, S., Levermann, A., Merrifield, M. A., Milne, G. A., Nerem, R. S., Nunn, P. D., Pfeffer, W. T., Stammer, D., and Unnikrishnan, A. S. (2013). *Sea level change*. In: *Climate change 2013: the physical science basis. Contribution of working group I to the fifth assessment report of the Intergovernmental Panel on Climate Change* [Stocker, T. F., Qin, D., Plattner, G.-K., Tignor, M., Allen, S. K., Boschung, J., Nauels, A., Xia, Y., Bex, V., and Midgley, P. M. (eds.).] Cambridge and New York: Cambridge University Press, pp. 1137–1216, https://doi.org/10.1017/CBO9781107415324.026.

Clarke, T. S. and Echelmeyer, K. (1996). Seismic-reflection evidence for a deep subglacial trough beneath Jakobshavns Isbræ, west Greenland. *Journal of Glaciology*, 41(141), 219–232, https://doi.org/10.3189/S0022143000004081.

Clason, C., Mair, D. W., Burgess, D. O., and Nienow, P. W. (2012). Modelling the delivery of supraglacial meltwater to the ice/bed interface: application to southwest Devon Ice Cap, Nunavut, Canada. *Journal of Glaciology*, 58(208), 361–374, https://doi.org/10.3189/2012JoG11J129.

Clason, C. C., Mair, D. W. F., Nienow, P. W., Bartholomew, I. D., Sole, A., Palmer, S., and Schwanghart, W. (2015). Modelling the transfer of supraglacial meltwater to the bed of Leverett Glacier, southwest Greenland. *The Cryosphere*, 9, 123–138, https://doi.org/10.5194/tc-9-123-2015.

Cogley, J. G. (2009). A more complete version of the World Glacier Inventory. *Annals of Glaciology*, 50, 32–38, https://doi.org/10.3189/172756410790595859.

Colgan, W., Rajaram, H., Anderson, R., Steffen, K., Phillips, T., Joughin, I., Zwally, H. J., and Abdalati, W. (2011a). The annual glaciohydrology cycle in the ablation zone of the Greenland ice sheet: part 1. Hydrology model. *Journal of Glaciology*, 57(204), 697–709, https://doi.org/10.3189/002214311797409668.

Colgan, W., Steffen, K., McLamb, W. S., Abdalati, W., Rajaram, H., Motyka, R., Phillips, T., and Anderson, R. (2011b). An increase in crevasse extent, west Greenland: hydrologic implications. *Geophysical Research Letters*, 38, L18503, https://doi.org/10.1029/2011GL048491.

Colgan, W., Rajaram, H., Anderson, R., Steffen, K., Zwally, J., Phillips, T., and Abdalati, W. (2012). The annual glaciohydrology in the ablation zone of the Greenland ice sheet: part 2. Observed and modeled ice flow. *Journal of Glaciology*, 58(207), 51–64, https://doi.org/10.3189/2012JoG11J081.

Colgan, W., Rajaram, H., Abdalati, W., McCutchan, C., Mottram, R., Moussavi, M. S., and Grigsby, S. (2016). Glacier crevasses: observations, models and mass balance implications. *Reviews of Geophysics*, 54(1), 119–161, https://doi.org/10.1002/2015RG000504.

Cook, J. M., Hodson, A. J., Gardner, A. S., Flanner, M., Tedstone, A. J., Williamson, C., Irvine-Fynn, T. D. L., Nilsson, J., Bryant, R., and Tranter, M. (2017). Quantifying bioalbedo: a new physically based model and discussion of empirical methods for characterising biological influence on ice and snow albedo. *The Cryosphere*, 11, 2611–2632, https://doi.org/10.5194/tc-11-2611-2017.

Cooley, S. W. and Christoffersen, P. (2017). Observation bias correction reveals more rapidly draining lakes on the Greenland Ice Sheet. *Journal of Geophysical Research: Earth Surface*, 122, 1867–1881, https://doi.org/10.1002/2017JF004255.

Cowton, T., Nienow, P., Sole, A., Wadham, J., Lis, G., Bartholomew, I., Mair, D., and Chandler, D. (2013). Evolution of drainage system morphology at a land-terminating Greenlandic outlet glacier. *Journal of Geophysical Research: Earth Surface*, 118, 29–41, https://doi.org/10.1029/2012jf002540.

Cowton, T., Nienow, P., Sole, A., Bartholomew, I., and Mair, D. (2016). Variability in ice motion at a land-terminating Greenlandic outlet glacier: the role of channelized and distributed drainage systems. *Journal of Glaciology*, 62(233), 451–466, https://doi.org/10.1017/jog.2016.36.

Craft, C., Clough, J., Ehman, J., Joye, S., Park, R., Pennings, S., Guo, H., and Machmuller, M. (2008). Forecasting the effects of accelerated sea-level rise on tidal marsh ecosystem services. *Frontiers in Ecology and the Environment*, 7(2), 73–78, https://doi.org/10.1890/070219.

Cuffey, K. M. and Marshall, S. J. (2000). Substantial contribution to sea-level rise during the last interglacial from the Greenland ice sheet. *Nature*, 404, 591–594, https://doi.org/10.1038/35007053.

Cuffey, K. M. and Paterson, W. S. B. (2010). *The physics of glaciers*. 4th ed. Oxford: Elsevier.

Dahl-Jensen, D., Mosegaard, K., Gundestrup, N., Clow, G. D., Johnsen, S. J., Hansen, A. W., and Balling, N. (1998). Past temperatures directly from the Greenland Ice Sheet. *Science*, 282, 268–271, https://doi.org/10.1126/science.282.5387.268.

Das, S. B., Joughin, I., Behn, M. D., Howat, I. M., King, M. A., Lizarralde, D., and Bhatia, M. P. (2008). Fracture propagation to the base of the Greenland Ice Sheet during supraglacial lake drainage. *Science*, 320, 778–781, https://doi.org/10.1126/science.1153360.

Dasgupta, S., Laplante, B., Meisner, C., Wheeler, D., and Yin, J. (2009). The impact of sea level rise on developing countries: a comparative analysis. *Climatic Change*, 93(3–4), 379–388, https://doi.org/10.1007/s10584-008-9499-5.

de Almeida, T. I. R., Penatti, N. C., Ferreira, L. G., Arantes, A. E., and Hummel do Amaral, C. (2015). Principal component analysis applied to a time series of MODIS images: the spatio-temporal variability of the Pantanal wetland, Brazil. *Wetlands Ecology and Management*, 23, 737–748, https://doi.org/10.1007/s11273-015-9416-4.

de Fleurian, B., Morlighem, M., Seroussi, H., Rignot, E., van den Broeke, M. R., Kuipers Munneke, P., Mouginot, J., Smeets, P. C. J. P., and Tedstone, A. J. (2016). A modeling study of the effect of runoff variability on the effective pressure beneath Russell Glacier, west Greenland. *Journal of Geophysical Research: Earth Surface*, 121, 1834–1848, https://doi.org/10.1002/2016JF003842.

Dow, C. F., Hubbard, A., Booth, A. D., Doyle, S. H., Gusmeroli, A., and Kulessa, B. (2013). Seismic evidence of mechanically weak sediments underlying Russell Glacier, west Greenland. *Annals of Glaciology*, 54(64), 135–141, https://doi.org/10.3189/2013AoG64A032.

Dow, C. F., Kulessa, B., Rutt, I. C., Doyle, S. H., and Hubbard, A. (2014). Upper bounds on subglacial channel development for interior regions of the Greenland ice sheet. *Journal of Glaciology*, 60, 1044–1052, https://doi.org/10.3189/2014JoG14J093.

Dow, C. F., Kulessa, B., Rutt, I. C., Tsai, V. C., Pimentel, S., Doyle, S. H., van As, D., Lindbäck, K., Pettersson, R., Jones, G. A., and Hubbard, A. (2015). Modeling of subglacial hydrological development following rapid supraglacial lake drainage. *Journal of Geophysical Research: Earth Surface*, 120, 1127–1147, https://doi.org/10.1002/2014JF003333.

Doyle, S. H., Hubbard, A. L., Dow, C. F., Jones, G. A., Fitzpatrick, A., Gusmeroli, A., Kulessa, B., Lindback, K., Pettersson, R., and Box, J. E. (2013). Ice tectonic deformation during the rapid in situ drainage of a supraglacial lake on the Greenland Ice Sheet. *The Cryosphere*, 7, 129–140, https://doi.org/10.5194/tc-7-129-2013.

Doyle, S. H., Hubbard, A., Fitzpatrick, A. A. W., van As, D., Mikkelsen, A. B., Pettersson, R., and Hubbard, B. (2014). Persistent flow acceleration within the interior of the Greenland ice sheet. *Geophysical Research Letters*, 41, 899–905, https://doi.org/10.1002/2013GL058933.

Doyle, S. H., Hubbard, A., van de Wal, R. S. W., Box, J. E., van As, D., Scharrer, K., Meierbachtol, T. W., Smeets, P. C. J. P., Harper, J. T., Johansson, E., Mottram, R. E., Mikkelsen, A. B., Willhelms, F., Patton, H., Christoffersen, P., and Hubbard, B. (2015). Amplified melt and flow of the Greenland ice sheet driven by late-summer cyclonic rainfall. *Nature Geoscience*, 8, 647–653, https://doi.org/10.1038/ngeo2482.

Doyle, S. H., Hubbard, B., Christoffersen, P., Young, T. J., Hofstede, C., Bougamont, M., Box, J. E., and Hubbard, A. (2018). Physical conditions of fast glacier flow: 1. measurements from boreholes drilled to the bed of Store Glacier, west Greenland. *Journal of Geophysical Research: Earth Surface*, 123(2), 324–348, https://doi.org/10.1002/2017JF004529.

Dronova, I., Gong, P., Wang, L., and Zhong, L. (2015). Mapping dynamic cover types in a large seasonally flooded wetland using extended principal component analysis and object-based classification. *Remote Sensing of Environment*, 158, 193–206, https://doi.org/10.1016/j.rse.2014.10.027.

Dutton, A., Carlson, A. E., Long, A. J., Milne, G. A., Clark, P. U., DeConto, R., Horton, B. P., Rahmstorf, S., and Raymo, M. E. (2015). Sea-level rise due to polar ice-sheet mass loss during past warm periods. *Science*, 349(6244), 153, https://doi.org/10.1126/science.aaa4019.

Echelmeyer, K., Clarke, T. S., and Harrison, W. D. (1991). Surficial glaciology of Jakobshavns Isbræ, west Greenland: part I. Surface morphology. *Journal of Glaciology*, 37(127), 368–382, https://doi.org/10.3189/S0022143000005803.

Enderlin, E. M., Howat, I. M., Jeong, S., Noh, M.-Y., van Angelen, J. H., and van den Broeke, M. R. (2014). An improved mass budget for the Greenland ice sheet. *Geophysical Research Letters*, 41, 866–872, https://doi.org/10.1002/2013GL059010.

ESA (2017). *Sentinel-2 spectral response functions (S2-SRF)*. Available at: https://earth.esa.int/web/sentinel/user-guides/sentinel-2-msi/document-library/-/asset_publisher/Wk0TKajiISaR/content/sentinel-2a-spectral-responses. Accessed 19 February 2018.

Everett, A., Murray, T., Selmes, N., Rutt, I. C., Luckman, A., James, T. D., Clason, C., O'Leary, M., Karunarathna, H., Moloney, V., and Reeve, D. E. (2016). Annual down-glacier drainage of lakes and water-filled crevasses at Helheim Glacier, southeast Greenland. *Journal of Geophysical Research: Earth Surface*, 121, 1819–1833, https://doi.org/10.1002/2016JF003831.

Fahnestock, M., Abdalati, W., Joughin, I., Brozena, J., and Gogineni, P. (2001). High geothermal heat flow, basal melt, and the origin of rapid ice flow in central Greenland. *Science*, 294(5550), 2338–2342, https://doi.org/10.1126/science.1065370.

Fahnestock, M., Scambos, T., Moon, T., Gardner, A., Haran, T., and Klinger, M. (2016). Rapid large-area mapping of ice flow using Landsat 8. *Remote Sensing of Environment*, 185, 84–94, https://doi.org/10.1016/j.rse.2015.11.023.

Favier, L., Durand, G., Cornford, S. L., Gudmundsson, G. H., Gagliardini, O., Gillet-Chaulet, F., Zwinger, T., Payne, A. J., and Le Brocq, A. M. (2014). Retreat of Pine Island Glacier controlled by marine ice-sheet instability. *Nature Climate Change*, 4, 117–121, https://doi.org/10.1038/nclimate2094.

Feng, L. and Hu, C. (2016). Cloud adjacency effects on top-of-atmosphere radiance and ocean color data products: a statistical assessment. *Remote Sensing of Environment*, 174, 301–313, https://doi.org/10.1016/j.rse.2015.12.020.

Fettweis, X., Box, J. E., Agosta, C., Amory, C., Kittel, C., Lang, C., van As, D., Machguth, H., and Gallée, H. (2017). Reconstructions of the 1900–2015 Greenland ice sheet surface mass balance using the regional climate MAR model. *The Cryosphere*, 11, 1015–1033, https://doi.org/10.5194/tc-11-1015-2017.

Fitzpatrick, A. A. W. (2014). *The dynamic response of Russell Glacier, a land terminating outlet of the Greenland Ice Sheet, to climatic change*. Unpublished Ph.D. thesis, Aberystwyth University, Aberystwyth, UK.

Fitzpatrick, A. A. W., Hubbard, A., Joughin, I., Quincey, D. J., van As, D., Mikkelsen, A. P. B., Doyle, S. H., Hasholt, B., and Jones, G. A. (2013). Ice flow dynamics and surface meltwater flux at a land-terminating sector of the Greenland ice sheet. *Journal of Glaciology*, 59, 687–696, https://doi.org/10.3189/2013JoG12J143.

Fitzpatrick, A. A. W., Hubbard, A. L., Box, J. E., Quincey, D. J., van As, D., Mikkelsen, A. P. B., Doyle, S. H., Dow, C. F., Hasholt, B., and Jones, G. A. (2014). A decade (2002–2012) of supraglacial lake volume estimates across Russell Glacier, west Greenland. *The Cryosphere*, 8, 107–121, https://doi.org/10.5194/tc-8-107-2014.

Flowers, G. E. (2015). Modelling water flow under glaciers and ice sheets. *Proceedings of the Royal Society A*, 471(2176), 20140907, https://doi.org/10.1098/rspa.2014.0907.

Forster, R. R., Box, J. E., van den Broeke, M. R., Miège, C., Burgess, E. W., van Angelen, J. H., Lenaerts, J. T. M., Koenig, L. S., Paden, J., Lewis, C., Gogineni, S. P., Leuschen, C., and McConnell, J. R. (2014). Extensive liquid meltwater storage in firn within the Greenland ice sheet. *Nature Geoscience*, 7, 95–98, https://doi.org/10.1038/ngeo2043.

Fountain, A. G. and Walder, J. S. (1998). Water flow through temperate glaciers. *Reviews of Geophysics*, 36(3), 299–328, https://doi.org/10.1029/97RG03579.

Fountain, A. G., Jacobel, R. W., Schlichting, R., and Jansson, P. (2005). Fractures as the main pathways of water flow in temperate glaciers. *Nature*, 433, 618–621, http://doi.org/10.1038/nature03296.

Fried, M. J., Catania, G. A., Bartholomaus, T. C., Duncan, D., Davis, M., Stearns, L. A., Nash, J., Shroyer, E., and Sutherland, D. (2015). Distributed subglacial discharge drives significant submarine melt at a Greenland tidewater glacier. *Geophysical Research Letters*, 42, 9328–9336, https://doi.org/10.1002/2015GL065806.

Gagliardini, O., Cohen, D., Raback, P., and Zwinger, T. (2007). Finite-element modeling of subglacial cavities and related friction law. *Journal of Geophysical Research: Earth Surface*, 112, F02027, https://doi.org/10.1029/2006JF000576.

Gardelle, J., Arnaud, Y., and Berthier, E. (2011). Contrasted evolution of glacial lakes along the Hindu Kush Himalaya mountain range between 1990 and 2009. *Global and Planetary Change*, 75(1–2), 47–55, https://doi.org/10.1016/j.gloplacha.2010.10.003.

Gardner, A. S., Moholt, G., Scambos, T., Fahnstock, M., Ligtenberg, S., van den Broeke, M., and Nilsson, J. (2018). Increased West Antarctic and unchanged East Antarctic ice discharge over the last 7 years. *The Cryosphere*, 12, 521–547, https://doi.org/10.5194/tc-12-521-2018.

Georgiou, S., Shepherd, A., McMillan, M., and Nienow, P. (2009). Seasonal evolution of supraglacial lake volume from ASTER imagery. *Annals of Glaciology*, 50(52), 95–100, https://doi.org/10.3189/172756409789624328.

Gledhill, L. A. and Williamson, A. G. (2018). Inland advance of supraglacial lakes in north-west Greenland under recent climatic warming. *Annals of Glaciology*, 1–17, https://doi.org/10.1017/aog.2017.31.

Greenwood, S. L., Clason, C. C., Helanow, C., and Margold, M. (2016). Theoretical, contemporary observational and palaeo-perspectives on ice sheet hydrology: processes and products. *Earth-Science Reviews*, 155, 1–27, https://doi.org/10.1016/j.earscirev.2016.01.010.

Gudmundsson, G. H. (2003). Transmission of basal variability to a glacier surface. *Journal of Geophysical Research: Solid Earth*, 108(B5), https://doi.org/10.1029/2002JB002107.

Gulley, J. D., Grabiec, M., Martin, J. B., Jania, J., Catania, G., and Glowacki, P. (2012). The effect of discrete recharge by moulins and heterogeneity in flow-path efficiency at glacier beds on subglacial hydrology. *Journal of Glaciology*, 58(211), 926–940, https://doi.org/10.3189/2012JoG11J189.

Gumley, L., Descloitres, J., and Schmaltz, J. (2007). *Creating Reprojected True Color MODIS Images: a Tutorial, version 1.0.2*. Available at: https://cdn.earthdata.nasa.gov/conduit/upload/946/MODIS_True_Color.pdf. Accessed 3 April 2018.

Hall, D. K., Williams, R. S., Luthcke, S. B., and Digirolamo, N. E. (2008). Greenland ice sheet surface temperature, melt and mass loss: 2000–06. *Journal of Glaciology*, 54(184), 81–93, https://doi.org/10.3189/002214308784409170.

Hall, D. K., Comiso, J. C., DiGirolamo, N. E., Shuman, C. A., Box, J. E., and Koenig, L. S. (2013). Variability in the surface temperature and melt extent of the Greenland ice sheet from MODIS. *Geophysical Research Letters*, 40(10), 2114–2120, https://doi.org/10.1002/grl.50240.

Hanna, E., Huybrechts, P., Steffen, K., Cappelen, J., Huff, R., Shuman, C., Irvine-Fynn, T., Wise, S., and Griffiths, M. (2008). Increased runoff from melt from the Greenland Ice Sheet: a response to global warming. *Journal of Climate*, 21(2), 331–341, https://doi.org/10.1175/2007JCLI1964.1.

Hanna, E., Cappelen, J., Fettweis, X., Huybrechts, P., Luckman, A., and Ribergaard, M. H. (2009). Hydrologic response of the Greenland ice sheet: the role of oceanographic warming. *Hydrological Processes*, 23, 7–30, https://doi.org/10.1002/hyp.7090.

Harper, J. T., Humphrey, N. F., Meierbachtol, T. W., Graly, J. A., and Fischer, U. H. (2017). Borehole measurements indicate hard bed conditions, Kangerlussuaq sector, western Greenland Ice Sheet. *Journal of Geophysical Research: Earth Surface*, 122(9), 1605–1618, https://doi.org/10.1002/2017JF004201.

Hawkings, J. R., Wadham, J. L., Tranter, M., Lawson, E., Sole, A., Cowton, T., Tedstone, A. J., Bartholomew, I., Nienow, P., Chandler, D., and Telling, J. (2015). The effect of warming climate on nutrient and solute export from the Greenland Ice Sheet. *Geochemical Perspectives Letters*, 1(1), 94–104, https://doi.org/10.7185/geochemlet.1510.

Hawkings, J., Wadham, J., Tranter, M., Telling, J., Bagshaw, E., Beaton, A., Simmons, S.-L., Chandler, D., Tedstone, A., and Nienow, P. (2016). The Greenland Ice Sheet as a hot spot of phosphorous weathering and export in the Arctic. *Global Biogeochemical Cycles*, 30(2), 191–210, https://doi.org/10.1002/2015GB005237.

Hays, J. D., Imbrie, J., and Shackleton, N. J. (1976). Variations in the Earth's orbit: pacemaker of the ice ages. *Science*, 194(4270), 1121–1132, https://doi.org/10.1126/science.194.4270.1121.

Hewitt, I. J. (2013). Seasonal changes in ice sheet motion due to melt water lubrication. *Earth and Planetary Science Letters*, 371–372, 16–25, https://doi.org/10.1016/j.epsl.2013.04.022.

Hill, E. A., Carr, J. R., and Stokes, C. R. (2017). A review of recent changes in major marine-terminating outlet glaciers in northern Greenland. *Frontiers in Earth Science*, 4, 111, https://doi.org/10.3389/feart.2016.00111.

Hill, E. A., Carr, J. R., Stokes, C. R., and Gudmundsson, G. H. (2018). Dynamic changes in outlet glaciers in northern Greenland from 1948 to 2015. *The Cryosphere Discussions*, https://doi.org/10.5194/tc-2018-17.

Hock, R., Hutchings, J. K., and Lehning, M. (2017). Grand challenges in cryospheric sciences: toward better predictability of glaciers, snow and sea ice. *Frontiers in Earth Science*, 5, 1–14, https://doi.org/10.3389/feart.2017.00064.

Hoffman, M. J., Catania, G. A., Neumann, T. A., Andrews, L. C., and Rumrill, J. A. (2011). Links between acceleration, melting, and supraglacial lake drainage of the western Greenland Ice Sheet. *Journal of Geophysical Research: Earth Surface*, 116(F4), F04035, https://doi.org/10.1029/2010JF001934.

Hoffman, M. J., Andrews, L. C., Price, S. F., Catania, G. A., Neumann, T. A., Lüthi, M. P., Gulley, J., Ryser, C., Hawley, R. L., and Morriss, B. (2016). Greenland subglacial drainage evolution regulated by weakly connected regions of the bed. *Nature Communications*, 7, 13903, https://doi.org/10.1038/ncomms13903.

Hoffman, M. J., Perego, M., Andrews, L. C., Price, S. F., Neumann, T. A., Johnson, J., Catania, G., and Lüthi, M. (2018). Widespread moulin formation during supraglacial lake drainages in Greenland. *Geophysical Research Letters*, 45(2), 778–788, https://doi.org/10.1002/2017GL075659.

Hofstede, C., Christoffersen, P., Hubbard, B., Doyle, S. H., Young, T. J., Diez, A., Eisen, A., and Hubbard, A. (2018). Physical conditions of fast glacier flow: 2. Variable extent of anisotropic ice and soft basal sediment from seismic reflection data acquired on Store Glacier, west Greenland. *Journal of Geophysical Research: Earth Surface*, 123(2), 349–362, https://doi.org/10.1002/2017JF004297.

Holland, D. M., Thomas. R. H., de Young, B., Ribergaard, M. H., and Lyberth, B. (2008). Acceleration of Jakobshavn Isbræ triggered by warm subsurface ocean waters. *Nature Geoscience*, 1, 659–664, https://doi.org/10.1038/ngeo316.

Houborg, R. and McCabe, M. F. (2017). Impacts of dust aerosol and adjacency effects on the accuracy of Landsat 8 and RapidEye surface reflectances. *Remote Sensing of Environment*, 194, 127–145, https://doi.org/10.1016/j.rse.2017.03.013.

Howat, I. M., Box, J. E., Ahn, Y., Herrington, A., and McFadden, E. M. (2010). Seasonal variability in the dynamics of marine-terminating outlet glaciers in Greenland. *Journal of Glaciology*, 56(198), 601–613, https://doi.org/10.3189/002214310793146232.

Howat, I. M., de la Peña, S., van Angelen, J. H., Lenaerts, T. M., and van den Broeke, M. R. (2013). Brief communication: "expansion of meltwater lakes on the Greenland ice sheet". *The Cryosphere*, 7, 201–204, https://doi.org/10.5194/tc-7-201-2013.

Howat, I. M., Negrete, A., and Smith, B. E. (2014). The Greenland Ice Mapping Project (GIMP) land classification and surface elevation data sets. *The Cryosphere*, 8, 1509–1518, https://doi.org/10.5194/tc-8-1509-2014.

Hubbard, B. and Nienow, P. (1997). Alpine subglacial hydrology. *Quaternary Science Reviews*, 16(9), 939–955, https://doi.org/10.1016/S0277-3791(97)00031-0.

Huggel, C., Kääb, A., Haeberli, W., Teysseire, P., and Paul, F. (2002). Remote sensing based assessment of hazards from glacier lake outbursts: a case study in the Swiss Alps. *Canadian Geotechnical Journal*, 39(2), 316–330, https://doi.org/10.1139/T01-099.

Hurkmans, R. T. W. L., Bamber, J. L., Davis, C. H., Joughin, I. R., Khvorostovsky, K. S., Smith, B. S., and Schoen, N. (2014). Time-evolving mass loss of the Greenland Ice Sheet from satellite imagery. *The Cryosphere*, 8, 1725–1740, https://doi.org/10.5194/tc-8-1725-2014.

Huybers, P. J. (2006). Early Pleistocene glacial cycles and the integrated summer insolation forcing. *Science*, 313, 508–511, https://doi.org/10.1126/science.1125249.

Ignéczi, A., Sole, A. J., Livingstone, S. J., Leeson, A. A., Fettweis, X., Selmes, N., Gourmelen, N., and Briggs, K. (2016). Northeast sector of the Greenland Ice Sheet to undergo the greatest inland expansion of supraglacial lakes during the 21st century. *Geophysical Research Letters*, 43(18), 9729–9738, https://doi.org/10.1002/2016GL070338.

IPCC (2013). *Climate change 2013: the physical science basis. Contribution of working group I to the fifth assessment report of the Intergovernmental Panel on Climate Change* [Stocker, T. F., Qin, D., Plattner, G.-K., Tignor, M., Allen, S. K., Boschung, J., Nauels, A., Xia, Y., Bex, V., and Midgley, P. M. (eds.).] Cambridge and New York: Cambridge University Press, 1535 pp., https://doi.org/10.1017/CBO9781107415324.

Iken, A. (1981). The effect of the subglacial water pressure on the sliding velocity in an idealised numerical model. *Journal of Glaciology*, 27(97), 407–421, https://doi.org/10.3189/s0022143000011448.

Iken, A., Echelmeyer, K., Harrison, W., and Funk, M. (1993). Mechanisms of fast flow in Jakobshavns Isbræ, west Greenland: part I. Measurements of temperature and water level in deep boreholes. *Journal of Glaciology*, 39(131), 15–25, https://doi.org/10.3189/S0022143000015689.

Irvine-Fynn, T. D. L., Hodson, A. J., Moorman, B. J., Vatne, G., and Hubbard, A. L. (2011). Polythermal glacier hydrology: a review. *Reviews of Geophysics*, 49, 1–37, https://doi.org/10.1029/2010RG000350.

Jeong, S. and Howat, I. M. (2015). Performance of Landsat 8 Operational Land Imager for mapping ice sheet velocity. *Remote Sensing of Environment*, 170, 90–101, https://doi.org/10.1016/j.rse.2015.08.023.

Jenkins, A. (2011). Convection-driven melting near the grounding lines of ice shelves and tidewater glaciers. *Journal of Physical Oceanography*, 41(12), 2279–2294, https://doi.org/10.1175/JPO-D-11-03.1.

Jevrejeva, S., Moore, J. C., and Grinsted, A. (2012). Sea level projections to AD2500 with a new generation of climate change scenarios. *Global and Planetary Change*, 80–81, 14–20, https://doi.org/10.1016/j.gloplacha.2011.09.006.

Jin, S. and Zou, F. (2015). Re-estimation of glacier mass loss in Greenland from GRACE with correction of land-ocean leakage effects. *Global and Planetary Change*, 135, 170–178, https://doi.org/10.1016/j.gloplacha.2015.11.002.

Jin, S., Abd-Elbaky, M., and Feng, G. (2016). Accelerated ice-sheet mass loss in Antarctica from 18-year satellite laser ranging measurements. *Annals of Geophysics*, 59(1), S0101, https://doi.org/10.4401/ag-6782.

Johansson, A. M. and Brown, I. A. (2012). Observations of supra-glacial lakes in west Greenland using winter wide swath Synthetic Aperture Radar. *Remote Sensing Letters*, 3(6), 531–539, https://doi.org/10.1080/01431161.2011.637527.

Johansson, A. M. and Brown, I. A. (2013). Adaptive classification of supra-glacial lakes on the west Greenland Ice Sheet. *IEEE Journal of Selected Topics in Applied Earth Observation and Remote Sensing*, 6(4), 1998–2007, https://doi.org/10.1109/JSTARS.2012.2233722.

Johansson, A. M., Jansson, P., and Brown, I. A. (2013). Spatial and temporal variations in lakes on the Greenland Ice Sheet. *Journal of Hydrology*, 476, 314–320, https://doi.org/10.1016/j.jhydrol.2012.10.045.

Jolliffe, I. T. (2002). *Principal component analysis*. New York: Springer.

Joughin, I. and Alley, R. B. (2011). Stability of the West Antarctic ice sheet in a warming world. *Nature Geoscience*, 4, 506–513, https://doi.org/10.1038/ngeo1194.

Joughin, I., Das, S. B., King, M. A., Smith, B. E., Howat, I. M., and Moon, T. (2008a). Seasonal speedup along the western flank of the Greenland Ice Sheet. *Science*, 320, 781–783, https://doi.org/10.1126/science.1153288.

Joughin, I., Howat, I., Alley, R. B., Ekstrom, G., Fahnestock, M., Moon, T., Nettles, M., Truffer, M., and Tsai, V. C. (2008b). Ice-front variation and tidewater behaviour on Helheim and Kangerdlugssuaq Glaciers, Greenland. *Journal of Geophysical Research: Earth Surface*, 113(F1), F01004, https://doi.org/10.1029/2007JF000837.

Joughin, I., Smith, B. E., Howat, I. M., Scambos, T., and Moon, T. (2010). Greenland flow variability from ice-sheet-wide velocity mapping. *Journal of Glaciology*, 56(197), 415–430, https://doi.org/10.3189/002214310792447734.

Joughin, I., Das, S. B., Flowers, G. E., Behn, M. D., Alley, R. B., King, M. A., Smith, B. E., Bamber, J., van den Broeke, M. R., and van Angelen, J. H. (2013). Influence of ice-sheet geometry and supraglacial lakes on seasonal ice-flow variability. *The Cryosphere*, 7, 1185–1192, https://doi.org/10.5194/tc-7-1185-2013.

Joughin, I., Smith, B. E., and Medley, B. (2014). Marine ice sheet collapse potentially under way for the Thwaites Glacier basin, West Antarctica. *Science*, 344(6185), 735–738, https://doi.org/10.1126/science.1249055.

Joughin, I., Smith, B. E., Howat, I. M., Moon, T., and Scambos, T. (2016). A SAR record of early 21st century change in Greenland. *Journal of Glaciology*, 62(231), 62–71, https://doi.org/10.1017/jog.2016.10.

Joughin, I., Smith, B. E., and Howat, I. M. (2018). A complete map of Greenland ice velocity derived from satellite data collected over 20 years. *Journal of Glaciology*, 64(243), 1–11, https://doi.org/10.1017/jog.2017.73.

Justice, C. O., Townshend, J. R. G., Vermote, E. F., Masuoka, E., Wolfe, R. E., Saleous, N., Roy, D. P., and Morisette, J. T. (2002). An overview of MODIS Land data processing and product status. *Remote Sensing of Environment*, 83(1–2), 3–15, https://doi.org/10.1016/S0034-4257(02)00084-6.

Kääb, A., Winsvold, S. H., Altena, B., Nuth, C., Nagler, T., and Wuite, J. (2016). Glacier remote sensing using Sentinel-2. Part I: radiometric and geometric performance, and application to ice velocity. *Remote Sensing*, 8, 598, https://doi.org/10.3390/rs8070598.

Kamb, B. (1987). Glacier surge mechanism based on linked cavity configuration of the basal water conduit system. *Journal of Geophysical Research: Solid Earth*, 92(B9), 9083–9100, https://doi.org/10.1029/JB092iB09p09083.

Kargel, J. S., Ahlstrøm, A. P., Alley, R. B., Bamber, J. L., Benham, T. J., Box, J. E., Chen, C., Christoffersen, P., Citterio, M., Cogley, J. G., Jiskoot, H., Leonard, G. J., Morin, P., Scambos, T., Sheldon, T., and Willis, I. (2012). Brief communication: Greenland's shrinking ice cover: "fast times" but not that fast. *The Cryosphere*, 6, 533–537, https://doi.org/10.5194/tc-6-533-2012.

Karlstrom, L. and Yang, K. (2016). Fluvial supraglacial landscape evolution on the Greenland Ice Sheet. *Geophysical Research Letters*, 43, 2683–2692, https://doi.org/10.1002/2016GL067697.

Khan, S. A., Aschwanden, A., Bjørk, A. A., Wahr, J., Kjeldsen, K. K., and Kjær, K. H. (2015). Greenland ice sheet mass balance: a review. *Reports on Progress in Physics*, 78, 048601, https://doi.org/10.1088/0034-4885/78/4/046801.

Kingslake, J., Ng, F., and Sole, A. (2015). Modelling channelized surface drainage of supraglacial lakes. *Journal of Glaciology*, 61(225), 185–199, https://doi.org/10.3189/2015JoG14J158.

Kingslake, J., Ely, J. C., Das, I., and Bell, R. E. (2017). Widespread movement of meltwater onto and across Antarctic ice shelves. *Nature*, 544, 349–352, https://doi.org/10.1038/nature22049.

Kirkham, J. D. (2017). *Constraining the pathways and fluxes of subglacial meltwater beneath the palaeo-Antarctic Ice Sheet*. Unpublished M.Phil. thesis, Scott Polar Research Institute, University of Cambridge, Cambridge, UK. https://doi.org/10.17863/CAM.13694.

Kjeldsen, K. K., Khan, S. A., Bjørk, A. A., Nielsen, K., and Mouginot, J. (2017). Ice-dammed lake drainage in west Greenland: drainage pattern and implications on ice flow and bedrock motion. *Geophysical Research Letters*, 44, 7320–7327, https://doi.org/10.1002/2017GL074081.

Knighton, A. D. (1972). Meandering habit of supraglacial streams. *GSA Bulletin*, 83(1), 201–204, https://doi.org/10.1130/0016-7606(1972)83[201:MHOSS]2.0.CO;2.

Knighton. A. D. (1981). Channel form and flow characteristics of supraglacial streams, Austre Okstindbreen, Norway. *Arctic and Alpine Research*, 13(3), 295–306, https://doi.org/10.2307/1551036.

Koenig, L. S., Miège, C., Forster, R. R., and Brucker, L. (2014). Initial in situ measurements of perennial meltwater storage in the Greenland firn aquifer. *Geophysical Research Letters*, 41, 81–85, https://doi.org/10.1002/2013GL058083.

Koenig, L. S., Lampkin, D. J., Montgomery, L. N., Hamilton, S. L., Turrin, J. B., Joseph, C. A., Moutsafa, S. E., Panzer, B., Casey, K. A., Paden, J. D., Leuschen, C., and Gogineni, P. (2015). Wintertime storage of water in buried supraglacial lakes across the Greenland Ice Sheet. *The Cryosphere*, 9, 1333–1342, https://doi.org/10.5194/tc-9-1333-2015.

Koziol, C. P. (2018). *Modelling the impact of surface melt on the hydrology and dynamics of the Greenland Ice Sheet*. Unpublished Ph.D. thesis, Department of Geography, University of Cambridge, Cambridge, UK. https://doi.org/10.17863/CAM.20372.

Koziol, C. P. and Arnold, N. (2018). Modelling seasonal meltwater forcing of the velocity of land-terminating margins of the Greenland Ice Sheet. *The Cryosphere*, 12, 971–991, https://doi.org/10.5194/tc-12-971-2018.

Koziol, C., Arnold, N., Pope, A., and Colgan, W. (2017). Quantifying supraglacial meltwater pathways in the Paakitsoq region, west Greenland. *Journal of Glaciology*, 63, 464–476, https://doi.org/10.1017/jog.2017.5.

Krawczynski, M. J., Behn, M. D., Das, S. B., and Joughin, I. (2009). Constraints on the lake volume required for hydro-fracture through ice sheets. *Geophysical Research Letters*, 36, L10501, https://doi.org/10.1029/2008GL036765.

Kuipers Munneke, P., Ligtenberg, S. R. M., van den Broeke, M. R., van Angelen, J. H., and Forster, R. R. (2014). Explaining the presence of perennial liquid water bodies in the firn of the Greenland Ice Sheet. *Geophysical Research Letters*, 41, 476–483, https://doi.org/10.1002/2013GL058389.

Kulessa, B., Hubbard, A. L., Booth, A. D., Bougamont, M., Dow, C. F., Doyle, S. H., Christoffersen, P., Lindbäck, K., Pettersson, R., Fitzpatrick, A. A. W., and Jones, G. A. (2017). Seismic evidence for complex sedimentary control of Greenland Ice Sheet flow. *Science Advances*, 3, 1–8, https://doi.org/10.1126/sciadv.1603071.

Lampkin, D. J. (2011). Supraglacial lake spatial structure in western Greenland during the 2007 ablation season. *Journal of Geophysical Research: Earth Surface*, 116, F04001, https://doi.org/10.1029/2010JF001725.

Lampkin, D.J. and VanderBerg, J. (2011). A preliminary investigation of the influence of basal and surface topography on supraglacial lake distribution near Jakobshavn Isbrae, western Greenland. *Hydrological Processes*, 25, 3347–3355, https://doi.org/10.1002/hyp.8170.

Law, R. (2018). *The development and application of IceLake, an accurate and computationally efficient model of supraglacial lake evolution in the ablation zone of the Greenland Ice Sheet.* Unpublished M.Phil. thesis, Scott Polar Research Institute, University of Cambridge, Cambridge, UK.

Leeson, A. A., Shepherd, A., Palmer, S., Sundal, A., and Fettweis, X. (2012). Simulating the growth of supraglacial lakes at the western margin of the Greenland ice sheet. *The Cryosphere*, 6, 1077–1086, https://doi.org/10.5194/tc-6-1077-2012.

Leeson, A. A., Shepherd, A., Sundal, A. V., Johansson, A. M., Selmes, N., Briggs, K., Hogg, A. E., and Fettweis, X. (2013). A comparison of supraglacial lake observations derived from MODIS imagery at the western margin of the Greenland ice sheet. *Journal of Glaciology*, 59(218), 1179–1188, https://doi.org/10.3189/2013JoG13J064.

Leeson, A. A., Shepherd, A., Briggs, K., Howat, I., Fettweis, X., Morlighem, M., and Rignot, E. (2015). Supraglacial lakes on the Greenland ice sheet advance inland under warming climate. *Nature Climate Change*, 5(1), 51–55, https://doi.org/10.1038/nclimate2463.

Legleiter, C. J., Tedesco, M., Smith, L. C., Behar, A. E., and Overstreet, B. T. (2014). Mapping the bathymetry of supraglacial lakes and streams on the Greenland ice sheet using field measurements and high-resolution satellite images. *The Cryosphere*, 8, 215–228, https://doi.org/10.5194/tc-8-215-2014.

Lettang, F. J., Crocker, R. I., Emery, W. J., and Maslanik, J. A. (2013). Estimating the extent of drained supraglacial lakes on the Greenland Ice Sheet. *International Journal of Remote Sensing*, 34(13), 4754–4768, https://doi.org/10.1080/01431161.2013.782118.

Liang, Y., Colgan, W., Lv, Q., Steffen, K., Abdalati, W., Stroeve, J., Gallaher, D., and Bayou, N. (2012). A decadal investigation of supraglacial lakes in west Greenland using a fully automatic detection and tracking algorithm. *Remote Sensing of Environment*, 123, 127–138, https://doi.org/10.1016/j.rse.2012.03.020.

Licciardi, G. and Chanussot, J. (2018). Spectral transformation based on nonlinear principal component analysis for dimensionality reduction of hyperspectral images. *European Journal of Remote Sensing*, 51, 375–390, https://doi.org/10.1080/22797254.2018.1441670.

Lovelock, C. E., Cahoon, D. R., Friess, D. A., Guntenspergen, G. R., Krauss, K. W., Reef, R., Rogers, K., Saunders, M. L., Sidik, F., Swales, A., Saintilan, N., Thuyen, L. X., and Triet, T. (2015). The vulnerability of Indo-Pacific mangrove forests to sea-level rise. *Nature*, 526, 559–563, https://doi.org/10.1038/nature15538.

Luo, G., Chen, G., Tian, L., Qin, K., and Qian, S.-E. (2016). Minimum noise fraction versus principal component analysis as a preprocessing step for hyperspectral imagery denoising. *Canadian Journal of Remote Sensing*, 42, 106–116, https://doi.org/10.1080/07038992.2016.1160772.

Lüthi, M., Funk, M., Iken, A., Gogineni, S., and Truffer, M. (2002). Mechanisms of fast flow in Jakobshavn Isbræ, west Greenland: part III: Measurements of ice deformation, temperature and cross-borehole conductivity in boreholes to the bedrock. *Journal of Glaciology*, 48(162), 369–385, https://doi.org/10.3189/172756502781831322.

Lüthi, M. P., Ryser, C., Andrews, L. C., Catania, G. A., Funk, M., Hawley, R. L., Hoffman, M. J., and Neumann, T. A. (2015). Heat sources within the Greenland Ice Sheet: dissipation, temperature paleo-firn and cryo-hydrologic warming. *The Cryosphere*, 9, 245–253, https://doi.org/10.5194/tc-9-245-2015.

Lüthje, M., Pedersen, L. T., Reeh, N., and Greuell, W. (2006). Modelling the evolution of supraglacial lakes on the west Greenland ice-sheet margin. *Journal of Glaciology*, 52, 608–618, https://doi.org/10.3189/172756506781828386.

Macdonald, G. J., Banwell, A. F., and MacAyeal, D. R. (2018). Seasonal evolution of supraglacial lakes on a floating ice tongue, Petermann Glacier, Greenland. *Annals of Glaciology*, 1–10, https://doi.org/10.1017/aog.2018.9.

Machguth, H., MacFerrin, M., van As, D., Box, J. E., Charalampidis, C., Colgan, W., Fausto, R. S., Meijer, H. A. J., Mosley-Thompson, E., and van de Wal, R. S. W. (2016). Greenland meltwater storage in firn limited by near-surface ice formation. *Nature Climate Change*, 6, 390–393, https://doi.org/10.1038/nclimate2899.

Mankoff, K. D. and Tulaczyk, S. M. (2017). The past, present and future viscous heat dissipation available for Greenland subglacial conduit formation. *The Cryosphere*, 11, 303–317, https://doi.org/10.5194/tc-11-303-2017.

Maritorena, S., Morel, A., and Gentili, B. (1994). Diffuse reflectance of oceanic shallow waters: influence of water depth and bottom albedo. *Limnology and Oceanography*, 39, 1689–1703, https://doi.org/10.4319/lo.1994.39.7.1689.

Marzeion, B., Jarosch, A. H., and Hofer, M. (2012). Past and future sea-level change from the surface mass balance of glaciers. *The Cryosphere*, 6, 1295–1322, https://doi.org/10.5194/tc-6-1295-2012.

Mayaud, J. R., Banwell, A. F., Arnold, N. S., and Willis, I. C. (2014). Modeling the response of subglacial drainage at Paakitsoq, west Greenland, to 21st century climate change. *Journal of Geophysical Research: Earth Surface*, 119, 2619–2634, https://doi.org/10.1002/2014JF003271.

McGrath, D., Colgan, W., Steffen, K., Lauffenburger, P., and Balog, J. (2011). Assessing the summer water budget of a moulin basin in the Sermeq Avannarleq ablation region, Greenland ice sheet. *Journal of Glaciology*, 57(205), 954–964, https://doi.org/10.3189/002214311798043735.

McMillan, M., Nienow, P., Shepherd, A., Benham, T., and Sole, A. (2007). Seasonal evolution of supra-glacial lakes on the Greenland Ice Sheet. *Earth and Planetary Science Letters*, 262(3–4), 484–492, https://doi.org/10.1016/j.epsl.2007.08.002.

McMillan, M., Leeson, A., Shepherd, A., Briggs, K., Armitage, T. W. K., Hogg, A., Kuipers Munneke, P., van den Broeke, M. R., Noël, B. P. Y., van de Berg, W. J., Ligtenberg, S., Horwath, M., Groh, A., Muir, A., and Gillbert, L. (2016). A high-resolution record of Greenland mass balance. *Geophysical Research Letters*, 43(13), 7002–7010, https://doi.org/10.1002/2016GL069666.

Meierbachtol, T., Harper, J., and Humphrey, N. (2013). Basal drainage system response to increasing surface melt on the Greenland ice sheet. *Science*, 341(6147), 777–779, https://doi.org/10.1126/science.1235905.

Meierbachtol, T. W., Harper, J. T., Humphrey, N. F., and Wright, P. J. (2016). Mechanical forcing of water pressure in a hydraulically isolated reach beneath Western Greenland's ablation zone. *Annals of Glaciology*, 57(72), 62–70, https://doi.org/10.1017/aog.2016.5.

Messerli, A. (2011). *Identifying spatio-temporal patterns of supraglacial lake drainage and the implications for further understanding of the hydrology of the Greenland ice sheet*. Unpublished M.Phil. thesis, Scott Polar Research Institute, University of Cambridge, Cambridge, UK.

Miège, C., Forster, R. R., Box, J. E., Burgess, E. W., McConnell, J. R., Pasteris, D. R., and Spikes, V. B. (2013). Southeast Greenland high accumulation rates derived from firn cores and ground-penetrating radar. *Annals of Glaciology*, 54(63), 322–332, https://doi.org/10.3189/2013AoG63A358.

Miège, C., Forster, R. R., Brucker, L., Koenig, L. S., Solomon, D. K., Paden, J. D., Box, J. E., Burgess, E. W., Miller, J. Z., McNerney, L., Brautigam, N., Fausto, R. S., and Gogineni, S. (2016). Spatial extent and temporal variability of Greenland firn aquifers detected by ground and airborne radars. *Journal of Geophysical Research: Earth Surface*, 121, 2381–2398, https://doi.org/10.1002/2016JF003869.

Miles, B. W. J., Stokes, C. R., Vieli, A., and Cox, N. J. (2013). Rapid, climate-driven changes in outlet glaciers on the Pacific coast of East Antarctica. *Nature*, 500, 563–567, https://doi.org/10.1038/nature12382.

Miles, E. S., Willis, I. C., Arnold, N. S., Steiner, J. F., and Pellicciotti, F. (2017). Spatial, seasonal and interannual variability of supraglacial ponds in the Langtang Valley of Nepal, 1999 to 2013. *Journal of Glaciology*, 63(237), 88–105, https://doi.org/10.1017/jog.2016.120.

Miles, K. E., Willis, I. C., Benedek, C. L., Williamson, A. G., and Tedesco, M. (2017). Toward monitoring surface and subsurface lakes on the Greenland Ice Sheet using Sentinel-1 SAR and Landsat 8 OLI imagery. *Frontiers in Earth Science*, 5, 58, https://doi.org/10.3389/feart.2017.00058.

Miles, V. V., Miles, M. W., and Johannessen, O. M. (2016). Satellite archives reveal abrupt changes in behavior of Helheim Glacier, southeast Greenland. *Journal of Glaciology*, 62(231), 137–146, https://doi.org/10.1017/jog.2016.24.

Mobley, C. D. (1994). *Light and water: radiative transfer in natural waters*. San Diego: Academic Press.

Moon, T., Joughin, I., Smith, B., and Howat, I. (2012). 21st-century evolution of Greenland outlet glacier velocities. *Science*, 336, 576–578, https://doi.org/10.1126/science.1219985.

Moon, T., Joughin, I., Smith, B., van den Broeke, M. R., van de Berg, W. J., Noël, B., and Usher, M. (2014). Distinct patterns of seasonal Greenland glacier velocity. *Geophysical Research Letters*, 41(20), 7209–7216, https://doi.org/10.1002/2014GL061836.

Moon, T., Joughin, I., and Smith, B. (2015). Seasonal to multiyear variability of glacier surface velocity, terminus position, and sea ice/ice mélange in northwest Greenland. *Journal of Geophysical Research: Earth Surface*, 120(5), 818–833, https://doi.org/10.1002/2015JF003494.

Morlighem, M., Rignot, E., Mouginot, J., Seroussi, H., and Larour, E. (2014). Deeply incised submarine glacial valleys beneath the Greenland Ice Sheet. *Nature Geoscience*, 7, 418–422, https://doi.org/10.1038/ngeo2167.

Morlighem, M., Williams, C. N., Rignot, E., An, L., Arndt, J. E., Bamber, J. L., Catania, G., Chauché, N., Dowdeswell, J. A., Dorschel, B., Fenty, I., Hogan, K., Howat, I., Hubbard, A., Jakobsson, M., Jordan, T. M., Kjeldsen, K. K., Millan, R., Mayer, L., Mouginot, J., Noël, B. P. Y., O'Cofaigh, C., Palmer, S., Rysgaard, S., Seroussi, H., Siegert, M. J., Slabon, P., Straneo, F., van den Broeke, M. R., Weinrebe, W., Wood, M., and Zinglersen, K. B. (2017). BedMachine v3: complete bed topography and ocean bathymetry mapping of Greenland from multibeam echo sounding combined with mass conservation. *Geophysical Research Letters*, 44(21), 11051–11061, https://doi.org/10.1002/2017GL074954.

Morriss, B. F., Hawley, R. L., Chipman, J. W., Andrews, L. C., Catania, G. A., Hoffman, M. J., Lüthi, M. P., and Neumann, T. (2013). A ten-year record of supraglacial lake evolution and rapid drainage in west Greenland using an automated processing algorithm for multispectral imagery. *The Cryosphere*, 7, 1869–1877, https://doi.org/10.5194/tc-7-1869-2013.

Mouginot, J., Rignot, E., Scheuchl, B., and Millan, R. (2017). Comprehensive annual ice sheet velocity mapping using Landsat-8, Sentinel-1, and RADARSAT-2 data. *Remote Sensing*, 9(4), 364, https://doi.org/10.3390/rs9040364.

Moussavi, M. S., Abdalati, W., Pope, A., Scambos, T., Tedesco, M., MacFerrin, M., and Grigsby, S. (2016). Derivation and validation of supraglacial lake volumes on the Greenland Ice Sheet from high-resolution satellite imagery. *Remote Sensing of Environment*, 183, 294–303, https://doi.org/10.1016/j.rse.2016.05.024.

Moyer, A. N., Nienow, P. W., Gourmelen, N., Sole, A. J., and Slater, D. A. (2017). Estimating spring terminus submarine melt rates at a Greenlandic tidewater glacier using satellite imagery. *Frontiers in Earth Science*, 5, 107, https://doi.org/10.3389/feart.2017.00107.

Naegeli, K., Damm, A., Huss, M., Wulf, H., Schaepman, M., and Hoelzle, M. (2017). Cross-comparison of albedo products for glacier surfaces derived from airborne and satellite (Sentinel-2 and Landsat 8) optical data. *Remote Sensing*, 9(2), 110, https://doi.org/10.3390/rs9020110.

Nathan-King, H. (2015). *Marine-terminating outlet glacier response to hydrological mechanisms: a comparative study at Store Gletscher and Rink Isbrae, Uummannaq Bay, west Greenland*. Unpublished M.Phil. thesis, Scott Polar Research Institute, University of Cambridge, Cambridge, UK. https://doi.org/10.17863/CAM.8765.

Nerem, R. S., Beckley, B. D., Fasullo, J. T., Hamlington, B. D., Masters, D., and Mitchum, G. T. (2018). Climate-change-driven accelerated sea-level rise detected in the altimeter era. *Proceedings of the National Academy of Sciences*, https://doi.org/10.1073/pnas.1717312115.

Neumann, J. E., Emanuel, K., Ravela, S., Ludwig, L., Kirshen, P., Bosma, K., and Martinich, J. (2015). Joint effects of storm surge and sea-level rise on US Coasts: new economic estimates of impacts, adaptation and benefits of mitigation policy. *Climatic Change*, 129(1–2), 337–349, https://doi.org/10.1007/s10584-014-1304-z.

Nghiem, S. V., Hall, D. K., Mote, T. L., Tedesco, M., Albert, M. R., Keegan, K., Shuman, C. A., DiGirolamo, N. E., and Neumann, G. (2012). The extreme melt across the Greenland ice sheet in 2012. *Geophysical Research Letters*, 39(20), L20502, https://doi.org/10.1029/2012GL053611.

Nicholls, R. J. and Cazenave, A. (2010). Sea-level rise and its impact on coastal zones. *Science*, 328(5985), 1517–1520, https://doi.org/10.1126/science.1185782.

Nicholls, R. J., Hoozemans, F. M. J., and Marchand, M. (1999). Increasing flood risk and wetland losses due to global sea-level rise: regional and global analyses. *Global Environmental Change*, 9(S1), S69–S87, https://doi.org/10.1016/S0959-3780(99)00019-9.

Nick, F. M., Vieli, A., Howat, I. M., and Joughin, I. (2009). Large-scale changes in Greenland outlet glacier dynamics triggered at the terminus. *Nature Geoscience*, 2, 110–114, https://doi.org/10.1038/ngeo394.

Nienow, P. W., Sole, A. J., Slater, D. A., and Cowton, T. R. (2017). Recent advances in our understanding of the role of meltwater in the Greenland ice sheet system. *Current Climate Change Reports*, 3(4), 330–344, https://doi.org/10.1007/s40641-017-0083-9.

Noël, B., van de Berg, W. J., Machguth, H., Lhermitte, S., Howat, I., Fettweis, X., and van den Broeke, M. R. (2016). A daily, 1 km resolution data set of downscaled Greenland ice sheet mass balance (1958–2015). *The Cryosphere*, 10, 2361–2377, https://doi.org/10.5194/tc-10-2361-2016.

Noël, B., van de Berg, W., van Wessem, J. M., van Meijgaard, E., van As, D., Lenaerts, J. T. M., Lhermitte, S., Kuipers Munneke, P., Smeets, C. J. P. P., van Ulft, L. H., van de Wal, R. S. W., and van den Broeke, M. R. (2018). Modelling the climate and surface mass balance of polar ice sheets using RACMO2 – part 1: Greenland (1958–2016). *The Cryosphere*, 12, 811–831, https://doi.org/10.5194/tc-12-811-2018.

Nye, J. F. (1957). The distribution of stress and velocity in glaciers and ice-sheets. *Proceedings of the Royal Society of London A*, 239(1216), 113–133, https://doi.org/10.1098/rspa.1957.0026.

Palmer, S., Shepherd, A., Nienow, P., and Joughin, I. (2011). Seasonal speedup of the Greenland Ice Sheet linked to routing of surface water. *Earth and Planetary Science Letters*, 302, 423–428, https://doi.org/10.1016/j.epsl.2010.12.037.

Palmer, S. J., Dowdeswell, J. A., Christoffersen, P., Young, D. A., Blankenship, D. D., Greenbaum, J. S., Benham T., Bamber, J., and Siegert, M. J. (2013). Greenland subglacial lakes detected by radar. *Geophysical Research Letters*, 40, 6154–6159, https://doi.org/10.1002/2013GL058383.

Palmer, S., McMillan, M., and Morlighem, M. (2015). Subglacial lake drainage detected beneath the Greenland ice sheet. *Nature Communications*, 6, 8408, https://doi.org/10.1038/ncomms9408.

Paul, F., Winsvold, S. H., Kääb, A., Nagler, T., and Schwaizer, G. (2016). Glacier remote sensing using Sentinel-2. Part II: mapping glacier extents and surface facies, and comparison to Landsat 8. *Remote Sensing*, 8, 575, https://doi.org/10.3390/rs8070575.

Phillips, T., Rajaram, H., and Steffen, K. (2010). Cryo-hydrologic warming: a potential mechanism for rapid thermal response of ice sheets. *Geophysical Research Letters*, 37(20), L20503, https://doi.org/10.1029/2010GL044397.

Phillips, T., Rajaram, H., Colgan, W., Steffen, K., and Abdalati, W. (2013). Evaluation of cryo-hydrologic warming as an explanation for increased ice velocities in the wet snow zone, Sermeq Avannarleq, west Greenland. *Journal of Geophysical Research: Earth Surface*, 118, 1241–1256, https://doi.org/10.1002/jgrf.20079.

Philpot, W. D. (1989). Bathymetric mapping with passive multispectral imagery. *Applied Optics*, 28(8), 1569–1578, https://doi.org/10.1364/AO.28.001569.

Plummer, J., Gogineni, S., van der Veen, C., Leuschen, C., and Li, J. (2008). Ice thickness and bed map for Jakobshavn Isbræ. *CReSIS Technical Report 2008-1*.

Podrasky, D., Truffer, M., Fahnestock, M., Amundson, J. M., Cassotto, R., and Joughin, I. (2012). Outlet glacier response to forcing over hourly to interannual timescales, Jakobshavn Isbræ, Greenland. *Journal of Glaciology*, 58(212), 1212–1226, https://doi.org/10.3189/2012JoG12J065.

Poinar, K. (2015). *The influence of meltwater on the thermal structure and flow of the Greenland Ice Sheet*. Unpublished Ph.D. thesis, University of Washington, Seattle, WA, USA. Available at: http://hdl.handle.net/1773/35062.

Poinar, K., Joughin, I., Das, S. B., Behn, M. D., Lenaerts, J., and van den Broeke, M. R. (2015). Limits to future expansion of surface-melt-enhanced ice flow into the interior of western Greenland. *Geophysical Research Letters*, 42, 1800–1807, https://doi.org/10.1002/2015GL063192.

Poinar, K., Joughin, I., Lilien, D., Brucker, L., Kehrl, L., and Nowicki, S. (2017a). Drainage of southeast Greenland firn aquifer water through crevasses to the bed. *Frontiers in Earth Science*, 5, 5, https://doi.org/10.3389/feart.2017.00005.

Poinar, K., Joughin, I., Lenaerts, J. T. M., and van den Broeke, M. R. (2017b). Englacial latent-heat transfer has limited influence on seaward ice flux in western Greenland. *Journal of Glaciology*, 63, 1–16, https://doi.org/10.1017/jog.2016.103.

Poinar, K., Andrews, L. C., Moon, T. A., and Nowicki, S. (2017c). Challenges in understanding and predicting Greenland lake drainage events. *American Geophysical Union Fall Meeting, abstract C11A-0893*. New Orleans, December 2017.

Pope, A. (2016). Reproducibly estimating and evaluating supraglacial lake depth with Landsat 8 and other multispectral sensors. *Earth and Space Science*, 3, 176–188, https://doi.org/10.1002/2015EA000125.

Pope, A. and Rees, W. G. (2014a). Impact of spatial, spectral, and radiometric properties of multispectral imagers on glacier surface classification. *Remote Sensing of Environment*, 141, 1–13, https://doi.org/10.1016/j.rse.2013.08.028.

Pope, A. and Rees, G. (2014b). Using *in situ* spectra to explore Landsat classification of glacier surfaces. *International Journal of Applied Earth Observation and Geoinformation*, 27, 42–52, https://doi.org/10.1016/j.jag.2013.08.007.

Pope, A., Rees, W. G., Fox, A. J., and Fleming, A. (2014). Open access data in polar and cryospheric remote sensing. *Remote Sensing*, 6, 6183–6220, https://doi.org/10.3390/rs6076183.

Pope, A., Scambos, T. A., Moussavi, M., Tedesco, M., Willis, M., Shean, D., and Grigsby, S. (2016). Estimating supraglacial lake depth in west Greenland using Landsat 8 and comparison with other multispectral sensors. *The Cryosphere*, 10, 15–27, https://doi.org/10.5194/tc-10-15-2016.

Pope, R. M. and Fry, E. S. (1997). Absorption spectrum (380–700 nm) of pure water. II. Integrating cavity measurements. *Applied Optics*, 36, 8710–8723, https://doi.org/10.1364/AO.36.008710.

Pritchard, H. D., Arthern, R. J., Vaughan, D. G., and Edwards, L. A. (2009). Extensive dynamic thinning on the margins of the Greenland and Antarctic ice sheets. *Nature*, 461, 971–975, https://doi.org/10.1038/nature08471.

Quincey, D. J. and Luckman, A. (2009). Progress in satellite remote sensing of ice sheets. *Progress in Physical Geography*, 33(4), 547–567, https://doi.org/10.1177/0309133309346883.

Raper, S. C. B. and Braithwaite, R. J. (2006). Low sea level rise projections from mountain glaciers and icecaps under global warming. *Nature*, 439, 311–313, https://doi.org/10.1038/nature04448.

Raymo, M. E., Lisiecki, L. E., and Nisancioglu, K. H. (2006). Plio-Pleistocene ice volume, Antarctic climate, and the Global $\delta^{18}O$ record. *Science*, 313(5786), 492–495, https://doi.org/10.1126/science.1123296.

Rees, W. G. (2012). *Physical principles of remote sensing*. 3rd ed. New York: Cambridge University Press.

Rignot, E. and Kanagaratnam, P. (2006). Changes in the velocity structure of the Greenland ice sheet. *Science*, 311(5763), 986–990, https://doi.org/10.1126/science.1121381.

Rignot, E., Bamber, J. L., van den Broeke, M. R., Davis, C., Li, Y., van de Berg, W. J., and van Meijgaard, E. (2008a). Recent Antarctic ice mass loss from radar interferometry and regional climate modelling. *Nature Geoscience*, 1, 106–110, https://doi.org/10.1038/ngeo102.

Rignot, E., Box, J. E., Burgess, E., and Hanna, E. (2008b). Mass balance of the Greenland ice sheet from 1958 to 2007. *Geophysical Research Letters*, 35(20), L20502, https://doi.org/10.1029/2008GL035417.

Rignot, E., Velicogna, I., van den Broeke, M. R., Monaghan. A., and Lenaerts, J. T. M. (2011). Acceleration of the contribution of the Greenland and Antarctic ice sheets to sea level rise. *Geophysical Research Letters*, 38, L05503, https://doi.org/10.1029/2011GL046583.

Rignot, E., Fenty, I., Xu, Y., Cai, C., and Kemp, C. (2015). Undercutting of marine-terminating glaciers in west Greenland. *Geophysical Research Letters*, 42(14), 5909–5917, https://doi.org/10.1002/2015GL064236.

Ringnér, M. (2008). What is principal component analysis? *Nature Biotechnology*, 26(3), 303–304, https://doi.org/10.1038/nbt0308-303.

Röthlisberger, H. (1972). Water pressure in intra- and subglacial channels. *Journal of Glaciology*, 11(62), 177–203, https://doi.org/10.3189/S0022143000022188.

Roy, D. P., Wulder, M. A., Loveland, T. R., Woodcock, C. E., Allen, R. G., Anderson, M. C., Helder, D., Irons, J. R., Johnson, D. M., Kennedy, R., Scambos, T. A., Schaaf, C. B., Schott, J. R., Sheng, Y., Vermote, E. F., Belward, A. S., Bindschadler, R., Cohen, W. B., Gao, F., Hipple, J. D., Hostert, P., Huntington, J., Justice, C. O., Kilic, A., Kovalskyy, V., Lee, Z. P., Lymburner, L., Masek, J. G., McCorkel, J., Shuai, Y., Trezza, R., Vogelmann, J., Wynne, R. H., and Zhu, Z. (2014). Landsat-8: science and product vision for terrestrial global change research. *Remote Sensing of Environment*, 145, 154–172, https://doi.org/10.1016/j.rse.2014.02.001.

Ryan, J. C., Hubbard, A. L., Box, J. E., Todd, J., Christoffersen, P., Carr, J. R., Holt, T. O., and Snooke, N. (2015). UAV photogrammetry and structure from motion to assess calving dynamics at Store Glacier, a large outlet draining the Greenland ice sheet. *The Cryosphere*, 9, 1–11, https://doi.org/10.5194/tc-9-1-2015.

Ryser, C., Lüthi, M. P., Andrews, L. C., Hoffman, M. J., Catania, G. A., Hawley, R. L., Neumann, T. A., and Kristensen, S. S. (2014). Sustained high basal motion of the Greenland ice sheet revealed by borehole deformation. *Journal of Glaciology*, 60(222), 647–660, https://doi.org/10.3189/2014JoG13J196.

Schlegel, N.-J., Wiese, D. N., Larour, E. Y., Watkins, M. M., Box, J. E., Fettweis, X., and van den Broeke, M. R. (2016). Application of GRACE to the assessment of model-based estimates of monthly Greenland Ice Sheet mass balance (2003–2012). *The Cryosphere*, 10, 1965–1989, https://doi.org/10.5194/tc-10-1965-2016.

Schoof, C. (2005). The effect of cavitation on glacier sliding. *Proceedings of the Royal Society A*, 461(2055), 609–627, https://doi.org/10.1098/rspa.2004.1350.

Schoof, C. (2010). Ice-sheet acceleration driven by melt supply variability. *Nature*, 468, 803–806, https://doi.org/10.1038/nature09618.

Selmes, N. (2011). *Remote sensing of supraglacial lakes on the Greenland Ice Sheet*. Unpublished Ph.D. thesis, Department of Geography, Swansea University, Swansea, UK.

Selmes, N., Murray, T., and James, T. D. (2011). Fast draining lakes on the Greenland Ice Sheet. *Geophysical Research Letters*, 38, L15501, https://doi.org/10.1029/2011GL047872.

Selmes, N., Murray, T., and James, T. D. (2013). Characterizing supraglacial lake drainage and freezing on the Greenland Ice Sheet. *The Cryosphere Discussions*, 7, 475–505, https://doi.org/10.5194/tcd-7-475-2013.

Sergienko, O. V. (2013). Glaciological twins: basally controlled subglacial and supraglacial lakes. *Journal of Glaciology*, 59(213), 3–8, https://doi.org/10.3189/2013JoG12J040.

Seroussi, H., Morlighem, M., Rignot, E., Khazendar, A., Larour, E., and Mouginot, J. (2013). Dependence of century-scale projections of the Greenland ice sheet on its thermal regime. *Journal of Glaciology*, 59(218), 1024–1034, https://doi.org/10.3189/2013JoG13J054.

Shannon, S. R., Payne, A. J., Bartholomew, I. D., van den Broeke, M. R., Edwards, T. L., Fettweis, X., Gagliardini, O., Gillet-Chaulet, F., Goelzer, H., Hoffman, M. J., Huybrechts, P., Mair, D. W. F., Nienow, P. W., Perego, M., Price, S. F., Smeets, C. J. P. P., Sole, A. J., van de Wal, R. S. W., and Zwinger, T. (2013). Enhaced basal lubrication and the contribution of the Greenland ice sheet to future sea-level rise. *Proceedings of the National Academy of Sciences*, 110(35), 14156–14161, https://doi.org/10.1073/pnas.1212647110.

Shepherd, A. and Wingham, D. (2007). Recent sea-level contributions of the Antarctic and Greenland ice sheets. *Science*, 315(5818), 1529–1532, https://doi.org/10.1126/science.1136776.

Shepherd, A., Hubbard, A., Nienow, P., King, M., McMillan, M., and Joughin, I. (2009). Greenland ice sheet motion coupled with daily melting in late summer. *Geophysical Research Letters*, 36, L01501, https://doi.org/10.1029/2008GL035758.

Shepherd, A., Ivins, E. R., Geruo, A., Barletta, V. R., Bentley, M. J., Bettadpur, S., Briggs, K. H., Bromwich, D. H., Forsberg, R., Galin, N., Horwarth, M., Jacobs, S., Joughin, I., King, M. A., Lenaerts, J. T. M., Li, J., Ligtenberg, S. J., Luckman, A., Luthcke, S. B., McMillan, M., Meister, R., Milne, G., Mouginot, J., Muir, A., Nicolas, J. P., Paden, J., Payne, A. J., Pritchard, H., Rignot, E., Rott, H., Sanberg Sørensen, L., Scambos, T. A., Scheuchl, B., Scharma, E. J. O., Smith, B., Sundal, A. V., van Angelen, J. H., van de Berg, W. J., van den Broeke, M. R., Vaughan, D. G., Velicogna, I., Wahr, J., Whitehouse, P. J., Wingham, D. J., Yi, D., Young, D., and Zwally, H. J. (2012). A reconciled estimate of ice-sheet mass balance. *Science*, 338(6111), 1183–1189, https://doi.org/10.1126/science.1228102.

Shreve, R. L. (1972). Movement of water in glaciers. *Journal of Glaciology*, 11(62), 205–214, https://doi.org/10.3189/S002214300002219X.

Slater, D. A., Nienow, P. W., Cowton, T. R., Goldberg, D. N., and Sole, A. J. (2015). Effect of near-terminus subglacial hydrology on tidewater glacier submarine melt rates. *Geophysical Research Letters*, 42(8), 2861–2868, https://doi.org/10.1002/2014GL062494.

Slater, D. A., Goldberg, D. N., Nienow, P. W., and Cowton, T. R. (2016). Scalings for submarine melting at tidewater glaciers and buoyant plume theory. *Journal of Physical Oceanography*, 46, 1839–1855, https://doi.org/10.1175/JPO-D-15-0132.1.

Slater, D. A., Nienow, P. W., Goldberg, D. N., Cowton, T. R., and Sole, A. J. (2017). A model for tidewater glacier undercutting by submarine melting. *Geophysical Research Letters*, 44(5), 2360–2368, https://doi.org/10.1002/2016GL072374.

Smith, L. C., Chu, V. W., Yang, K., Gleason, C. J., Pitcher, L. H., Rennermalm, A. K., Legleiter, C. J., Behar, A. E., Overstreet, B. T., Moustafa, S. E., Tedesco, M., Forster, R. R., LeWinter, A. L., Finnegan, D. C., Sheng, Y., and Balog, J. (2015). Efficient meltwater drainage through supraglacial streams and rivers on the southwest Greenland ice sheet. *Proceedings of the National Academy of Sciences*, 112(4), 1001–1006, https://doi.org/10.1073/pnas.1413024112.

Smith, L. C., Yang, K., Pitcher, L. H., Overstreet, B. T., Chu, V. W., Rennermalm, A. K., Ryan, J. C., Cooper, M. G., Gleason, C. J., Tedesco, M., Jeyaratnam, J., van As, D., van den Broeke, M. R., van de Berg, W. J., Noël, B., Langen, P. L., Cullather, R. I., Zhao, B., Willis, M. J., Hubbard, A., Box, J. E., Jenner, B. A., and Behar, A. E. (2017). Direct measurements of meltwater runoff on the Greenland ice sheet surface. *Proceedings of the National Academy of Sciences*, 114(50), E10622–E10631, https://doi.org/10.1073/pnas.1707743114.

Smith, R. C. and Baker, K. S. (1981). Optical properties of the clearest natural waters (200–800 nm). *Applied Optics*, 20, 177–184, https://doi.org/10.1364/AO.20.000177.

Sneed, W. A. and Hamilton, G. S. (2007). Evolution of melt pond volume on the surface of the Greenland Ice Sheet. *Geophysical Research Letters*, 34, L03501, https://doi.org/10.1029/2006GL028697.

Sole, A., Nienow, P., Bartholomew, I., Mair, D., Cowton, T., Tedstone, A., and King, M. A. (2013). Winter motion mediates dynamic response of the Greenland Ice Sheet to warmer summers. *Geophysical Research Letters*, 40, 3940–3944, https://doi.org/10.1002/grl.50764.

Stevens, L. A., Behn, M. D., McGuire, J. J., Das, S. B., Joughin, I., Herring, T., Shean, D. E., and King, M. A. (2015). Greenland supraglacial lake drainages triggered by hydrologically induced basal slip. *Nature*, 522, 73–76, https://doi.org/10.1038/nature14480.

Stevens, L. A., Behn, M. D., Das, S. B., Joughin, I., Noël, B. P. Y., van den Broeke, M., and Herring, T. (2016a). Greenland Ice Sheet flow response to runoff variability. *Geophysical Research Letters*, 43, 11295–11303, https://doi.org/10.1002/2016GL070414.

Stevens, L. A., Straneo, F., Das, S. B., Pludeemann, A. J., Kukulya, A. L., and Morlighem, M. (2016b). Linking glacially modified waters to catchment-scale subglacial discharge using autonomous underwater vehicle observations. *The Cryosphere*, 10, 417–432, https://doi.org/10.5194/tc-10-417-2016.

Stibal, M., Box, J. E., Cameron, K. A., Langen, P. L., Yallop, M. L., Mottram, R. H., Khan, A. L., Molotch, N. P., Chrismas, N. A. M., Cali Quaglia, F., Remias, D., Smeets, C. J. P. P., van den Broeke, M. R., Ryan, J. C., Hubbard, A. L., Tranter, M., van As, D., and Ahlstrøm, A. P. (2017). Algae drive enhanced darkening of bare ice on the Greenland ice sheet. *Geophysical Research Letters*, 44, 11463–11471, https://doi.org/10.1002/2017GL075958.

Storey, J., Roy, D. P., Masek, J., Gascon, F., Dwyer, J., and Choate, M. (2016). A note on the temporary misregistration of Landsat-8 Operational Land Imager (OLI) and Sentinel-2 Multi Spectral Instrument (MSI) imagery. *Remote Sensing of Environment*, 186, 121–122, https://doi.org/10.1016/j.rse.2016.08.025.

Straneo, F., Heimbach, P., Sergienko, O., Hamilton, G., Catania, G., Griffies, S., Hallberg, R., Jenkins, A., Joughin, I., Motyka, R., Pfeffer, W. T., Price, S. F., Rignot, E., Scambos, T., Truffer, M., and Vieli, A. (2013). Challenges to understanding the dynamic response of Greenland's marine terminating glaciers to oceanic and atmospheric forcing. *Bulletin of the American Meteorological Society*, 94(8), 1131–1144, https://doi.org/10.1175/BAMS-D-12-00100.1.

Strunk, A., Knudsen, M. F., Egholm, D. L., Jansen, J. D., Levy, L. B., Jacobsen, B. H., and Larsen, N. K. (2017). One million years of glaciation and denudation history in west Greenland. *Nature Communications*, 8, 14199, https://doi.org/10.1038/ncomms14199.

Sundal, A. V., Shepherd, A., Nienow, P., Hanna, E., Palmer, S., and Huybrechts, P. (2009). Evolution of supra-glacial lakes across the Greenland Ice Sheet. *Remote Sensing of Environment*, 113, 2164–2171, https://doi.org/10.1016/j.rse.2009.05.018.

Sundal, A. V., Shepherd, A., Nienow, P., Hanna, E., Palmer, S., and Huybrechts, P. (2011). Melt-induced speed-up of Greenland ice sheet offset by efficient subglacial drainage. *Nature*, 469, 521–524, https://doi.org/10.1038/nature09740.

Tebaldi, C., Strauss, B. H., and Zervas, C. E. (2012). Modelling sea level rise impacts on storm surges along US coasts. *Environmental Research Letters*, 7(1), 014032, https://doi.org/10.1088/1748-9326/7/1/014032.

Tedesco, M. (2015). *Remote sensing and the cryosphere*. In: Tedesco, M. (ed.): *Remote sensing of the cryosphere*. Chichester: John Wiley & Sons, Ltd. https://doi.org/10.1002/9781118368909.ch1.

Tedesco, M. and Steiner, N. (2011). In-situ multispectral and bathymetric measurements over a supraglacial lake in western Greenland using a remotely controlled watercraft. *The Cryosphere*, 5, 445–452, https://doi.org/10.5194/tc-5-445-2011.

Tedesco, M., Lüthje, M., Steffen, K., Steiner, N., Fettweis, X., Willis, I., Bayou, N., and Banwell, A. (2012). Measurement and modeling of ablation of the bottom of supraglacial lakes in western Greenland. *Geophysical Research Letters*, 39, L02052, https://doi.org/10.1029/2011GL049882.

Tedesco, M., Willis, I. C., Hoffman, M. J., Banwell, A. F., Alexander, P., and Arnold, N. S. (2013). Ice dynamic response to two modes of surface lake drainage on the Greenland ice sheet. *Environmental Research Letters*, 8, 034007, https://doi.org/10.1088/1748-9326/8/3/034007.

Tedstone, A. J., Nienow, P. W., Sole, A. J., Mair, D. W. F., Cowton, T. R., Bartholomew, I. D., and King, M. A. (2013). Greenland ice sheet motion insensitive to exceptional melt water forcing. *Proceedings of the National Academy of Sciences*, 110(49), 19719–19724, https://doi.org/10.1073/pnas.1315843110.

Tedstone, A. J., Nienow, P. W., Gourmelen, N. and Sole, A. J. (2014). Greenland ice sheet annual motion insensitive to spatial variations in subglacial hydraulic structure. *Geophysical Research Letters*, 41, 8910–8917, https://doi.org/10.1002/2014GL062386.

Tedstone, A. J., Nienow, P. W., Gourmelen, N., Dehecq, A., Goldberg, D., and Hanna, E. (2015). Decadal slowdown of a land-terminating sector of the Greenland Ice Sheet despite warming. *Nature*, 526, 692–695, https://doi.org/10.1038/nature15722.

Tedstone, A. J., Bamber, J. L., Cook, J. M., Williamson, C. J., Fettweis, X., Hodson, A. J., and Tranter, M. (2017). Dark ice dynamics of the south-west Greenland Ice Sheet. *The Cryosphere*, 11, 2491–2506, https://doi.org/10.5194/tc-11-2491-2017.

Todd, J. and Christoffersen, P. (2014). Are seasonal calving dynamics forced by buttressing from ice mélange or undercutting by melting? Outcomes from full-Stokes simulations of Store Glacier, west Greenland. *The Cryosphere*, 8, 2353–2365, https://doi.org/10.5194/tc-8-2353-2014.

Townshend, J. R. G. and Justice, C. O. (1988). Selecting the spatial resolution of satellite sensors required for global monitoring of land transformations. *International Journal of Remote Sensing*, 9(2), 187–236, https://doi.org/10.1080/01431168808954847.

Tsai, V. C. and Rice, J. R. (2010). A model for turbulent hydraulic fracture and application to crack propagation at glacier beds. *Journal of Geophysical Research: Earth Surface*, 115, F03007, https://doi.org/10.1029/2009jf001474.

Tukey, J. W. (1977). *Exploratory data analysis*. Reading, MA: Addison-Wesley.

USGS (2013). *Using the USGS Landsat 8 Product*. Available at: http://landsat.usgs.gov/Landsat8_Using_Product.php. Accessed 20 September 2016.

van Angelen, J. H., Lenaerts, J. T. M., Lhermitte, S., Fettweis, X., Kuipers Munneke, P., van den Broeke, M. R., van Meijgaard, E., and Smeets, C. J. P. P. (2012). Sensitivity of Greenland Ice Sheet surface mass balance to surface albedo parameterization: a study with a regional climate model. *The Cryosphere*, 6, 1175–1186, https://doi.org/10.5194/tc-6-1175-2012.

van de Wal, R. S. W., Boot, M., van den Broeke, M. R., Smeets, C. J. P. P., Reijmer, C. H., Donker, J. J. A., and Oerlemans, J. (2008). Large and rapid melt-induced velocity changes in the ablation zone of the Greenland Ice Sheet. *Science*, 321, 111–113, https://doi.org/10.1126/science.1158540.

van de Wal, R. S. W., Smeets, C. J. P. P., Boot, W., Stoffelen, M., van Kampen, R., Doyle, S. H., Wilhelms, F., van den Broeke, M. R., Reijmer, C. H., Oerlemans, J., and Hubbard, A. (2015). Self-regulation of ice flow varies across the ablation area in south-west Greenland. *The Cryosphere*, 9, 603–611, https://doi.org/10.5194/tc-9-603-2015.

van den Broeke, M. R., Bamber, J. L., Ettema, J., Rignot, E., Schrama, E., van de Berg, W. J., van Meijgaard, W., Velicogna, I., and Wouters, B. (2009). Partitioning recent Greenland mass loss. *Science*, 326(5955), 984–986, https://doi.org/10.1126/science.1178176.

van den Broeke, M. R., Enderlin, E. M., Howat, I. M., Kuipers Munneke, P., Noël, B. P. Y., van de Berg, W. J., van Meijgaard, E., and Wouters, B. (2016). On the recent contribution of the Greenland ice sheet to sea level change. *The Cryosphere*, 10, 1933–1946, https://doi.org/10.5194/tc-10-1933-2016.

van den Broeke, M., Box, J., Fettweis, X., Hanna, E., Noël, B., Tedesco, M., van As, D., van de Berg, W. J., and van Kampenhout, L. (2017). Greenland Ice Sheet surface mass loss: recent developments in observation and modelling. *Current Climate Change Reports*, 3, 345–356, https://doi.org/10.1007/s40641-017-0084-8.

van der Veen, C. J. (2007). Fracture propagation as means of rapidly transferring surface meltwater to the base of glaciers. *Geophysical Research Letters*, 34(1), L01501, https://doi.org/10.1029/2006GL028385.

Vaughan, D. (1993). Relating the occurrence of crevasses to surface strain rates. *Journal of Glaciology*, 39(132), 255–266, https://doi.org/10.1017/S0022143000015926.

Vaughan, D. G., Cosimo, J. C., Allison, I., Carrasco, J., Kaser, G., Kwok. R., Mote, P., Murray, T., Paul, F., Ren, J., Rignot, E., Solomina, O., Steffen, K., and Zhang, T. (2013). *Observations: cryosphere*. In: *Climate change 2013: the physical science basis. Contribution of working group I to the fifth assessment report of the Intergovernmental Panel on Climate Change* [Stocker, T. F., Qin, D., Plattner, G.-K., Tignor, M., Allen, S. K., Boschung, J., Nauels, A., Xia, Y., Bex, V. and Midgley, P. M. (eds.).] Cambridge and New York: Cambridge University Press, pp. 317–382, https://doi.org/10.1017/CBO9781107415324.012.

Velicogna, I. (2009). Increasing rates of ice mass loss from the Greenland and Antarctic ice sheets revealed by GRACE. *Geophysical Research Letters*, 36, L19503, https://doi.org/10.1029/2009GL040222.

Velicogna, I. and Wahr, J. (2006). Measurements of time-variable gravity show mass loss in Antarctica. *Science*, 311(5768), 1754–1756, https://doi.org/10.1126/science.1123785.

Velicogna, I., Sutterley, T. C., and van den Broeke, M. R. (2014). Regional acceleration in ice mass loss from Greenland and Antarctica using GRACE time-variable gravity data. *Geophysical Research Letters*, 41(22), 8130–8137, https://doi.org/10.1002/2014GL061052.

Voytenko, D., Stern, A., Holland, D. M., Dixon, T. H., Christianson, K., and Walker, R. T. (2015). Tidally driven ice speed variation at Helheim Glacier, Greenland, observed with terrestrial radar interferometry. *Journal of Glaciology*, 61(226), 301–308, https://doi.org/10.3189/2015JoG14J173.

Walder, J. S. and Fowler, A. (1994). Channelized subglacial drainage over a deformable bed. *Journal of Glaciology*, 40(134), 3–15, https://doi.org/10.3189/S0022143000003750.

Walter, F., Chaput, J., and Lüthi, M. P. (2014). Thick sediments beneath Greenland's ablation zone and their potential role in future ice sheet dynamics. *Geology*, 42(6), 487–490, https://doi.org/10.1130/G35492.1.

Wang, Q., Blackburn, G. A., Onojeghuo, A. O., Dash, J., Zhou, L., Zhang, Y., and Atkinson, P. M. (2017). Fusion of Landsat 8 OLI and Sentinel-2 MSI data. *IEEE Transactions on Geoscience and Remote Sensing*, 55(7), 3885–3899, https://doi.org/10.1109/TGRS.2017.2683444.

Weidick, A. (1995). *Satellite image atlas of glaciers of the world*. Denver, CO: US Geological Survey.

Weisberg, S. (2005). *Applied linear regression*. 3rd ed. Hoboken: John Wiley & Sons Ltd. https://doi.org/10.1002/0471704091.

Werder, M. A., Hewitt, I. J., Schoof, C. G., and Flowers, G. E. (2013). Modeling channelized and distributed subglacial drainage in two dimensions. *Journal of Geophysical Research: Earth Surface*, 118(4), 2140–2158, https://doi.org/10.1002/jgrf.20146.

Williamson, A. G., Arnold, N. S., Banwell, A. F., and Willis, I. C. (2017). A Fully Automated Supraglacial lake area and volume Tracking ("FAST") algorithm: development and application using MODIS imagery of west Greenland. *Remote Sensing of Environment*, 196, 113–133, https://doi.org/10.1016/j.rse.2017.04.032.

Williamson, A. G., Willis, I. C., Arnold, N. S., and Banwell, A. F. (2018a). Controls on rapid supraglacial lake drainage in west Greenland: an Exploratory Data Analysis approach. *Journal of Glaciology*, 64(244), 208–226, https://doi.org/10.1017/JoG.2018.8.

Williamson, A. G., Banwell, A. F., Willis, I. C., and Arnold, N. S. (2018b). Dual-satellite (Sentinel-2 and Landsat 8) remote sensing of supraglacial lakes in Greenland. *The Cryosphere Discussions*, in review, https://doi.org/10.5194/tc-2018-56.

Willis, M. J., Herried, B. G., Bevis, M. G., and Bell, R. E. (2015). Recharge of a subglacial lake by surface meltwater in northeast Greenland. *Nature*, 518, 223–227, https://doi.org/10.1038/nature14116.

Xu, H. (2006). Modification of normalised difference water index (NDWI) to enhance open water features in remotely sensed imagery. *International Journal of Remote Sensing*, 27(14), 3025–3033, https://doi.org/10.1080/01431160600589179.

Xu, Y., Rignot, E., Menemenlis, D., and Koppes, M. (2012). Numerical experiments on subaqueous melting of Greenland tidewater glaciers in response to ocean warming and enhanced subglacial discharge. *Annals of Glaciology*, 53, 229–234, https://doi.org/10.3189/2012AoG60A139.

Xu, Y., Rignot, E., Fenty, I., Menemenlis, D., and Flexas, M. M. (2013). Subaqueous melting of Store Glacier, west Greenland from three-dimensional, high-resolution numerical modeling and ocean observations. *Geophysical Research Letters*, 40(17), 4648–4653, https://doi.org/10.1002/grl.50825.

Xu, Z., Schrama, E. J. O., van der Wal, W., van den Broeke, M., and Enderlin, E. M. (2016). Improved GRACE regional mass balance estimates of the Greenland ice sheet cross-validated with the input-output method. *The Cryosphere*, 10, 895–912, https://doi.org/10.5194/tc-10-895-2016.

Yallop, M. L., Anesio, A. M., Perkins, R. G., Cook, J., Telling, J., Fagan, D., MacFarlane, J., Stibal, M., Barker, G., Bellas, C., Hodson, A., Tranter, M., Wadham, J., and Roberts, N. W. (2012). Photophysiology and albedo-changing potential of the ice algal community on the surface of the Greenland ice sheet. *The ISME Journal*, 6, 2302–2313, https://doi.org/10.1038/ismej.2012.107.

Yang, K. and Smith, L. C. (2013). Supraglacial streams on the Greenland Ice Sheet delineated from combined spectral-shape information in high-resolution satellite imagery. *IEEE Geoscience and Remote Sensing Letters*, 10(4), 801–805, https://doi.org/10.1109/LGRS.2012.2224316.

Yang, K. and Smith, L. C. (2016). Internally drained catchments dominate supraglacial hydrology of the southwest Greenland Ice Sheet. *Journal of Geophysical Research: Earth Surface*, 121, 1891–1910, https://doi.org/10.1002/2016JF003927.

Yang, K., Smith, L. C., Chu, V. W., Gleason, C. J., and Li, M. (2015). A caution on the use of surface digital elevation models to simulate supraglacial hydrology of the Greenland Ice Sheet. *IEEE Journal of Selected Topics in Applied Earth Observations and Remote Sensing*, 8(11), 5212–5224, https://doi.org/10.1109/JSTARS.2015.2483483.

Young, T., Christoffersen, P., Nicholls, K., Lok, L., Doyle, S., Hubbard, B., Stewart, C., Hofstede, C., Bougamont, M., Todd, J., Brennan, P., and Hubbard, A. (2016). High basal melt rates observed on Store Glacier, west Greenland, using phase-sensitive FMCW radar. *American Geophysical Union Fall Meeting, abstract C33A-0769*. San Francisco, December 2016.

Zhao, J., Wang, W., Cheng, Q., and Agterberg, F. (2016). Mapping of Fe mineral potential by spatially weighted principal component analysis in the eastern Tianshan mineral district, China. *Journal of Geochemical Exploration*, 164, 107–121, https://doi.org/10.1016/j.gexplo.2015.11.004.

Zwally, H. J., Abdalati, W., Herring, T., Larson, K., Saba, J., and Steffen, K. (2002). Surface melt-induced acceleration of Greenland ice-sheet flow. *Science*, 297, 218–222, https://doi.org/10.1126/science.1072708.

Zwally, H. J., Li, J., Brenner, A. C., Beckley, M., Cornejo, H. G., DiMarzio, J., Giovinetto, M. B., Neumann, T. A., Robbins, J., Saba, J. L., Yi, D., and Wang, W. (2011). Greenland ice sheet mass balance: distribution of increased mass loss with climate warming; 2003–07 versus 1992–2002. *Journal of Glaciology*, 57(201), 88–102, https://doi.org/10.3189/002214311795306682.

# Appendix A

# Supplementary data tables

**Table A.1:** Summary of the 11 Landsat 8 tiles used as the training dataset for the validation of the algorithms for calculating MODIS lake area and depth in Chapter 3.

| Region | Scene ID | Path | Row | Day of year (2014) | Date | Year |
|---|---|---|---|---|---|---|
| Paakitsoq | LC80090112014184LGN00 | 009 | 011 | 184 | 3 Jul | 2014 |
| Paakitsoq | LC80812332014192LGN00 | 081 | 233 | 192 | 11 Jul | 2014 |
| Paakitsoq | LC80090112014200LGN00 | 009 | 011 | 200 | 19 Jul | 2014 |
| Paakitsoq | LC80090112014216LGN00 | 009 | 011 | 216 | 4 Aug | 2014 |
| Paakitsoq | LC80100112014239LGN00 | 010 | 011 | 239 | 27 Aug | 2014 |
| Store Glacier | LC80110102014182LGN00 | 011 | 010 | 182 | 1 Jul | 2014 |
| Store Glacier | LC80090102014184LGN00 | 009 | 010 | 184 | 3 Jul | 2014 |
| Store Glacier | LC80812342014192LGN00 | 081 | 234 | 192 | 11 Jul | 2014 |
| Store Glacier | LC80110102014214LGN00 | 011 | 010 | 214 | 2 Aug | 2014 |
| Store Glacier | LC80100102014223LGN00 | 010 | 010 | 223 | 11 Aug | 2014 |
| Store Glacier | LC80100102014239LGN00 | 010 | 010 | 239 | 27 Aug | 2014 |

**Table A.2:** Performance indicators for all thresholds tested in Chapter 3 for the dynamic red band thresholding technique for calculating lake areas for the Paakitsoq region. All values of $r$ are significant at the 95% confidence interval ($p < 0.05$). The best-performing threshold is shown in bold italicised text.

| Threshold | Total Landsat 8 lake area ($km^2$) | Landsat 8 lake number | Total MODIS lake area ($km^2$) | Difference (%) in lake area | Number of Landsat 8 lakes predicted | Detection (%) of Landsat 8 lakes | RMSE ($km^2$) | $r$ |
|---|---|---|---|---|---|---|---|---|
| 0.600 | | | 87.9 | 49.4 | 133 | 32.8 | 0.345 | 0.728 |
| 0.610 | | | 92.6 | 46.7 | 140 | 34.5 | 0.347 | 0.717 |
| 0.620 | | | 97.6 | 43.8 | 145 | 35.7 | 0.344 | 0.712 |
| 0.630 | | | 104.0 | 40.1 | 155 | 38.2 | 0.342 | 0.707 |
| 0.640 | | | 110.1 | 36.6 | 161 | 39.7 | 0.338 | 0.706 |
| ***0.645*** | | | ***114.3*** | ***34.2*** | ***169*** | ***41.6*** | ***0.338*** | *0.702* |
| 0.650 | 173.7 | 406 | 117.6 | 32.3 | 171 | 42.1 | 0.341 | 0.696 |
| 0.660 | | | 125.2 | 27.9 | 177 | 43.6 | 0.342 | 0.688 |
| 0.670 | | | 133.7 | 23.0 | 187 | 46.1 | 0.351 | 0.670 |
| 0.680 | | | 142.6 | 17.9 | 197 | 48.5 | 0.353 | 0.663 |
| 0.700 | | | 167.3 | 3.7 | 217 | 53.4 | 0.367 | 0.643 |
| 0.720 | | | 202.1 | -16.3 | 231 | 56.9 | 0.406 | 0.602 |
| 0.750 | | | 278.9 | -60.5 | 262 | 64.5 | 0.490 | 0.535 |

**Table A.3:** Performance indicators for all thresholds tested in Chapter 3 for the dynamic red band thresholding technique for calculating lake areas for the Store Glacier region. All values of $r$ are significant at the 95% confidence interval ($p < 0.05$). The best-performing threshold is shown in bold italicised text.

| Threshold | Total Landsat 8 lake area ($km^2$) | Landsat 8 lake number | Total MODIS lake area ($km^2$) | Difference (%) in lake area | Number of Landsat 8 lakes predicted | Detection (%) of Landsat 8 lakes | RMSE ($km^2$) | $r$ |
|---|---|---|---|---|---|---|---|---|
| 0.600 | | | 61.5 | 49.3 | 116 | 38.9 | 0.306 | 0.700 |
| 0.610 | | | 65.3 | 46.1 | 122 | 40.9 | 0.303 | 0.695 |
| 0.620 | | | 70.6 | 41.8 | 127 | 42.6 | 0.303 | 0.683 |
| 0.630 | | | 75.3 | 37.9 | 129 | 43.3 | 0.301 | 0.680 |
| 0.635 | | | 77.2 | 36.4 | 133 | 44.6 | 0.301 | 0.679 |
| ***0.640*** | | | ***79.1*** | ***34.7*** | ***135*** | ***45.3*** | ***0.301*** | ***0.678*** |
| 0.645 | 121.3 | 298 | 81.2 | 33.0 | 135 | 45.3 | 0.303 | 0.674 |
| 0.650 | | | 84.4 | 30.4 | 137 | 46.0 | 0.303 | 0.671 |
| 0.660 | | | 91.0 | 25.0 | 147 | 49.3 | 0.305 | 0.666 |
| 0.670 | | | 96.4 | 20.5 | 153 | 51.3 | 0.314 | 0.654 |
| 0.680 | | | 103.5 | 14.7 | 163 | 54.7 | 0.314 | 0.661 |
| 0.690 | | | 111.2 | 8.3 | 170 | 57.0 | 0.320 | 0.658 |
| 0.700 | | | 119.7 | 1.3 | 179 | 60.1 | 0.333 | 0.647 |
| 0.720 | | | 128.5 | -5.9 | 184 | 61.7 | 0.342 | 0.643 |

**Table A.4:** Performance indicators for all thresholds tested in Chapter 3 for the NDWI technique for calculating lake areas for the Paakitsoq region. All values of $r$ are significant at the 95% confidence interval ($p < 0.05$). The best-performing threshold is shown in bold italicised text.

| Threshold | Total Landsat 8 lake area ($km^2$) | Landsat 8 lake number | Total MODIS lake area ($km^2$) | Difference (%) in lake area | Number of Landsat 8 lakes predicted | Detection (%) of Landsat 8 lakes | RMSE ($km^2$) | $r$ |
|---|---|---|---|---|---|---|---|---|
| 0.100 | | | 172.6 | 0.6 | 150 | 36.9 | 0.515 | 0.612 |
| 0.110 | | | 125.6 | 27.7 | 126 | 31.0 | 0.404 | 0.703 |
| 0.120 | | | 94.7 | 45.5 | 106 | 26.1 | 0.368 | 0.752 |
| ***0.125*** | | | ***82.2*** | ***52.7*** | ***95*** | ***23.4*** | ***0.369*** | *0.762* |
| 0.130 | | | 73.8 | 57.5 | 86 | 21.2 | 0.374 | 0.760 |
| 0.140 | | | 60.7 | 65.1 | 78 | 19.2 | 0.384 | 0.761 |
| 0.150 | 173.7 | 406 | 49.8 | 71.3 | 67 | 16.5 | 0.401 | 0.750 |
| 0.160 | | | 42.6 | 75.5 | 58 | 14.3 | 0.412 | 0.739 |
| 0.170 | | | 36.3 | 79.1 | 49 | 12.1 | 0.427 | 0.724 |
| 0.180 | | | 31.7 | 81.7 | 48 | 11.8 | 0.438 | 0.715 |
| 0.190 | | | 27.8 | 84.0 | 44 | 10.8 | 0.448 | 0.705 |
| 0.200 | | | 23.9 | 86.2 | 36 | 8.9 | 0.461 | 0.687 |
| 0.250 | | | 13.5 | 92.2 | 23 | 5.7 | 0.493 | 0.658 |

**Table A.5:** Performance indicators for all thresholds tested in Chapter 3 for the NDWI technique for calculating lake areas for the Store Glacier region. All values of $r$ are significant at the 95% confidence interval ($p < 0.05$). The best-performing threshold is shown in bold italicised text.

| Threshold | Total Landsat 8 lake area ($km^2$) | Landsat 8 lake number | Total MODIS lake area ($km^2$) | Difference (%) in lake area | Number of Landsat 8 lakes predicted | Detection (%) of Landsat 8 lakes | RMSE ($km^2$) | $r$ |
|---|---|---|---|---|---|---|---|---|
| 0.100 | | | 171.0 | -41.0 | 130 | 43.6 | 1.434 | 0.182 |
| 0.110 | | | 130.5 | -7.6 | 113 | 37.9 | 1.260 | 0.194 |
| 0.120 | | | 97.6 | 19.5 | 94 | 31.5 | 1.139 | 0.196 |
| 0.130 | | | 77.5 | 36.1 | 81 | 27.2 | 1.047 | 0.193 |
| 0.140 | | | 58.6 | 51.7 | 59 | 19.8 | 0.904 | 0.198 |
| 0.150 | 121.3 | 298 | 47.0 | 61.2 | 50 | 16.8 | 0.730 | 0.229 |
| 0.160 | | | 35.8 | 70.5 | 43 | 14.4 | 0.563 | 0.308 |
| 0.170 | | | 27.1 | 77.7 | 40 | 13.4 | 0.454 | 0.425 |
| 0.180 | | | 21.2 | 82.5 | 34 | 11.4 | 0.425 | 0.487 |
| ***0.190*** | | | ***17.2*** | ***85.8*** | ***30*** | ***10.1*** | ***0.418*** | ***0.541*** |
| 0.200 | | | 13.1 | 89.2 | 26 | 8.7 | 0.423 | 0.583 |
| 0.250 | | | 6.4 | 94.7 | 15 | 5.0 | 0.448 | 0.545 |

**Table A.6:** Performance indicators for all thresholds tested in Chapter 3 for the red/blue band thresholding technique for calculating lake areas for the Paakitsoq region. All values of $r$ are significant at the 95% confidence interval ($p < 0.05$). The best-performing threshold is shown in bold italicised text. Since there is a numerical association between this technique and the NDWI technique, the thresholds in Table A.4 can be used to derive performance indicators for a wider range of thresholds than those presented here.

| **Threshold** | **Total Landsat 8 lake area ($km^2$)** | **Landsat 8 lake number** | **Total MODIS lake area ($km^2$)** | **Difference (%) in lake area** | **Number of Landsat 8 lakes predicted** | **Detection (%) of Landsat 8 lakes** | **RMSE ($km^2$)** | ***r*** |
|---|---|---|---|---|---|---|---|---|
| 0.710 | | | 36.4 | 79.0 | 49 | 12.1 | 0.426 | 0.724 |
| 0.750 | | | 57.5 | 66.9 | 73 | 18.0 | 0.389 | 0.760 |
| 0.760 | | | 65.3 | 62.4 | 81 | 20.0 | 0.378 | 0.763 |
| 0.770 | | | 74.1 | 57.3 | 87 | 21.4 | 0.374 | 0.760 |
| ***0.775*** | | | ***79.2*** | ***54.4*** | ***90*** | ***22.2*** | ***0.371*** | *0.760* |
| 0.780 | | | 84.4 | 51.4 | 96 | 23.6 | 0.372 | 0.755 |
| 0.790 | 173.7 | 406 | 102.1 | 41.2 | 109 | 26.8 | 0.379 | 0.736 |
| 0.800 | | | 121.7 | 30.0 | 121 | 29.8 | 0.400 | 0.707 |
| 0.810 | | | 145.8 | 16.1 | 137 | 33.7 | 0.442 | 0.669 |
| 0.820 | | | 179.9 | -3.5 | 153 | 37.7 | 0.541 | 0.598 |
| 0.830 | | | 226.4 | -30.3 | 176 | 43.3 | 0.695 | 0.531 |
| 0.840 | | | 300.9 | -73.3 | 193 | 47.5 | 0.995 | 0.416 |
| 0.850 | | | 412.7 | -137.6 | 219 | 53.9 | 2.593 | 0.289 |

**Table A.7:** Performance indicators for all thresholds tested in Chapter 3 for the red/blue band thresholding lake technique for calculating lake areas for the Store Glacier region. All values of $r$ are significant at the 95% confidence interval ($p < 0.05$). The best-performing threshold is shown in bold italicised text. Since there is a numerical association between this technique and the NDWI technique, the thresholds in Table A.5 can be used to derive performance indicators for a wider range of thresholds than those presented here.

| Threshold | Total Landsat 8 lake area ($km^2$) | Landsat 8 lake number | Total MODIS lake area ($km^2$) | Difference (%) in lake area | Number of Landsat 8 lakes predicted | Detection (%) of Landsat 8 lakes | RMSE ($km^2$) | $r$ |
|---|---|---|---|---|---|---|---|---|
| ***0.710*** | | | ***27.3*** | ***77.5*** | ***40*** | ***13.4*** | ***0.458*** | ***0.417*** |
| 0.750 | | | 54.8 | 54.8 | 55 | 18.5 | 0.871 | 0.199 |
| 0.760 | | | 63.9 | 47.3 | 63 | 21.1 | 0.942 | 0.196 |
| 0.770 | | | 77.6 | 36.0 | 81 | 27.2 | 1.048 | 0.194 |
| 0.780 | | | 88.8 | 26.8 | 89 | 29.9 | 1.106 | 0.194 |
| 0.790 | 121.3 | 298 | 104.2 | 14.0 | 100 | 33.6 | 1.180 | 0.196 |
| 0.800 | | | 126.8 | -4.5 | 112 | 37.6 | 1.253 | 0.194 |
| 0.810 | | | 147.5 | -21.7 | 120 | 40.3 | 1.363 | 0.186 |
| 0.820 | | | 176.4 | -45.4 | 131 | 44.0 | 1.445 | 0.183 |
| 0.830 | | | 213.8 | -76.3 | 146 | 49.0 | 1.583 | 0.181 |
| 0.840 | | | 262.5 | -116.5 | 164 | 55.0 | 1.855 | 0.163 |
| 0.850 | | | 328.4 | -170.8 | 180 | 60.4 | 2.084 | 0.179 |

**Table A.8:** Full details of all rapid lake-drainage events identified by the application of the FAST algorithm to the Paakitsoq region in Chapter 3.

| Start day of year (2014) | End day of year (2014) | Volume loss ($\times 10^5$ m$^3$) | Surface elevation (m a.s.l.) | Bed elevation (m a.s.l.) | Ice thickness beneath lake (m) |
|---|---|---|---|---|---|
| 192 | 193 | 2.4 | 608 | 297 | 295 |
| 194 | 195 | 2.8 | 829 | 292 | 537 |
| 163 | 164 | 2.2 | 294 | -167 | 455 |
| 191 | 192 | 2.1 | 294 | -167 | 455 |
| 174 | 175 | 2.8 | 721 | 183 | 538 |
| 220 | 223 | 0.7 | 904 | 289 | 617 |
| 230 | 231 | 0.6 | 661 | 245 | 416 |
| 185 | 186 | 5.7 | 951 | 231 | 718 |
| 172 | 173 | 4.8 | 903 | 209 | 694 |
| 193 | 194 | 0.8 | 933 | 174 | 759 |
| 172 | 173 | 3.6 | 907 | 232 | 677 |
| 185 | 186 | 9.1 | 962 | 60 | 899 |
| 192 | 193 | 1.4 | 1056 | 525 | 531 |
| 172 | 173 | 7.6 | 717 | -8 | 723 |
| 194 | 195 | 2.7 | 957 | 63 | 895 |
| 172 | 173 | 3.4 | 1049 | 255 | 794 |
| 191 | 192 | 0.9 | 1097 | 409 | 688 |
| 189 | 190 | 10.8 | 978 | 125 | 850 |
| 196 | 197 | 1.2 | 976 | 245 | 730 |
| 184 | 185 | 0.9 | 1095 | 57 | 1038 |
| 195 | 196 | 6.8 | 1102 | 17 | 1086 |
| 199 | 200 | 3.7 | 1213 | 254 | 960 |
| 194 | 195 | 20.2 | 1124 | 62 | 1064 |
| 189 | 190 | 6.4 | 1171 | 163 | 1007 |
| 194 | 196 | 18.0 | 1162 | 45 | 1117 |
| 223 | 226 | 7.9 | 1055 | 227 | 828 |
| 189 | 190 | 3.2 | 1189 | 116 | 1073 |
| 189 | 190 | 10.1 | 1217 | -54 | 1272 |
| 203 | 205 | 7.8 | 1143 | 232 | 911 |
| 195 | 196 | 2.5 | 1228 | 334 | 893 |
| 199 | 200 | 2.9 | 1101 | 94 | 1008 |
| 194 | 195 | 2.4 | 1239 | 119 | 1121 |
| 181 | 182 | 1.8 | 997 | 75 | 922 |
| 188 | 189 | 0.8 | 1250 | 319 | 928 |
| 207 | 208 | 1.7 | 1341 | 135 | 1206 |
| 190 | 194 | 2.5 | 1018 | -60 | 1078 |
| 230 | 231 | 3.1 | 1379 | 121 | 1258 |
| 199 | 200 | 1.1 | 1333 | 83 | 1250 |
| 206 | 207 | 2.7 | 1437 | 297 | 1140 |
| 185 | 186 | 1.0 | 1257 | 177 | 1082 |
| 230 | 232 | 1.6 | 1454 | 285 | 1170 |
| 230 | 233 | 1.4 | 1453 | 280 | 1173 |
| 215 | 216 | 1.2 | 1449 | 163 | 1286 |

**Table A.9:** Full details of all rapid lake-drainage events identified by the application of the FAST algorithm to the Store Glacier region in Chapter 3.

| Start day of year (2014) | End day of year (2014) | Volume loss ($\times 10^5$ m$^3$) | Surface elevation (m a.s.l.) | Bed elevation (m a.s.l.) | Ice thickness beneath lake (m) |
|---|---|---|---|---|---|
| 169 | 170 | 1.8 | 739 | 242 | 497 |
| 174 | 175 | 1.9 | 915 | 95 | 819 |
| 178 | 181 | 1.0 | 1254 | 579 | 675 |
| 181 | 182 | 1.2 | 952 | -3 | 955 |
| 183 | 184 | 0.9 | 958 | 136 | 822 |
| 184 | 185 | 5.1 | 487 | 26 | 461 |
| 184 | 185 | 3.3 | 975 | 339 | 636 |
| 184 | 185 | 5.8 | 1030 | 346 | 684 |
| 184 | 187 | 5.1 | 948 | 166 | 782 |
| 188 | 189 | 2.1 | 991 | 379 | 612 |
| 189 | 190 | 1.1 | 380 | -224 | 604 |
| 192 | 193 | 6.3 | 1354 | 394 | 960 |
| 197 | 199 | 1.8 | 1205 | 513 | 693 |
| 197 | 199 | 5.9 | 1283 | 514 | 768 |
| 197 | 201 | 3.4 | 1071 | 293 | 777 |
| 199 | 200 | 1.2 | 1355 | 525 | 830 |
| 208 | 209 | 6.8 | 1412 | 504 | 907 |
| 213 | 217 | 2.1 | 1406 | 375 | 1031 |
| 223 | 226 | 15.0 | 1186 | 406 | 779 |

**Table A.10:** Eigenvectors (i.e. loadings) for the PCA conducted in Chapter 4. Eigenvectors are presented for the first three PCs to show the contribution of the original 23 potential controlling factors (Table 4.1) to each PC. Data are presented after the potential controlling factor variables were normalised to correct for their different scales and units (Section 4.3.3). Negative eigenvectors are shown in bold text, and indicate a negative relationship of the original variable to the PC.

| **Potential controlling factor** | **PC1** | **PC2** | **PC3** |
|---|---|---|---|
| Ice thickness | **-0.293** | **-0.120** | 0.189 |
| Ice-surface elevation | **-0.260** | **-0.176** | 0.312 |
| Ice-bed elevation | 0.080 | **-0.117** | 0.261 |
| Lake eccentricity | 0.044 | **-0.016** | **-0.109** |
| Lake orientation | **-0.022** | **-0.021** | 0.064 |
| Lake volume | **-0.136** | 0.405 | **-0.036** |
| Lake area | **-0.097** | 0.394 | **-0.031** |
| Maximum lake water depth | **-0.209** | 0.370 | 0.081 |
| Mean lake water depth | **-0.200** | 0.359 | 0.103 |
| Standard deviation of lake water depth | **-0.210** | 0.334 | 0.141 |
| Lake mean filling rate | **-0.159** | 0.312 | 0.074 |
| Ice-surface slope | 0.278 | 0.136 | **-0.194** |
| Background winter ice velocity | 0.034 | 0.030 | **-0.455** |
| Principal strain rate | 0.010 | 0.060 | **-0.336** |
| von Mises yield criterion | 0.105 | 0.144 | **-0.441** |
| Melt within catchment on day | 0.244 | 0.112 | 0.101 |
| Rain within catchment on day | 0.184 | 0.033 | 0.190 |
| Melt within catchment on previous day | 0.261 | 0.118 | 0.116 |
| Rain within catchment on previous day | 0.197 | 0.036 | 0.187 |
| Cumulative melt within catchment | 0.315 | 0.146 | 0.163 |
| Cumulative rain within catchment | 0.267 | 0.105 | 0.133 |
| Cumulative runoff within catchment | 0.313 | 0.146 | 0.155 |
| Difference between catchment runoff and lake volume | 0.314 | 0.144 | 0.156 |

**Table A.11:** Properties of the 123 Sentinel-2 images used in Chapter 5. All images are from WGS 84 UTM zone 22N, latitude band W and square EC; bold dates indicate Sentinel-2B images; dates marked with an asterisk are sequence-1 images, and all others are sequence-0 images. Cloud cover was determined from the image metadata, representing the percentage of cloud-covered pixels both within the ice-sheet area and off the ice-sheet edge. Data cover was determined from the image metadata, representing the percentage of the total area of the region (i.e. the area on the ice sheet plus the ice-marginal area) over which satellite data were collected.

| Scene ID | Date | Year | Cloud cover (%) | Data cover (%) |
|---|---|---|---|---|
| S2A_OPER_MSI_L1C_DS_MTI__20160502T202602_S20160502T151916_N02.01 | 2 May | 2016 | 38.9 | 100.0 |
| S2A_OPER_MSI_L1C_DS_SGS__20160505T205541_S20160505T152915_N02.02 | 5 May | 2016 | 44.7 | 100.0 |
| S2A_OPER_MSI_L1C_DS_MTI__20160515T203516_S20160515T152912_N02.02 | 15 May | 2016 | 5.4 | 100.0 |
| S2A_OPER_MSI_L1C_DS_SGS__20160518T210306_S20160518T154153_N02.02 | 18 May | 2016 | 31.4 | 38.3 |
| S2A_OPER_MSI_L1C_DS_MTI__20160522T202416_S20160522T151915_N02.02 | 22 May | 2016 | 29.8 | 100.0 |
| S2A_OPER_MSI_L1C_DS_MTI__20160529T201543_S20160529T150918_N02.02 | 29 May | 2016 | 66.1 | 94.3 |
| S2A_OPER_MSI_L1C_DS_SGS__20160601T173946_S20160601T151916_N02.02 | 1 Jun | 2016 | 18.1 | 99.9 |
| S2A_OPER_MSI_L1C_DS_MTI__20160604T203539_S20160604T152915_N02.02 | 4 Jun | 2016 | 60.0 | 99.9 |
| S2A_OPER_MSI_L1C_DS_SGS__20160608T202646_S20160608T150916_N02.02 | 8 Jun | 2016 | 16.2 | 94.2 |
| S2A_OPER_MSI_L1C_DS_MTI__20160611T202435_S20160611T151937_N02.02 | 11 Jun | 2016 | 42.5 | 100.0 |
| S2A_OPER_MSI_L1C_DS_SGS__20160617T192017_S20160617T153910_N02.04 | 17 Jun | 2016 | 25.7 | 38.9 |
| S2A_OPER_MSI_L1C_DS_SGS__20160618T202441_S20160618T151305_N02.04 | 18 Jun | 2016 | 46.7 | 93.2 |
| S2A_OPER_MSI_L1C_DS_MTI__20160621T220258_S20160621T151912_N02.04 | 21 Jun | 2016 | 4.3 | 100.0 |
| S2A_OPER_MSI_L1C_DS_MTI__20160624T203434_S20160624T152911_N02.04 | 24 Jun | 2016 | 16.0 | 100.0 |
| S2A_OPER_MSI_L1C_DS_SGS__20160628T202858_S20160628T150914_N02.04 | 28 Jun | 2016 | 0.1 | 94.0 |
| S2A_OPER_MSI_L1C_DS_MTI__20160701T202434_S20160701T151913_N02.04 | 1 Jul | 2016 | 73.3 | 100.0 |
| S2A_OPER_MSI_L1C_DS_SGS__20160707T192822_S20160707T153908_N02.04 | 7 Jul | 2016 | 0.0 | 38.6 |
| S2A_OPER_MSI_L1C_DS_SGS__20160708T202909_S20160708T151305_N02.04 | 8 Jul* | 2016 | 1.6 | 94.2 |
| S2A_OPER_MSI_L1C_DS_SGS__20160711T203749_S20160711T151912_N02.04 | 11 Jul | 2016 | 0.1 | 100.0 |
| S2A_OPER_MSI_L1C_DS_MTI__20160714T203553_S20160714T152910_N02.04 | 14 Jul | 2016 | 0.3 | 99.9 |
| S2A_OPER_MSI_L1C_DS_SGS__20160718T202939_S20160718T150915_N02.04 | 18 Jul | 2016 | 23.7 | 94.2 |
| S2A_OPER_MSI_L1C_DS_MTI__20160721T202530_S20160721T151913_N02.04 | 21 Jul | 2016 | 0.0 | 100.0 |
| S2A_OPER_MSI_L1C_DS_SGS__20160724T205100_S20160724T153051_N02.04 | 24 Jul | 2016 | 0.0 | 99.9 |
| S2A_OPER_MSI_L1C_DS_SGS__20160727T192945_S20160727T153910_N02.04 | 27 Jul | 2016 | 0.0 | 38.2 |
| S2A_OPER_MSI_L1C_DS_SGS__20160728T202436_S20160728T151306_N02.04 | 28 Jul | 2016 | 63.6 | 94.3 |
| S2A_OPER_MSI_L1C_DS_SGS__20160731T203724_S20160731T151913_N02.04 | 31 Jul | 2016 | 0.0 | 100.0 |
| S2A_OPER_MSI_L1C_DS_MTI__20160803T203554_S20160803T152910_N02.04 | 3 Aug | 2016 | 3.1 | 100.0 |
| S2A_OPER_MSI_L1C_DS_MTI__20160806T204409_S20160806T153909_N02.04 | 6 Aug | 2016 | 14.1 | 38.1 |
| S2A_OPER_MSI_L1C_DS_SGS__20160807T202758_S20160807T150914_N02.04 | 7 Aug | 2016 | 55.9 | 94.4 |
| S2A_OPER_MSI_L1C_DS_MTI__20160810T202535_S20160810T151912_N02.04 | 10 Aug | 2016 | 13.0 | 100.0 |
| S2A_OPER_MSI_L1C_DS_SGS__20160813T204833_S20160813T153046_N02.04 | 13 Aug | 2016 | 0.0 | 100.0 |
| S2A_OPER_MSI_L1C_DS_SGS__20160817T202447_S20160817T151257_N02.04 | 17 Aug | 2016 | 0.7 | 94.4 |
| S2A_OPER_MSI_L1C_DS_MTI__20160830T202522_S20160830T151909_N02.04 | 30 Aug | 2016 | 2.2 | 100.0 |
| S2A_OPER_MSI_L1C_DS_SGS__20160902T204312_S20160902T153051_N02.04 | 2 Sep | 2016 | 0.7 | 100.0 |
| S2A_OPER_MSI_L1C_DS_SGS__20160906T202733_S20160906T151257_N02.04 | 6 Sep | 2016 | 35.9 | 94.5 |

| Scene ID | Date | Year | Cloud cover (%) | Data cover (%) |
|---|---|---|---|---|
| S2A_OPER_MSI_L1C_DS_SGS__20160909T203815_S20160909T151907_N02.04 | 9 Sep | 2016 | 21.0 | 100.0 |
| S2A_OPER_MSI_L1C_DS_MTI__20160912T203709_S20160912T152817_N02.04 | 12 Sep | 2016 | 0.0 | 100.0 |
| S2A_OPER_MSI_L1C_DS_SGS__20160915T210159_S20160915T154130_N02.04 | 15 Sep | 2016 | 1.7 | 38.2 |
| S2A_OPER_MSI_L1C_DS_MTI__20160926T201345_S20160926T150955_N02.04 | 26 Sep | 2016 | 0.3 | 93.9 |
| S2A_OPER_MSI_L1C_DS_MTI__20170501T214510_S20170501T150245_N02.05 | 1 May | 2017 | 5.8 | 12.0 |
| S2A_OPER_MSI_L1C_DS_SGS__20170503T191736_S20170503T153908_N02.05 | 3 May | 2017 | 53.4 | 38.3 |
| S2A_OPER_MSI_L1C_DS_SGS__20170504T184715_S20170504T150913_N02.05 | 4 May | 2017 | 6.2 | 94.3 |
| S2A_OPER_MSI_L1C_DS_SGS__20170510T190516_S20170510T152952_N02.05 | 10 May | 2017 | 74.0 | 100.0 |
| S2A_OPER_MSI_L1C_DS_SGS__20170513T191640_S20170513T153908_N02.05 | 13 May | 2017 | 17.1 | 38.3 |
| S2A_OPER_MSI_L1C_DS_SGS__20170520T204519_S20170520T152909_N02.05 | 20 May | 2017 | 85.4 | 100.0 |
| S2A_OPER_MSI_L1C_DS_MTI__20170521T214508_S20170521T150303_N02.05 | 21 May | 2017 | 32.3 | 12.0 |
| S2A_OPER_MSI_L1C_DS_SGS__20170523T191718_S20170523T153908_N02.05 | 23 May | 2017 | 27.9 | 38.4 |
| S2A_OPER_MSI_L1C_DS_SGS__20170524T184910_S20170524T150914_N02.05 | 24 May | 2017 | 53.2 | 94.3 |
| S2A_OPER_MSI_L1C_DS_SGS__20170527T203457_S20170527T151941_N02.05 | 27 May | 2017 | 0.0 | 100.0 |
| S2A_OPER_MSI_L1C_DS_SGS__20170530T190629_S20170530T152909_N02.05 | 30 May | 2017 | 3.6 | 100.0 |
| S2A_OPER_MSI_L1C_DS_MTI__20170531T200345_S20170531T150133_N02.05 | 31 May | 2017 | 0.0 | 12.0 |
| S2A_OPER_MSI_L1C_DS_SGS__20170602T191856_S20170602T153908_N02.05 | 2 Jun | 2017 | 0.0 | 38.4 |
| S2A_OPER_MSI_L1C_DS_SGS__20170603T202739_S20170603T150913_N02.05 | 3 Jun | 2017 | 28.4 | 94.2 |
| S2A_OPER_MSI_L1C_DS_SGS__20170606T190320_S20170606T151911_N02.05 | 6 Jun | 2017 | 75.9 | 100.0 |
| S2A_OPER_MSI_L1C_DS_SGS__20170610T203751_S20170610T145915_N02.05 | 10 Jun | 2017 | 1.6 | 11.7 |
| S2A_OPER_MSI_L1C_DS_MTI__20170612T204838_S20170612T153906_N02.05 | 12 Jun | 2017 | 1.9 | 38.6 |
| S2A_OPER_MSI_L1C_DS_SGS__20170613T184952_S20170613T150911_N02.05 | 13 Jun | 2017 | 12.5 | 94.2 |
| S2A_OPER_MSI_L1C_DS_SGS__20170616T204414_S20170616T152036_N02.05 | 16 Jun | 2017 | 22.1 | 100.0 |
| S2A_OPER_MSI_L1C_DS_SGS__20170619T191008_S20170619T152906_N02.05 | 19 Jun | 2017 | 42.4 | 100.0 |
| S2A_OPER_MSI_L1C_DS_SGS__20170626T190855_S20170626T151907_N02.05 | 26 Jun | 2017 | 73.4 | 100.0 |
| S2A_OPER_MSI_L1C_DS_SGS__20170629T205426_S20170629T152904_N02.05 | 29 Jun | 2017 | 83.7 | 100.0 |
| S2B_OPER_MSI_L1C_DS_SGS__20170701T190010_S20170701T152119_N02.05 | **1 Jul** | 2017 | 75.7 | 100.0 |
| S2A_OPER_MSI_L1C_DS_SGS__20170703T184913_S20170703T151120_N02.05 | 3 Jul | 2017 | 60.7 | 94.0 |
| S2A_OPER_MSI_L1C_DS_SGS__20170706T204345_S20170706T152002_N02.05 | 6 Jul | 2017 | 47.9 | 100.0 |
| S2B_OPER_MSI_L1C_DS_SGS__20170707T210324_S20170707T153917_N02.05 | **7 Jul** | 2017 | 11.3 | 38.2 |
| S2A_OPER_MSI_L1C_DS_SGS__20170709T173703_S20170709T152906_N02.05 | 9 Jul | 2017 | 11.8 | 100.0 |
| S2B_OPER_MSI_L1C_DS_MTI__20170711T202537_S20170711T152300_N02.05 | **11 Jul*** | 2017 | 0.7 | 99.7 |
| S2A_OPER_MSI_L1C_DS_MTI__20170712T205120_S20170712T154011_N02.05 | 12 Jul | 2017 | 7.6 | 38.6 |
| S2A_OPER_MSI_L1C_DS_SGS__20170713T204140_S20170713T150911_N02.05 | 13 Jul | 2017 | 8.6 | 94.2 |
| S2A_OPER_MSI_L1C_DS_SGS__20170716T192027_S20170716T151910_N02.05 | 16 Jul | 2017 | 77.8 | 72.1 |
| S2B_OPER_MSI_L1C_DS_SGS__20170717T193432_S20170717T153906_N02.05 | **17 Jul** | 2017 | 86.0 | 38.1 |
| S2B_OPER_MSI_L1C_DS_SGS__20170718T190218_S20170718T150911_N02.05 | **18 Jul** | 2017 | 0.0 | 94.5 |
| S2B_OPER_MSI_L1C_DS_SGS__20170721T204016_S20170721T152003_N02.05 | **21 Jul** | 2017 | 1.0 | 100.0 |
| S2A_OPER_MSI_L1C_DS_SGS__20170722T192842_S20170722T153907_N02.05 | 22 Jul | 2017 | 7.9 | 32.6 |
| S2A_OPER_MSI_L1C_DS_MTI__20170723T201421_S20170723T151115_N02.05 | 23 Jul | 2017 | 31.2 | 94.3 |
| S2B_OPER_MSI_L1C_DS_SGS__20170724T190805_S20170724T152928_N02.05 | **24 Jul** | 2017 | 67.5 | 100.0 |
| S2B_OPER_MSI_L1C_DS_SGS__20170727T205402_S20170727T153905_N02.05 | **27 Jul** | 2017 | 26.4 | 37.9 |
| S2B_OPER_MSI_L1C_DS_MTI__20170728T215826_S20170728T151149_N02.05 | 28 Jul | 2017 | 2.9 | 94.6 |
| S2A_OPER_MSI_L1C_DS_SGS__20170729T190656_S20170729T152908_N02.05 | 29 Jul | 2017 | 0.0 | 100.0 |
| S2A_OPER_MSI_L1C_DS_MTI__20170730T200122_S20170730T150103_N02.05 | 30 Jul | 2017 | 12.2 | 0.1 |

| Scene ID | Date | Year | Cloud cover (%) | Data cover (%) |
|---|---|---|---|---|
| S2B_OPER_MSI_L1C_DS_SGS__20170731T190742_S20170731T151908_N02.05 | **31 Jul** | 2017 | 2.9 | 100.0 |
| S2A_OPER_MSI_L1C_DS_EPA__20170825T184028_S20170801T154207_N02.05 | 1 Aug | 2017 | 92.8 | 38.2 |
| S2A_OPER_MSI_L1C_DS_SGS__20170802T203514_S20170802T150912_N02.05 | 2 Aug | 2017 | 44.2 | 94.4 |
| S2B_OPER_MSI_L1C_DS_SGS__20170803T204915_S20170803T152905_N02.05 | **3 Aug** | 2017 | 0.1 | 100.0 |
| S2A_OPER_MSI_L1C_DS_EPA__20170813T200652_S20170805T151911_N02.05 | 5 Aug | 2017 | 7.3 | 100.0 |
| S2B_OPER_MSI_L1C_DS_EPA__20170817T011450_S20170806T153908_N02.05 | **6 Aug** | 2017 | 8.4 | 38.0 |
| S2B_OPER_MSI_L1C_DS_EPA__20170821T205056_S20170807T150909_N02.05 | **7 Aug** | 2017 | 90.7 | 94.5 |
| S2A_OPER_MSI_L1C_DS_SGS__20170808T205239_S20170808T152908_N02.05 | 8 Aug | 2017 | 8.3 | 100.0 |
| S2A_OPER_MSI_L1C_DS_MTI__20170814T165608_S20170809T150205_N02.05 | 9 Aug | 2017 | 0.0 | 12.2 |
| S2B_OPER_MSI_L1C_DS_SGS__20170810T204110_S20170810T151907_N02.05 | **10 Aug** | 2017 | 1.8 | 100.0 |
| S2A_OPER_MSI_L1C_DS_MTI__20170811T205221_S20170811T153907_N02.05 | 11 Aug | 2017 | 0.0 | 38.0 |
| S2A_OPER_MSI_L1C_DS_MTI__20170812T201217_S20170812T150912_N02.05 | 12 Aug | 2017 | 0.0 | 94.5 |
| S2B_OPER_MSI_L1C_DS_SGS__20170813T191710_S20170813T152922_N02.05 | **13 Aug** | 2017 | 3.9 | 100.0 |
| S2B_OPER_MSI_L1C_DS_MTI__20170814T200114_S20170814T150211_N02.05 | **14 Aug** | 2017 | 18.3 | 12.5 |
| S2A_OPER_MSI_L1C_DS_SGS__20170815T204038_S20170815T152131_N02.05 | 15 Aug | 2017 | 13.5 | 100.0 |
| S2B_OPER_MSI_L1C_DS_SGS__20170820T190822_S20170820T151905_N02.05 | **20 Aug** | 2017 | 87.2 | 100.0 |
| S2A_OPER_MSI_L1C_DS_SGS__20170821T192359_S20170821T153907_N02.05 | 21 Aug | 2017 | 2.4 | 38.0 |
| S2A_OPER_MSI_L1C_DS_SGS__20170822T203406_S20170822T150912_N02.05 | 22 Aug | 2017 | 87.8 | 94.5 |
| S2B_OPER_MSI_L1C_DS_MTI__20170824T200111_S20170824T145909_N02.05 | **24 Aug** | 2017 | 59.0 | 12.5 |
| S2A_OPER_MSI_L1C_DS_MTI__20170825T202402_S20170825T152102_N02.05 | 25 Aug | 2017 | 2.1 | 100.0 |
| S2B_OPER_MSI_L1C_DS_SGS__20170826T175058_S20170826T153901_N02.05 | **26 Aug**[*] | 2017 | 1.6 | 35.3 |
| S2B_OPER_MSI_L1C_DS_SGS__20170827T190042_S20170827T150906_N02.05 | **27 Aug** | 2017 | 0.4 | 94.6 |
| S2A_OPER_MSI_L1C_DS_SGS__20170904T203819_S20170904T152129_N02.05 | 4 Sep | 2017 | 31.2 | 100.0 |
| S2B_OPER_MSI_L1C_DS_SGS__20170905T205951_S20170905T154040_N02.05 | **5 Sep** | 2017 | 14.5 | 38.0 |
| S2B_OPER_MSI_L1C_DS_SGS__20170906T204006_S20170906T150903_N02.05 | **6 Sep** | 2017 | 50.8 | 94.6 |
| S2A_OPER_MSI_L1C_DS_SGS__20170907T191313_S20170907T153100_N02.05 | 7 Sep | 2017 | 81.2 | 100.0 |
| S2A_OPER_MSI_L1C_DS_MTI__20170908T200118_S20170908T150039_N02.05 | 8 Sep | 2017 | 67.6 | 12.5 |
| S2A_OPER_MSI_L1C_DS_SGS__20170911T204135_S20170911T150909_N02.05 | 11 Sep | 2017 | 91.4 | 94.7 |
| S2B_OPER_MSI_L1C_DS_SGS__20170912T204938_S20170912T152922_N02.05 | **12 Sep** | 2017 | 72.1 | 100.0 |
| S2A_OPER_MSI_L1C_DS_SGS__20170918T202053_S20170918T145910_N02.05 | 18 Sep | 2017 | 0.1 | 12.5 |
| S2A_OPER_MSI_L1C_DS_SGS__20170920T193016_S20170920T153925_N02.05 | 20 Sep | 2017 | 41.2 | 37.7 |
| S2A_OPER_MSI_L1C_DS_SGS__20170921T185435_S20170921T150919_N02.05 | 21 Sep | 2017 | 58.5 | 93.9 |
| S2B_OPER_MSI_L1C_DS_SGS__20170922T174220_S20170922T152925_N02.05 | **22 Sep** | 2017 | 70.8 | 100.0 |
| S2B_OPER_MSI_L1C_DS_MPS__20170928T190017_S20170923T145920_N02.05 | **23 Sep** | 2017 | 12.3 | 24.3 |
| S2A_OPER_MSI_L1C_DS_MTI__20170924T202301_S20170924T151944_N02.05 | 24 Sep | 2017 | 76.0 | 100.0 |
| S2B_OPER_MSI_L1C_DS_MTI__20170925T205126_S20170925T153949_N02.05 | **25 Sep** | 2017 | 28.9 | 38.0 |
| S2B_OPER_MSI_L1C_DS_SGS__20170926T203803_S20170926T150943_N02.05 | **26 Sep** | 2017 | 94.5 | 36.3 |
| S2A_OPER_MSI_L1C_DS_SGS__20170927T174015_S20170927T153010_N02.05 | 27 Sep | 2017 | 69.5 | 100.0 |
| S2B_OPER_MSI_L1C_DS_SGS__20170929T185920_S20170929T152113_N02.05 | **29 Sep** | 2017 | 29.9 | 100.0 |
| S2A_OPER_MSI_L1C_DS_SGS__20170930T191945_S20170930T154036_N02.05 | 30 Sep | 2017 | 1.9 | 38.9 |

**Table A.12:** Properties of the 17 Landsat 8 images used in Chapter 5. Cloud cover was calculated as the percentage of pixels both on and off the ice sheet that were obscured by clouds (i.e. those with a band-6 value > 0.100; Section 5.3.2). Data cover was calculated as the percentage of the total area of the region (i.e. the area on the ice sheet plus the ice-marginal area) for which satellite data had been collected. An asterisk denotes that the image was used for comparing lake areas calculated from the two satellites and for validating the lake depths from Sentinel-2, but that the image was not used for lake tracking in summer 2016 because a contemporaneous higher-resolution, and therefore more favourable, Sentinel-2 image was available (cf. Table A.11).

| Scene ID | Path | Row | Date | Year | Cloud cover (%) | Data cover (%) |
|---|---|---|---|---|---|---|
| LC80100112016149LGN01 | 010 | 011 | 28 May | 2016 | 85.9 | 95.1 |
| LC80080112016151LGN01 | 008 | 011 | 30 May | 2016 | 8.4 | 72.8 |
| LC80822332016157LGN01 | 082 | 233 | 5 Jun | 2016 | 17.3 | 100.0 |
| LC80090112016158LGN01 | 009 | 011 | 6 Jun | 2016 | 21.6 | 100.0 |
| LC80100112016165LGN01 | 010 | 011 | 13 Jun | 2016 | 43.9 | 95.3 |
| LC80090112016174LGN01 | 009 | 011 | 22 Jun | 2016 | 33.9 | 100.0 |
| LC80100112016181LGN01 | 010 | 011 | 29 Jun | 2016 | 35.0 | 95.2 |
| LC80080112016183LGN01 | 008 | 011 | 1 Jul* | 2016 | 60.8 | 72.6 |
| LC80100112016197LGN01 | 010 | 011 | 15 Jul | 2016 | 21.0 | 95.1 |
| LC80812332016198LGN01 | 081 | 233 | 16 Jul | 2016 | 19.0 | 93.7 |
| LC80080112016199LGN01 | 008 | 011 | 17 Jul | 2016 | 5.9 | 72.8 |
| LC80100112016213LGN01 | 010 | 011 | 31 Jul* | 2016 | 18.5 | 95.2 |
| LC80080112016215LGN01 | 008 | 011 | 2 Aug | 2016 | 12.2 | 72.6 |
| LC80090112016222LGN01 | 009 | 011 | 9 Aug | 2016 | 18.4 | 100.0 |
| LC80100112016229LGN01 | 010 | 011 | 16 Aug | 2016 | 18.3 | 95.2 |
| LC80080112016231LGN01 | 008 | 011 | 18 Aug | 2016 | 6.5 | 72.7 |
| LC80080112016247LGN01 | 008 | 011 | 3 Sep | 2016 | 8.8 | 73.2 |